Dissertation

Comparative analyses of DNA damage response pathways in healthy and NBS-patient derived iPSCs, hepatic endoderm, neural progenitor cells and neurons

Vanessa Cristina Meira de Amorim

2025

Aus dem Institut für Stammzellforschung und Regenerative Medizin
der Heinrich-Heine-Universität Düsseldorf
Direktor Leiter Dr. James Adjaye

Comparative analyses of DNA damage response pathways in healthy and NBS-patient derived iPSCs, hepatic endoderm, neural progenitor cells and neurons

Dissertation

zur Erlangung des Grades eines Doktors der Medizin der Medizinischen Fakultät der Heinrich-Heine-Universität Düsseldorf

vorgelegt von

Vanessa Cristina Meira de Amorim

2025

As an inaugural dissertation printed by permission of the
Faculty of Medicine at Heinrich Heine University Düsseldorf
signed:
Dean: Prof. Dr. med. Nikolaj Klöcker
First examiner: Prof. Dr. James Adjaye
Second examiner: Prof. Constantin Czekelius

Zusammenfassung (Deutsch)

Der ubiquitär vorkommende Umweltschadstoff Benzo[a]pyren entsteht als Nebenprodukt bei unvollständiger Verbrennung von organischem Material und wird im Körper zu dem hochkarzinogenen Benzo[a]pyren-diol-epoxid (BPDE) verstoffwechselt. BPDE reagiert mit der DNA und bildet Addukte, die zu einer Basensubstitution führen, falls sie nicht durch die Nukleotidexzisionsreparatur (NER) entfernt werden. Aus den so entstandenen Mutationen können sich im Laufe der Zeit Tumore entwickeln. Es ist bekannt, dass verschiedene Zelltypen unterschiedlich auf genotoxische Schäden reagieren. Stammzellen und insbesondere pluripotente Stammzellen (pluripotent stem cells, PSCs), haben eine robuste DNA-Schadensreparatur. Diese ist essentiell, um zu verhindern, dass sich mutierte Zellen stabilisieren und so rasch vermehren, dass Tumore entstehen.

Vor diesem Hintergrund wurde in dieser Arbeit zum ersten Mal eine vergleichende Analyse der DNA-Schadensantwort nach BPDE Exposition in humanen induzierten pluripotenten Stammzellen (human induced pluripotent stem cells, hiPSCs) und ihren Nachkommen der ektodermalen und endodermalen Linie durchgeführt. Darüber hinaus wurden auch hiPSC und aus ihnen differenzierte neuronale Vorläuferzellen (neuroprogenitor cells, NPCs) von Patienten, die am Nijmegen Breakage Syndrom, einer Erkrankung bei der die DNA-Reparatur defekt ist, und die durch Mikrozephalie, chromosomale Instabilität und ein erhöhtes Tumorrisiko gekennzeichnet ist, nach BPDE Exposition untersucht und mit ihren gesunden Pendants verglichen.

Transkriptomanalysen zeigten, zusammen mit Proteinanalysen durch Immunfärbungen und Western Blots, dass hiPSC im Vergleich zu NPCs und Zellen des hepatischen Endoderms eine robustere Reaktion auf BPDE aufweisen. Hierbei ist in iPSCs die Expression verschiedener Zielgene im Kontext der p-53-vermittelten DNA-Schadensantwort erhöht. Dies umfasst z.B. den Bypass von DNA-Läsionen, Zellzyklus-Kontrollpunkte und den extrinsischen Apoptoseweg. Interessanterweise zeigten die zu neuronalen Zellen differenzierten hiPSC nach BPDE-Exposition eine erhöhte Expression von Genen der NER und des intrinsischen Apoptosewegs was stärker der in der Literatur beschrieben klassischen Reaktion auf BPDE ähnelt. hiPSCs und NPCs von NBS Patienten reagierten anders auf die BPDE-Behandlung als Wildtyp-Zellen. Ihre Apoptoseantwort war reduziert und sie zeigten keinen Anstieg von p53 oder MDM2-Expression. Insbesondere die NBS-hiPSC zeigten eine erhöhte Transkription von tumorassoziierten Genen und eine Repression von Genen der DNA-Reparatur.

Insgesamt hat diese Arbeit die Unterschiede der DNA-Schadensreparatur zwischen somatischen Zellen und Stammzellen aufgezeigt und dass weitere Untersuchungen des Effekts von BPDE auf die embryonale Entwicklung notwendig sind. Außerdem wurde die spezifische DNA-Schadensantwort auf BPDE von gesunden Zellen und Zellen mit einer NBS-Mutation untersucht.

Summary (English)

Benzo[a]pyrene diol epoxide (BPDE) is a highly carcinogenic metabolite of the environmental contaminant Benzo[a]pyrene, which is commonly found as a byproduct of incomplete combustion of organic matter. BPDE reacts with the DNA to form BPDE-DNA bulky adducts which, if not removed by the nucleotide excision repair (NER) pathway, can lead to mutations due to DNA base-pair substitution and consequently to tumorigenesis. It is well-known that different cell types react differently to genotoxic insults. Stem cells, and particularly pluripotent stem cells (PSC), have a robust DNA damage response, essential to avoid the stabilization and fast propagation of mutant cells that can lead to malignancies.

With that in mind, this work performed for the first time a comparative analysis of the DNA damage response to BPDE in human induced pluripotent stem cells (hiPSCs) and their progeny differentiated into cells from the ectoderm and endoderm embryonic layers. Furthermore, hiPSCs and differentiated neuroprogenitor cells (NPCs) derived from patients suffering from Nijmegen Breakage Syndrome, a chromosomal instability disorder characterized by microcephaly, defective DNA repair and increased risk of malignancies, were also investigated in the context of BPDE exposure and compared to their healthy counterparts. Transcriptomics analysis, coupled with protein content analysis through immunostaining and western blots, revealed that hiPSCs have a robust reaction to BPDE exposure when compared to NPCs and hepatic endoderm cells, with an enhanced expression of several targets related to the p-53mediated DNA damage response, including DNA lesion bypass, cell cycle checkpoints and extrinsic apoptosis.

Interestingly, hiPSCs differentiated into somatic cells (neuronal cultures) were also subjected to BPDE exposure and showed a response to BPDE more in line with the classic response seen in the literature in other somatic cells, with enhanced expression of NER and intrinsic apoptosis markers. Additionally, hiPSC and NPCs harbouring an NBS mutation reacted differently to BPDE treatment than WT cells, showing less apoptotic response, no p53 or MDM2 increase and particularly in the case of NBS-hiPSCs, increased transcription of cancer-related targets and the repression of DNA-repair pathways transcription. Overall, this work emphasized the differences between the DNA damage response in somatic cells and stem cells and highlighted the need for further investigation of the effects of BPDE on the embryonic developmental stage, while also exploring the differential DNA damage response to BPDE mounted by healthy cells and those with an NBS mutation.

Abbreviations

53BP1	Tumor suppressor p53-binding protein 1
ABCG2	ATP binding cassette subfamily g member 2 (JR Blood Group)
AD	Alzheimer's disease
AFP	Alfa fetoprotein
ALB	Albumin
ALS	Amyotrophic lateral sclerosis
ALS/PDC	Western Pacific amyotrophic lateral sclerosis and Parkinsonism-dementia complex
ATM	Ataxia telangiectasia mutated
ATR	Ataxia telangiectasia and Rad3 related
ATRIP	ATR interactin protein
B[a]p	Benzo[a]pyrene
BAX	BCL2 associated X, apoptosis regulator
BBC3	Bcl-2-binding component 3
BDNF	Brain-derived neurotrophic growth factor
BER	Base excision repair
BMP	Bone morphogenic protein
BMP4	Bone morphogenic protein 4
BPDE	Benzo[a]pyrene diol epoxide
BRCA1	Breast cancer type 1 susceptibility protein
BRCA2	Breast cancer type 2 susceptibility protein
BSA	Bovine serum albumine
BTG2	BTG anti-Proliferation Factor 2
CALCR	Calcitonin receptor
CDC25A	cell division cycle 25A
CDH1	Cadherin 1
CDK7	Cyclin dependent kinase 7
CDKN1A	Cyclin Dependent Kinase Inhibitor 1A
cDNA	Complementary deoxyribonucleic acid
CER1	Cerberus 1, DAN Family BMP Antagonist
CETN2	Centrin 2
CHEK1	Checkpoint kinase 1
CHEK2	Checkpoint kinase 2
c-MYC	MYC proto-oncogene, bHLH transcription factor
CNS	Central nervous system
CSA	Cockayne Syndrome A
CSB	Cockayne Syndrome B
CtIP	CtBP-interacting protein
CXCL12	C-X-C motif chemokine 12
CXCR4	Chemokine receptor 4
CYP	Cytochrome-P450-dependent monooxygenases
DCX	Doublecortin
DDB1	DNA damage-binding protein 1
DDB2	DNA damage-binding protein 2
DDIT3	DNA damage inducible transcript 3

DE	Definitive endoderm
DMEM/F12	Dulbecco's Modified Eagle Medium/Nutrient Mixture F-12
DMSO	Dimethyl sulfoxide
DNA	Deoxyribonucleic acid
DNA-PK	DNA-dependent protein kinase catalytic subunit
DNAse	Deoxyribonuclease
DNMT3B	DNA methyltransferase 3 Beta
DPBS	Dulbecco's Phosphate-Buffered Saline
DRR	DNA damage response
DSBR	Double-strand break repair
E2F1	E2F Transcription Factor 1
EdU	5-ethynyl-2'-deoxyuridine
EGF	Epidermal growth factor
ERCC1	ERCC excision repair 1, endonuclease non-catalytic subunit
ERK1	Extracellular signal-regulated kinase 1
ERK2	Extracellular signal-regulated kinase 2
ESC	Embryonic stem cell
EXO1	Exonuclease 1
EZH2	Enhancer Of Zeste 2 Polycomb Repressive Complex 2 Subunit
FANCC	Fanconi Anemia complementation group C
FAS	Fas cell surface death receptor
FDA	Food and Drugs Administration
FEN1	Flap structure-specific endonuclease 1
FGF2	Fibroblast growth factor 2
GADD45A	Growth arrest and DNA damage inducible alpha
GDNF	Glial cell line-derived neurotrophic factor
GFAP	Glial fibrillary acidic protein
GG-NER	Global genome repair
GO	Gene ontology
GREM1	Gremlin 1, DAN Family BMP Antagonist
GSK3	Glycogen synthase kinase 3
H2AX	H2A histone family member X
HE	Hepatic endoderm
hESC	Human embryonic stem cell
HGF	Hepatocyte growth factor
hiPSC	Human induced pluripotent stem cell
HLCs	Hepatocyte-like cells
HNF4α	Hepatocyte nuclear factor 4 alpha
HR	Homologous recombination
HRP	Horseradish peroxidase
HSP1B	Heat shock protein family B (Small) member 1
IGF	Insulin-like groth factor
INHBA	Inhibin Subunit Beta A
INO80	INO80 Complex ATPase Subunit
iPSC	Induced pluripotent stem cell
JNK	c-Jun N-terminal kinase

KEGG	Kyoto Encyclopedia of Genes and Genomes
Ki67	Antigen Kiel 67
KLF4	Krüppel-like factor 4
KRT18	Keratin 18
KRT19	Keratin 19
LCL	Lymphoblastoid cell lines
LIG1	Dna ligase I
LIG3	Dna ligase III
LigIV	Dna ligase IV
MAP2	Microtubule-associated protein 2
MAPK	Mitogen-Activated Protein Kinase 1
MAT1	Ménage à trois-1
MCM9	Minichromosome Maintenance 9 Homologous Recombination Repair Factor
MDM2	Mouse double minute 2 homolog
MEF	Murine embrzonic fibroblast
MMR	Mismatch repair pathway
MRE11	MRE11 Homolog Double Strand Break Repair Nuclease
mRNA	Messenger ribonucleic acid
MSH6	MutS homolog 6
NAM	New Alternative Methods
NAP1L1	Nucleosome Assembly Protein 1 Like 1
NBN	Nibrin
NBS	Nijmegen Breakage Syndrome
NDM	Neural differentiation medium
NEEA	Non-essential amino acids
NEIL1	Nei like DNA glycosylase 1
NEIL2	Nei like DNA glycosylase 2
NER	Nucleotide excision repair
NESTIN	Neuroepithelial stem cell protein
NHDF	Normal human dermal fibroblast
NHEJ	Non-homologous end joining
NIM	Neural induction medium
NODAL	Activin/nodal growth differentiation factor
NPC	Neural progenitor cell
NT3	Neurotrophic factor 3
OCT4	Octamer-binding transcription factor 4
OECD	Organisation for Economic Co-operation and Development
OSM	Oncostatin M
PAH	Polycyclic aromatic hydrocarbons
PAX6	Paired box 6
PAXX	Paralog of XRCC4 and XLF
PBS	Phosphate buffered saline
PCNA	Proliferating cell nuclear agent
PFA	Paraformaldehyde
PHH	Primary human hepatocytes
PI	Propidium iodine

PLK2	Polo kinase 2
POLB	Dna polymerase beta
POLD1	Dna polymerase D1
POLE	DNA polymerase epsilon
POLδ	DNA polymerase delta
POLζ	DNA polymerase zeta
POLη	DNA polymerase eta
POLι	DNA polymerase iota
POLκ	DNA polymerase kappa
POU5F1	POU Class 5 Homeobox 1
PPARGC1A	PPARG coactivator 1 alpha
PPM1D	Protein phosphatase, Mg2+/Mn2+ dependent 1D
PRAP1	Proline rich acidic protein 1
PSC	Pluripotent stem cell
qRT-PCR	Quantitative real time polymerase chain reaction
RAD17	Cell cycle checkpoint protein RAD17
RAD23B	Human Rad23 homolog B
RAD50	RAD50 double strand break repair protein
RAD51	DNA repair protein RAD51 homolog 1
RAD51C	CX3 complex formed by RAD51 homolog C
RAD54	DNA repair and recombination protein RAD54-like
RAP1	Ras-related protein 1
RBFOX3	RNA binding fox-1 homolog 3
RNA	Ribonucleic acid
RNAas	Ribonuclase
RNF168	Ring finger protein 168
RNF8	Ring finger protein 8
ROCK	Rho kinase
RPA	Replication protein A
RPA2	Replication protein A2
RPL0	Ribosomal protein lateral stalk subunit P0
RT	Room temperature
S100B	S100 calcium-binding protein B
SCC	Saline sodium citrate
SD	Standard deviation
SDS	Sodium dodecyl sulfate
SEM	Standard error of the mean
SESN1	Sestrin 1
SETMAR	SET domain and mariner transposase fusion gene
SFN	Stratifin
SHH	Sonic Hedgehog
SMARCAD1	SWI/SNF-related, matrix-Associated Actin-Dependent Regulator Of Chromatin, Subfamily A, Containing DEAD/H Box 1
SOX1	SRY-Box Transcription Factor 1
SOX17	SRY-box transcription factor 17

SOX2	SRY-box transcription factor 2
ssDNA	3′ single-stranded DNA
SSEA4	Stage-specific embryonic antigen-4
TBST buffer	Tris-buffered saline and polysorbate 20 buffer
TC-NER	Trancription coupled repair
TE buffer	Tris-EDTA buffer
TFIIH	Transcription factor II H complex
TGFB1	Transforming Growth Factor Beta 1
TGF-β	Transforming growth factor beta
TLS	Translesion synthesis
TNFRSF10A	TNF Receptor Superfamily Member 10A
TNFRSF10B	TNF Receptor Superfamily Member 10B
TNFRSF10C	TNF Receptor Superfamily Member 10C
TNFRSF10D	TNF Receptor Superfamily Member 10D
TOPBP1	DNA topoisomerase 2-binding protein 1
TP53	Tumor protein p53
TP53BP1	Tumor Protein P53 Binding Protein 1
TP73	Tumour supressor protein 73
TUJ1	Class III beta-tubulin
UNG1	Uracil DNA glycosylase 1
UNG2	Uracil DNA glycosylase 2
UV-DDB	DNA damage-binding protein complex
UVSSA	UV stimulated scaffold protein A
VEGF	Vascular endothelial growth factor
WB	Western blot
WNT	Wingless and Int-1
XLF	XRCC4-like factor
XPB	Xeroderma pigmentosum group B
XPC	Xeroderma pigmentosum group C
XPF	Xeroderma pigmentosum group F
XPG	Xeroderma pigmentosum group G
XRCC3	X-ray repair cross complementing 3
XRCC4	X-ray repair cross complementing 4

List of figures

List of supplementary figures

List of tables

Table of Contents

1. Introduction

1.1. Human induced pluripotent stem cells

In the past few decades, there has been a worldwide push to replace animal experimentation and the 3Rs, with its tenets of replacement, reduction and refinement, serve as a guideline in this goal (1). There are many problems with animal experimentation including ethical issues and difficulties in recreating specific pathologies. The pharmaceutical and chemical industries contend with the high costs of animal experiments as well as a failure rate in translating animal effects to human subjects of up to 90% (2,3). A promising alternative for animal experimentation is the use of human pluripotent stem cells (hiPSCs) and their differentiated progeny as *in vitro* substitutes. Pluripotent stem cells (PSCs) are characterized by two abilities: they can undergo unlimited self-renewal, meaning they can proliferate indefinitely; and they are capable of differentiating into all three germ layers, ectoderm, mesoderm and endoderm (4). Currently, there are two possible sources for hPSCs.

Embryonic stem cells (ESC) are isolated from the inner cell mass of a pre-implantation embryo, also called a blastocyst (5) (Thomson et al., 1998). Because of their origin, there are many ethical and legal issues involved in the use of human ESCs (hESC), since this discussion is directly linked to the question of when human life begins (6). The Euro Stem Cell, a cooperation of over 400 stem cell laboratories in the European Union, has detailed information about the legislation concerning hESC use on different member countries (www.eurostemcell.org). In Germany, hESCs are highly restricted. Generation of new hESC lines is a criminal offence and pre-existing lines can only be imported into the country after approval by the German parliament, and if they were generated before 1 May 2007.

A relatively recent alternative to ESCs are induced pluripotent stem cells (iPSCs), a type of pluripotent cell that can be generated from somatic cells. They were first described by Takahashi and Yamanaka (7), who transfected mouse fibroblasts with four transcription factors, octamer-binding transcription factor 4 (Oct4), SRY-box transcription factor 2 (Sox2), MYC proto-oncogene, bHLH transcription factor (c-Myc) and Krüppel-like factor 4 (Klf4). These transcription factors were enough to induce pluripotency.

Their protocol for iPSC generation relied on the use of integrating vectors from retroviruses for gene transfer, a technique prone to insertional mutagenesis which can lead to unforeseen consequences such as *in vitro* immortalization and oncogenesis *in vivo* (8). Thus, the use of non-integrative approaches for iPSC reprogramming was developed in an effort to improve cell safety and stability. Stadtfeld et al. (9) generated integration-free iPSCs using non-integrative adenoviruses like the Sendai virus. Okita et al. (10) used episomal delivery to generate iPSCs without viral involvement, by repeated transfection of expression plasmids containing the complementary DNAs (cDNAs) of *Oct3/4, Sox2, Klf4* and *c-Myc*. Other groups have utilized direct delivery of reprogramming proteins fused with a cell-penetrating peptide (11) and direct delivery of mRNA encoding reprogramming factors (12).

iPSCs offer many advantages regarding their use in research. Since they can be generated from virtually any somatic cell, they bypass the ethical issues of human embryo destruction. With the appropriate protocol, they can be differentiated into a plethora of cell types, which makes it easier to do comparative analysis between not only different cell types, but also different stages of development of each cell type (13). hiPSCs are advantageous for modeling specific diseases, particularly genetic disorders. They can be generated from patients suffering from a specific condition and may reproduce aspects of that condition *in vitro*. In that same way, they allow for patient specific modeling and are therefore an attractive platform for personalized medicine (14). iPSCs can also be the base for the creation of organoids, which are cell assemblies that mimic organ-like characteristics. They can recapitulate some aspects of organ development and structural and metabolic features observed in adult organs, which makes them an attractive model for studying embryogenesis and modeling genetic diseases, among other applications (15).

However, there are of course disadvantages to the use of iPSCs. While researchers have improved at generating these cells over the years, it is well-documented that fully reprogrammed iPSCs retain epigenetic memories from their parental cell line, leading to differentiation bias (reviewed in Scesa et al. (16)). We have also not managed to perfect the differentiation of iPSCs into every single cell type and there are particular difficulties when modeling mature cells, with hepatocytes and cardiomyocytes being classical examples (17,18). Another aspect to consider is the difficulty of modeling complex cell-cell interactions, although the technology in this field is rapidly advancing (19,20).

Despite that, iPSCs are a valuable tool for a broad range of applications, including toxicity studies (21,22), disease modeling (23–25) and therapeutic uses (26).

1.2. The use of hiPSC-based models in toxicological assessment

Toxicological risk assessment encompasses many toxicological disciplines and aims to determine the harm caused by a substance to the people exposed to it. Some of the first steps in this assessment is to identify potentially hazardous substances and how their toxicity manifests (cytotoxicity, carcinogenicity, developmental abnormalities, genotoxicity, etc…) (27).

Developmental toxicity testing aims to identify substances that can cause disturbances during embryo-foetal development. Currently, the gold standard for identification of potential developmental adverse effects of a drug or chemical are animal-based assays which are time consuming, expensive and do not always reliably translate to human physiology (28). A classic example is the case of thalidomide, a drug sold during the 1950s as a cure for morning sickness during pregnancy. Experiments performed in pregnant rats prior to the drug release in the market led the developers to believe it was safe to be used during human pregnancy (29), which resulted in an estimated 10.000 children being born with malformations caused by thalidomide exposure during development (30).

Besides developmental toxicological evaluation, the identification and investigation of the effects of DNA-damaging agents (genotoxins) is of high importance. For certain agents such as cosmetic ingredients, genotoxicity testing on animals has been banned in the European Union and there are currently no suitable approved in vitro replacements (https://health.ec.europa.eu/publications/sccs-notes-guidance-testing-cosmetic-ingredients-and-their-safety-evaluation-12th-revision_en, accessed on March 2024). While DNA-repair mechanisms remain mostly constant among mammals, there are marked differences on the efficiency of such repair between different species (31). And although in vitro tests are also part of the standard battery of tests used for genotoxic assessment (32), they show high sensitivity, but their specificity is often lacking (33,34).

The Organisation for Economic Co-operation and Development (OECD) has recently announced a call for the urgent mobilization of resources to support the validation of

new tests for the safety of chemicals, with the intent to reduce the use of laboratory animals in safety testing while still protecting nature and human health (https://web-archive.oecd.org/2023-01-23/650072-urgent-mobilisation-national-regional-resources-to-support-the-validation-of-new-methods-safety-testing-of-chemicals.pdf, accessed on March 2024). This reflects a growing trend on the substitution of animal models for *in vitro* and *in silico* testing for toxicological assessment, both for general chemicals and in drug development (35,36).

The Food and Drug Administration (FDA) supports and funds the developing of New Alternative Methods (NAMs) for toxicological testing (https://www.fda.gov/media/144891/download, accessed on March 2024) and the U.S. Congress has approved in 2023 the FDA Modernization Act 2.0, stating that drug developers can now propose alternative methods, including the use of hiPSC-derived models, for the assessment of drug safety during the pre-clinical phase instead of mandating the use of animal models (37).

There is a pressing need to develop useful human-relevant model for toxicological evaluation and hiPSCs-based models can provide a reliable platform for assessment of different toxicological parameters and allow for the easy testing of the same compound on different cell types and stages of development.

In the case of developmental toxicology, for example, Cherianidou et al. (38) established a transcriptomics and hiPSC-based assay where they exposed hiPSCs to relevant human plasma concentrations of non-teratogenic and teratogenic substances during cell differentiation into mesodermal precursors and did a genome-wide expression profiling of the differentiated cells. The test was able to identify developmental toxicants with high in vivo concordance. Similar transcriptomics-based tests were performed by differentiating hiPSCs into cardiomyocytes and neuroepithelial cells, and the combined analysis of hiPSCs differentiated into different germ layers led to a more accurate prediction of teratogenicity (39,40).

3D hiPSC-based models, such as embryoid bodies and organoids, are an interesting alternative since they mimic the developing embryo and parts of organ development. Lauschke et al. (41) employed hiPSC-derived embryoid bodies, which are subsequently differentiated into cardiomyocytes, to establish an assay that can detect human-specific teratogens like Thalidomide. Organoids add an extra layer of

complexity in the culture model, being better able to represent individual organs. Yin et al. (42) created a platform based on the use of hiPSC-derived brain organoids to investigate heavy metal cadmium deleterious influence on neurogenesis and the platform can be adapted for in vitro study of abnormal neurodevelopment induced by different factors.

Despite not being a well-developed area yet, there are a few examples of hiPSC-based models used to investigate the genotoxic effects of compounds. The chemotherapeutic agents doxorubicin and cisplatin are genotoxic and their use for treating malignancies can contribute to the development of secondary cancers (43,44). That makes it particularly important to understand their DNA-damaging effects on human cells to come up with strategies to mitigate them. Transcriptomic analysis of hiPSC-derived cardiomyocytes after exposure to doxorubicin reveals a host of differentially regulated genes related to DNA damage repair and cell cycle, helping to elucidate the effects of this drug on the heart (45,46) developed an hiPSC-derived kidney organoid model with nephron-like structures that, upon being exposed to the genotoxic chemotherapeutic cisplatin, showed γH2AX foci consistent with DNA damage. hiPSC-derived organoids can also be useful to model DNA damage. Das et al. (47) optimized a protocol for the generation of forebrain organoids to study the genotoxic effects of ionizing radiation on mature neurons and neuroprogenitors.

Studies have shown the feasibility of using hiPSC-based models as a screening platform to assess developmental toxicity and genotoxicity. In the future, they could become a reliable and versatile tool in the battery of tests performed during drug development and the evaluation of chemicals. In particular, the assessment of hepatotoxicity and neurotoxicity is of great interest. The liver's role in toxin metabolization means that it is often exposed to potentially harmful substances (48) while there is mounting evidence that exposure to toxins found in the environment can lead to neurological issues, including neurodegenerative diseases (49).

1.3. *In vitro* neural differentiation of hiPSCs

In recent years, iPSC derived from patients have allowed for more detailed study of the mechanisms behind many genetic neurological diseases such as Huntington's disease (50), Nijmegen Breakage Syndrome (51), familial Alzheimer's (52) and Williams syndrome (53). Those cells can be differentiated into neural progenitor cells (NPCs) and neurons, replicating many of the hallmarks of these genetic afflictions *in*

vitro. Another important avenue of research is the use of iPSC-derived neural cells for neurotoxicological assessment. The use of animal models is the current gold standard, but it is time-consuming, expensive, and critical from an ethical point of view, while iPSC-based models are far more suited for high-throughput screening (54). In the past decade, efforts have been made to establish hiPSC-derived platforms for neurotoxicological assessment (55–57).

The most common strategy for the generation of NPCs *in vitro* is called dual-SMAD inhibition. In this method, the bone morphogenic protein (BMP) pathway and the transforming growth factor beta (TGF-β)/Activin/nodal growth differentiation factor (NODAL) pathway are inhibited using small molecules, inducing the differentiation of iPSCs into NPCs expressing key markers such as paired box 6 (PAX6) and neuroepithelial stem cell protein (Nestin). The first group to describe dual-SMAD inhibition used Noggin as a BMP inhibitor and SB431542 an Activin/Nodal/TGF- inhibitor (58). While SB431542 is currently still widely used for NPC generation, other molecules are often used in place of Noggin, particularly due to its high cost. Dorsomorphin is a common replacement (59) and more recently, LDN 193189 has risen as an effective alternative (60).

NPCs can be further differentiated into many neuron subtypes, including forebrain, midbrain, hindbrain and spinal cord neurons. A common approach is the use of an inhibitor of glycogen synthase kinase 3 (GSK3) such as CHIR99021 that induces the activation of canonical Wingless and Int-1 (Wnt) signaling. Low GSK3 inhibition patterns the cells towards a forebrain fate, while high inhibition predisposes them to a hindbrain fate. A medium level of inhibition patterns the cells towards the midbrain and the combination of Sonic Hedgehog (SHH) and GSK3 inhibitor further specifies NPCs into ventral midbrain neurons (61). Neuronal maturation is usually achieved by employing neurotrophic factors, which promote neuron survival and stimulate the generation of neuronal networks. Some of the most common examples are brain-derived growth factor (BDNF), insulin-derived growth factor (IGF) and glia-derived growth factor (GDNF) (62).

A weakness of 2D models is the difficulty in recapitulating the complexity of the human brain. The use of organoids, 3D assembloids of different neural cells, can partially circumvent this problem and many protocols have been established for the generation of organoids from different areas of the brain, called brain region-specific organoids.

This can be accomplished using small molecules to stimulate specific patterning, particularly through the modulation of the Wnt and SHH pathways. Examples include organoids mimicking the cerebellum (63), forebrain (64) and midbrain (65). Cortical organoids with mixed cellular identity are also widely used in research. They rely on dual-SMAD inhibition to stimulate the initial formation of neuroepithelial tissue, which has the capacity to self-organize into mature cortical organoids (66,67). The addition of Matrigel, an extracellular matrix, in the culture medium of developing organoids acts as a 3D scaffold and enhances neuroepithelium formation and organoid maturation (68).

1.4. In vitro hepatic differentiation of hiPSC

The liver is an essential organ with various functions. They range from protein and hormone synthesis to bile acid production and nutrient storage. One of the liver's main roles is the metabolism and detoxification of exogenous substances, which involves the addition of functional groups and covalent binding of hydrophilic endogenous molecules to turn exogenous substances more hydrophilic and thus, facilitate their excretion (69). In some cases, the metabolites produced in this process can be harmful to the body. A classic example is acetaminophen, a widely used drug that is harmless in low doses but is metabolized in the liver by the Cytochrome-P450-dependent monooxygenases (CYPs) family of enzymes into metabolites that can cause hepatotoxicity (70).

During the development of new drugs or chemicals, important aspects that are investigated are the effects of hepatic metabolism on the substance, as well as its hepatotoxicity. Primary human hepatocytes (PHH) are the gold standard for hepatotoxicity assessment *in vitro*, but they are derived from human liver biopsies, have limited expansion in culture, and dedifferentiate in monolayer culture within 24 hours which restricts their application(71,72). Immortalized liver cell lines are easily accessible and expandable but suffer from the loss of several phenotypic characteristics found in normal liver cells (73). Animal experiments, besides being costly and time-consuming, poorly predict human toxicity (74).

Due to these limitations, the use of hiPSC-derived liver cells, such as hepatocyte-like cells, is an attractive prospect (75,76). They are a human-relevant model that also allows researchers to account for genetic diversity and its influence in liver metabolism (77). In addition, it allows the modeling of genetic diseases that influence the liver (24).

In vitro hepatic differentiation of hiPSCs follows a procedure, which simulates hepatic differentiation *in vivo* using small molecules and growth factors. Firstly, the Wnt and Nodal signaling pathways are stimulated on hiPSCs and lead to the generation of definitive endoderm (DE). Commonly, Activin A and CHIR99021 are used to that effect. At this stage, the cells undergo morphological changes and loose markers associated with pluripotency such as OCT4 and express DE typical markers such as SRY-box transcription factor 17 (SOX17) (78). Following that, the cells are exposed to dimethyl sulfoxide (DMSO) to induce the formation of hepatic endoderm (HE), which are bipotential cells capable of transforming into hepatocytes and cholangiocytes. The mechanism of action of DMSO is not fully elucidated but after a few days, the cells express typical markers such as alfa fetoprotein (AFP) and HNF4α and have typical HE morphology (79). The last step is the maturation of these cells into hepatocyte-like cells (HLCs), and it is the step with the highest amount of variation between different protocols. A variety of growth factors can be employed such as Epidermal growth factor (EGF), hepatocyte growth factor (HGF), Fibroblast growth factor 2 (FGF2), Oncostatin M (OSM) and/or Bone Morphogenetic Protein 4 (BMP4). Insulin and dexamethasone are also common additions. At the end of the process, HLCs express several key markers, including albumin, HNF4α and CYP3A4. Their morphology is similar to hepatocytes, large cells with tight junctions and multiple nuclei (80).

1.5. DNA damage response and repair in mammalian cells

During our lifetime, our cells are under constant threat of DNA damage, either through endogenous (e.g. free radicals generated through normal metabolic activity) or exogenous (e.g. solar radiation, environmental toxins) means. To combat that, organisms developed the DNA damage response, a set of damage detection systems, signaling mechanisms and repair pathways responsible for preserving DNA genomic integrity (81). DNA damage can take different forms and eucaryotes have developed a variety of mechanisms to repair said damage. This introduction focuses on nucleotide excision repair (NER), DNA double-strand break repair (DSBR) and translesion DNA synthesis (TLS) and gives two examples of threats to genomic integrity which are repaired by or interfere with those repair mechanisms: the genotoxin benzo[a]pyrene diol epoxide (BPDE) and the genetic disease Nijmegen Breakage Syndrome (NBS). Lastly, a more detailed look into the protein p53, often dubbed the “guardian of the genome” (82) for its roles in the maintenance of genomic integrity.

1.5.1. Nucleotide excision repair (NER)

Nucleotide excision repair is a complex and versatile pathway, capable of repairing diverse DNA lesions such as bulky adducts and DNA crosslinks. DNA bulky adducts are caused by the covalent binding of a substance to the DNA. This binding can occur on different areas of the DNA molecule and depends on the chemical agent performing the binding (83). DNA crosslinking happens through the covalent binding of two nucleotides of DNA (84).

It can be caused by endogenous agents, such as the aldehydes produced during lipid peroxidation (85), or by exogenous agents such as certain chemotherapeutic agents (86). NER relies on a template to complete its repair mechanism, necessitating an intact strand of DNA to use as a base (87).

There is a complex system for lesion detection involved in NER with two different pathways (Figure 1), global genome repair (GG-NER) and transcription coupled repair (TC-NER). In the case of GG-NER, a protein complex consisting of xeroderma pigmentosum group C (XPC), human Rad23 homolog B (RAD23B) and Centrin-2 (CETN2) can identify and bind itself to DNA lesions, often assisted by the DNA damage-binding protein complex (UV-DDB), a dimer comprised of the proteins DDB1 and DDB2 (88). When transcription is stalled at the replication forks, TC-NER recognition starts with the recruiting of the proteins Cockayne Syndrome A (CSA), Cockayne syndrome B (CSB) and UV stimulated scaffold protein A (UVSSA) to the affected area (89). In both pathways, the transcription factor II H (TFIIH) complex is recruited, and they then proceed through the same repair mechanism (90).

TFIIH is composed by ten different proteins, xeroderma pigmentosum group D (XPD), xeroderma pigmentosum group B (XPB), p8, p34, p44, p52, p62, cyclin dependent kinase 7 (CDK7), Cyclin-H, and ménage à trois-1 (MAT1) (91). This complex performs lesion verification and recruits the xeroderma pigmentosum group F (XPF)/ERCC excision repair 1, endonuclease non-catalytic subunit (ERCC1) complex which performs the incision on the DNA (Graf et al., 2011), and initiates the synthesis of a

new strand mediated by proliferating cell nuclear antigen (PCNA) and DNA polymerases. The synthesis progress stimulates the excision of the damaged strand by xeroderma pigmentosum group G (XPG), and the new strand is sealed in by DNA

ligases (Staresincic et al., 2009). If a bulky DNA adduct is not promptly repaired, it can result in a stalled replication fork which can be bypassed by translesion DNA synthesis.

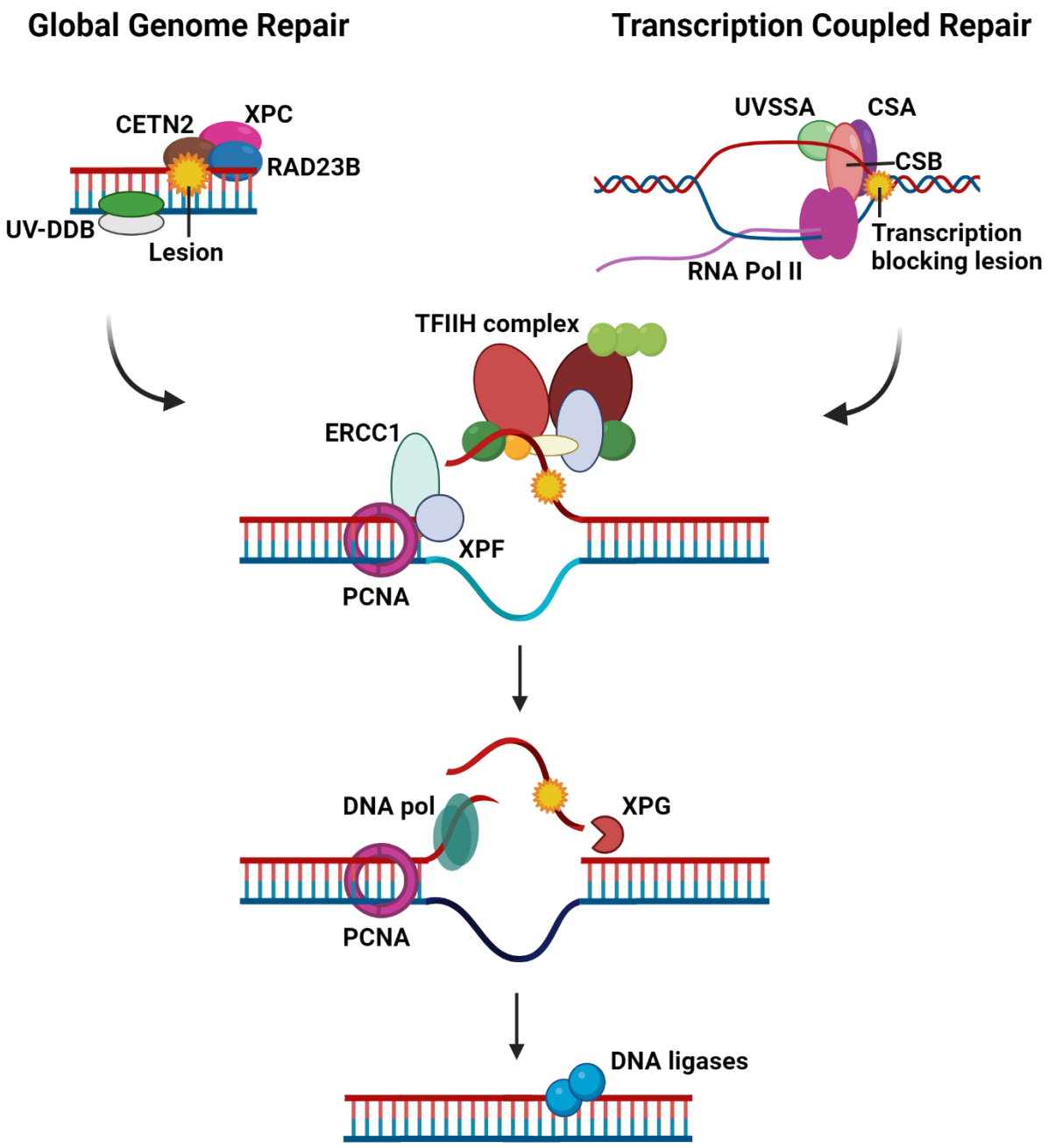

Figure 1: Nucleotide excision repair (NER) pathway. The start of NER occurs either by identification of DNA lesions through the global genome repair machinery or by recognition of stalled replication forks by the transcription coupled repair subpathway. Both pathways result in the recruiting of the TFIIH complex which verifies the lesion and recruits the XPF/ERCC1 complex to perform the DNA incision. XPG excises the damaged DNA strand while PCNA and DNA polymerases synthetize a new strand, which is sealed in by DNA ligases. Figure generated with BioRender.

1.5.2. Translesion DNA synthesis (TLS)

Translesion DNA synthesis (TLS) is a pathway that allows the cell to bypass DNA base lesions that are causing stalled replication forks, in a process known as DNA damage tolerance (Figure 2). Translesion synthesis DNA polymerases from the Y family (POLη, ι, κ, and Rev1), as well and polymerase ζ, are responsible for this repair pathway in eukaryotes (92). TLS polymerases lack the proofreading mechanisms present in replicative polymerases and depending on the type of lesion being repaired, and which TLS polymerase is doing the repair, the insertion of nucleotides on DNA-damage sites is prone to mistakes, resulting in the insertion of point mutations in the genome (93).

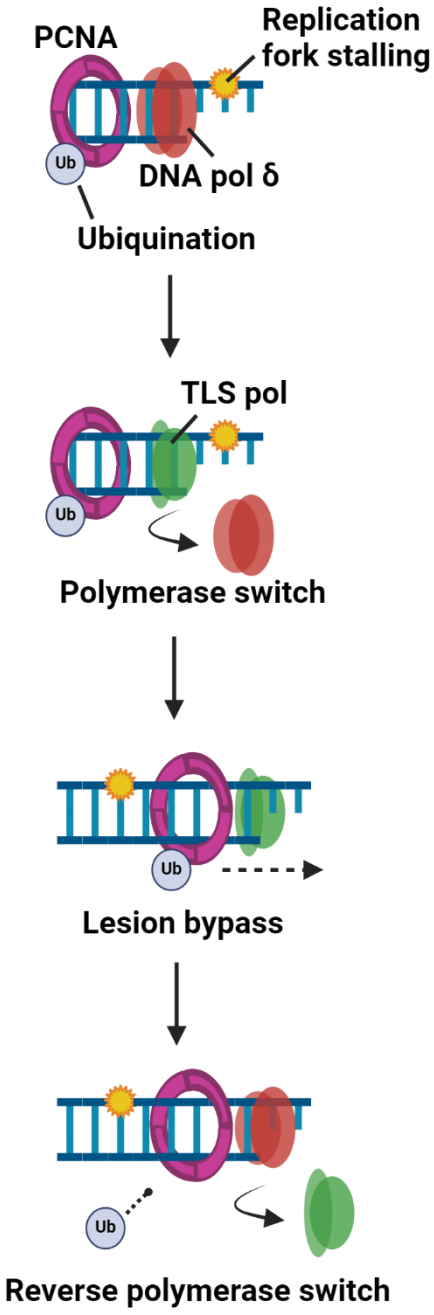

Figure 2: Translesion DNA Synthesis. DNA synthesis can be stalled at the replication fork due to DNA lesions. When that happens, PCNA is mono-ubiquinated and the replicative polymerase is substituted for a TLS polymerase, which can bypass the lesion. Once the fork stalling is resolved, PCNA is deubiquinated and normal replication proceeds with DNA polymerase δ. Figure generated with BioRender.

In the occurrence of a stalled replication fork due to a DNA lesion, PCNA is mono-ubiquinated, allowing for a switch of its partner polymerase from DNA polymerase δ to a TLS polymerase (94). Once this happens, the TLS polymerase can insert a nucleotide opposite to the replication impediment. PCNA is then deubiquitinated and DNA synthesis resumes once again with DNA polymerase δ (95).

Polycyclic aromatic hydrocarbons (PAH) are organic compounds that can form bulky DNA adducts, which can either be resolved through NER or bypassed through TLS (96). The next segment expands upon one such PAH, benzo[a] pyrene (B[a]p), and its metabolite benzo[a]pyrene diol epoxide (BPDE).

1.5.3. Benzo[a] pyrene and benzo[a] pyrene diol epoxide

Benzo[a]pyrene (B[a]p) is a PAH formed during incomplete combustion of organic matter, such as exhaust fumes, cigarette smoke and charbroiled food. It is a widespread environmental contaminant, found in the water, air and soil (97) and a common presence in human dietary intake worldwide (98). B[a]p is metabolized in the body by cytochrome P450 enzymes and epoxide hydrolase into Benzo[a]pyrene diol epoxide, or BPDE, a potent mutagen and carcinogen. BPDE causes bulky DNA adducts by binding to the N2 atom of guanine (dG-N^2-BPDE adduct) and this DNA damage is repaired mainly through the NER pathway (99), (Figure 3).

B[a]p binds to the aryl hydrocarbon receptor, a transcription factor that regulates the gene expression of several targets related to xenobiotic response, including the cytochrome P450 family member CYP1B1. This can lead to increased CYP1B1 protein production and consequent increase in bioactivation of B[a]p into carcinogenic metabolites (100). BPDE, which is considered the most carcinogenic of those metabolites, binds to the DNA and if not removed, can lead to base-pair substitution mutations via translesion DNA synthesis (101) resulting in tumorigenesis (102). Evidence suggests that tumor protein p53 (*TP53*), whose protein product p53 is important for DNA damage response and tumorigenesis suppression, is a favored target for BPDE-induced mutagenesis (103,104).

Cigarette smoking is a strong risk factor for hepatocellular carcinoma (105,106). Studies carried out on rodent models reveal the presence of BPDE-DNA adducts in the liver for several days after one-time B[a]p exposure, orally or through intraperitoneal injection (107,108). Chen et al. reported that patients suffering from hepatocellular carcinoma had a much higher number of BPDE-DNA adducts in tumor and adjacent nontumor liver tissues than non- hepatocellular carcinoma controls (109). While the harmful effects of BPDE on the liver are well known, its effects on the developing liver and on liver progenitor cells have not been investigated.

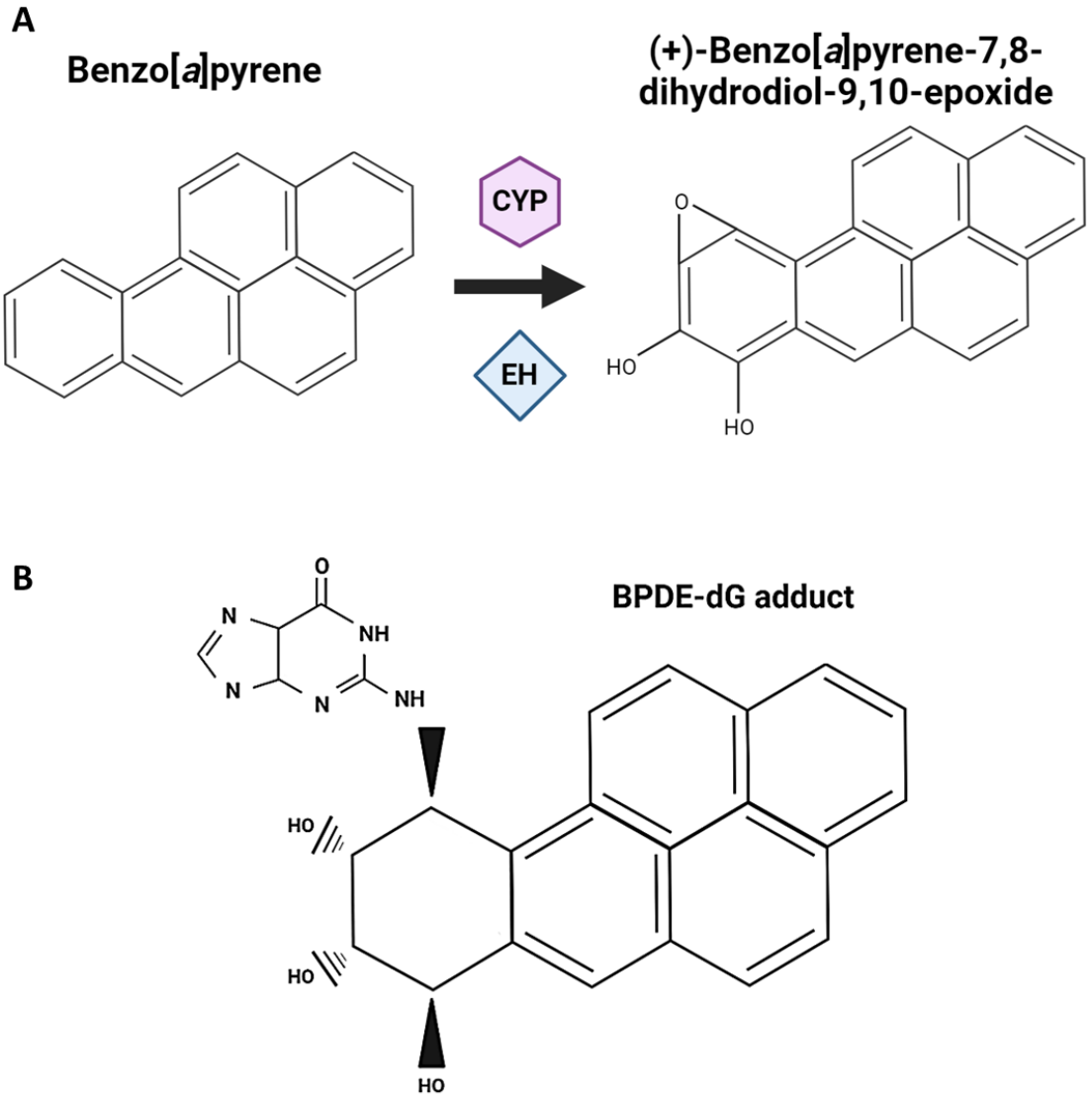

Figure 3: Chemical structure of B[a]p, BPDE and BPDE-dG adduct. (A) B[a]p undergoes metabolization by CYPs and EHs into BPDE. **(B)** BPDE binds to the N2 atom of guanine, forming a DNA adduct. CYP: Cytochrome P450. EH: Epoxide hydrolase. Image generated with BioRender.com.

Due to its lipophilic nature, B[a]p can cross the placenta to reach the developing fetus and it has been shown that the placenta of mice, rats and humans can metabolize B[a]p into BPDE, which can lead to fetal genotoxic exposure. Additionally, the fetuses themselves are metabolically capable (110–112). Mouse fetuses exposed to BPDE suffer embryotoxicity and malformations, hinting at a teratogenic effect cause by this compound (113,114). Teratogenic effects have also been observed in fish exposed to B[a]p during embryogenesis (115).

Besides direct embryonic exposure, BPDE-DNA adducts are detectable in the sperm (116) and ovarian cells (117) of cigarette smokers, and these DNA modifications can be paternally transmitted through the spermatozoa to the embryo (118). The potential issues that could arise from the presence of BPDE adducts on pre-implantation embryos are currently unknown.

B[a]p can traverse the blood-brain barrier and there is strong evidence that it and its metabolites, such as BPDE, can accumulate in the brain and cause neurobehavioral and neurotoxic effects (119–125). Besides mouse and rat brains being capable of metabolic activation of B[a]p (111,126), it is also hypothesized that part of the BPDE-DNA adducts found in rodent brains and cerebellum after B[a]p ingestion may occur due to B[a]p metabolites being carried via the circulatory system to the brain (127–129).

In vivo experiments show that the offspring of rats exposed to low levels of B[a]p during pregnancy have neurological deficits, particularly of cortical neuronal function (130). Similarly, exposure to B[a]p in adult Medaka fish leads to offspring neurotoxicity (131) and embryonic exposure to B[a]p in zebrafish also negatively affects the developing nervous system (132,133).

Despite the growing body of evidence regarding the deleterious effects of B[a]p on neurodevelopment and brain function, the potential adverse effects of BPDE on the nervous system are mostly unknown. In the human neuroblastoma cell line SH-SY5Y, BPDE exposure downregulated genes related to redox regulation (134). BPDE is also involved in the neuroinflammatory process, being capable of inducing the production of inflammatory mediators on primary rat cerebral cortex cells, and on rat neuron and astrocyte cell lines (135).

There is rising evidence supporting a link between DNA damage and neurodegeneration. This includes neurodegenerative diseases like amyotrophic lateral sclerosis (ALS), Parkinson's disease and Alzheimer's disease (136–139). It also applies to diseases which are triggered by exposure to specific genotoxic chemicals, like Western Pacific amyotrophic lateral sclerosis and Parkinsonism-dementia complex (ALS/PDC) and the genotoxin methylazoxymethanol (140–142). It is unknown whether BPDE-mediated genotoxicity in the central nervous system could facilitate the onset of neurodegenerative afflictions.

1.5.4. DNA Double-Strand Break Repair (DSBR)

DNA double-strand breaks are caused by a break on both strands of DNA. They can occur in a programmed manner due to the normal DNA metabolism of the cell or can form due to the actions of an exogenous agent such as radiation and certain genotoxins (143).

There are two main forms of double-strand break repair in mammalian cells, homologous recombination (HR) and non-homologous end joining (NHEJ) (Figure 4). They are regulated by the DNA damage response mediated by the kinases ataxia telangiectasia mutated (ATM), ataxia telangiectasia and Rad3 related (ATR) and DNA-dependent protein kinase catalytic subunit (DNA-PK). ATM and ATR are involved in cell cycle checkpoint activation and inhibition of cell cycle progression in response to double-strand breaks, allowing for DNA repair and cell survival, while DNA-PK is a double-strand break sensor and promotes NHEJ (144). HR depends on the presence of a homologous DNA strand to use as a template during repair, therefore it is mostly only available during S and G2 phases, while NHEJ acts by ligating the damaged DNA ends and can be active during the whole cell cycle, at the expense of being a mutation-prone form of repair (145).

In eukaryotes, chromatin is formed by DNA wrapped around structural proteins called histones. When a double-strand break occurs one of these histones, H2A histone family member X (H2AX), becomes its phosphorylated form γ-H2AX. Cell cycle checkpoint protein RAD17 (RAD17) is a DNA damage sensor protein and together with γ-H2AX, they recruit the MRN complex to the damage site (146,147), starting a recognition and signaling cascade.

The MRN complex is composed of three proteins: Nibrin (NBN), MRE11 Homolog Double Strand Break Repair Nuclease (MRE11) and RAD50 double strand break repair protein (RAD50). Once the MRN complex is bound to the lesion, NBN recruits ATM, which dissociates from its dimer form into monomers, leading to its autophosphorylation and thus activation (148). Activated ATM activates different downstream signaling pathways involved in checkpoint activation and cell cycle arrest, one of the most important ones being the ATM/checkpoint kinase 2 (CHEK2)/p53 axis (149). It also phosphorylates targets in all three components of the MRN complex, controlling MRE11-mediated resection of damaged DNA strands, an essential step for the start of homologous recombination repair.

The start of homologous recombination repair depends on the end resection of the damaged strands of DNA performed through the endonuclease activity of the MRN complex and the CtBP-interacting protein (CtIP) (150). These DNA ends are then referred to as 3′ single-stranded DNA (ssDNA) and are promptly covered by the replication protein A (RPA) complex. ATR and its partner protein ATR Interacting Protein (ATRIP) are recruited to damaged DNA strands coated with RPA where ATR is activated by DNA topoisomerase 2-binding protein 1 (TOPBP1) (151). ATR then phosphorylates and activates Checkpoint kinase 1 (CHEK1), helping to maintain cell cycle progression arrest (152). Breast cancer type 1 susceptibility protein (BRCA1) and Breast cancer type 2 susceptibility protein (BRCA2) act as scaffolding to organize the repair proteins at the lesion site, including DNA repair protein RAD51 homolog 1 (RAD51), which displaces RPA and forms a nucleoprotein filament (153). The RAD51–ssDNA nucleoprotein filament invades the homologous DNA template, forming a temporary three-stranded DNA and then displacing the non-sister strand of the invaded DNA (154). At the same time, the CX3 complex formed by RAD51 homolog C (RAD51C) and X-ray repair cross complementing 3 (XRCC3) acts in concert with DNA repair and recombination protein RAD54-like (RAD54) to maintain fork stability and facilitate homologous DNA pairing (155,156). DNA polymerases can then act to synthetize the missing DNA and DNA ligase attaches it to the existing incomplete strands. Finally, the fixed DNA and the template DNA separate from each other (157).

Initiation of non-homologous end joining (NHEJ) repair happens through Ku, a heterodimer composed of the subunits Ku70 and Ku80 that is able to bind to DNA double-strand breaks and recruit DNA-PK to the damage site, which is responsible for starting NHEJ (158).

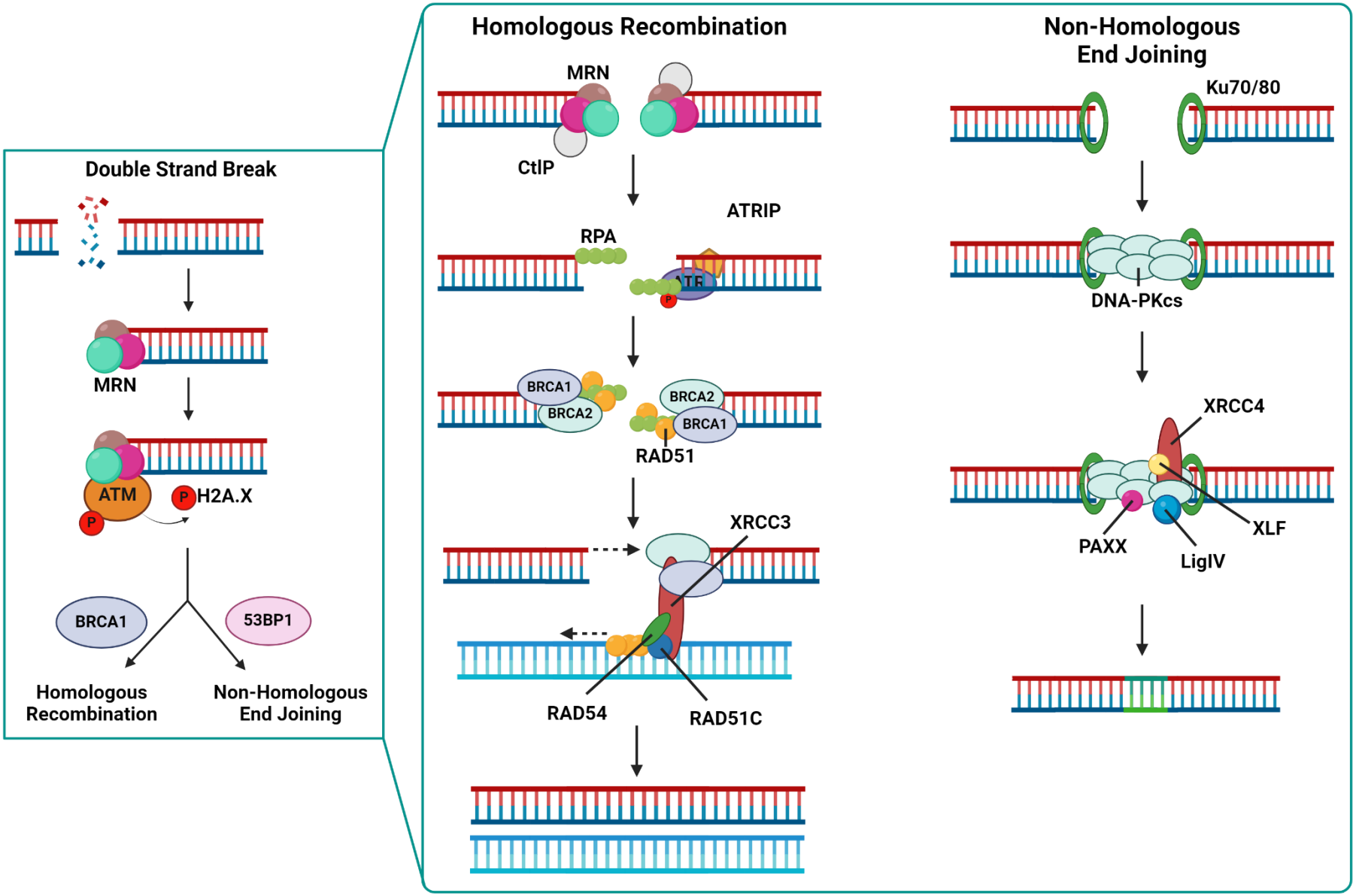
Double Strand Break
MRN
ATM
P
H2A.X
P
BRCA1
53BP1
Homologous Recombination
Non-Homologous End Joining
Homologous Recombination
MRN
CtIP
ATRIP
RPA
ATR
P
BRCA1
BRCA2
BRCA2
BRCA1
RAD51
XRCC3
RAD54
RAD51C
Non-Homologous End Joining
Ku70/80
DNA-PKcs
XRCC4
XLF
PAXX
LigIV

Figure 4: DNA double-strand break repair pathways. DNA double-strand breaks induce the phosphorylation of H2A.X, which in turns recruits the MRN complex, starting damage recognition and repair. NBN recruits ATM, which autophosphorylates and activates several downstream targets related to cell cycle arrest. BRCA1 and 53BP1 are key proteins that steer the repair pathway towards HR or NHEJ, respectively. At the start of HR, MRN and CtIP perform the end-resection of the damaged DNA strands, which are covered by RPA. ATR/ATRIP are recruited to the RPA covered strands where ATR phosphorylates and activates mechanisms of cell cycle arrest maintenance. BRCA1 and BRCA2 acts as scaffolding for proteins involved in repair, including RAD51, which displaces RPA and forming nucleoprotein filaments that invade the homologous DNA template. XRCC3, RAD54 and RAD51C maintain fork stability and facilitate repair by DNA polymerase and DNA ligase. Alternatively, double-strand breaks can also be detected by Ku70/80, which recruits DNA-PKs and starts NHEJ. DNA-PK recruits XRCC4, XLF, PAXX and LigIV. The first three form the scaffolding around the damaged strands, while LigIV performs the DNA end joining.

Once DNA-PK is present, four more factors are recruited to the complex, forming the scaffolding and repair machinery of NHEJ. They are X-ray repair cross complementing protein 4 (XRCC4), XRCC4-like factor (XLF), paralog of XRCC4 and XLF (PAXX), and DNA ligase IV (LigIV) (159). Subsequent autophosphorylation and dissociation of DNA-PK changes the conformation of the complex and allows for LigIV-mediated DNA end joining (160).

The repair choice between HR and NHEJ is a complex affair with many key decision points. One of the main limiting factors that was already mentioned is the presence of homologous DNA sequences to serve as templates for HR, restricting this repair pathway to mostly the G2 and S phases. Another influence is which damage recognition complex first binds to the DNA ends, MRN or Ku70/80, which shifts repair to HR or NHEJ, respectively. Other proteins are also involved at later stages in the repair choice, two essential ones being tumor suppressor p53-binding protein 1 (53BP1) and BRCA1 (161).

Germline mutations in genes involved in DSBR cause a host of developmental disorders linked with increased cancer predisposition. Examples include Ataxia telangiectasia, caused by mutations on *ATM*; ataxia telangiectasia-like disorder (A-TLD), where *MRE11* is mutated; and Nijmegen breakage syndrome (NBS), incurred by mutations on *NBS* (162). The next section will take a more comprehensive look into NBS and its pathology.

1.5.5. Nijmegen Breakage Syndrome (NBS)

Nijmegen Breakage Syndrome (NBS) is a chromosomal instability disorder, which manifests in patients as an impaired immune system, microcephaly, growth retardation, premature aging, premature ovarian failure and increased susceptibility to malignancies such as lymphomas, gliomas, and medulloblastomas (163) (Figure 5). It is caused by a mutation in the *NBS* gene, also known as *NBN*, which codes for the protein Nibrin (NBN), part of the MRN complex.

Most NBS patients (90%) carry a homozygous founder mutation in the *NBS* gene, a five base pair deletion in exon 6 (c.657_661del5). The mutation results in a hypomorphic defect, generating a truncated version of Nibrin which parts in two fragments: a 26-kDa protein ($NBNp^{26}$) and a 70-kDa protein ($NBNp^{70}$) (164).

MRE11 and RAD50, together with Nibrin, form the MRN complex. This complex is involved in DNA damage signaling and repair, particularly of DNA double-strand breaks, a pathway that is severely impaired in NBS patients. Due to this deficiency in DNA repair, NBS patients have marked chromosomal instability, developing breakages and chromosomal rearrangements (165). That in turn leads to the development of malignancies, with over 40% of NBS patients developing one by the age of 20, predominantly hematological cancers (166). Indeed, cells obtained from NBS patients are particularly sensitive to some DNA-damaging agents such as bleomycin (167). Moreover, the MRN complex is also involved in cell cycle regulation and apoptosis (168) and cultures of fibroblasts obtained from NBS patients reveal cells with deficient cell cycle regulation (167).

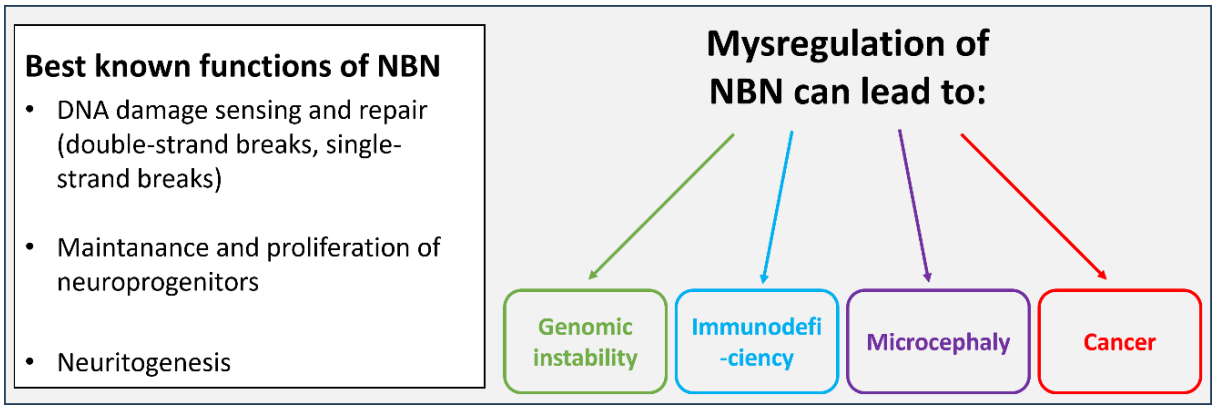

Figure 5: General functions of NBN and consequences NBN impairment.

Another important aspect of NBS is the dysregulation of p53 function. In vitro, NBS NPCs have less p53 than wild type NPCs and microarray analysis reveals the downregulation of gene clusters downstream of p53 (51). NBS fibroblasts exposed to ionizing radiation and NBS iPSC-derived cerebral organoids exposed to bleomycin, have a delayed and reduced p53-mediated response to DNA damage (169,170). Considering the importance of p53 signaling for tumor suppression (171) and brain development and homeostasis (172), this dysregulation likely contributes to the phenotype observed in NBS patients.

1.5.6. P53 in DNA damage repair

Tumor protein P53 (p53) is a multifunctional protein with roles in the regulation of apoptosis, cell cycle and the DNA damage response. Its involvement has been demonstrated during different forms of DNA damage repair, including NER and DSBR (173). *TP53* mutations and/or the dysregulation of p53 function is a common feature in human cancers (174).

P53 plays a significant role during NER. It acts as a transcriptional regulator towards *XPC* and *DBB2*, enhancing their expression (175,176) and it also localizes to DNA lesions and helps in the recruiting of DDB1 to the damage site (177), helping in the identification of DNA lesions and repair initiation.

When a DNA double strand break occurs, ATR and ATM phosphorylate the effector kinases CHEK1 and CHEK2, which in turn phosphorylate and activate p53. P53 enhances transcription of cyclin-dependent kinase inhibitor 1 (p21) and starts a cascade which leads to cell cycle arrest, stopping transcription and allowing the cell time to repair the DNA lesion (178). Besides that, p53 also acts as a transcription factor by upregulating the expression of *RAD51* (179).

Because of its numerous critical roles, p53 has different mechanisms which regulate its functions. Perhaps its most evolutionarily conserved relationship is with the protein Mouse double minute 2 homolog (MDM2), which negatively regulates p53 through ubiquitination, targeting it for degradation by proteosomes (180). Conversely, MDM2 transcription is induced by p53, forming a regulatory feedback loop between the two (181)

1.6. Challenges of genetic disease modeling: an overview focused on NBS

Studying genetic diseases in the laboratory, particularly the ones in which DNA repair is compromised, like NBS, is a challenging proposition. Cell cultures derived from patients can suffer premature senescence due to their inability to properly repair DNA damage (167) while animal models fail to recapitulate key aspects of the disease (182,183).

The usefulness of primary cell culture is limited. Since this disorder is rare, access to primary cells from patients can be difficult and premature senescence hinders cell passaging *in vitro*. In addition, while they are effective for initial gene function analyses, they cannot encapsulate the multi-systemic impact of these disorders.

Primary lymphocytes obtained from the peripheral blood of NBS patients can be cultured for short periods of time, usually for a few days, and have mainly been used for cytogenetic studies and irradiation exposure experiments (163,184). The generation of Epstein Barr virus (EBV) transduced lymphoblastoid cell lines (LCL) immortalizes primary lymphocytes, allowing for extended periods in culture, as well as freezing and thawing of cells (185). Different groups have generated LCLs from NBS patients, which are useful for targeted experiments related to Nibrin function (186–189).

The first attempt to produce a mouse model of NBS was done via the inactivation of *Nbs* which allowed for the generation of chimeric *Nbs*+/- mice. These mice were then interbred for the generation of *Nbs*-/- animals but the homozygous mutation led to early embryonic lethality in utero, associated with poor embryonic development (183). Although the model was not successful, these results were the first indication that the phenotype observed in NBS patients and cell lines were not the effect of a complete absence of Nibrin but rather, of a hypomorphic mutation of *NBS*.

Williams et al. pursued an alternative approach and generated a mouse model ($Nbs^{\Delta B/\Delta B}$) with a phenotype closer to what is seen in humans, by using a hypomorphic mutation of *NBS* resulting in a truncated version of Nibrin still compatible with cell viability. The allele produces an 80kDa NBN protein ($NBNp^{80}$) which can still interact with Mre11, like the $NBNp^{70}$. $Nbs1^{\Delta B/\Delta B}$ murine embryonic fibroblasts (MEFs) are highly sensitive to ionizing radiation, similar to NBS fibroblasts. Despite that, the animals

failed to recapitulate important phenotypes observed in NBS such as immune system defects, higher cancer incidence, ovarian dysgenesis and microcephaly (182).

Recent progress has been made regarding the study of NBS with the introduction of iPSCs derived from NBS patients (190). The return to pluripotency allows the cells to bypass premature senescence *in vitro* and provide a reliable and flexible platform for studying the influence of the disease during early development as well as how exposure to different compounds affects the cells carrying the mutation (51,167,170,191). It is even possible to model key aspects of the disease that are not present in mouse models. Martins et al. generated cerebral organoids from NBS patient-derived iPSCs that revealed premature neuronal differentiation, leading to disrupted cyto-architecture and a smaller size than the wild-type organoids, possibly recapitulating *in vitro* the developmental microcephaly associated with the disease (170).

1.7. Aims of the thesis

Each cell type reacts differently to genotoxic stress. Therefore, the aim of this work was to do a comparative analysis of the DNA damage response to BPDE in hiPSCs and their progeny differentiated into cells from the ectoderm and endoderm embryonic layers. Furthermore, this work also aimed to analyze the differences in the DNA damage response to BPDE between hiPSCs and NPCS derived from healthy subjects and those suffering from NBS.

2. Materials and methods

2.1. Cell culture

hiPSCs were maintained in the incubator at 37°C, 5% CO2 and 5% O_2, in a humid atmosphere. Differentiated cells were kept in the same conditions, but at 20% O_2. All cell culture was done in sterile conditions under the cell culture hood.

2.1.1. Human induced pluripotent stem cells (hiPSCs) maintenance

hiPSCs were maintained in feeder-free conditions, cultivated on Matrigel extracellular matrix and fed with mTeSR™ Plus, a serum-free media for maintenance and expansion of iPSCs. 6, 12, or 24-well plates were coated in Corning®Matrigel® hESC-qualified Matrix for 1 hour at room temperature as per manufacturer specifications and hiPSCs were plated. Medium change was performed daily. Cell passage was done with ReLeSR™, an enzyme-free reagent for dissociation and passaging of iPSCs as aggregates, as specified by the manufacturer. ReLeSR™ was added to the cells for 1 minute, aspirated, then 3-5 minutes later 1mL mTeSR™ Plus was added, followed by gentle tapping of the plate to allow for detachment. The aggregates were seeded on Matrigel and cells were passaged once a week. For experiments, cells were dissociated into single cells using accutase and seeded on Matrigel. The hiPSC lines used in this work are detailed on

Table 1: Cell lines used in this work. M: male, F: female.

Cell line	Gender	Genotype	Age of Donor	Derived from	Reprogramming method	Source
UJ (ISRM-UM51)	M	-	51 years old	SIX2-positive renal cells	Episomal reprogramming	(189)
iPSC-12	F	-	Neonatal	Dermal fibroblast	Retroviral transduction	Cell applications Inc.
NBS8	F	Heterozygous NBN 657del5	7 years old	Dermal fibroblasts	Retroviral transduction	(188)
NBS2		Homozygous NBN 657del5	3 years old	Dermal fibroblast	Episomal reprogramming	---
Normal human dermal fibroblasts (NHDF)	M	-	Juvenile (exact age not specified)	Juvenile foreskin	-	PromoCell®

UJ hiPSCs (ISRM-UM51) (192) were generated by our working group. NBS8 (190) hiPSCs were derived from a Nijmegen Breakage Syndrome patient and generated by our working group, as was the NBS2 hiPSC line (unpublished). iPSC-12 is a commercially available iPSC line from Cell Applications Inc. (https://www.cellapplications.com/). Normal human dermal fibroblast (NHDF) is a commercially available fibroblast line from PromoCell® (https://promocell.com/product/normal-human-dermal-fibroblasts-nhdf/). NBS2, ISRM-UM51 and NBS8 are under the ethical approval of the Ethikkommission der Medizinischen Fakultät der Heinrich-Heine-Universität Düsseldorf (protocol code: 5704 and date of approval: 22 February 2017; protocol code 5013 and date of approval: 09 June 2015).

2.1.2. hiPSCs-derived cerebral organoids

hiPSCs were cultivated until 75-90% confluence. The cells were washed once with DPBS -/- and dissociated with accutase for 5 min at 37°C. The accutase reaction was stopped with mTeSR Plus and the single cell suspension was centrifuged at 110xg for 3 min. The supernatant was discarded, and the cells were resuspended in mTeSR Plus supplemented with 10 µM ROCK inhibitor (Y-27632, Sigma-Aldrich) in a concentration of 10^4 cells/100 µl of cell suspension was then plated into each well of a 96 well plate, U-bottom, low attachment (Thermo Scientific) and the plate centrifuged at 100xg for 2 min. The cells were incubated at 37°C with 5% CO_2 for 24 hours, after which 50 µl of the medium was aspirated and replaced by 100 µl of neural induction medium (NiM, consisting of 47% DMEM/F12 (Gibco), 47% Neurobasal Medium (Gibco), 2% B27 w/o retinoic acid (Gibco), 1% N2 (Gibco), 1% GlutaMAX (Gibco), 1% MEM non-essential amino acids (NEEA) (Gibco) and 1% Penicillin/Streptomycin (Gibco). In the following 5 days, 100 µl of medium was replaced daily with fresh NIM supplemented with 10 µM SB-431542 (Tocris), 500 nM LDN-193189 (Merck) and, until day 3, 10 µM ROCK inhibitor. On day seven, the neurospheres were collected from the 96-well plate and transferred to a floating culture in a 10 cm petri dish with 10 mL Neural Differentiation Medium (NDM, consisting of 95% Neurobasal Medium (Gibco), 2% B27 w/o retinoic acid (Gibco), 1% N2 (Gibco), 1% GlutaMAX (Gibco), and 1% Penicillin/Streptomycin (Gibco) supplemented with 20 ng/ml epidermal growth factor (EGF) (Peprotech) and 20 ng/ml fibroblast growth factor 2 (FGF2) (Peprotech). The dish was kept in a shaking incubator at 60 rpm and medium was replaced every other day with fresh NDM supplemented with 20 ng/ml EGF and 20 ng/ml FGF2.

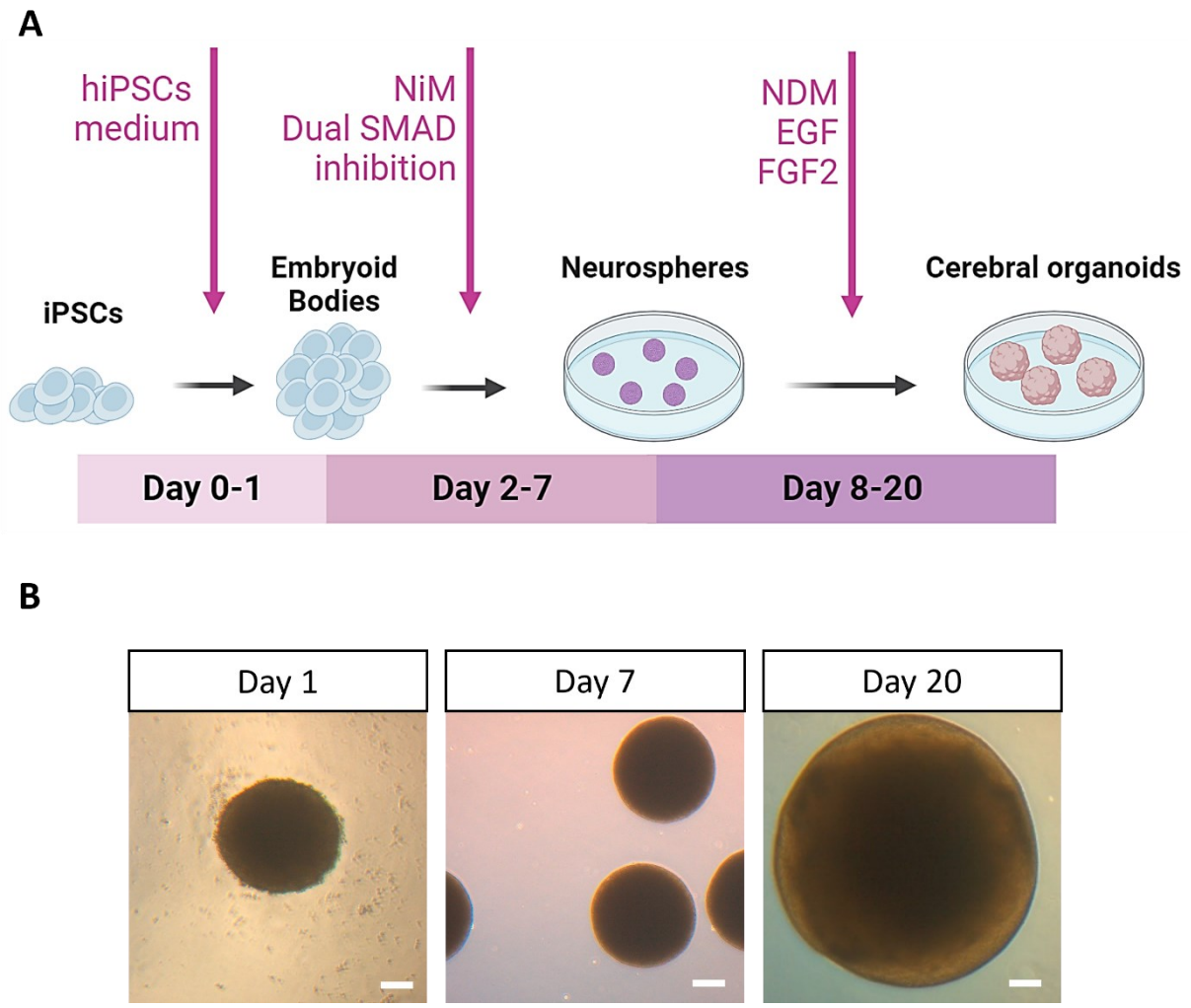

Figure 6: Generation of hiPSC-derived cerebral organoids. (A) Schematics of the differentiation of hiPSCs into cerebral organoids. **(B)** Representative brightfield images of embryoid bodies and cerebral organoids at different culture stages. Scale bar 150µm. Schematics were generated with BioRender.com.

2.1.3. hiPSCs-derived neural progenitor cells (NPCs)

The NPC differentiation followed the same protocol for the cerebral organoid differentiation until day 7. Instead of being transferred to free floating cultures, ten to twelve neurospheres were seeded per well in Growth Factor Reduced Matrigel (Corning) coated 6-well plates and fed daily with NDM supplemented with 20 ng/ml EGF and 20 ng/ml FGF2. On day 18, neural rosettes were selected with STEMdiff™ Neural Rosette Selection Reagent (Stem Cell Technologies) as per the manufacturer's recommendation. The rosettes were then incubated with accutase for 30 min at 37°C and the resulting cell aggregates were seeded at a density of 1:4 on Growth Factor Reduced Matrigel (Corning) coated 6-well plates for expansion and fed daily with NDM supplemented with 20 ng/ml EGF and 20 ng/ml FGF2. For passaging, the NPCs were incubated with accutase for 5 min at 37°C and the resulting aggregates were seeded

at a density of 1:4 on Growth Factor Reduced Matrigel (Corning) coated 6-well plates every 5-6 days.

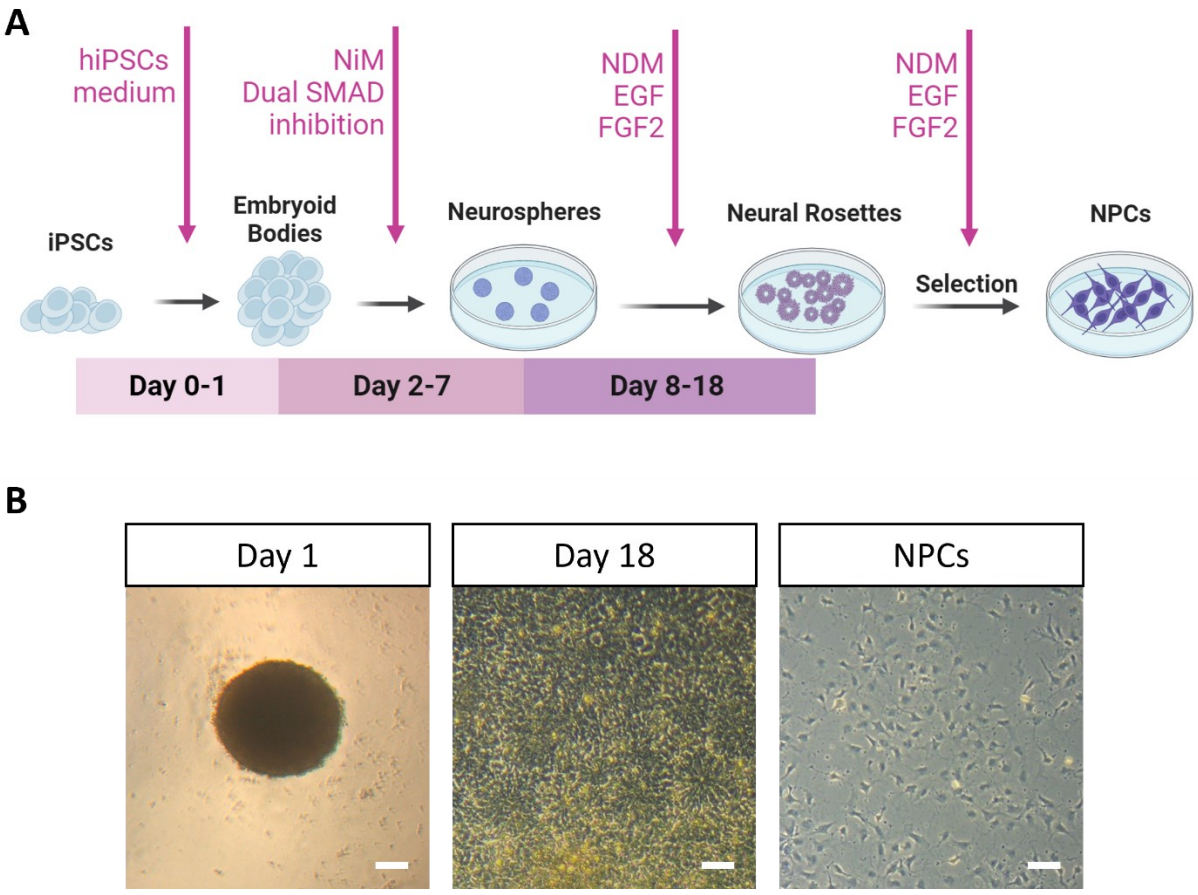

Figure 7 Generation of hiPSC-derived NPCs. (A) Schematics of the differentiation of hiPSCs into NPCs. **(B)** Representative brightfield images of embryoid bodies, neural rosettes and NPCs. Scale bar 150µm on Day 1, 100µm on day 18 and NPCs. Schematics were generated with BioRender.com.

2.1.4. hiPSCs-derived neuronal culture

The NPCs generated in 2.1.3 were seeded at a density of $4x10^4/cm^2$ on plates coated with Growth Factor Reduced Matrigel (Corning). They were fed every three days with NDM supplemented with 20 ng/ml of Brain-derived neurotrophic factor (BDNF, Peprotech) and 20 ng/ml of neurotrophic factor 3 (NT3, Peprotech) for 15 days, for the development and maturation of neuronal networks.

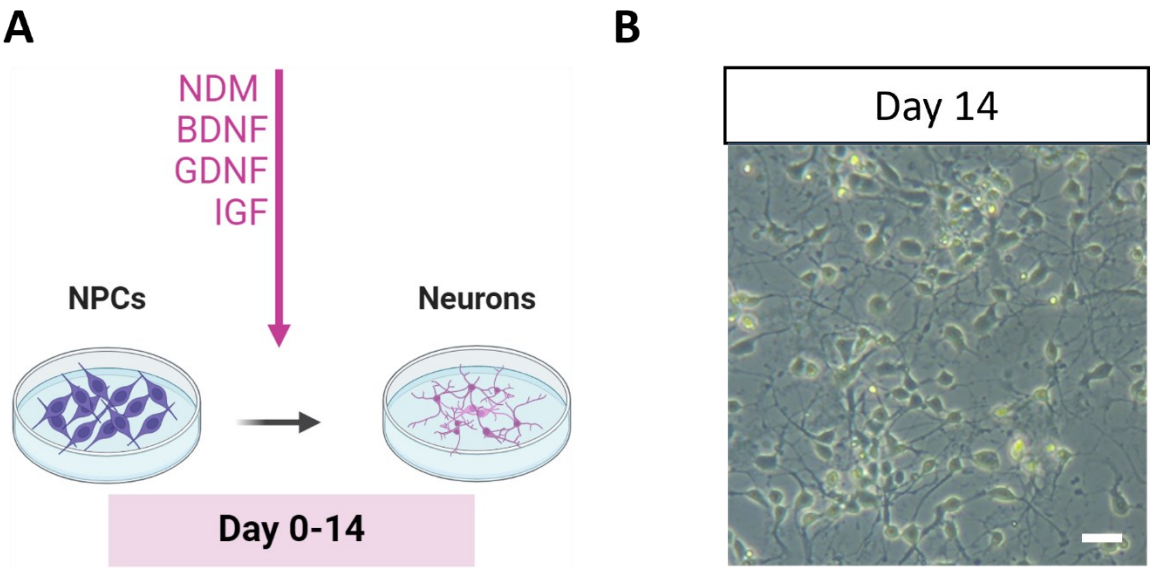

Figure 8: Generation of hiPSC-derived Neurons. (A) Schematics of the differentiation of NPCs into Neurons. **(B)** Representative brightfield image of neurons. Scale bar 50µm Schematics were generated with BioRender.com.

2.1.5. hiPSCs-derived hepatic endoderm (HE)

hiPSCs were cultivated until 75-90% confluence. The cells were washed once with DPBS -/- and dissociated with accutase for 5 min at 37°C. The accutase reaction was stopped with mTeSR Plus and the single cell suspension was centrifuged at 110xg for 3 min. The supernatant was discarded, and the cells were resuspended in mTeSR Plus supplemented with 10 µM ROCK inhibitor (Y-27632, Sigma-Aldrich). They were then seeded on Matrigel (Corning) covered plates at a density of approximately 10^5 cells/cm^2. After 24h, the medium was aspirated in full and replaced with DE medium (consisting of 97% RPMI (Gibco), 2% B27 w/o retinoic acid (Gibco), 1% GlutaMAX (Gibco) and 2 µM Doxycycline (Sigma-Aldrich)). On day 1, DE medium was supplemented with 2.5 µM CHIR99021 (Sigma-Aldrich) and 100 ng/ml Activin A (Stem Cell Technologies), and on days 2 and 3, only with 100 ng/ml Activin A. On days 4 to 7, the cells were fed with HE medium (composed of 77.5% DMEM/F12 (Gibco), 20% Knockout-Serum (Gibco), 0.5% GlutaMAX (Gibco), 2 µM Doxycycline (Sigma-Aldrich) and 0.01% 2-Mercaptoethanol (Merck)) supplemented with 1% DMSO (Sigma-Aldrich).

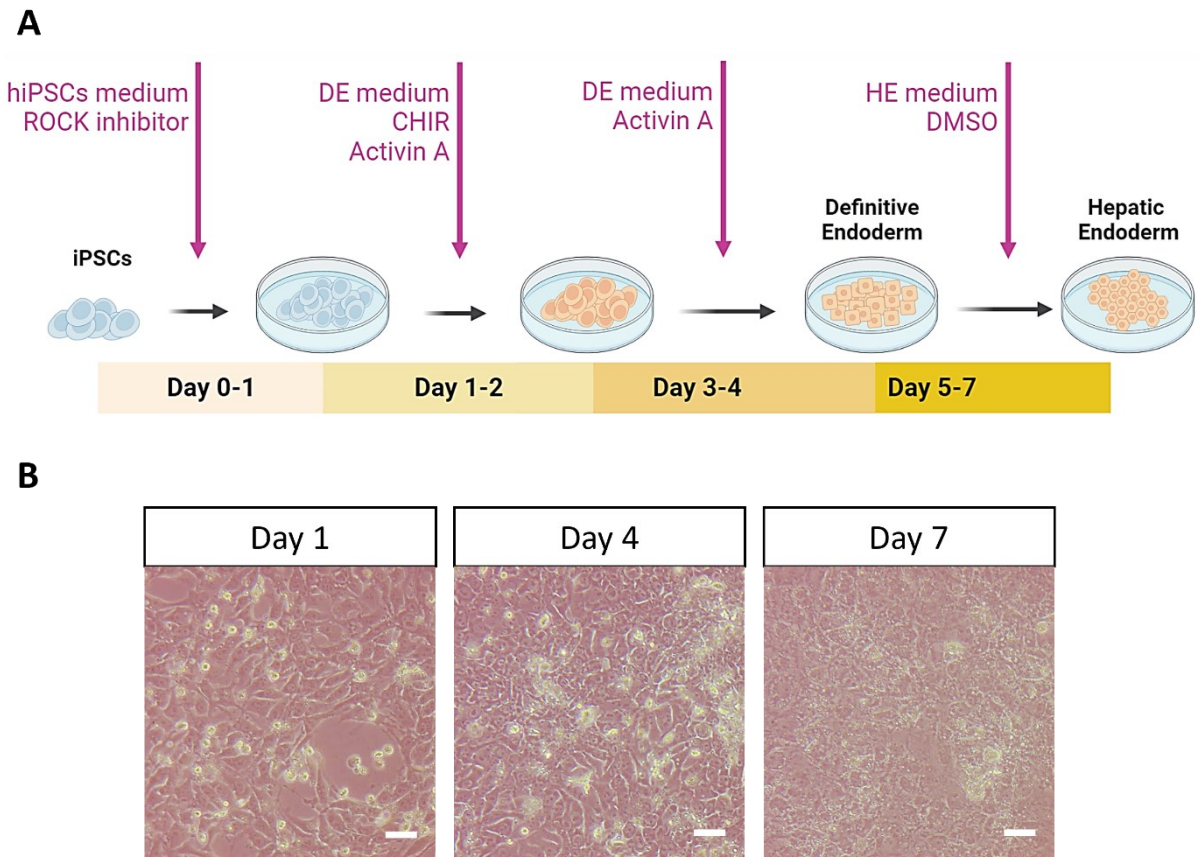

Figure 9: Generation of hiPSC-derived HEs (A) Schematics of the differentiation of hiPSCs into HEs. **(B)** Representative brightfield images of day 1 cells, DEs and HEs. Scale bar 50µm. Schematics were generated with BioRender.com.

2.2. Molecular biology assays

2.2.1. Genomic DNA extraction

Media was aspirated from a well of a 6-well plate, cells washed once with DPBS and dissociated with 10min incubation with accutase. The reaction was stopped with DPBS, and the cell solution was centrifuged, and the supernatant discarded. Genomic DNA was extracted from the cells with the QIAGEN DNA Blood and Tissue DNA extraction kit (QIAGEN) according to the manufacturer specifications. The amount and quality of the isolated RNA was measured with the spectrophotometer NanoDrop2000 (Thermo Fisher).

2.2.2. RNA extraction

Media was aspirated from a well of a 6-well plate and the cells washed once with DPBS. 500 µl of TRIzol® was then added to the well and the plate was moved to a shaker for gentle shaking for 5min at room temperature (RT). The cell solution was homogenized and transferred to an Eppendorf tube. The solution can then be kept at

-80°C until RNA extraction is completed. Total RNA was extracted using the Zymo Research Direct-zol™ RNA MiniPrep kit according to the manufacturer's instructions. To avoid DNA contamination, a 30 min treatment with Deoxyribonuclease (DNAse) was applied. The amount and quality of the isolated RNA was measured with the spectrophotometer NanoDrop2000 (Thermo Fisher).

2.2.3. cDNA synthesis

The isolated RNA was transcribed into cDNA using the Reverse Transcription TaqMan® Kit (Applied Biosystems Roche, Foster City, USA) following manufacturer's instructions. 500ng of RNA was used for each reaction, diluted to a total volume of 4 µl in DNase/ RNase free water. Then 6µl of Master Mix (1 µl 10X RT buffer, 2.2 µl 1.75mM MgCl2, 2 µl 0.5mM dNTPs, 0.5 µl 2.5mM oligoDT primers, 0.2 µl RNAse inhibitor (20 U/µl), 0.25 µl Reverse Transcriptase) was added to the mixture. The samples were loaded in a peqStar 21 Thermocycler and amplified using the following program: 25 °C for 10 min-annealing, 48 °C for 30 min-reverse transcription and 95 °C for 5 min-enzyme inactivation. The PCR products were diluted to a final concentration of 5ng/ µl in nuclease free water and stored at -80 °C.

2.2.4. Quantitative Real Time Polymerase Chain Reaction (PCR)

qRT-PCR was used to assess the expression levels of genes of interest. Reactions were carried out in triplicates in a 384-well plate, in a total volume of 10 µl/well (1 µl of 5ng/ µl of cDNA sample, 0,5 µl each of forward and reverse primers, 5 µl of 2X Power SYBR® Green (Applied biosystems) and 3 µl of DNase/RNase-free water). 1 µl of water was used as negative control for each primer pair. Amplification followed the program: denaturation at 95°C for 10 minutes, followed by 40 cycles of denaturation at 95°C for 30 seconds, annealing at 60°C for 30 seconds, and extension at 72°C for 30 seconds. Mean values were normalized to the housekeeping gene RPL0 and the cycle threshold (CT) for each sample was determined with the ViiA7 Software v1.2 from Applied Biosystems. Data was analyzed using Microsoft Excel (Microsoft, Redmond, USA) and the 2^(-Delta Delta (CT)) method (193). Values are depicted in fold-change, as mean values with 95% confidence interval. Statistical significance was measured using 2*way ANOVA and Turkey's multiple comparison test. P values ≤ 0.05 were considered statistically significant. Primer sequences are listed on Table 2.

Table 2: Primer sequences used in this work. All primers were produced by Eurofins Scientific.

AFP	AGCAGCTTGGTGGTGGATGA	CCTGAGCTTGGCACAGATCCT
ALB	AGCTGTTATGGATGATTTCGCAG	CCTCGGCAAAGCAGGTCTC
ATM	TTTTCAACCAGTTTTCCGTTACTTC	ACA CTG CGC GTA TAA GCC AAT C
ATR	CTGCCACTCAGCTTACCACT	AAGCTGTGCTGGGCTACATT
BBC3	TCCTGGGTCCCTGGCCAAGAAG	GTGTCACCCCTGCAGCTGGAAC
CASPASE 3	TCATTATTCAGGCCTGCCGTGGTA	TGGATGAACCAGGAGCCATCCTTT
CDKN1A	GATGTCCGTCAGAACCCATGCG	GTCGAAGTTCCATCGCTCACGG
CHEK1	CAAGAAAGGGGCAAAAAGG	TGTATGAGGGGCTGGTATCC
CHEK2	TTCAGCAAGAGAGGCAGACC	GCGTTTATTCCCCACCACTT
DDB2	GCCATCTGTCCAGCAGGGGC	GGGGTGAGTTGGGTGCCACG
cJUN	ACCTTGAAAGCTCAGAACTCGG	TTAGCATGAGTTGGCACCCAC
GADD45A	CAGGCGTTTTGCTGCGAGAACG	TGTGGATTCGTCACCAGCACGC
HNF4a	GCACTCGAAGGTCAAGCTA	GACTCACACACATCTGCGA
KRT18	GAGGTTGGAGCTGCTGAGAC	CAAGCTGGCCTTCAGATTTC
KRT19	CCGCGACTACAGCCACTACT	ATTGTCGATCTGCAGGACAATC
MAP2	GTCACAGTGGAGGAAGCAGC	CTGGGCTCTTGGTTACTCCG
MDM2	AAACTGGGGAGTCTTGAGGG	TGCACATTTGCCTGCTCCTC
MUC1	CCTTGGCTGTCTGTCAGTGCCG	ACGATCGGTACTGCTAGGGGGC
NANOG	CCTGTGATTTGTGGGCCTG	GACAGTCTCCGTGTGAGGCAT
NAP1L1	CATGTTGGCCAGGCTGGTCTCG	AAGAAACTGGCTGGGCGTGGTG
OCT4	AGTTTGTGCCAGGGTTTTTG	ACTTCACCTTCCCTCCAACC
PAX6	CAGAGAAGACAGGCCAGCAA	CCATGGTGAAGCTGGGCATA
POLH	GCCCACAACAGCCAAAGCATGC	GGGGTTTGAAGAGTGGGGCTGC
RBFOX3	GGCCAGGCTGTGCGT	AATTTCAACCTCCAGGACCGA
SOX1	TTGGCATCTAGGTCTTGGCTCA	CGGGCGCACTAACTCAGCTT
SOX2	GTATCAGGAGTTGTCAAGGCAGAG	TCCTAGTCTTAAAGAGGCAGCAAAC
TNFRSF10A	CACACCCTGCTGGATGCCTTGG	CAAGGACACGGCAGAGCCTGTG
TP53	CAG GGC AGC TAC GGT TTC C	CAG TTG GCA AAA CAT CTT GTT GAG
TUJ1	ATGAACACCTTCAGCGTCGT	CATCCGTGTTTTCCACCAGC
XPC	GACCTCAAGAAGGCACACCA	TGGCTTCACAGGCAGAAGAG

2.2.5. Immunocytochemistry staining

Immunocytochemistry was done in 12 or 24-well plates. The medium was aspirated and the cells were briefly washed with DPBS and then immediately fixed with 4% paraformaldehyde (PFA) 4% for 15 minutes at RT on a shaking platform. The fixed cells were washed 3 times for5min with DPBS. For staining of intracellular proteins the cells were permeabilized with 0.5% Triton-x-100/DPBS for 10min and then washed 2x with DPBS. Cells were then incubated with blocking buffer containing 10% normal goat serum (Sigma-Aldritch)/DPBS (for HNF4α staining) or 3% bovine serum albumine (BSA, Sigma-Aldritch)/DPBS (for all other antibodies) for 1h at RT. After the blocking

period, cells were incubated with primary antibody diluted in blocking buffer overnight at 4°C shaking. In the next morning the cells were then washed 3x/5min with DPBS, then further incubated with a secondary antibody solution diluted in blocking buffer, supplemented with the nuclear stain Hoechst 33258 (Thermo Fisher) for 2h RT (antibodies used can be seen in Table 3). Pictures were taken using a Zeiss LMS 700 and analyzed using the software Zen Blue 2.5. When applicable, cells were counted manually using the programme image J and ratios of treated conditions and control were calculated using Microsoft Excel, as were standard deviations (SD). Ratios and SD were visualized as bar graphs. Statistical significance was measured using 2*way ANOVA and Turkey's multiple comparison test. P values ≤ 0.05 were considered statistically significant.

2.2.6. PI staining and cell cycle FACS analysis

Cells were treated with BPDE for 24h. At the end of treatment cells were harvested using 0.25 % Trypsin-EDTA (Sigma-Aldritch) and centrifuged at 500xgfor 5min at 4°C. 10 x 10^4 cells were transferred to FACS tubes (Corning), washed with 1ml of PBS and centrifuged as stated above. The supernatant was discarded, and the cells were incubated for 1h in 25µl of staining solution composed of 0,1% sodium citrate, 0.1% Triton-x-100 and 50mg/L of propidium iodide (Invitrogen), diluted in ionized water. Cell cycle measurement was carried out through FACS on a CytoFlex BA26183 from Beckman Coulter and analysis were done on CytExpert 2.3. Statistical significance was measured using 2*way ANOVA and Turkey's multiple comparison test. P values ≤ 0.05 were considered statistically significant.

2.2.7. Western blot

2.2.7.1. Protein isolation

Cells were cultivated in a 6-well plate and total protein was extracted with RIPA buffer (Sigma-Aldrich), with protease and phosphatase inhibitors (Roche, Mannheim, Germany). First, the cells were washed with ice cold DPBS, then 150 µl of RIPA buffer mix was added directly to the well and incubated for 5min. The cells were then scrapped from the well and the solution was transferred to an Eppendorf tube and kept on ice for 30min under constant agitation. The samples were then centrifuged at 20000xg and 4°C for 20 min. Supernatant was collected in ice-cold Eppendorf tubes and stored at -80°C for later use.

2.2.7.2. Protein quantification

Protein concentration of the cell lysate was measured using the Pierce BCA Protein Assay Kit (Thermo Fisher) following the manufacturer's instructions. All standards and samples were prepared in duplicate. The BSA standard curve was prepared in 1%SDS for a final volume of 25 µl and went from 2000 µg/mL to 25 µg/mL. 5 µl of the samples were diluted to a final volume of 25 µl. The standard and the samples were platted on a flat bottom 96-well plate. 200 µl of the Master mixed reagent prepared according to the manufacture's instructions were added to the well and then the plate was incubated at 37°C for 30min. The absorbance was measured at 560nM wavelength using the ELISA plate reader AF2200 (Eppendorf). Protein concentration was measured using a linear regression curve stablished from the standard values (Protein Concentration in µg/ml = m*Abs560 + b).

2.2.7.3. SDS-page

The samples were diluted to a final volume of 20µL with a protein amount of 20µg in RIPA buffer containing 4X loading buffer (2.5 ml Tris 1M (pH 6.8), 0.8 g sodium dodecyl sulfate (SDS) 4 ml Glycerol, 2 ml 2-Mercaptoethanol, 1 mg Bromophenol blue, adjusted to 10 ml with dH2O). They were then heated in a thermoblock at 95°C for 3 minutes and subsequently loaded in completely onto a 10% SDS resolving gel along with 4 µl of the Protein Marker V protein ladder (PEQLAB Biotechnology, Erlangen, Germany). Gel electrophoresis was performed at 100 V until the samples reached the resolving gel and then at 150 V until they reached the bottom of the gel. The running buffer used was 25 mM Tris, 250 mM Glycine, and 0.1 % SDS in distilled water with a pH of 8.3.

2.2.7.4. Membrane transfer and blotting

Wet blotting was used to transfer the proteins to a nitrocellulose membrane (GE Healthcare). The gel was removed from the electrophoresis machine, laid on a nitrocellulose membrane and sandwiched between 2x Whatman papers and a sponge on each side. The whole construct was put in a transfer tank filled with transfer buffer (0.25 mM Tris-base and 0.192 mM Glycine, pH 8.3, and 20% methanol) and transferred at 0.2A for 3h. Ponceau S was used to confirm protein transfer, and then washed with 0.05% TBS-Tween-20 (TBS-T).

After washing, the membrane was blocked for 2h in 5 % milk/TBS-T. The primary antibodies were diluted in either 5 % milk/TBS-T or 5 % BSA/TBS-T, according to the manufacturer's specifications (more details on Table 3) and incubated with the membrane overnight in a shaker at 4°C, after which they were washed 3x/5min with TBST and incubated with anti mouse-HRP or anti rabbit-HRP (1:1000) for 2h. After that, the membrane was washed 3x/5min with TBS-T and then developed using AmershamTM ECL™ Primary Western Blotting Detection Reagent. Signaling was visualized using FusionCapt Advance FX7 and band intensities were quantified in the software Fusion Capt Advance (PeqLab) using rolling ball background correction.

Table 3: Antibodies and dilutions used on immunocytochemistry (ICC) and Western blot. For ICC, all antibodies were diluted in 3%BSA/DPBS unless stated otherwise. For western blot, all antibodies were diluted in 5% BSA/TBS-T unless stated otherwise. CST: Cell signaling Technologies. R&D: R&D Systems. SySy: Synaptic Systems. gp: guinea pig; gt: goat; ms: mouse; rb: rabbit. MW: expected molecular weight of protein band.

Antibody	Brand	ICC	Western Blot	ID number
gp GFAP	SySy	1:500	-	173004
gt SOX17	R&D	1:50	-	AF1924
ms PAX6	SySy	1:1000	-	153011
ms Tuj1	CST	1:750	-	TU-20
ms Ki67	CST	1:200	-	9449S
ms p53	CST	1:1000	1:1000 in 5% milk/TBS-T. (MW: 53kDa)	mAb2524
ms SSEA4	CST	1:1000	-	4755S
ms TRA-1-60	CST	1:1000	-	4746S
ms TRA-1-81	CST	1:1000	-	4745S
ms b-Actin	CST		1:5000 in 5% milk/TBS-T (MW:45kDa)	3700S
rb AFP	SigmaAldrich	1:300	-	HPA023600-100UL
rb cJUN	CST		1:1000. (MW: 43 kDa)	9165S
rb Cleaved Caspase 3	CST		1:1000. (MW: 17-19 kDa)	9664S
rb anti NANOG	CST	1:800	-	4903S
rb anti OCT4	CST	1:400	-	mAb2840
rb anti p-cJUN	CST		1:1000. (MW: 43 kDa)	3270S

rb anti pHiston H2A.X	CST	1:150	1:1000. (MW: 15 kDa)	9718S
rb anti SOX2	CST	1:400	-	3579S
rb CASPASE 3	CST		1:1000. (MW: 35 kDa)	9662S
rb Map2	SySy	1:1000	-	188002
rb MDM2	CST		1:1000 (90 kDa)	86934S
rb Nestin	SigmaAldrich	1:1000	-	N5413
rb RPL0	Proteintech		1:1000 (34kDa)	
rb S100beta	Abcam	1:100	-	ab52642
Rb HNF4A	Abcam	1:250 in 10%NGS/DPBS	-	92378

The ratio of mean signal intensity of protein of interest and housekeeping protein (RPL0 or β-actin) expression was calculated using Microsoft Excel, as were standard deviations (SD). SD were calculated when two or more biological replicates were available. Ratios and SD were visualized as bar graphs. Statistical significance was measured using 2-way ANOVA and Turkey's multiple comparison test. P values ≤ 0.05 were considered statistically significant.

2.2.8. Southern slot blot

Genomic DNA was extracted as described on 2.2.1 and an amount of 250ng or 500ng was diluted in TE buffer (1% 1 M Tris-HCl and 0.2% 500 mM EDTA in distilled water) to a final volume of 100µl. Samples were denatured for 10min at 95°C, cooled on ice, then 100 µl ice-cold ammonium acetate (2 M) was added to the solution. A nitrocellulose membrane was soaked in 1M ammonium acetate and placed in the slot blot apparatus, and 200µl of the prepared DNA solution was pipetted into the slots. A vacuum pump was used to transfer the DNA solution from the slots to the membrane. The membrane was washed with 1M ammonium acetate, then with distilled water and then incubated for 5min with saline-sodium citrate (SCC) buffer made with 1.5M NaCl and 150mM sodium citrate diluted in distilled water. The DNA was fixed to the membrane by baking the it for 2h at 80°C, then the membrane was blocked with either 5%milk/TBST or 5%BSA/TBST for 1h RT, washed 3x/5min with TBST and incubated with primary antibody (more details on dilution on Table 4) overnight at 4°C. The membrane was then again washed 3x/5min with TBST and incubated with anti-mouse HRP (1:2000) for 2h RT. The membrane was once again washed 3x/5min with TBST and the antibody binding was detected using the AmershamTM ECL™ Primary

Western Blotting Detection Reagent and the ChemiDoc imaging system (Bio-Rad). To check for DNA loading, membranes were incubated for 5min with methylene blue solution (0.4g/l-methylene blue in 0.5M sodium acetate), washed with distilled water and photographed on ChemiDoc.

Table 4: Antibody and dilutions used for Southern blot. ms: mouse.

Antibody	Brand	Southern Blot	ID number
msBPDE-DNA	Santa Cruz	1:500 in 5% BSA/TBS-T	sc-52625
		1:1000 in 5% BSA/TBS-T	
		1:2000 in 5% BSA/TBS-T	
		1:1000 in 5% milk/TBS-T	
		1:2000 in 5% milk/TBS-T	

2.2.9. Focused qRT-PCR arrays

In the case of hiPSCs, media was aspirated from a well of a 6-well plate, cells washed once with DPBS and dissociated with 10min incubation with accutase. The cells pellets were sent to the Institute of Toxicology (UKD, Germany) where RNA was purified using the RNeasy Mini Kit (QIAGEN). Normal human dermal fibroblast (NHDF) RNA was provided by the Institute of Toxicology (**Error! Reference source not found.**). The f ocused qRT-PCR arrays were performed using the High-Capacity cDNA Reverse Transcription Kit (Applied Biosystems, Darmstadt, Germany) with 6000 ng of RNA of NBS8 hiPSCs and NHDF, and 3600ng of RNA of iPSC-12 hiPSCs. For each PCR reaction, 20 ng of cDNA of NBS8 hiPSCs and NHDF, and 17 ng of cDNA of iPSC-12 hiPSCs and 0.25 µM of the corresponding primers (Eurofins MWG Synthesis GmbH, Ebersberg, Germany) were used. Quantitative RT-PCR was performed as follows: 1) 95°C, 10 min; 2) 45 amplification cycles with 95°C, 15 s, 55°C, 15 s, and 72°C 17 s; 3. 95°C, 1 min, 55°C, 1 min, 65°C, 5 s, 95°C, 1 min. Analyses were performed in triplicates (NBS8 hiPSCs and NHDF) and duplicates (iPSC-12 hiPSCs) using a CFX96 cycler (BioRad) and the SensiMix SYBR Kit (Bioline, London, UK). At the end of the run, melting curves were analyzed to ensure the specificity of the amplification product. mRNA expression levels were normalized to those of β-ACTIN and GAPDH. Relative mRNA expression of untreated control cells was set to 1.0.

2.2.10. Affymetrix microarray analysis

Total RNA was extracted from iPSCs UM51, iPSC-12 and NBS8, in CTRL conditions and after 24h treatment with 75nM BPDE. The RNA was sent for analysis to the Biomedizinisches Forschungszentrum (BMFZ) facility at Heinrich-Heine University, Duesseldorf. The quality and integrity of the RNA was investigated using a Fragment Analyzer from Advanced Analytical Technologies. After quality assessment, 100ng of RNA was hybridized using a Human Clariom S Array (Affymetrix, Thermo Fisher Scientific).

2.2.10.1. Gene expression analysis

Raw data (CEL files) were received from the BMFZ. The Affymetrix CEL files were imported into the R/Bioconductor (194) environment, background-corrected and normalized using the Robust Multi-array Average (RMA) method from the package oligo (195). Tables of Pearson correlation coefficients were generated using the R-built-in method “cor”, hierarchical clustering dendrograms with the method “hclust” using Pearson correlation as similarity measure and “complete linkage” as cluster agglomeration method. The “heatmap.2” function from the “gplots” package (196) was applied either with Pearson correlation as similarity measure and color scaling per gene or with Euclidean distance as distance measure and color scaling over the whole heatmap. Genes were considered expressed when their detection p-values - calculated as described in Graffmann et al. (197) were below a threshold of 0.05. Using these expressed genes, expression was dissected with venn diagrams employing the R package “VennDiagram” (198) for comparisons between NBS8_BPDE vs NBS8_CTRL, UJ_BPDE vs UJ_CTRL, iPSC12_BPDE vs iPSC12_CTRL, BPDE vs CTRL (all BPDE vs all CTRL samples), iPSC12_BPDE and UJ_BPDE vs iPSC12_CTRL and UJ_CTRL (healthy BPDE vs healthy CTRL), NBS8_CTRL vs iPSC12_CTRL and UJ_CTRL (NBS CTRL vs. healthy CTRL), NBS8_BPDE vs iPSC12_BPDE and UJ_BPDE (NBS BPDE vs. healthy BPDE). Genes from the intersection of the venn diagrams, i.e. expressed in both conditions were further filtered for up-regulation by a ratio > 1.5 and down-regulation by a ratio < 0.67. When there were replicates, a threshold of 0.05 for the p-value of the differential expression test from the Bioconductor “limma” package (199) was added to the filter criteria.

2.2.10.2. Gene ontology (GO) and KEGG pathway analysis

Differentially up- and down-regulated genes were subjected to GO analysis via the Bioconductor package “GOstats” (200) . Resulting GOs were further filtered for at least three genes per GO term and conditional on the GO structure, i.e. “GOstats” checks if there is evidence for over-representation beyond that given by the GO term’s children. The most significantly over-represented GO terms were plotted in a dot plot indicating p-value on a color scale, number of contributing genes by point size and ratio of regulated genes compared to all genes in the term on the x-axis via the Bioconductor package “ggplot2” (201) . KEGG pathways and genes associated with them were downloaded from the KEGG database (202) in February 2023 . Over-represented KEGG pathways were calculated for up- and down-regulated genes employing the R-built-in hypergeometric test. The most significantly over-represented KEGG pathways were plotted in a dot plot analogously to the dot plot of GO terms.

2.2.10.3. Metascape analysis

The enrichment analysis tool Metascape (203) was used to compare input gene lists extracted from the microarray data to thousands of available gene sets defined by their involvement in biological processes, protein localization, enzymatic function, pathway membership, among other features. The top non-redundant enrichment clusters are represented in bar graphs.

2.3. Treatment and assays

2.3.1. BPDE treatment

BPDE (Santa Cruz Biotechnology) was dissolved in DMSO (SIGMA) at a concentration of 40mM and the aliquots were kept at -80°C for up to six months. The doses used on iPSC, NPC, neurons HE experiments were selected based on IC90 and IC80 values following Resazurin (2.2.11.2) testing on iPSCs. The doses used on organoids were selected based on IC50 testing values for CellTiter-Glo 3D Cell Viability Assay. For hiPSCs and NPCs treatment, the cells were cultured until 60-70% confluence, then their medium was replaced with fresh medium containing BPDE or vehicle control (0.02% DMSO). For HEs, the cells were cultivated until day 7 of differentiation and then treated. Organoids were treated at day 20. The cells were exposed to BPDE for72h in the case of neurons, 24h for the other 2D cultures and both for the organoids; thereafter, the medium was discarded, and the cells were prepared for analysis.

2.3.2. Resazurin reduction assay

A 0.15 mg/ml stock solution of resazurin was prepared by dissolving 5mg of resazurin in powder form in 50mL of sterile PBS. The solution was filtered through a 0.2 µm syringe filter and kept at 4°C until use. Cells were cultivated in triplicates on a 96-well plate and continuously exposed to BPDE in concentrations raging from 10nM to 21µM for 22h, then medium supplemented with resazurin stock solution in a 1:10 dilution was added to the culture. The plates were returned to 37°C and incubated for 2h to allow the cells to metabolize resazurin into resorufin, which is a fluorescent compound. The fluorescence was measured using a microplate fluorimeter (Eppendorf PlateReader AF2200) equipped with a filter set of 560nm excitation and 590nm emission. Measurements of cell cultures treated with increasing doses of BPDE and normalized according to the manufacturer's protocol were imported into the R environment (204). The packages dr4pl (205)(An et al. 2019) and ggplot2 (201) were employed to use a logistic model for curve-fitting, plotting the curve and calculating the IC50 and additionally IC80 and IC90.

2.3.3. CellTiter-Glo 3D Cell Viability Assay

The viability of cerebral organoids after BPDE exposure was evaluated using the CellTiter-Glo 3D Cell Viability Assay (Promega). Day 20 cerebral organoids were continuously exposed to BPDE for 24h or 72h, in concentrations ranging from 0.01 µM to 100 µM. At the end of the treatment, the organoids were transferred with 100 µL of cell culture medium to a black Eppendorf tube and allowed to reach room temperature. An Eppendorf tube with only culture medium, without organoids, was prepared as a negative control. Then, 100 µL of CellTiter-Glo 3D Cell Viability Assay reagent was added to each Eppendorf. The solution was mixed vigorously to induce cell lysis and incubated at room temperature for 25min. After that, the mixture was transferred to a polypropylene tube (Corning) and read at the Luminometer Lumat LB9507.

2.3.4. 5-ethynyl-2'-deoxyuridine (EdU) incorporation assay

The fluorescence staining for incorporated EdU was performed using the Click-iT™ EdU Cell Proliferation Kit for Imaging, Alexa Fluor™ 488 dye (Invitrogen), as instructed by the manufacturer. hiPSCs were treated for 24h with BPDE, then labelled with EdU. In order to not disturb cell proliferation, the EdU stock solution was diluted in mTeSR Plus to a concentration of 20 µM and only 100 µL of cell culture media was replaced

by this EdU solution, for a final in-culture concentration of 10 µM. The cells were incubated with EdU for 2h and afterwards the medium was aspirated, and the cells were washed, fixed and permeabilized as described in 2.2.5. The EdU Reaction Mix was prepared fresh as described by the manufacturer and used within 15min of preparation. 100 µL of EdU Reaction Mix was added to each well and the plate was incubated for 30min at RT, protected from light and under gentle agitation. Then cells were washed once with the washing buffer provided in the kit, then once with DPBS. Hoechst 33258 was used for DNA staining. Pictures were taken using a Zeiss LMS 700 and analyzed using the software Zen Blue 2.5. EdU+ cells were counted manually using the programme image J and ratios of treated conditions and control were calculated using Microsoft Excel, as were standard deviations (SD). Ratios and SD were visualized as bar graphs. Statistical significance was measured using 2*way ANOVA and Turkey's multiple comparison test. P values ≤ 0.05 were considered statistically significant.

3. Results

3.1. Stabilization of a new NBS-derived iPSC line – NBS2

A former member of our working group, Dr. Soraia Martins, attempted to generate a new NBS-derived iPSC line through episomal reprograming, named NBS2. The generation was only partially successful. The line was unstable, showing elevated death rates while in culture and after passaging, and was highly prone to differentiation. Immunocytochemistry revealed the presence of classic pluripotency markers such as OCT4, but also the presence of markers of the ectoderm lineage, like nestin and PAX6. (Figure 10).

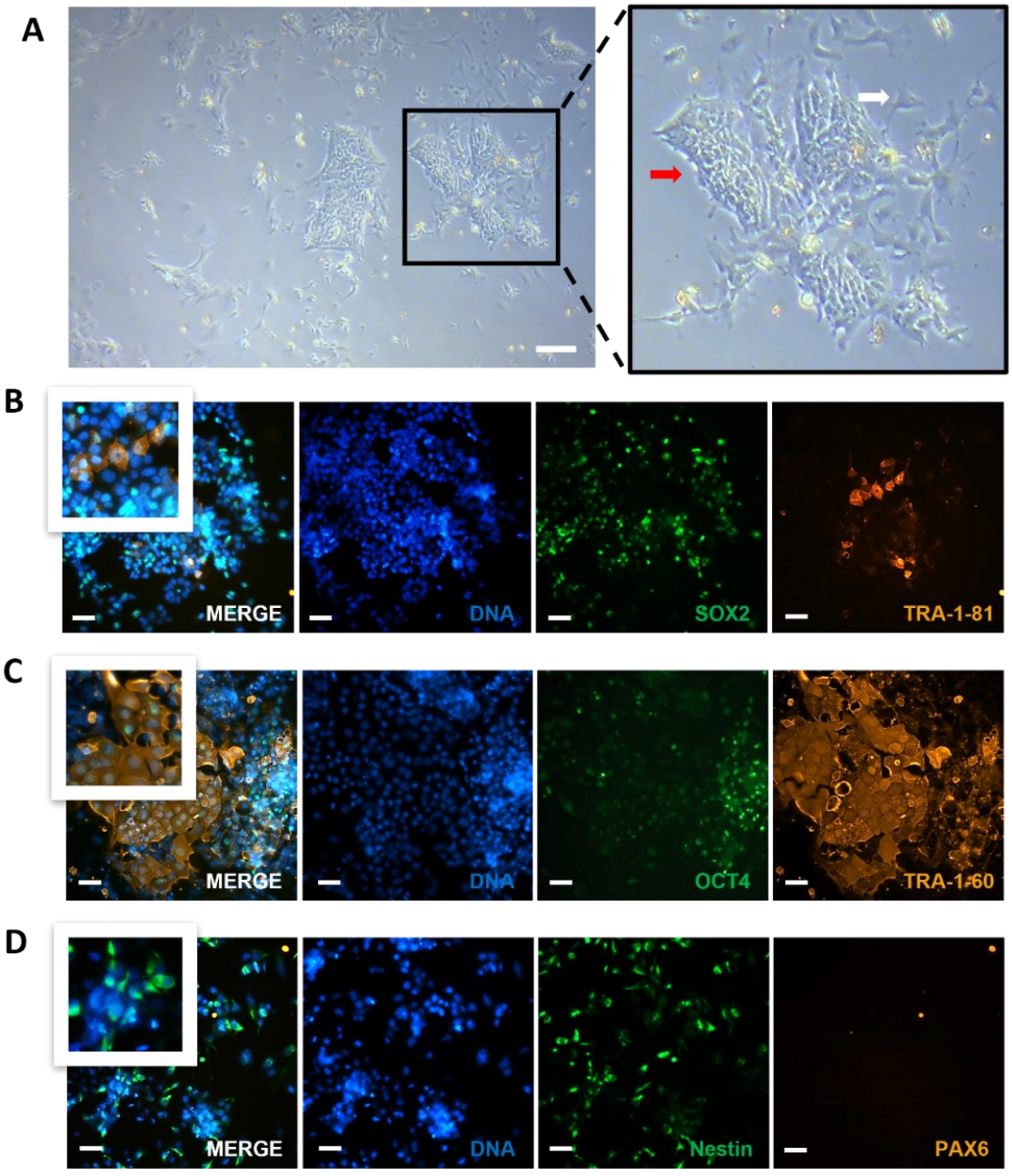

Figure 10: Immunocytochemistry of non-stable NBS2 iPSC. The NBS2 iPSC line was unstable and prone to spontaneous differentiation. **(A)** Red arrow shows an iPSC colony and white arrow shows a differentiated cell. **(B and C)** Immunocytochemistry revealed the presence of key pluripotency markers such as SOX2, TRA-1-81, OCT4 and TRA-1-60, **(D)** but also many cells stained with ectoderm lineage markers like Nestin and PAX6. Scale bars 200µm in figure A and 100µm on B, C and D.

In an attempt to stabilize the line, during culture as well as after passaging, several passaging reagents were tested in search of one that provided higher cell viability and minimal iPSC spontaneous differentiation. All attempts were done using a clump passaging technique, passaging the cells in aggregates instead of single cells.

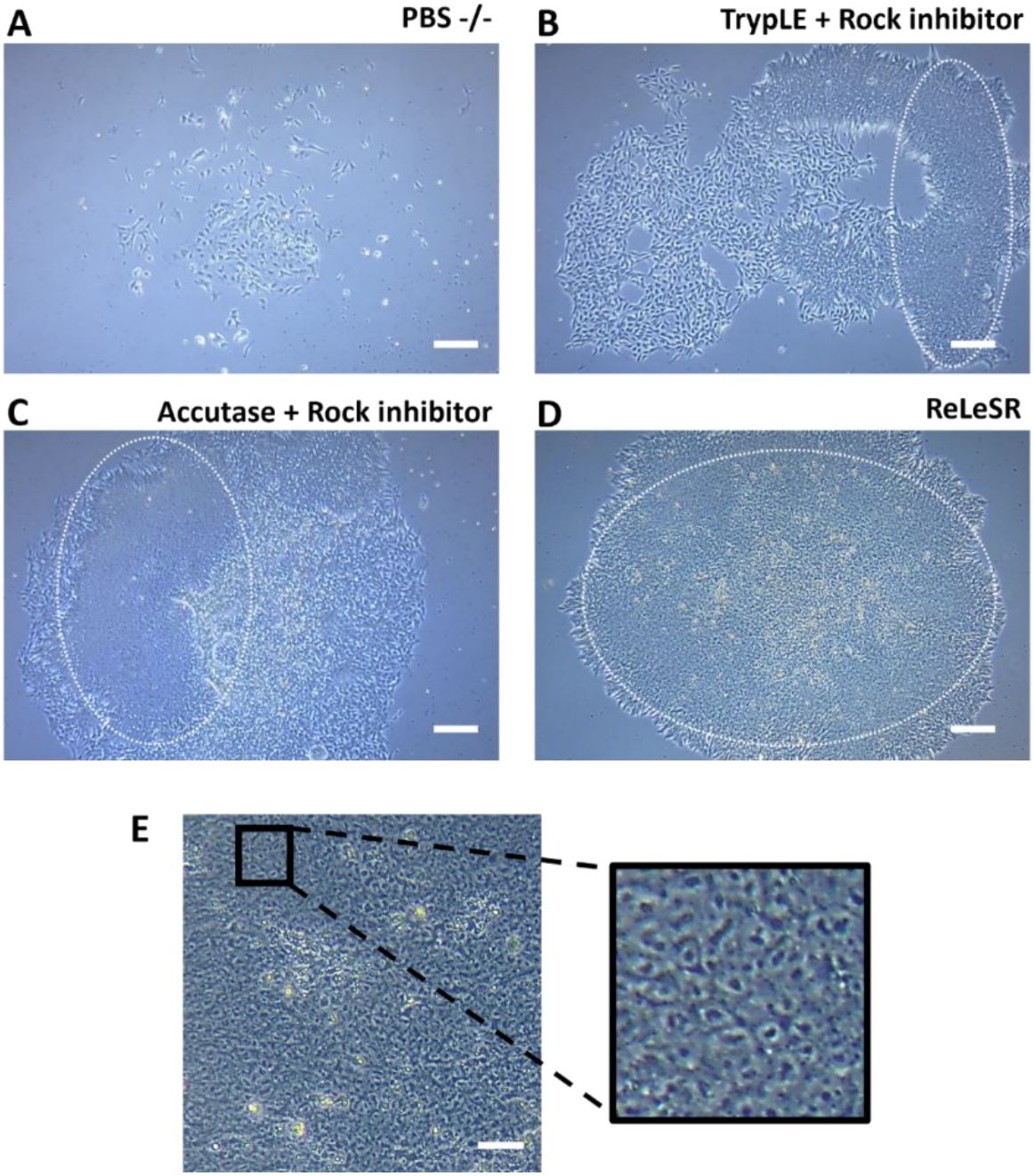

Figure 11: NBS2 iPSC maintenance and splitting protocol testing. iPSCs passaged with different reagents. **(A)** PBS -/-; **(B)** TrypLE + Y-27632; **(C)** Accutase + Y-27632; and **(D)** ReLeSR. **(E)** Close up of an iPSC colony, showing small cells, tightly packed cells with high nuclei to cytoplasm ratio. The dotted ovals highlight iPSC colonies. Scale bars 200μm.

Phosphate buffered saline (PBS) without Ca2+ and Mg2+ (Figure 10A); TrypLE, a recombinant enzyme used for dissociating mammalian cells, in combination with the rock inhibitor Y-27632, which supresses disassociation-induced apoptosis (206) (Figure 11B); and Accutase, an enzyme mixture with proteolytic activity, also in combination with Y-27632 (Figure 11C), were all unsuccessful. Eventually ReLeSR was chosen as the best candidate, an enzyme-free iPSC passaging and selection reagent (Figure 11D) which after a few passages, resulted in less cell death and good iPSC colony formation (Figure 11E). that provided higher cell viability and minimal iPSC spontaneous differentiation.

3.1.1. Immunocytochemistry characterization of NBS2

Once the cells were stable after passaging and maintaining good colony formation, they were characterized through immunocytochemistry. They were stained for six pluripotency markers; the transcription factors OCT4, SOX2 and Nanog homeobox (NANOG); and the surface markers TRA-1-81, TRA-1-60 and stage-specific embryonic antigen-4 (SSEA4). The majority of the NBS2 iPSC culture stained for these key markers (Figure 12, A to F).

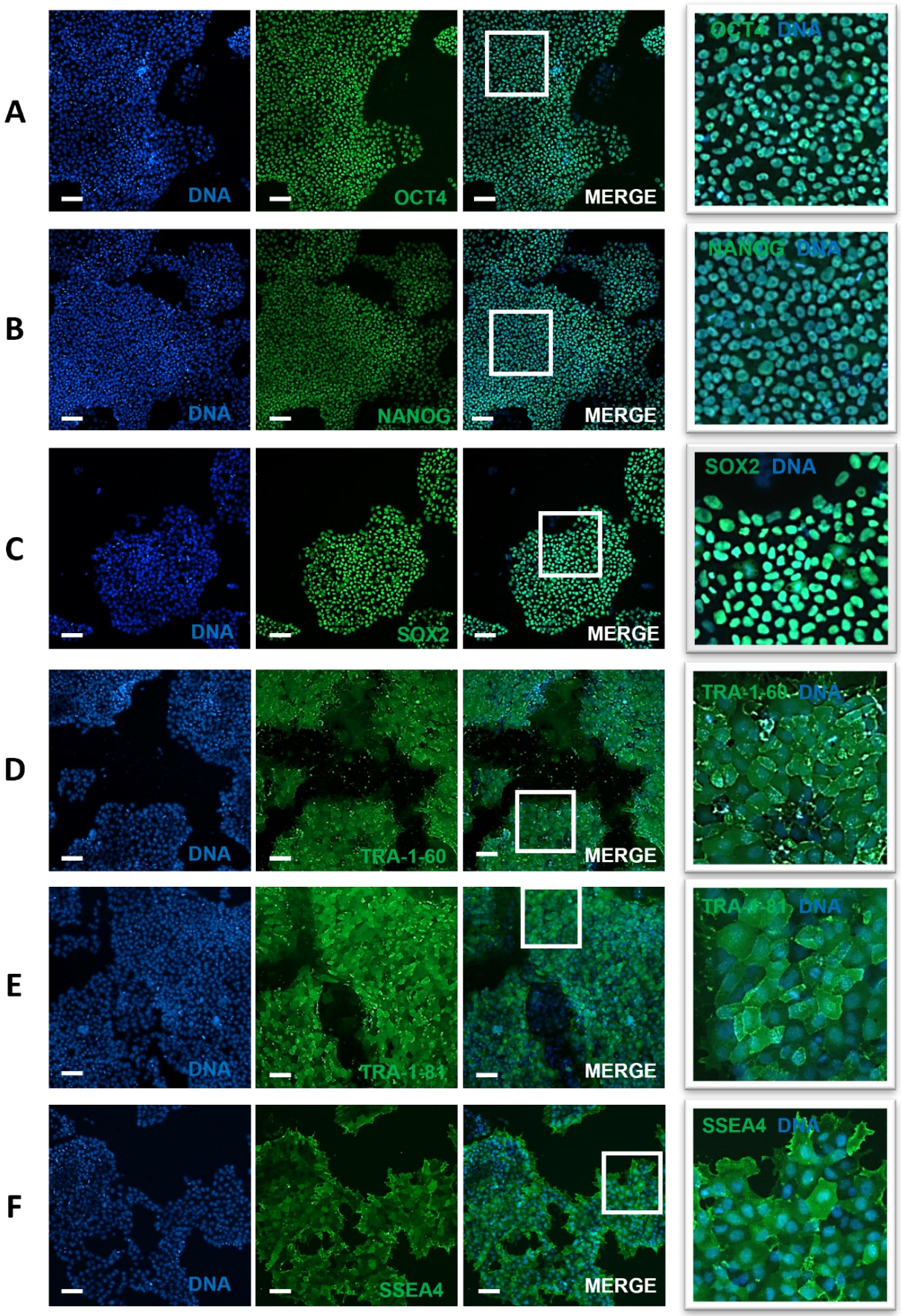
A
DNA
OCT4
MERGE
OCT4 DNA
B
DNA
NANOG
MERGE
NANOG DNA
C
DNA
SOX2
MERGE
SOX2 DNA
D
DNA
TRA-1-60
MERGE
TRA-1-60 DNA
E
DNA
TRA-1-81
MERGE
TRA-1-81 DNA
F
DNA
SSEA4
MERGE
SSEA4 DNA

Figure 12: NBS2 iPSC immunocytochemistry characterization. (A, B and C) Staining for transcription markers OCT4, SOX2 and NANOG. **(D, E and F)** Staining for surface markers TRA-1-60, TRA-1-81 and SSEA4. Scale bars 100µm.

3.1.2. Karyotyping of NBS2 revealed severe chromosomal aberration

Once the cells were stable after passaging, maintaining colony formation and iPSC morphology and markers, we proceeded to the next step of the characterization, the karyotyping. The cells were cultivated under the conditions described on 2.2.1 and sent for analysis at the Institut für Humangenetik at UKD – Düsseldorf. Chromosomal content analysis of NBS2 iPSCs revealed an abnormal karyotype, with all of the 25 investigated mitosis containing a partial trisomy, characterized by a duplication of the long arm of chromosome 1 (46,XX,dup(1)(q12q42)[25]) (Figure 13 and Supplementary Figure 3). The karyotyping of the parental fibroblast line could not be performed due to a lack of mitosis of the fibroblasts, however, the Institute for Medical Genetics - Charité Berlin who provided the original fibroblasts did not report the severe phenotype in the patient that is associated with the mutation. Further work with the NBS2 line was discontinued due to the mutation.

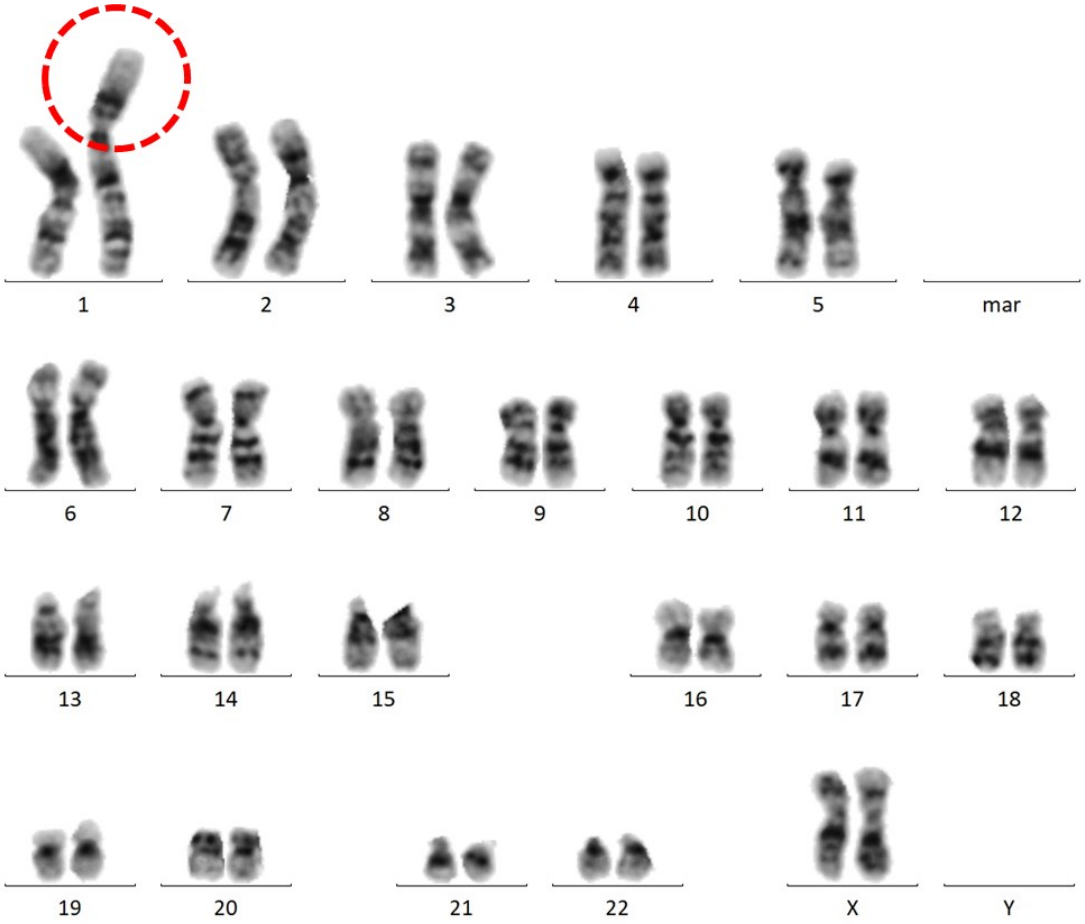

Figure 13: Karyotype analysis of NBS2. The chromosome content analysis revealed a duplication of the long arm of chromosome 1, highlighted by the dotted red line.

3.2. Generation of neuronal cell lineage from NBS-mutant hiPSCs

An attempt was made to generate 2D cultures of neuronal progenitor cells and neuronal cells, derived from induced pluripotent stem cells, following an established in-lab protocol. Two WT iPSC lines, UJ and iPSC-12, as well as the NBS-patient derived line NBS8, were utilized in the process. The protocol uses dual SMAD inhibition to generate NPCs from neural rosettes which can be plated in 2D for further passage and expansion or treated with BDNF and NT3 to generate neuronal cultures.

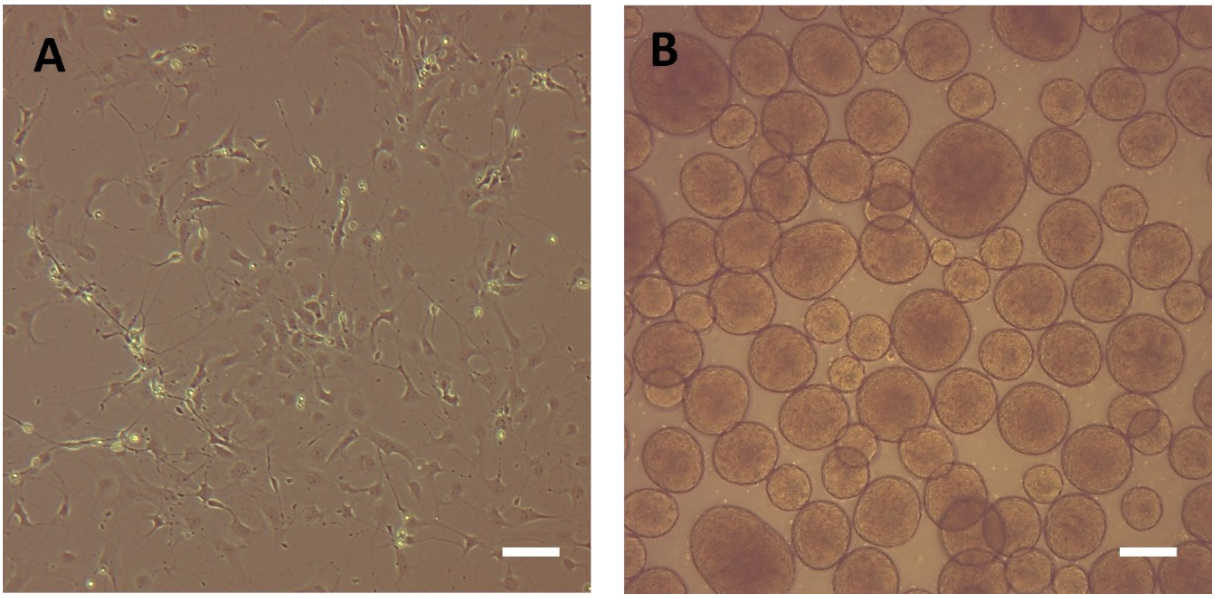

Figure 14: NBS8 NPC expansion methods. (A) Attempts to expand NBS8 NPCs in 2D faced high cell death and low proliferation rates. **(B)** 3D expansion of NBS8 NPCs as neurospheres partially circumvented these problems. Scale bars **(A)** 50µm and **(B)** 200µm.

While the generation of NPCs from the WT cells worked with little issue, the NBS8 NPC generation suffered complications. Attempts to expand or passage the NBS8 NPCs in a 2D monolayer were faced with high cell death and low proliferation rates. As an alternative, after neural rosette selection, instead of being treated with accutase to form aggregates and seeded in 2D (Figure 14A), they were kept in the form of neurospheres as floating cultures in a shaking incubator (Figure 14B). This yielded better NPC survival and proliferation, and NBS8 NPCs were therefore only plated in 2D for experiments.

Once NPCs were generated, the generation of neuronal cultures followed and the NBS8 line once again had difficulties. UJ NPCs behaved as expected during neuronal differentiation, with the progressive formation of neuronal clusters and robust neuronal arborization (Figure 15A and B). In contrast, the NBS8 NPCs had impaired neuronal differentiation, with high rates of cell death and an almost absence of neuronal formation and arborization (Figure 15C and D).

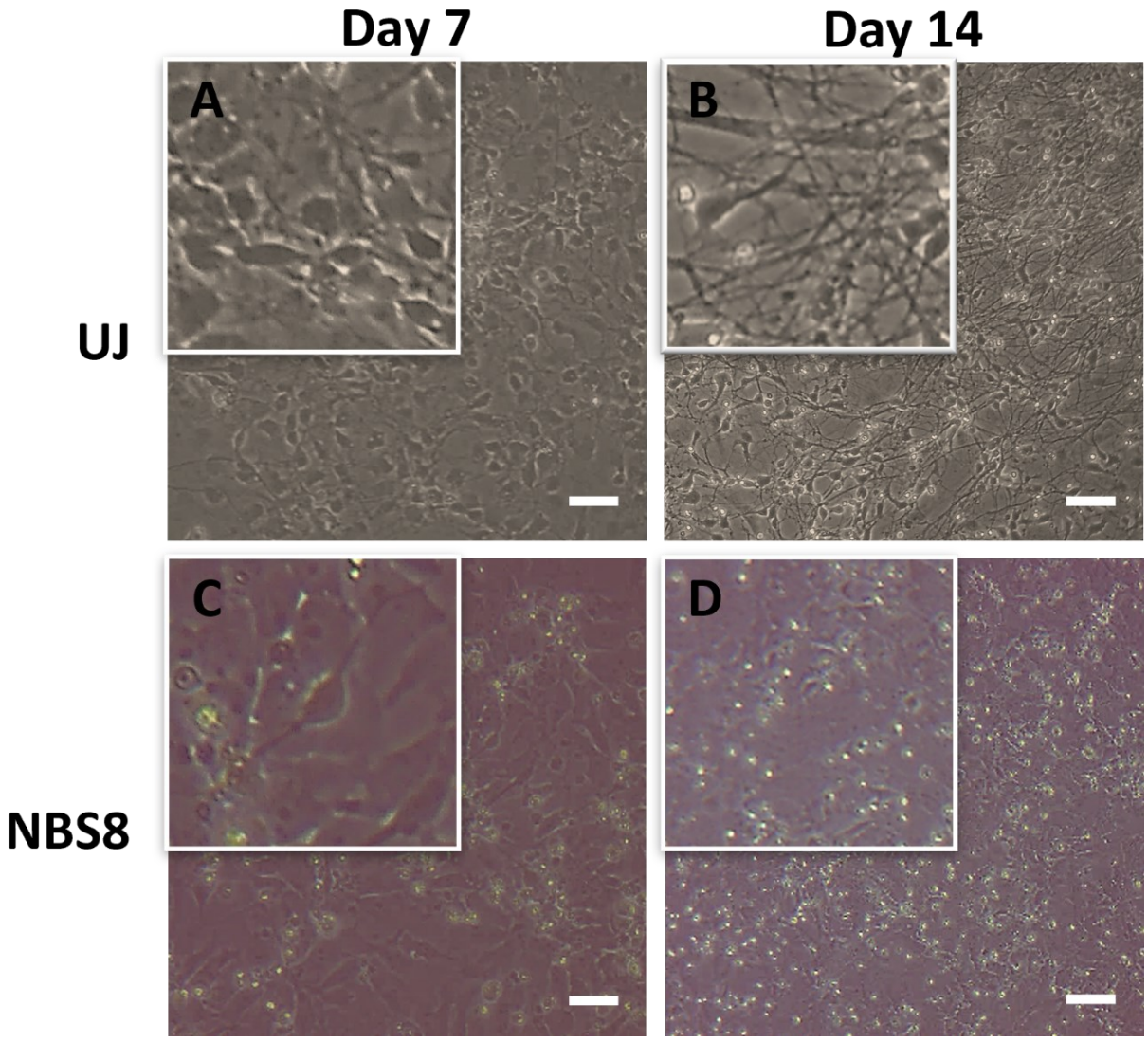

Figure 15: Impairment of the neuronal differentiation in the NBS8 line. (A and B) Neuronal differentiation in the UJ line shows progressive formation of neuronal clusters and neuronal arborization. **(C and D)** The NBS8 line has impaired neuronal differentiation, showing higher rates of cell death and poor neuronal formation and arborization. Scale bar 50µm.

To better understand the phenotype and cellular composition of the cultures, we did an immunocytochemistry for class III beta-tubulin (TUJ1), a marker for immature neurons; microtubule-associated protein 2 (MAP2), a marker for mature neurons; and S100 calcium-binding protein B (S100B) and Glial fibrillary acidic protein (GFAP), both

astrocyte markers. The UJ neuronal cultures revealed a dense TUJ1+ and MAP2+ neuronal network and the absence of GFAP+ or S100B+ cells (Figure 16A and C). The NBS8 neuronal cultures also had no GFAP+ or S100B+ cells, but they showed a much-reduced number of TUJ1+ cells, with scarce arborization. And although most cells were MAP2+, their morphology was highly abnormal. Unlike the neurons in the UJ culture which show small cell bodies from where neurites and axons extend, the NBS8 cells had large cell bodies with virtually no processes extending from them (Figure 16B and D).

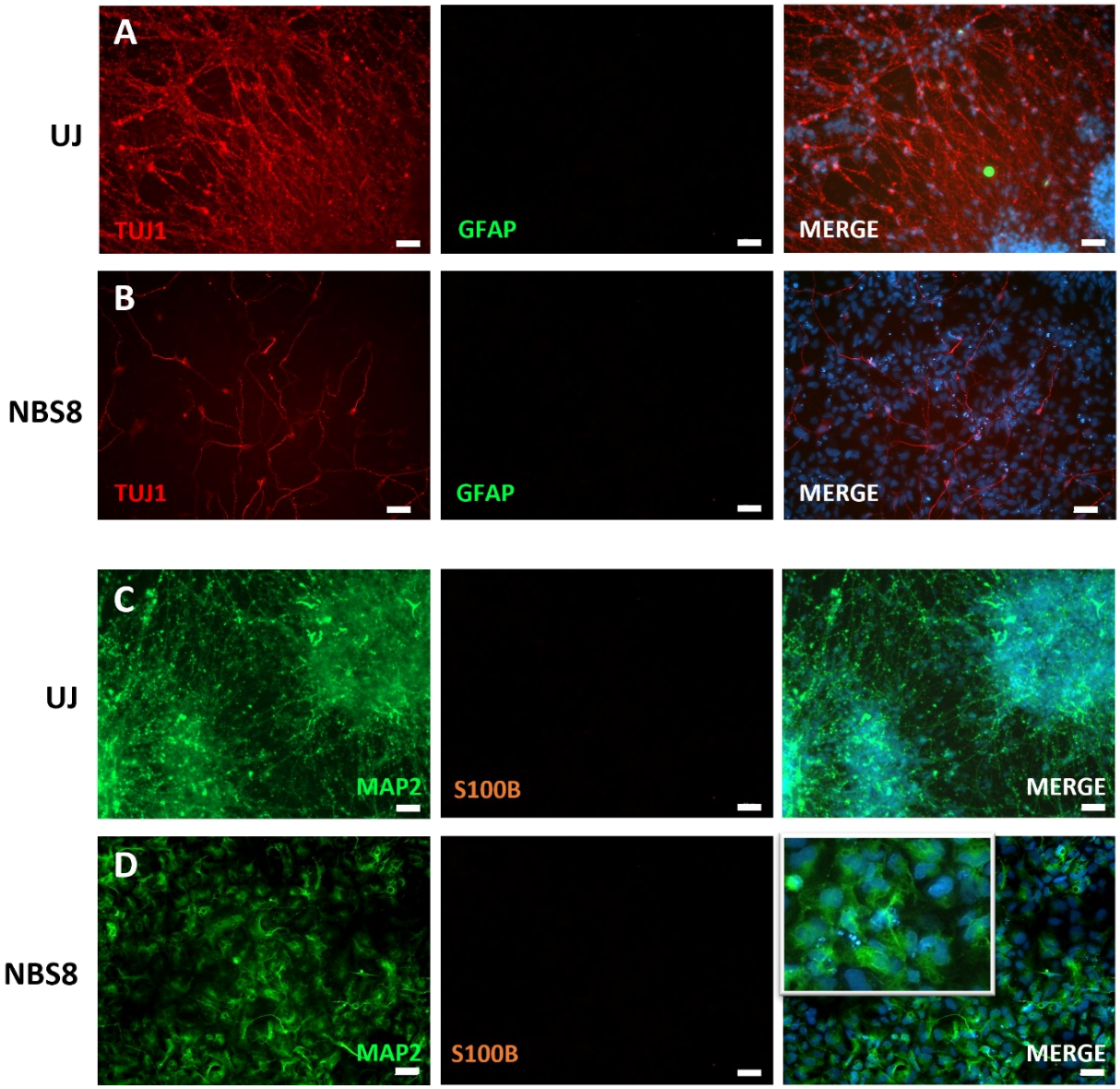

Figure 16: NBS8 neuronal cultures have an abnormal phenotype. Day 14 neuronal cultures were stained for TUJ1, GFAP, MAP2 and S100B. **(A and C)**. UJ neuronal cultures have a network of TUJ1+ and MAP2+ cells and no presence of GFAP+ or S100B+ cells. **(B and D)** The NBS8 neuronal culture has no GFAP+ or S100B+ cells, but it shows very few TUJ1+ cells and MAP2+ cells with abnormal morphology. Scale bar 50µm.

3.3. Generation of cerebral organoids from hiPSCs and viability after BPDE exposure

With the intention to investigate the effects of BPDE exposure on neural cells, we generated cerebral organoids derived from WT (UJ) and NBS8 hiPSCs using an established protocol (170). At day 20 in culture the cerebral organoids show SOX2 and neuroepithelial stem cell protein (Nestin) positive neural precursors aligned in neural rosettes, which are ventricular zone like structures. The rosettes are surrounded by doublecortin (DCX) positive neuroblasts and TUJ1+ neurons, forming the beginnings of a cortical plate (Figure 17A and B).

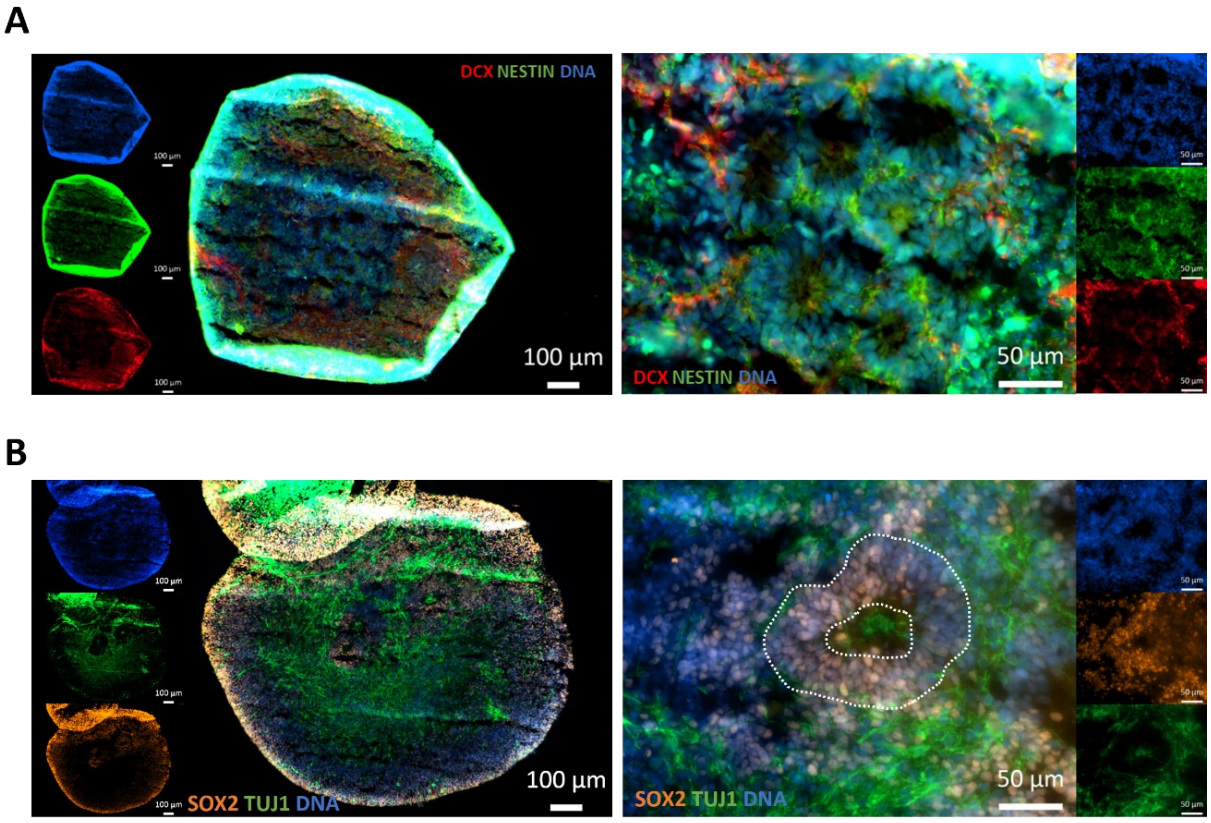

Figure 17: 20-day old cerebral organoids immunocytochemistry characterization. (A) Immunocytochemistry for DCX+ neuroblasts (in red) and Nestin+ NPCs (in green). **(B)** Immunocytochemistry for SOX2+ NPCs (in orange) and TUJ1+ neurons (in green). Hoechst (in blue) was used for DNA staining. The dotted lines delineate a neural rosette with SOX2+ neural precursors, surrounded by TUJ1+ neurons.

We measured the average diameter of our brain organoids and discovered that the NBS8-derived organoids were on average 25% smaller than their wild –type counterparts (Figure 18A and B).

Next, we wished to analyze the cell viability of the organoids after BPDE exposure. Therefore, we used the CellTiter-Glo 3D Cell Viability Assay, which quantifies ATP as a marker for the presence of metabolically active cells and generates a luminescent signal that can be read at a luminometer. Organoids derived from UJ showed no significant drop in viability in any of the observed time points and concentrations. Meanwhile, organoids derived from NBS8 showed loss of viability after 72h of BPDE exposure, starting at 20% loss of viability at 5µM and reaching a loss of 33% of viability at 100µM (Figure 18C).

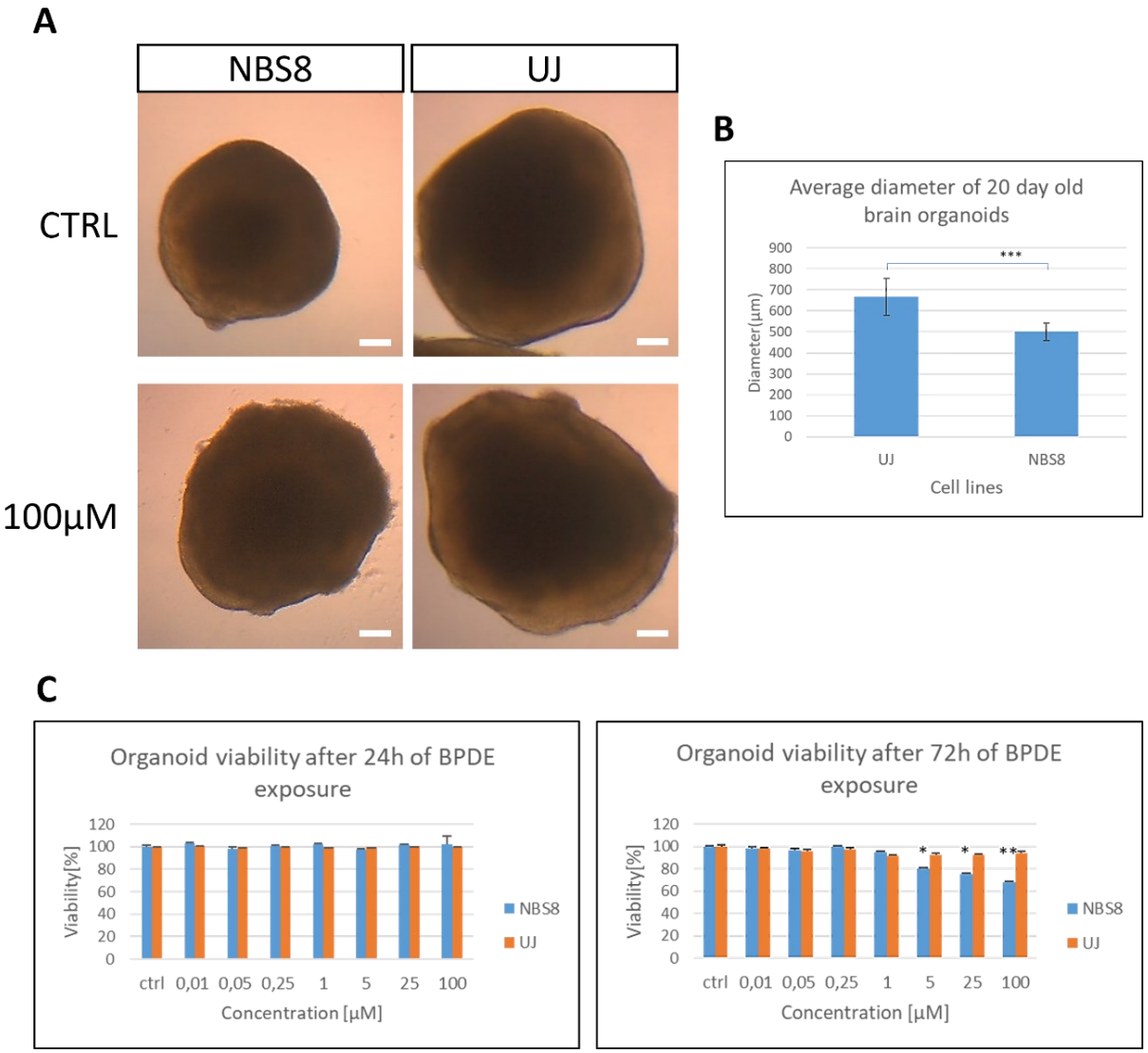

Figure 18: NBS8 cerebral organoids are smaller and more sensitive to BPDE exposure than WT organoids. (A) Representative brightfield images of NBS8 and UJ cerebral organoids at CTRL conditions and after 72h of 100µM BPDE exposure. Scale bar 100µm. **(B)** Bar graph of the average diameter of UJ and NBS8 20-day old cerebral organoids. N=8, mean +/- standard deviation, ***p<0.005. **(C)** Bar graph of cerebral organoid viability after 24h and 72h of BPDE exposure. N=3, mean +/- standard deviation. *p<0.05, **p<0.01.

3.4. Basal expression of genes related to the DNA damage response in healthy and NBS-patient derived hiPSC, and human fibroblasts

NBS-mutant hiPSCs have been reported as having an abnormal gene expression when compared to WT hiPSCs, particularly of genes relating to cancer, cell cycle and apoptosis (51). Therefore, focused qRT-PCR arrays comprised of 76 gene targets (Table 5) related to the response to exposure to genotoxic agents, including genes involved in detoxification, DNA damage response, cell cycle regulation, DNA damage repair and cell death, were used to evaluate the basal levels of these genes in healthy (iPSC-12) and NBS-patient derived (NBS8) hiPSCs, as well as in normal human dermal fibroblasts (NHDF). In a first instance, gene expression was compared between NBS8 hiPSCs vs iPSC-12 hiPSCs. Next, gene expression of NBS8 hiPSCs and iPSC-12 hiPSCs was compared against that of NHDF.

Table 5: List of genes involved in genotoxic exposure response investigated in iPSC-12 hiPSCs, NBS hiPSCs and NHDF through focused qRT-PCR array.

ATRX	ATP-dependent helicase ATRX
ABCB1	ATP Binding Cassette Subfamily B Member 1
ABCG2	ATP Binding Cassette Subfamily G Member 2 (JR Blood Group)
AKAP1	A-Kinase Anchoring Protein 1
AKT1	AKT Serine/Threonine Kinase 1
ATG3	Autophagy Related 3
ATG7	Autophagy Related 7
BAX	BCL2 Associated X, Apoptosis Regulator
BBC3	BCL2 Binding Component 3
BCL2	BCL2 Apoptosis Regulator
BECN1	Beclin 1
BRCA1	Breast Cancer Type 1 Susceptibility Protein
BRCA2	Breast Cancer Type 2 Susceptibility Protein
BRIP1	BRCA1 Interacting Helicase 1
CALCR	Calcitonin Receptor
CASP2	Caspase 2
CDC25A	Cell Division Cycle 25A
CDKN1A	Cyclin Dependent Kinase Inhibitor 1A
DDB2	Damage Specific DNA Binding Protein 2
DDIT3	DNA Damage Inducible Transcript 3
ERCC1	ERCC Excision Repair 1, Endonuclease Non-Catalytic Subunit

EXO1	Exonuclease 1
FANCC	Fanconi Anemia Complementation Group C
FANCD2	FA Complementation Group D2
FAS	Fas Cell Surface Death Receptor
FEN1	Flap Structure-Specific Endonuclease 1
GADD45A	Growth Arrest And DNA Damage Inducible Alpha
GPX1	Glutathione Peroxidase 1
GPX4	Glutathione Peroxidase 4
GSTM1	Glutathione S-Transferase Mu 1
HDAC1	Histone Deacetylase 1
HDAC4	Histone Deacetylase 4
HDAC6	Histone Deacetylase 6
HMOX1	Heme Oxygenase 1
HSPB1	Heat Shock Protein Family B (Small) Member 1
LAMP1	Lysosomal Associated Membrane Protein 1
LIG1	DNA Ligase 1
LIG3	DNA Ligase 3
LIG4	DNA Ligase 4
MGMT	O-6-Methylguanine-DNA Methyltransferase
MLH1	MutL Homolog 1
MPG	N-Methylpurine DNA Glycosylase
MSH6	MutS Homolog 6
NEIL1	Nei Like DNA Glycosylase 1
NEIL2	Nei Like DNA Glycosylase 2
OGG1	8-Oxoguanine DNA Glycosylase
PARP1	Poly(ADP-Ribose) Polymerase 1
PINK1	PTEN Induced Kinase 1
POLB	DNA Polymerase Beta
POLD1	DNA Polymerase Delta 1, Catalytic Subunit
POLE	DNA Polymerase Epsilon, Catalytic Subunit
POLI	DNA Polymerase Iota
PPARGC1A	PPARG Coactivator 1 Alpha
PRKN	Parkin RBR E3 Ubiquitin Protein Ligase
RAD18	RAD18 E3 Ubiquitin Protein Ligase
RAD51	RAD51 Recombinase
RAD52	RAD52 Homolog, DNA Repair Protein
REV1	REV1 DNA Directed Polymerase
RNF168	Ring Finger Protein 168
RNF8	ing Finger Protein 8
SIAH1	Siah E3 Ubiquitin Protein Ligase 1
SIRT1	Sirtuin 1
SIRT7	Sirtuin 7
SOD1	Superoxide Dismutase 1

SOD2	Superoxide Dismutase 2
TDG	Thymine DNA Glycosylase
TOP2B	DNA Topoisomerase II Beta
TOPBP1	DNA Topoisomerase II Binding Protein 1
TP53	Tumor Protein P53
TP73	Tumor Protein P73
ULK1	Unc-51 Like Autophagy Activating Kinase 1
UNG1	Uracil DNA Glycosylase 1
UNG2	Uracil DNA Glycosylase 2
XRCC1	X-Ray Repair Cross Complementing 1
XRCC3	X-Ray Repair Cross Complementing 3
XRCC4	X-Ray Repair Cross Complementing 4

3.4.1. NBS8 hiPSCs have differentiated gene expression of genes related to genotoxic exposure response when compared to a WT hiPSC line

In the interest of discovering whether the expression of genotoxic response related genes was different between NBS8 hiPSC and the WT iPSC-12 hiPSCs, 76 genes were compared in a focused qRT-PCR array. Among the 76 genes related to genotoxic exposure response (Table 5), 8 genes were identified as differentially regulated in NBS8 hiPSCs (Figure 19). Fas cell surface death receptor (*FAS*), heat shock protein family B (Small) member 1 (*HSP1B*), PPARG coactivator 1 alpha (*PPARGC1A*) and X-Ray repair cross complementing 4 (*XRCC4*) were upregulated (between 2-fold to 3-fold), while ATP binding cassette subfamily g member 2 (JR Blood Group) (*ABCG2*), calcitonin receptor (*CALCR*), DNA damage inducible transcript 3 (*DDIT3*) and growth arrest and DNA damage inducible alpha (*GADD45A*) were downregulated (between 0.3-fold and 0.5-fold). Of particular interest, both *HSP1B* and *XRCC4* are associated with the repair of DNA double-strand breaks (207,208), a pathway which is known to be deficient in NBN-impaired cells. From the downregulated genes, *CALCR*, *DDIT3* and *GADD45A* all have links to positive regulation of apoptosis upon cell stress (209,210), hinting at a lower basal apoptotic response in NBS8 hiPSCs, although *FAS* was upregulated (2.1-fold). Of note, ABCG2 is an important component of the cellular efflux transport system (211).

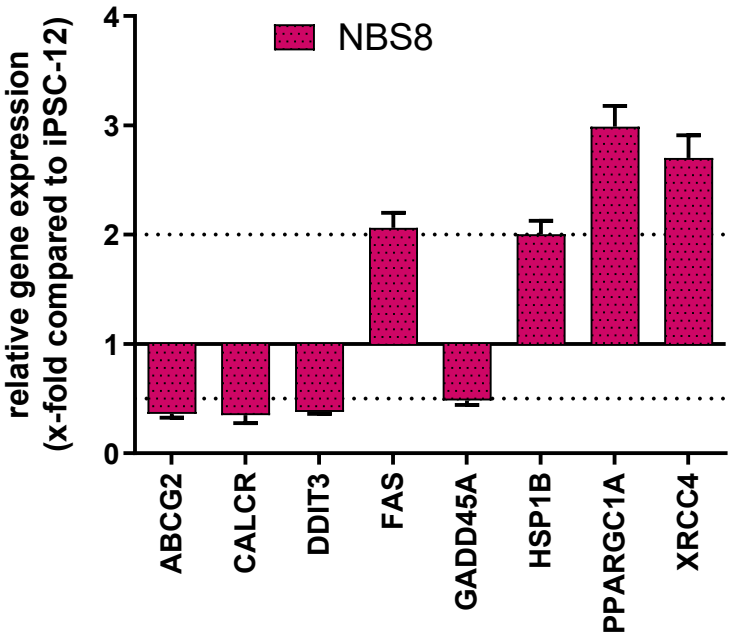

Figure 19: NBS8 hiPSCs have differentiated gene expression of genes related to genotoxic exposure response. Graph of 8 genes which were differentially regulated in NBS8 hiPSCs among the focused qRT-PCR array for 76 genes related to genotoxic exposure response. Fold change of NBS8 is shown, iPSC-12 hiPSCs were used as control. Mean of 3 technical triplicates, +/- standard deviation of the mean. Dashed lines mark 2- and 0.5 -fold.

3.4.2. hiPSCs have upregulated expression of dozens of DNA damage response related genes when compared to human fibroblasts.

Generally speaking, the DNA damage response is more robust in pluripotent stem cells than in their differentiated progeny (212). With that in mind, a qRT- PCR focused array was used to assess the gene expression of 76 genes related to genotoxic exposure response in the hiPSC lines NBS8 and iPSC-12, and in NHDF (Supplementary Figure 2). Among the 76 investigated genes, 27 were upregulated in both hiPSCs when compared to NHDF, while one was downregulated (Figure 20).

The downregulated gene was Cyclin Dependent Kinase Inhibitor 1A (*CDKN1A*, 0.2-fold), which codes for p21, a cell cycle arrest protein. Conversely, cell division cycle 25A (*CDC25A*, > 17-fold), which is essential for the progression of the cell cycle, was upregulated. Remarkably, the levels of tumour suppressor protein 73 (*TP73*, >10-fold), a member of the p53 family, were upregulated in hiPSCs. The other 25 upregulated genes included targets involved in different pathways of DNA damage repair.

RAD51, which is involved in double-strand break repair (DSBR), was upregulated over 60-fold. Ten other DSBR related genes were also increased: *BRCA1* (> 9-fold), *BRCA2*

(> 10-fold), Fanconi Anemia complementation group C (*FANCC*, > 3-fold), Fanconi Anemia complementation group D2, (*FANCD2*, > 12-fold), flap structure-specific endonuclease 1 (*FEN1*, > 2.5-fold), DNA ligase 3 (LIG3, > 4.5-fold), X-Ray repair cross complementing 3 (*XRCC3*, > 7-fold), ring finger protein 168 (*RNF168*, > 3.5-fold), ring finger protein 8 (*RNF8*, > 2.5-fold) and *XRCC4* (> 2-fold).

Uracil DNA glycosylase 2 (*UNG2*), one of the glycosylases involved in the repair of small DNA lesion through base excision repair (BER), was increased by over 33-fold, although its mitochondrial isoform *UNG1* was unchanged. Other four components of the BER pathway were also upregulated, DNA ligase 1 (*LIG1*, > 3-fold), Nei like DNA glycosylase 1 (*NEIL1*, > 3.5-fold), Nei like DNA glycosylase 2 (*NEIL2*, > 2.5-fold) and DNA polymerase beta (*POLB*, > 3.5-fold).

The genes exonuclease 1 (*EXO1*, > 5-fold) and MutS homolog 6 (*MSH6*, > 3.5-fold) are components of the mismatch repair pathway (MMR), which is responsible for recognizing and repairing DNA base-base and insertion-deletion mismatches (Kunkel and Erie, 2015).

Regarding components of the nucleotide excision repair pathway, *DDB2* (> 3-fold) was upregulated, as was DNA polymerase epsilon (*POLE*, > 5.5-fold). DNA polymerase D1 (*POLD1*, > 4.5-fold) is also involved in NER, while simultaneously being involved in translesion synthesis (TLS). The last upregulated DNA polymerase, DNA polymerase iota (*POLI*, > 2.5-fold), is only involved in TLS. Overall, the results indicate that hiPSCs, both WT and mutant, possess a more robust expression of dozens of genes involved in DNA damage response than NHDF.

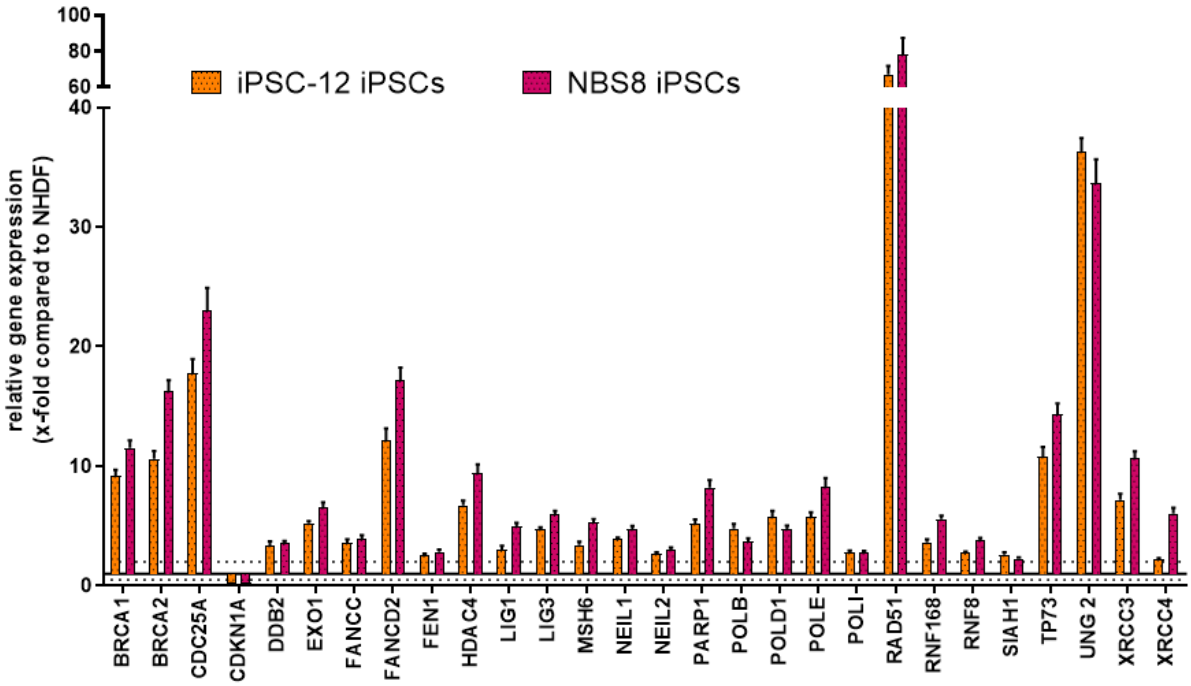

Figure 20: NBS8 and iPSC-12 hiPSCs have upregulated expression of genes related to genotoxic exposure response when compared to NHDF. Graph of 28 genes which were differentially regulated in NBS8 and iPSC-12 hiPSCs among the focused qRT-PCR array for 76 genes related to genotoxic exposure response. Fold change of NBS8 hiPSC and iPSC-12 hiPSCs is shown, NHDF were used as control. Mean of 3 technical triplicates, +/- standard deviation of the mean. Dashed lines mark 2- and 0.5 -fold.

3.5. Effects of BPDE exposure on healthy and NBS-derived hiPSCs

The effects of BPDE exposure in pluripotent stem cells are poorly understood, as are the effects of BPDE on NBS-mutant patients. With the intention to remedy both gaps in research, hiPSCs derived from NBS patients and healthy subjects were exposed to BPDE for 24h in the concentrations of 25nM and 75nM. The cells were then harvested and analysed as described in this chapter.

3.5.1. Southern Blot analysis of BPDE-DNA adducts

To assess the repair of DNA adducts, the southern blot (SB) protocol for BPDE-DNA adducts from Christmann et al (213) was followed, where the authors loaded 500 µg of DNA in a nylon membrane. The membrane was then blocked with 5% milk/TBS-T and a BPDE-DNA antibody was used to identify the adducts diluted 1:500 in 5%BSA/TBS-T. UJ, iPSC-12 and NBS8 hiPSCs were treated with 75nM of BPDE for 2h and 6h, and then subjected to the same procedure described above. Analysis of the membranes with chemiluminescence revealed no differences between the bands from the ctrl and treated samples (Figure 21A). The DNA on the membranes was

stained with methylene blue (Figure 21B) and used as loading control to calculate band density and confirm the visual observations (Figure 21C)

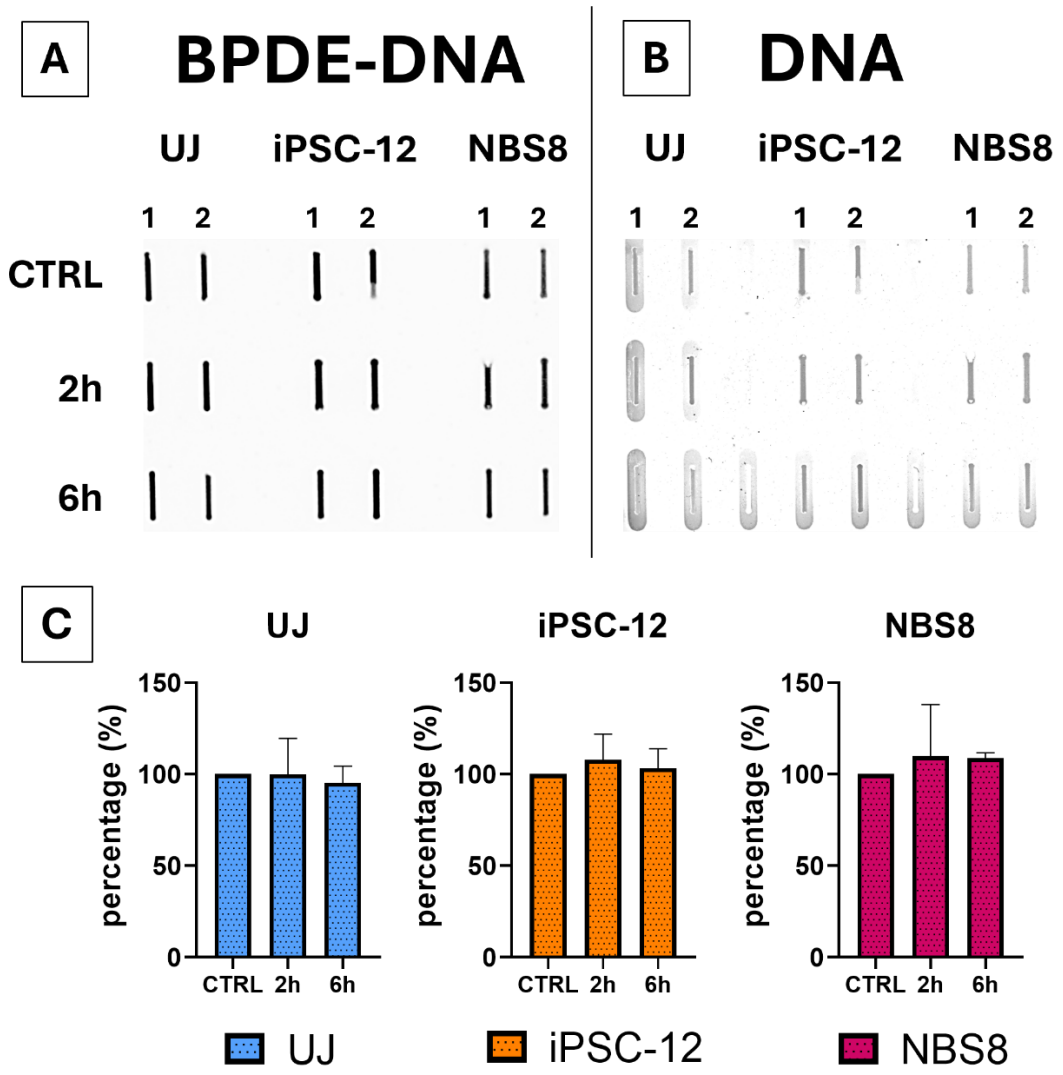

Figure 21: Southern blot (SB) for BPDE-DNA adducts. UJ, iPSC-12 and NBS8 hiPSCs were treated with 75nM of BPDE for 2h and 6h. Two samples from independent experiments were measured per condition and are indicated by the numbers 1 and 2. **(A)** Membrane was stained for BPDE-DNA adducts and photographed via chemiluminescence. **(B)** Membrane was stained with the DNA dye methylene blue to confirm DNA loading. **(C)** Methylene blue was used as loading control to quantify relative band intensity. N=2, mean +/- standard deviation shown.

These results were unexpected, since BPDE-DNA adducts should not be present in control conditions and furthermore, are expected to be increased after BPDE treatment. The original protocol was modified and, using only the UJ samples, a lower load of DNA (250 µg) was tested in different blocking conditions and antibody dilutions. Diluting the antibody in milk resulted in an extremely weak signal, although the control sample still appears stained (Figure 22A). Blocking the membrane in 5% BSA/TBS-T

and varying the concentration of the antibody diluted in the same solution also resulted in the same intensity of staining at all conditions (Figure 22B). This issue was likely caused by nonspecific antibody binding and precluded the BPDE-DNA adduct analysis.

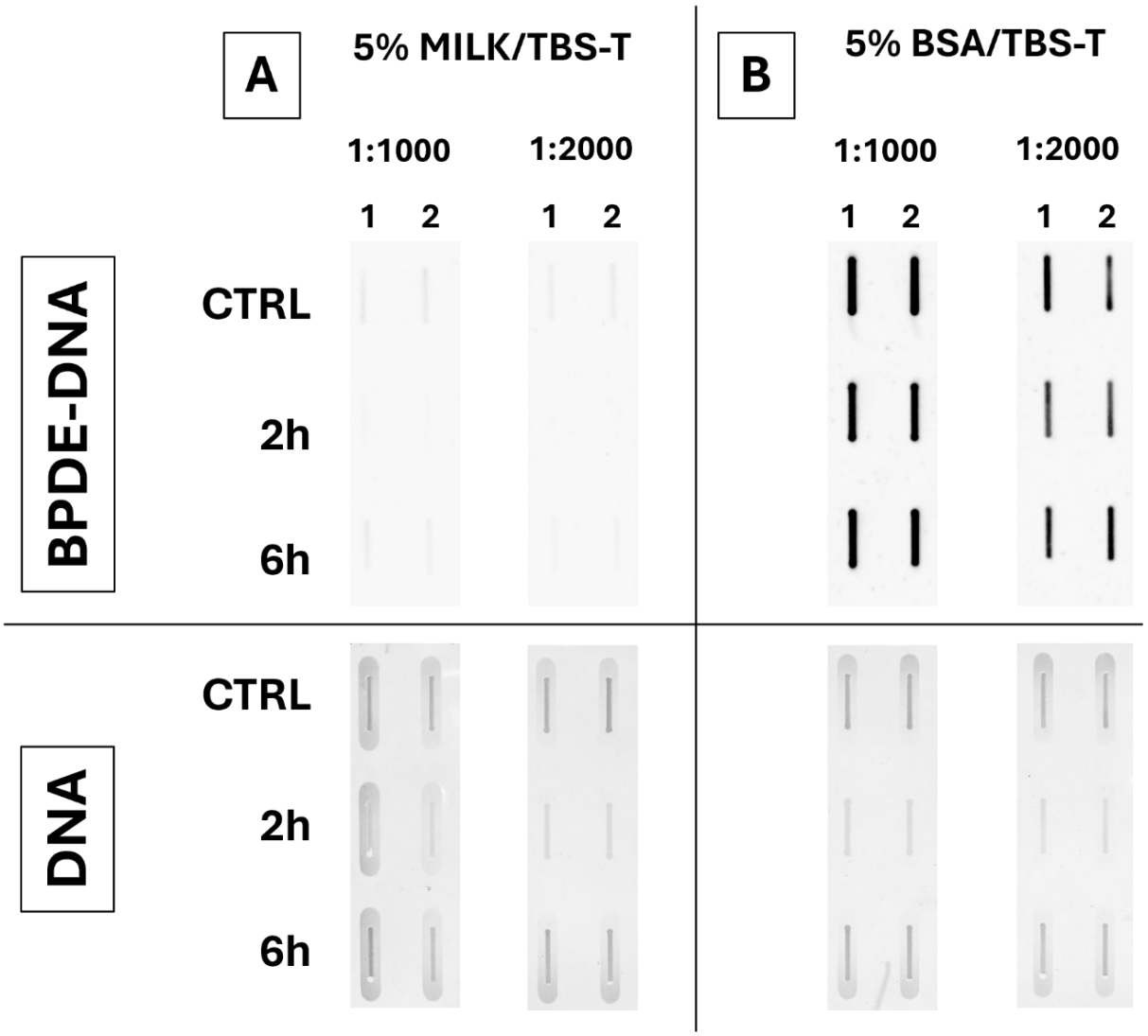

Figure 22: Testing of different blocking and staining conditions of BPDE-DNA southern blot. UJ hiPSCs were treated with 75nM of BPDE for 2h and 6h. Two samples from independent experiments were measured per condition and are indicated by the numbers 1 and 2. Membranes were stained with the DNA dye methylene blue to confirm DNA loading. **(A)** Membrane was blocked with 5% Milk in TBS-T and stained with BPDE-DNA antibody diluted in 5% Milk in TBS-T at the concentrations of 1:1000 and 1:2000. (**B)** Membrane was blocked with 5% BSA in TBS-T and stained with BPDE-DNA antibody diluted in 5% BSA in TBS-T at the concentrations of 1:1000 and 1:2000.

3.5.2. Affymetrix Microarray Analysis and Venn Diagrams generated from transcriptomic data

Affymetrix microarray analysis was performed as described on 2.2.10. The hiPSC lines UJ, iPSC-12 and NBS8 were exposed to BPDE for 24h at 75nM or kept in control conditions. To better identify Gene Ontologies (GO) and KEGG pathway targets that are directly activated by BPDE, we pooled the results of all samples into control and BPDE treated, as shown on Figure 23A. This allowed us to investigate the transcriptional changes caused by BPDE regardless of the mutation. We identified 513 targets that were present exclusively after BPDE exposure, as well as 254 targets which were upregulated and 56 targets which were downregulated. Our other objectives were to reveal the transcriptional downstream effects of the mutation, both in the absence of stimulus and after BPDE treatment. For such, we compared the WT and NBS8 lines in control conditions (Figure 23B) and after genotoxic exposure (Figure 23C). With the most relevant targets thus identified, we used them to generate the Gene Ontologies (GO) and KEGG pathways, as well as Metascape analyses, which are more thoroughly explored in the next chapters.

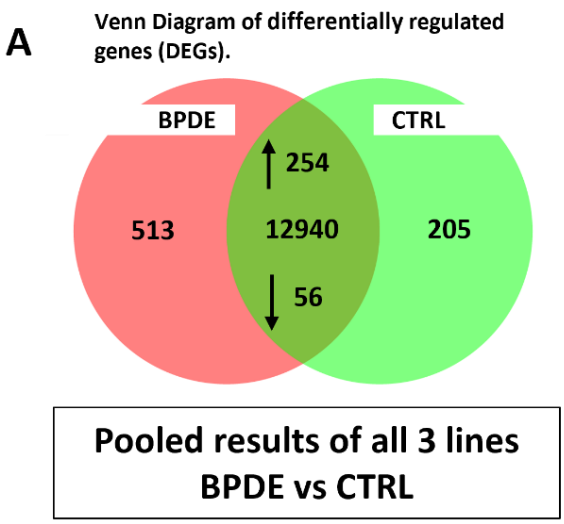

Objective 1: Investigate the transcription changes caused by BPDE exposure, regardless of mutation.

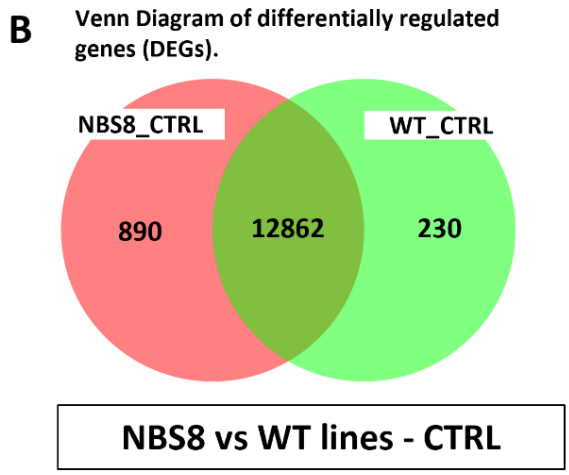

Objective 2: Reveal the downstream effects of the mutation in the absence of stimulus.

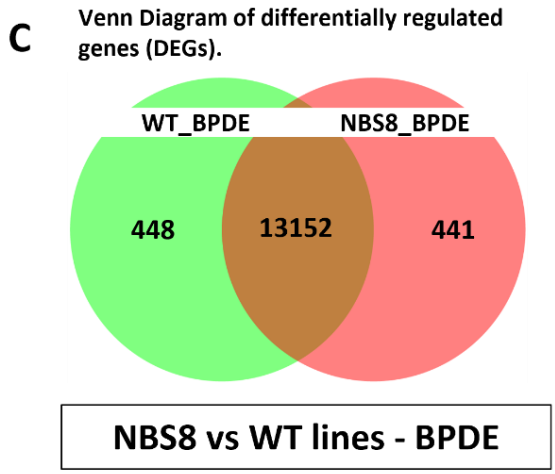

Objective 3: Reveal the downstream effects of the mutation after BPDE treatment.

Figure 23: Venn Diagrams of differentially regulated genes extracted from microarray analysis. WT and NBS8 hiPSCs were treated with 75nM BPDE for 24h, then harvested and subjected to Affymetrix analysis. The expression profiles were extracted, and the results investigated regarding the effects of **(A)** BPDE on hiPSCs as well as the differences between the WT and mutant lines, both in **(B)** control and **(C)** treated conditions.

3.5.3. BPDE treatment enhances expression of targets related to the extrinsic apoptotic pathway

To investigate the effects of BPDE on the cell viability of hiPSCs, cells were treated with BPDE for 24h in concentrations ranging from 30nM to 63µM and cell viability was measured using the resazurin assay (Figure 24). iPSC-12 and UJ cells showed similar sensibility to BPDE treatment, with an ic50 of 290nM and 380nM, respectively. NBS8 cells were the least sensitive, with an ic50 of 790nM. Further BPDE exposure experiments were performed with the concentrations of 25nM, corresponding roughly to a non-cytotoxic dose (ic90) and 75nM, representing a mildly cytotoxic dose (circa ic80).

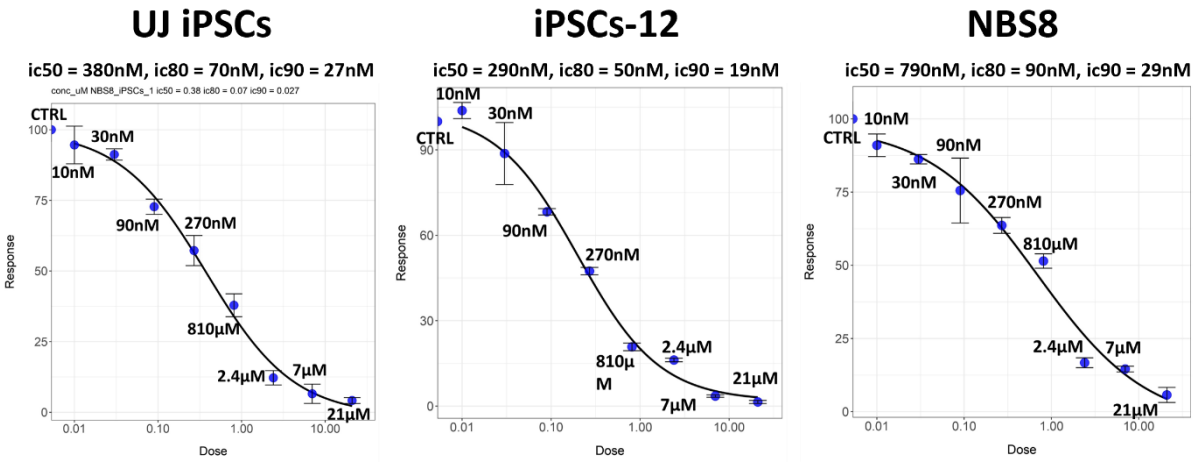

Figure 24: Dose-response curve of BPDE-treated hiPSCs. hiPSCs were treated with increasing concentrations of BPDE for 24h and resazurin assay was performed to measure cell viability. Dot plot graph represents the dose-response curve, with each dot representing the mean of three biological triplicates. +/- standard deviation is shown.

The gene ontology extracted from 254 genes upregulated after BPDE treatment (Figure 23A) revealed several clusters related to both positive and negative regulation of cell death (Figure 25). Notably, several genes related to the extrinsic apoptotic signaling pathway were upregulated including all four known receptors for TNF-related apoptosis-inducing ligand (TRAIL): TNF Receptor Superfamily Member 10A (*TNFRSF10A*), *TNFRSF10B*, *TNFRSF10C* and *TNFRSF10D.* qRT-PCR for *TNFRSF10A* confirmed its upregulation in all three lines (mean > 1.7-fold) (Figure 26B), while the expression of the intrinsic apoptosis genes BCL2 associated X, apoptosis regulator (*BAX*) and Bcl-2-binding component 3 (*BBC3*) remained unchanged (Figure 26C and D).

Both the extrinsic and intrinsic apoptotic pathways depend on caspases to induce cell death, therefore an executioner caspase essential in both pathways, caspase 3 (*CASP3*), was investigated. *CASP3* expression was increased (mean > 1.7-fold) after BPDE treatment in both WT cell lines, but not in NBS8 (Figure 26D). Caspase 3 protein expression was unchanged in all three lines, but the expression of cleaved caspase 3, the active form of caspase 3, was enhanced particularly in the WT lines and far less in NBS8 (Figure 26E).

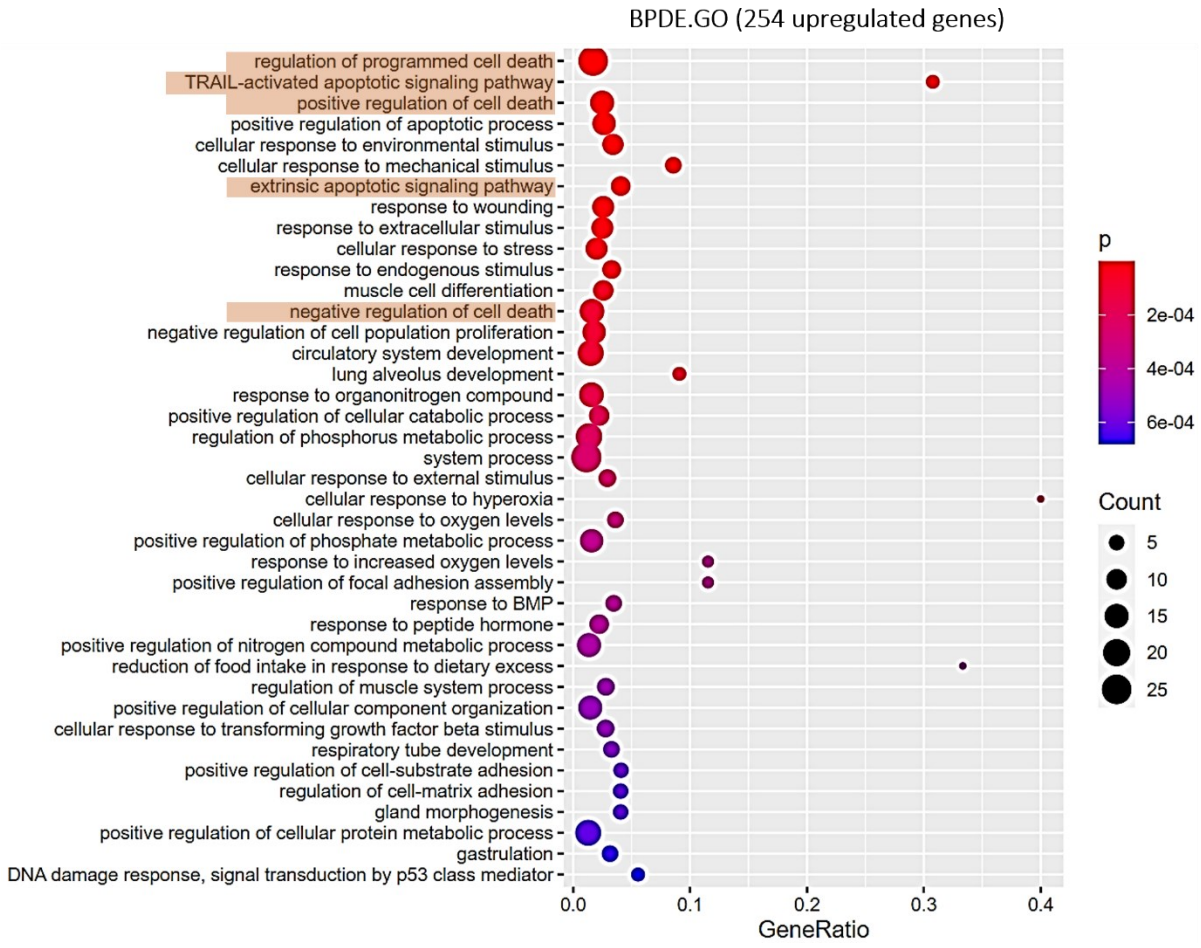

Figure 25: BPDE upregulates clusters related to both positive and negative regulation of cell death in hiPSCs. hiPSCs were treated with BPDE for 24h, then had their RNA harvested for affimetrix microarray. Gene ontology was extracted from 254 genes upregulated in hiPSCs after BPDE treatment in microarray analysis. Apoptosis related clusters are highlighted in orange.

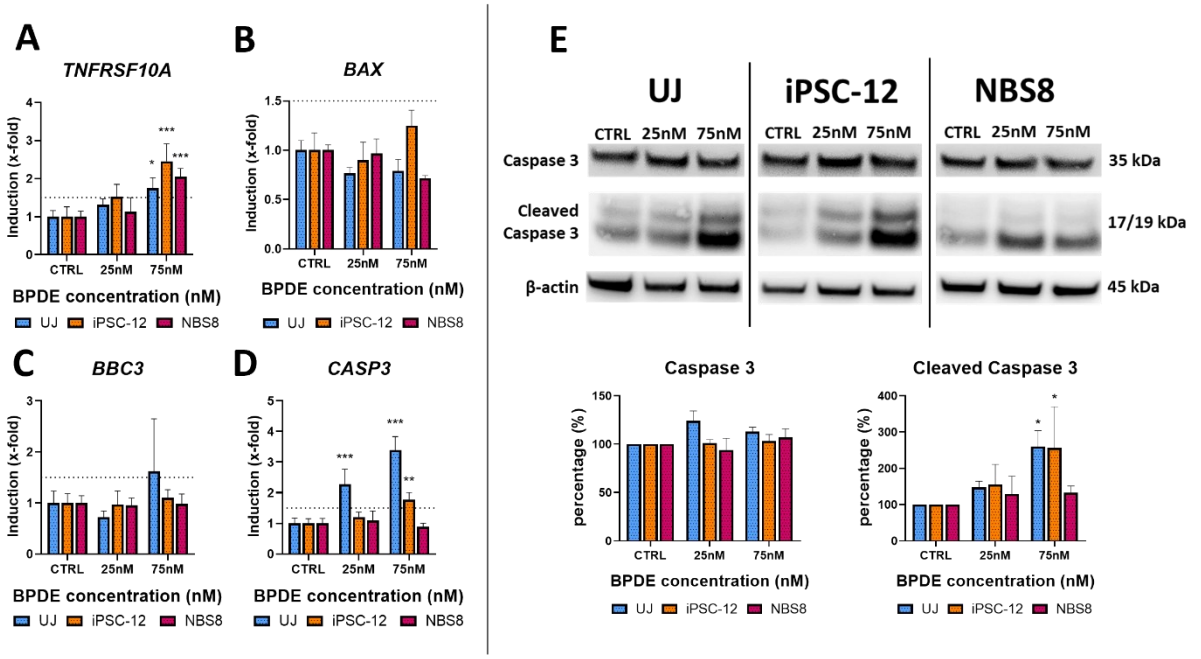

Figure 26: BPDE exposure differentially regulates apoptotic markers on WT and NBS8 hiPSCs. hiPSCs were treated with BPDE for 24h, then had their RNA harvested for qRT-PCR. **(A)** qRT-PCR for *TNFRSF10A.* **(B)** qRT-PCR for *BAX.* **(C)** qRT-PCR for *BBC3*. **(D)** qRT-PCR for *CASP3*. Error bar depicts 95% confidence interval. N=3, *p<0.05, ** = p<0.01, *** = p<0.001. Dashed lines mark 1.5-fold. **(E)** Western blot for caspase 3 and cleaved caspase 3. β-actin was used as loading control. N=2, mean +/- standard deviation shown, *p<0.05.

3.5.4. BPDE exposure does not impact pluripotency

In order to assert whether BPDE exposure had an effect on iPSC's pluripotency, the microarray data was used to generate a heatmap (Figure 27A) of twelve key genes associated with regulation of pluripotency: *SOX2,* DNA Methyltransferase 3 Beta (*DNMT3B*), *FGF2,* POU Class 5 Homeobox 1 (*POU5F1*), *NANOG,* Cadherin 1 (*CDH1*), Enhancer Of Zeste 2 Polycomb Repressive Complex 2 Subunit (*EZH2*), Transforming Growth Factor Beta 1 (*TGFB1*), Cerberus 1, DAN Family BMP Antagonist (*CER1*), *BMP4,* Gremlin 1, DAN Family BMP Antagonist (*GREM1*) *and* Inhibin Subunit Beta A (*INHBA*). The expression of major pluripotency maintenance genes such as *SOX2* and *POU5F1* remained high after BPDE treatment, while the expression of genes that trigger differentiation such as *BMP4* and *GREM1* remained low. The transcriptomic results are supported by the qRT-PCR data (Figure 27B), which shows no difference in the relative expression of the pluripotency maintenance genes *OCT4*, *SOX2* and *NANOG*. As further confirmation, we performed OCT4 immunostaining on the hiPSCs and saw no difference in expression after genotoxic exposure (Figure 27C).

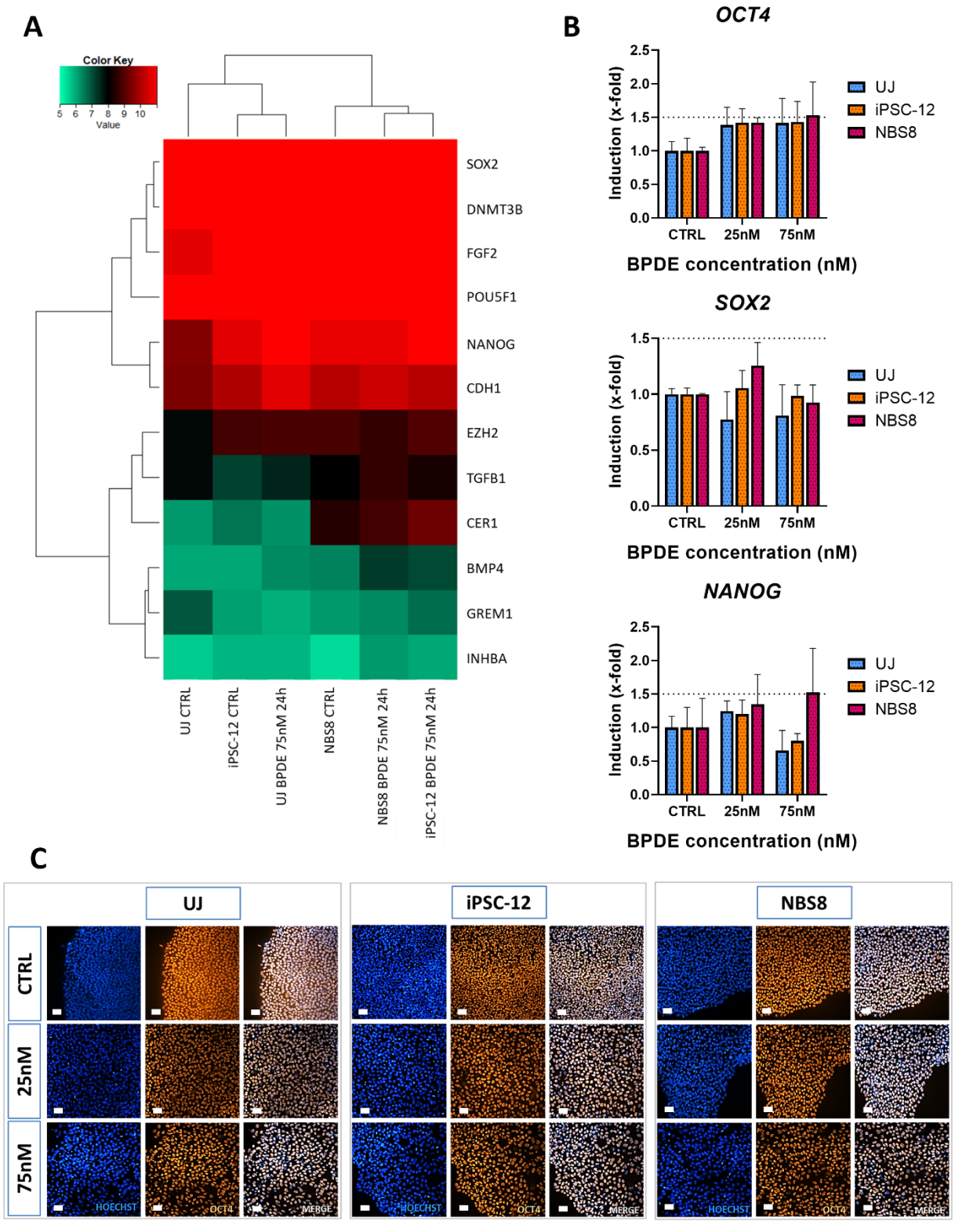

Figure 27: 24h of BPDE exposure does not affect pluripotency. WT and NBS8 hiPSCs were treated with 25nM and 75nM BPDE for 24h. RNA was extracted for microarray analysis or cells were fixed for immunocytochemistry. **(A)** Euclidean heatmap made with data extracted from microarray analysis represents relative expression of key genes involved in pluripotency maintenance after 24h of 75nM BPDE exposure. **(B)** BPDE treatment did not alter *OCT4*, *SOX2* and *NANOG* transcription as confirmed via qRT-PCR. **(C)** nor did it alter OCT4 expression as seen on immunocytochemistry. N=3. Error bar depicts 95% confidence interval. Scale bar 50µm. Dashed lines mark 1.5-fold.

3.5.5. BPDE exposure enhances gene expression of cell cycle arrest related genes, but does not impact cell cycle

The gene ontology extracted from 513 genes exclusively regulated after BPDE treatment (Figure 23A) revealed the cluster “DNA damage response, signal transduction by p53 class mediator resulting in cell cycle arrest” with four regulated genes, cyclin dependent kinase inhibitor 1A (*CDKN1A*); mucin 1, cell surface associated (*MUC1*); polo like kinase 2 (*PLK2*) and proline rich acidic protein 1 (*PRAP1*) (Figure 28).

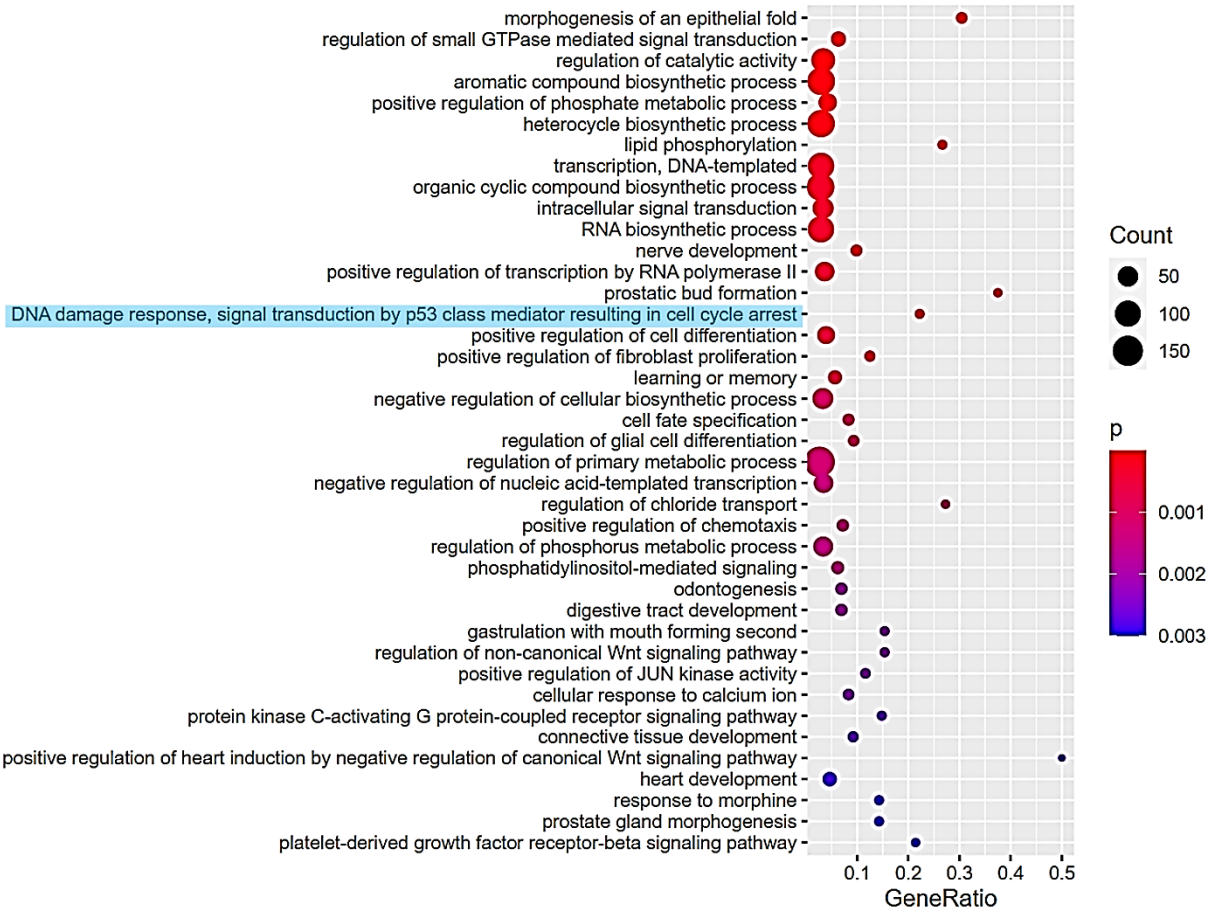

Figure 28: GO from 513 genes exclusively regulated after BPDE exposure in hiPSCs extracted from Affymetrix analysis reveals upregulated cluster associated with p53-mediated cell cycle arrest. WT and NBS8 hiPSCs were treated with 75nM BPDE for 24h. RNA was extracted for microarray analysis. Relevant cluster is highlighted in red.

We performed qRT-PCR for *CDKN1A*, *MUC1* and another p53 inducible, DNA damage and cell cycle arrest associated gene, growth arrest and DNA damage inducible alpha (*GADD45A*). The qRT-PCR revealed that all three cell lines had upregulated levels of *GADD45A* after BPDE exposure (mean > 3-fold). *CDKN1A* was upregulated more intensely on NBS8 (mean 1.6-fold at 25nM and 2.9-fold at 75nM) and slightly in iPSC-

12 (mean 1.6-fold at 75nM), while *MUC1* was upregulated in the WT lines only (mean 1.6-fold) (Figure 29).

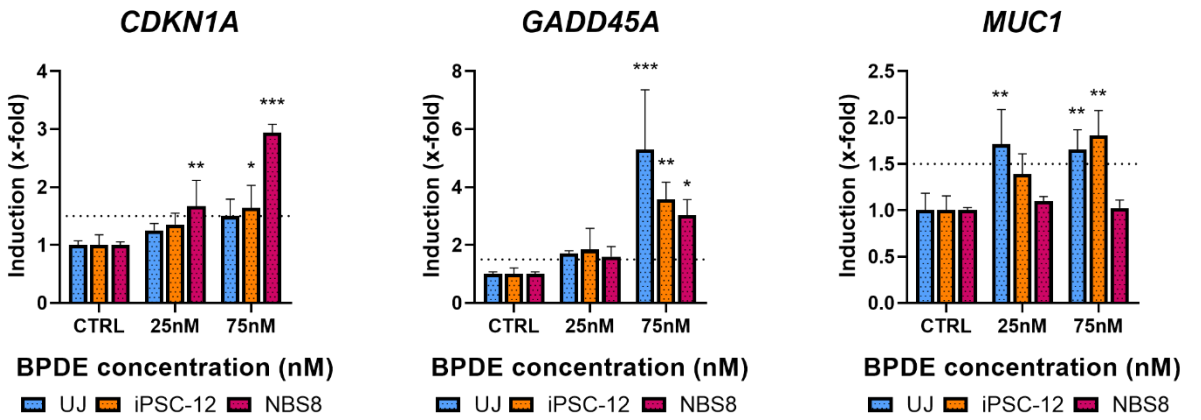

Figure 29: BPDE differentially increased the expression of cell cycle regulators *CDKN1A*, *GADD45A* and *MUC1* in NBS8 and WT hiPSCs. WT and NBS8 hiPSCs were treated with 25nM and 75nM BPDE for 24h, then RNA was extracted for qRT-PCR. Error bar depicts 95% confidence interval. N=3, *p<0.05, ** = p<0.01, *** = p<0.001. Dashed lines mark 1.5-fold.

To investigate if these transcriptional changes caused by BPDE influenced hiPSCs proliferation we stained them for antigen Kiel 67 (Ki67), a nuclear marker present during all active phases of the cell cycle (G_1, S, G_2, and mitosis) (214). The number of Ki67+ cells remained constant on all tested concentrations, including the highest concentration of 500nM which causes widespread cell death (Figure 30).

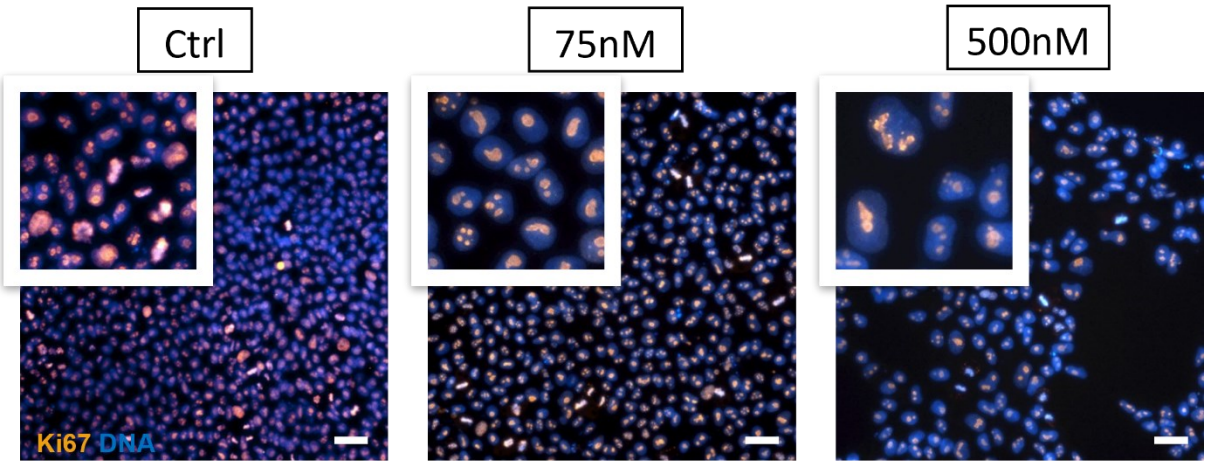

Figure 30: Ki67+ cell numbers remain constant after BPDE treatment in hiPSCs. Representative immunocytochemistry for Ki67 in control conditions and after 24h of BPDE exposure at 75nM and 500nM. Scale bar 50µm.

5-ethynyl-2′-deoxyuridine (EdU) is an analog of thymidine that is incorporated into DNA only during active DNA synthesis (215). Using EdU staining, we saw that BPDE exposure had no effect on the number of cells in S phase (Figure 31).

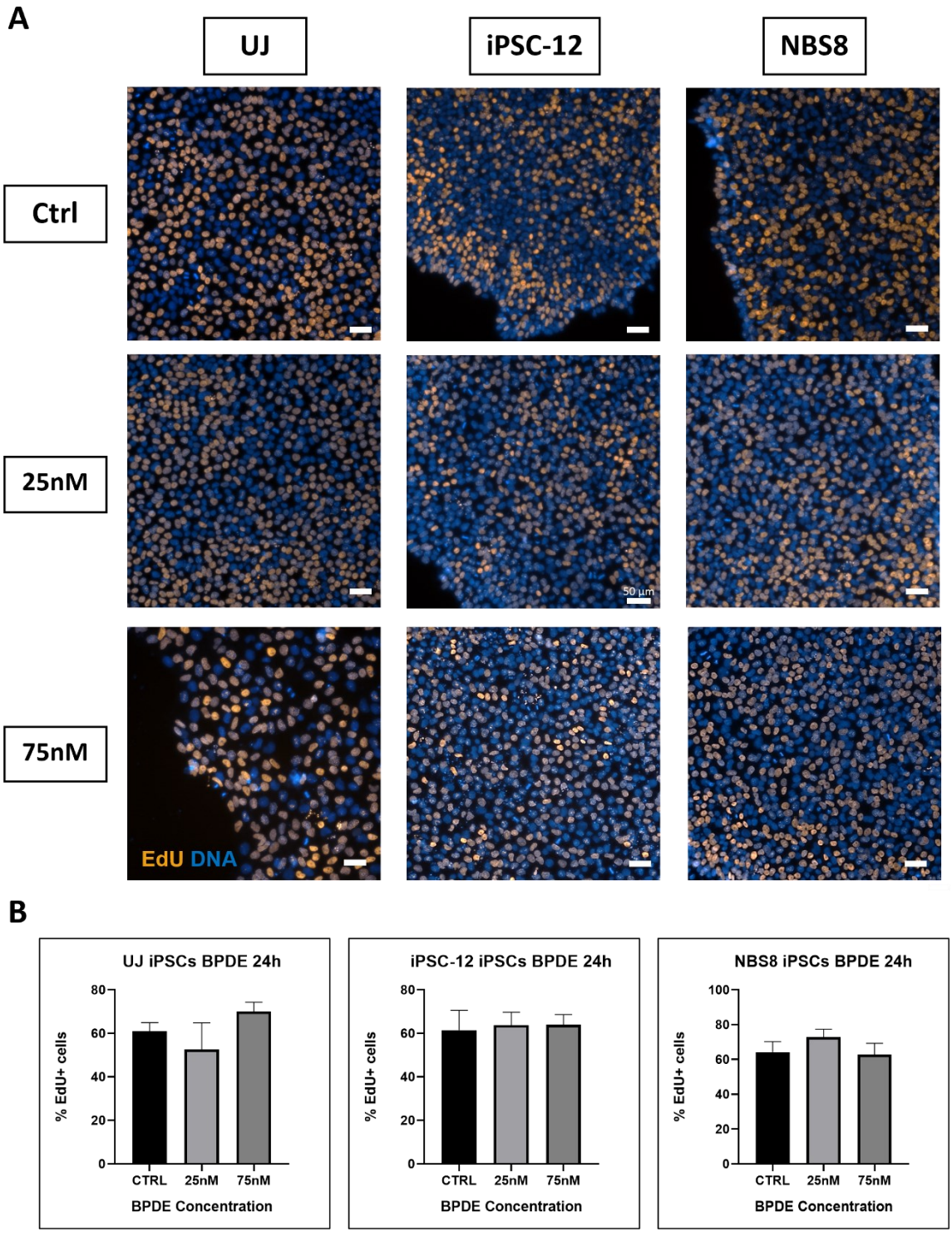

Figure 31: BPDE exposure does not affect percentage of cells in S phase in hiPSCs. hiPSCs were treated with BPDE for 24h at 25nM and 75nM, then stained for EdU. **(A)** Representative images of EdU staining of hiPSCs after CTRL, 25nM and 75nM treatment. Scale bar 50µm. **(B)** Bar graphs representing the percentage of EdU positive cells on each cell line after 24h treatment. N=3, mean +/- standard deviation.

Lastly, we performed a cell cycle analysis using propidium iodide staining and flow cytometry and confirmed that cell cycle distribution on all three lines was unaffected after BPDE exposure (Figure 32).

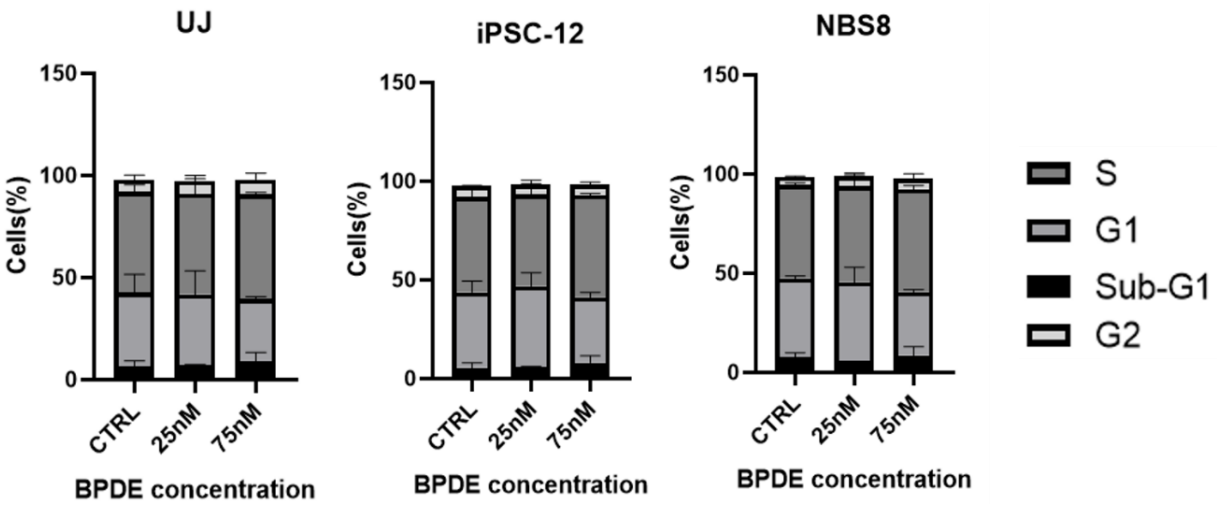

Figure 32: Cell cycle distribution is unaffected after 24h of BPDE exposure in hiPSCs. hiPSCs were exposed to 25nM or 75nM of BPDE for 24h. Cell cycle distribution was analyzed via propidium iodide staining measured by FACS and presented here in percentage as bar graphs. N=3, mean +/- standard deviation.

3.5.6. BPDE differentially regulates DNA damage response in WT and NBS8 hiPSCs

The enrichment analysis tool Metascape was used to compare the input gene list of 254 genes upregulated after BPDE exposure to thousands of available gene sets defined by their involvement in biological processes, protein localization, enzymatic function, pathway membership, among other features. Two of the top non-redundant enrichment clusters were related to the p53 signaling pathway with a total of 26 upregulated genes (Figure 33).

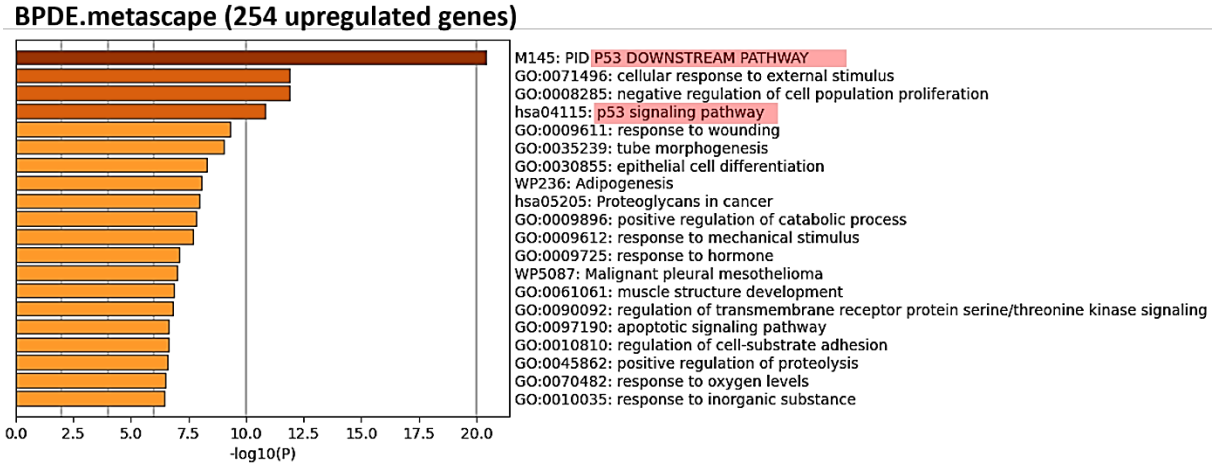

Figure 33: Metascape analysis of 254 genes upregulated in UJ, iPSC-12 and NBS8 hiPSCs after BPDE exposure. hiPSCs were exposed to 75nM of BPDE for 24h, then RNA was extracted for microarray analysis. P53-related clusters are highlighted in red.

Among them were three known regulators of p53 signaling, *cJUN, MDM2* and protein Phosphatase, Mg2+/Mn2+ Dependent 1D (*PPM1D*), as well as other genes involved in p53-mediated DNA damage response such as *GADD45A*, Sestrin 1 (*SESN1*), *POLH*, BTG Anti-Proliferation Factor 2 (*BTG2*) and Stratifin (*SFN*). qRT-PCR was performed to assert whether *TP53* itself was upregulated. The results show that *TP53* was downregulated (mean < 0.5-fold) in both WT lines (Figure 34A), while p53 protein expression was increased (Figure 34B). Both gene and protein expression remained unchanged in NBS8 (Figure 34A and B).

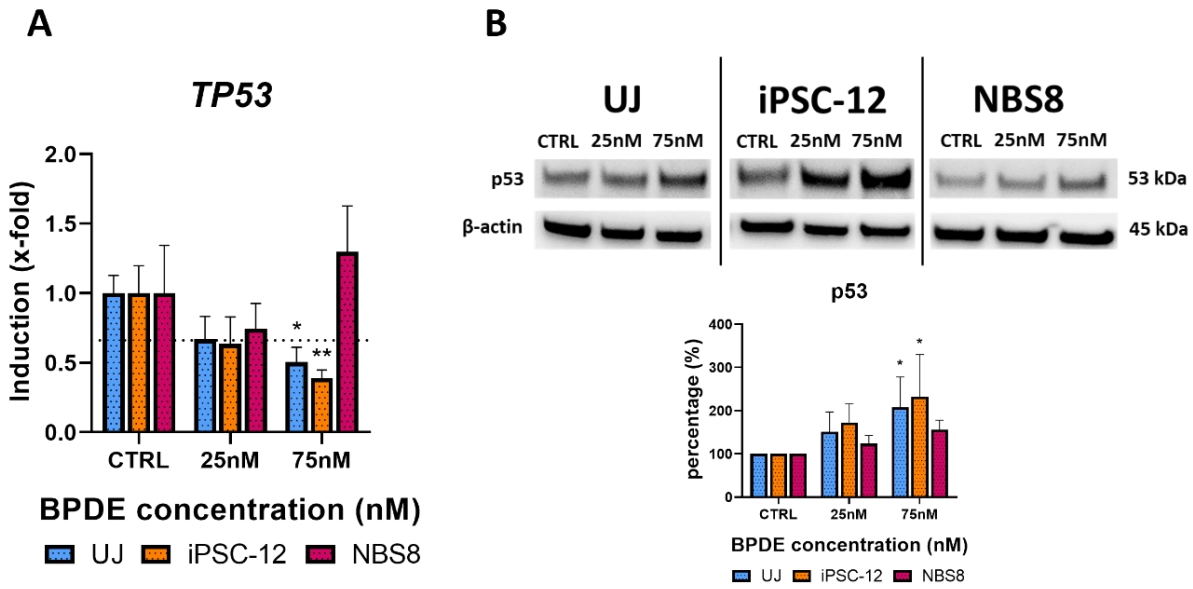

Figure 34 *TP53* and p53 expression differs between WT and NBS8 hiPSCs after BPDE treatment. hiPSCs were exposed to 25nM and 75nM of BPDE for 24h, then RNA was extracted for qRT-PCR and protein for western blot analysis. **(A)** qRT-PCR for *TP53*. Error bar depicts 95% confidence interval. N=3, *p<0.05, ** = p<0.01. Dashed lines mark 0.6 -fold. **(B)** Western blot for p53. β-actin was used as loading control. N=2, mean +/- standard deviation shown, *p<0.05.

Two targets related to p53 regulation, MDM2 and cJUN, were measured in an attempt to clarify the differences in the expression of *TP53* and p53 between WT and NBS8 cells after BPDE treatment. *MDM2* gene expression was exclusively downregulated (mean 0.56 -fold) in NBS8 (Figure 35A), while its protein levels were increased only in the WT cells Figure 35B)

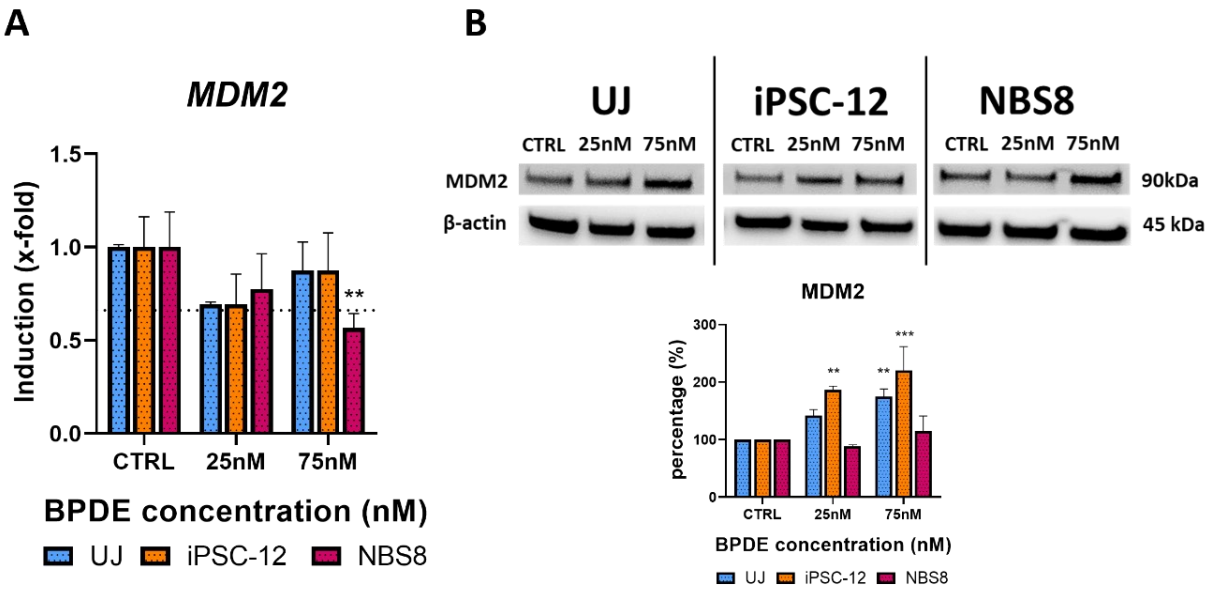

Figure 35 BPDE exposure increases expression of MDM2 in WT hiPSCs. hiPSCs were exposed to 25nM and 75nM of BPDE for 24h, then RNA was extracted for qRT-PCR and protein for western blot analysis. **(A)** qRT-PCR for *MDM2.* Error bar depicts 95% confidence interval. N=3, ** = p<0.01. Dashed lines mark 0.6 -fold. **(B)** Western blot for MDM2. β-actin was used as loading control. N=2, mean +/- standard deviation shown, ** = p<0.01, *** = p<0.001.

A similar pattern was observed with cJUN. The mRNA levels (mean > 3.2 -fold) and protein expression were both increased in WT cells after treatment, but unchanged in NBS8 (Figure 36A and B).

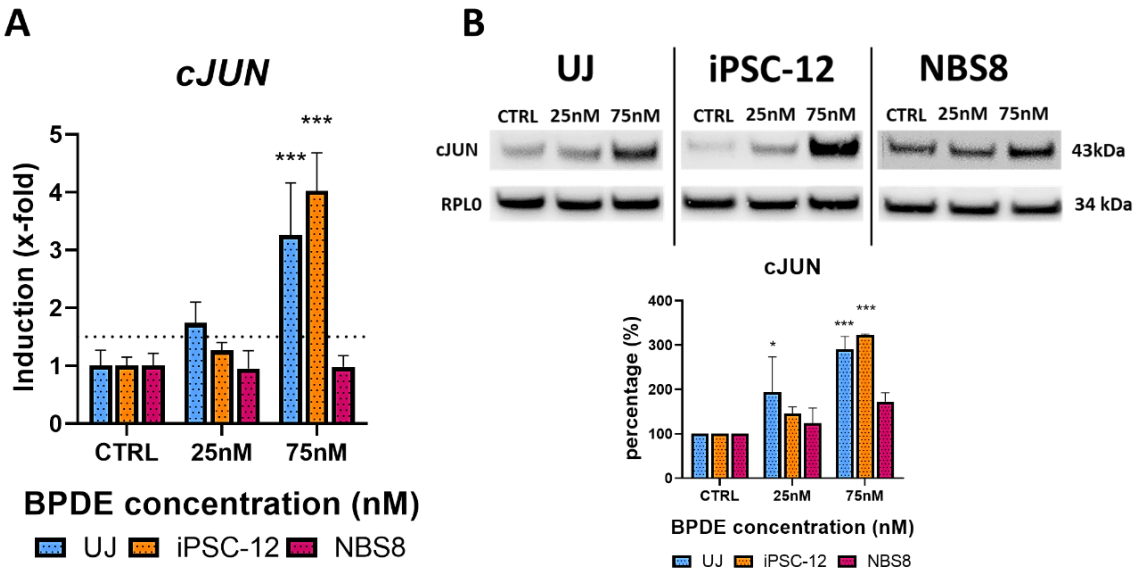

Figure 36: cJUN expression is increased in WT hiPSCs after BPDE treatment. hiPSCs were exposed to 25nM and 75nM of BPDE for 24h, then RNA was extracted for qRT-PCR and protein for western blot analysis. **(A)** qRT-PCR for *cJUN.* Error bar depicts 95% confidence interval. N=3, *** = p<0.001. Dashed lines mark 1.5-fold. **(B)** Western blot for cJUN. RPL0

was used as loading control. N=2, mean +/- standard deviation shown, * = p<0.05, ** = p<0.01, *** = p<0.001.

Since the transcriptional activities of cJUN are stimulated by its phosphorylation at serines 63/73, the protein levels of serine 73 p-cJUN were also measured and were revealed to be increased in the WT hiPSCs (Figure 37).

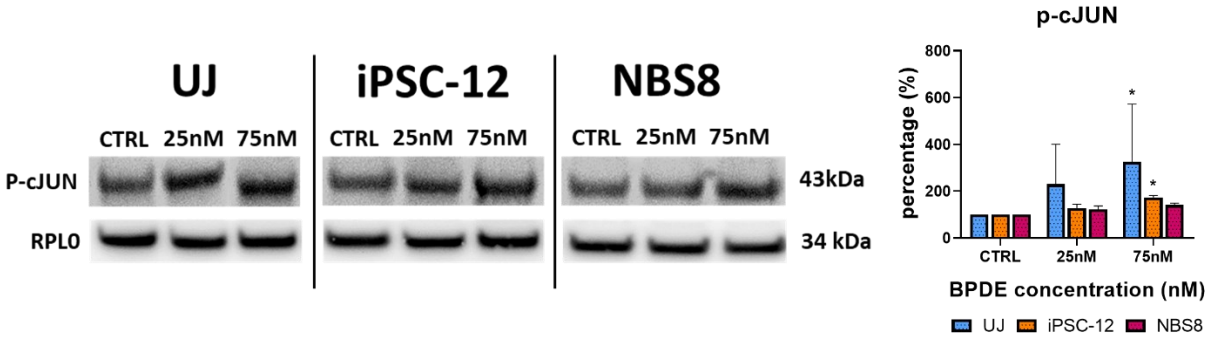

Figure 37: Serine 73 phospho- cJUN expression is increased after BPDE exposure in WT hiPSC cells. hiPSCs were exposed to 25nM and 75nM of BPDE for 24h, then protein was extracted for western blot for serine 73 p-cJUN. RPL0 was used as loading control. N=2, mean +/- standard deviation shown, * = p<0.05.

Next, we evaluated the mRNA expression of four upstream components of the p53 signaling cascade, *ATR*, *ATM,* and their respective downstream effectors, *CHEK1* and *CHEK2*. BPDE exposure did not affect the expression of *ATM*, *CHEK1* or *CHEK2* however, it sharply upregulated *ATR* expression (mean 7.1 -fold) in the NBS8 cell line (Figure 38A).

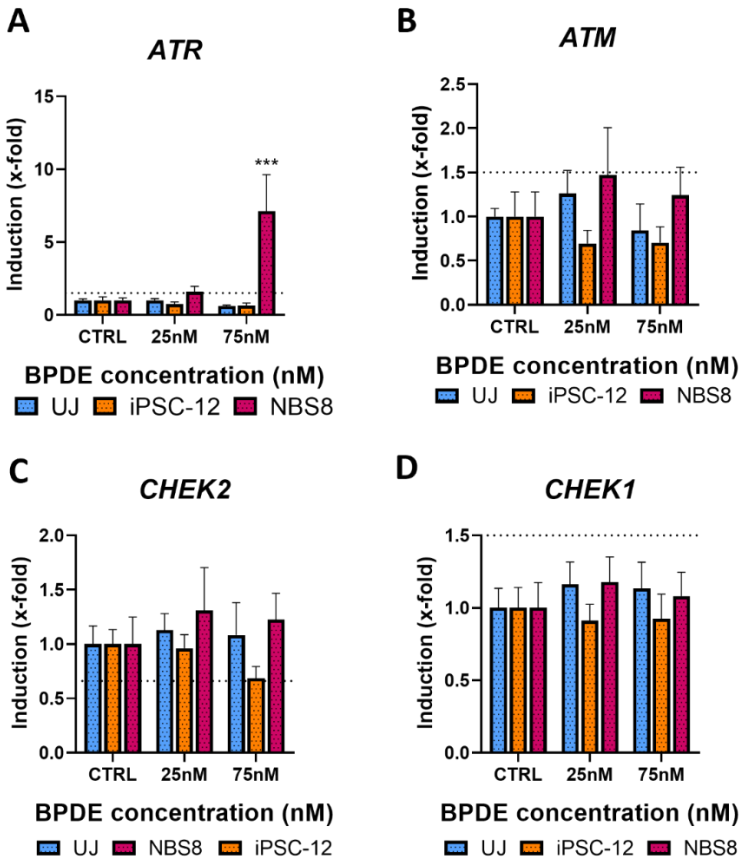

Figure 38: BPDE upregulated *ATR* expression in NBS8 hiPSCs. hiPSCs were exposed to 25nM and 75nM of BPDE for 24h, then RNA was extracted for qRT-PCR for **(A)** *ATR,* **(B)** *ATM,* **(C)** *CHEK2 and* **(D)** *CHEK1.* Error bar depicts 95% confidence interval. N=3, *** = p<0.001. Dashed lines mark 1.5- and 0.6 -fold.

ATR is a multifunctional kinase, acting upon many targets. Among its roles is the phosphorylation of H2AX during DNA repair, therefore the levels of γ-H2AX (the phosphorylated form of H2AX) were measured to assert whether *ATR* upregulation influenced γ-H2AX levels. Western blot revealed an increase in γ-H2AX expression in all three hiPSC lines, but it was particularly prominent in the WT cells (Figure 39), suggesting that it is not directly linked to ATR levels.

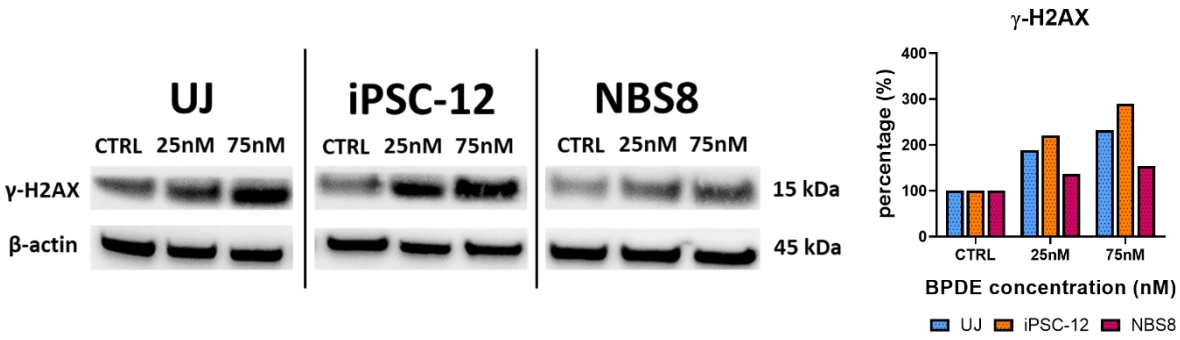

Figure 39 BPDE exposure increased the proteins levels of γ-H2AX. hiPSCs were exposed to 25nM and 75nM of BPDE for 24h, then protein was extracted for western blot for γ-H2AX. β-actin was used as loading control. N=1.

Lastly, p53 is highly involved in NER, regulating the expression of targets such as XPC and DDB2, and it has also been implicated in the transcriptional regulation of translesion synthesis DNA polymerases in reaction to DNA damage (173). After BPDE exposure the gene expression of the translesion synthesis DNA polymerase *POLH* was upregulated (mean > 1.8-fold) in all three cell lines (Figure 40A). Interestingly, XPC and DDB2 were upregulated exclusively in NBS8, and in both tested concentrations. *XPC* was upregulated by 1.5-fold in both concentrations, while the regulation of *DDB2* increased in a dose-dependent manner, 1.6-fold at 25nM and 3-fold at 75nM (Figure 40B and C).

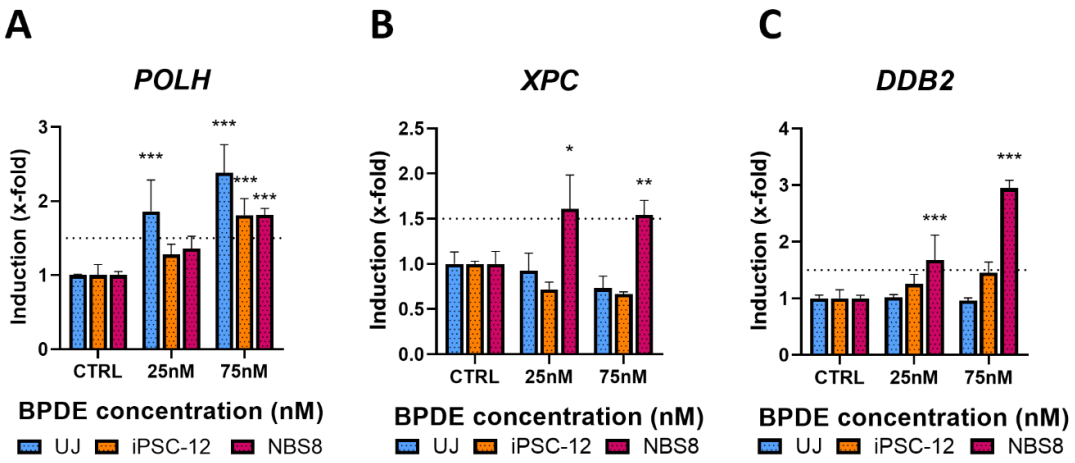

Figure 40: BPDE differentially modulated the gene expression of NER genes in WT and NBS8 hiPSCs. hiPSCs were exposed to 25nM and 75nM of BPDE for 24h, then RNA was extracted for qRT-PCR **(A)** *POLH,* **(B)** *XPC* and **(C)** *DDB2.* Error bar depicts 95% confidence interval. N=3, * = p<0.05, ** = p<0.01, *** = p<0.001. Dashed lines mark 1.5-fold.

3.5.7. BPDE exacerbates the cancerous transcriptional profile of NBS8 hiPSCs

Upon comparing genes extracted from the microarray analysis of WT and NBS8 hiPSC in control conditions (Figure 23B), we identified several enhanced KEGG pathways associated with cancer in the mutant line, with dozens of exclusively regulated genes (Figure 41). Remarkably, besides pathways which are associated with specific cancer types such as “Melanoma” and “Acute Myeloid Leukemia”, the pathway “Platinum drug resistance”, containing genes which confer resistance to chemotherapeutic drugs, was also represented.

BPDE treatment exacerbated this cancerous profile. The heatmap on Figure 42A shows the expression of the 27 genes identified in the cancer related KEGG pathways and gene ontologies in hiPSCs before and after BPDE exposure. UJ and iPSC-12 have in general a low expression of these genes of which a few are enhanced after BPDE treatment. But the NBS8 samples cluster together showing high expression of these genes in control conditions with several being even further enhanced after BPDE exposure.

A comparison between the GO and KEGG pathways from exclusively regulated genes of WT and NBS8 hiPSCs after BPDE exposure further exposes the cancer related transcriptional changes in the NBS8 line (Supplementary Figure 4 and Supplementary Figure 5).

An examination of the GO generated from 441 genes exclusively regulated in NBS8 after exposure to BPDE (Figure 23C) reveals the clusters “positive regulation of extracellular signal-regulated kinase 1 (*ERK1*) and *ERK2* cascade”, C-X-C motif chemokine 12 (*CXCL12*)-activated C-X-C motif chemokine receptor 4 (*CXCR4*) signaling pathway and “positive regulation of vascular endothelial growth factor (*VEGF*) production” (Figure 42B). These pathways are involved in several characteristics related to poor cancer prognosis (216–218). The KEGG pathways (

Figure 42C) have the enhanced pathways “Transcriptional misregulation in cancer” and “Melanoma”, besides “(Mitogen-Activated Protein Kinase) MAPK signaling pathway” and “Ras-related protein 1 (RAP1) signaling pathway”, all of which are frequently involved in oncogenesis, poor cancer prognosis and chemotherapeutic resistance (219).

.

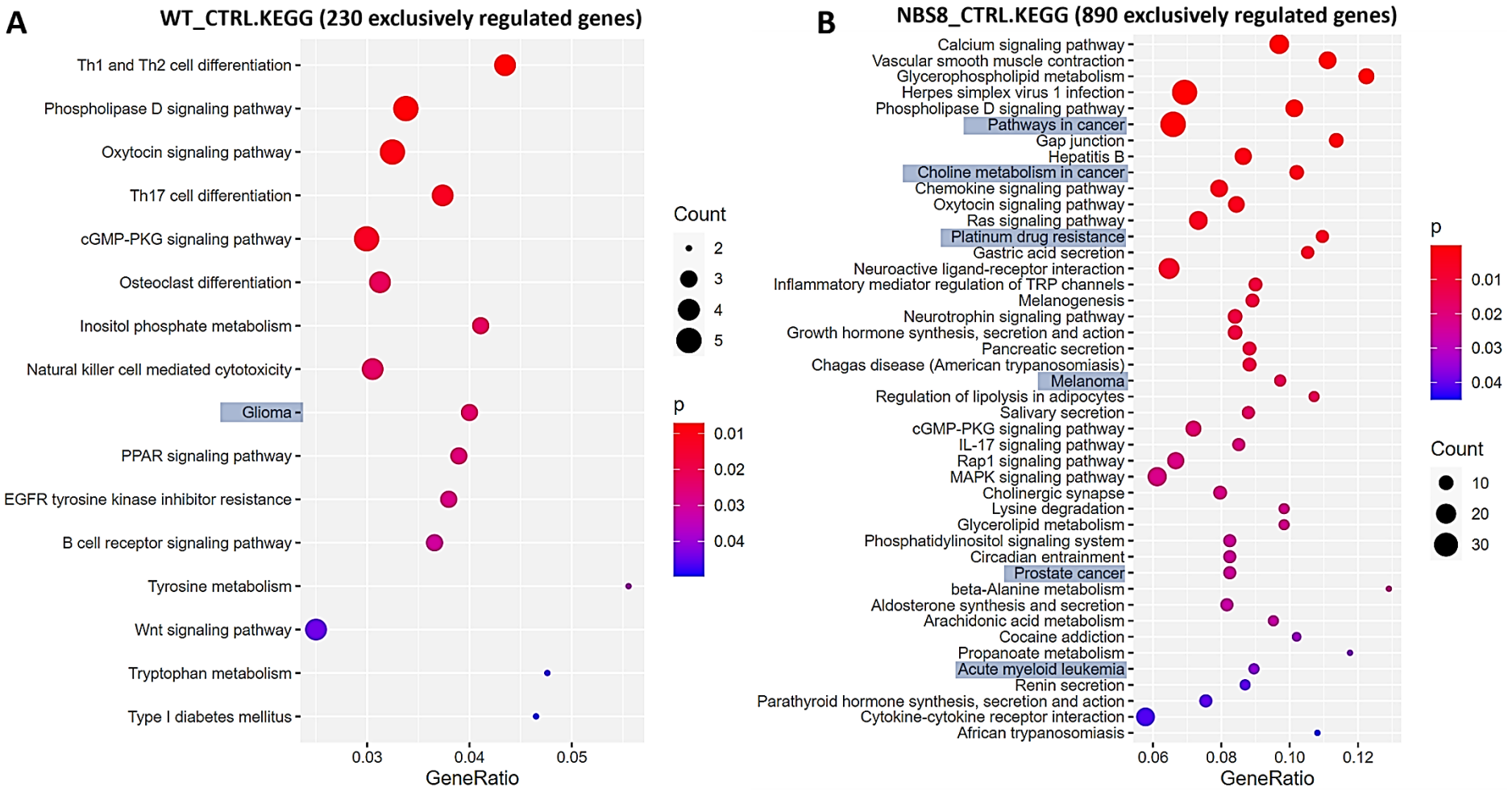

Figure 41: In control conditions, NBS8 hiPSCs have enhanced cancer related KEGG pathways compared to WT hiPSCs. hiPSCs were treated with BPDE for 24h, then had their RNA harvested for Affymetrix microarray. Cancer-related pathways are highlighted in purple. **(A)** KEGG pathways from 230 genes exclusively regulated in WT hiPSCs in control conditions. **(B)** KEGG pathways from 890 genes exclusively regulated in NBS8 hiPSCs in control conditions.

A

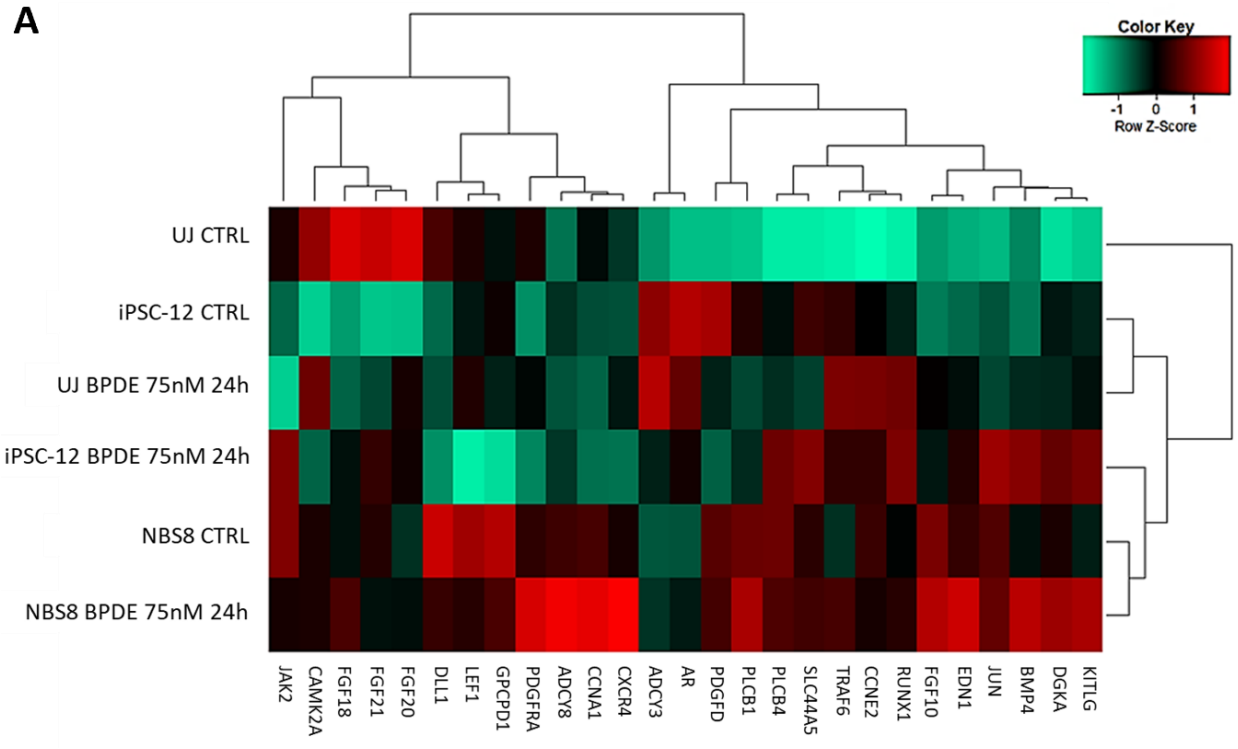

B

GO terms from 441 exclusively regulated genes from BPDE treated NBS8 hiPSCs

GO TERM	Genes	P Value
GO:0070374_Positive regulation of ERK1 and ERK2 cascade	ADRA1A, CCL3, DNAJC27, FGF10, FGF18, MARCO, NPNT, NTRK1, P2RY6, PDGFD, PDGFRA, TNFAIP8L3, TREM2	0.00012
GO:0038160_CXCL12-activated CXCR4 signaling pathway	CXCR4,TREM2	0.00095
GO:0010575_Positive regulation of vascular endothelial growth factor production	ADORA2B,CCBE1,HPSE,ISL1	0.00170

C

KEGG clusters from 441 exclusively regulated genes from BPDE treated NBS8 hiPSCs

KEGG name	Genes	P Value
hsa05202_Transcriptional misregulation in cancer - Homo sapiens (human)	CCNA1, DDIT3, ETV7, FEV, HHEX, MPO, NTRK1, PAX7, TLX1, TLX3	0,00255
Hsa04010_MAPK signaling pathway - Homo sapiens (human)	CHUK, DDIT3, DUSP9, FGF10, FGF18, IL1RAP, MAP2K5, MAPK11, NTRK1, PDGFD, PDGFRA, RPS6KA3	0.00095
Hsa04015_Rap1 signaling pathway - Homo sapiens (human)	ADCY8, ADORA2B, FGF10, FGF18, ITGB2, MAPK11, PDGFD, PDGFRA	0,03735
Hsa05218_Melanoma - Homo sapiens (human)	FGF10, FGF18, PDGFD, PDGFRA	0,04163

Figure 42: BPDE exposure exacerbates the cancerous transcriptional profile of NBS8 hiPSCs. Cells were treated with 75nM of BPDE for 24h, then had their RNA extracted and used for microarray analysis. **(A)** Pearson heatmap of the expression of the genes present in the enhanced cancer related GO and KEGG pathways before and after BPDE treatment. **(B)** Cancer related GO clusters from 441 exclusively regulated genes in NBS8 hiPSCs after BPDE exposure **(C)** Cancer related KEGG pathways from 441 exclusively regulated genes in NBS8 hiPSCs after BPDE exposure.

3.5.8. NBS8 hiPSCs exposed to BPDE have downregulated genes involved in DNA damage repair

After BPDE treatment, the microarray showed that 327 genes were downregulated in WT hiPSCs and 335 genes were downregulated in NBS8 hiPSCs. A metascape analysis of these downregulated genes (Supplementary Figure 6) revealed in NBS8 hiPSCs the cluster “regulation of response to DNA damage stimulus”, with 28 downregulated genes. A heatmap generated from these genes revealed that the majority of them are either slightly upregulated or unchanged in WT cells after BPDE exposure, while most are downregulated in NBS8 after treatment (Figure 43). The downregulation of one of the affected genes, *NAP1L1*, was confirmed through qRT-PCR (mean 0.5- fold) (Figure 44B). Seven of those genes, replication protein A2 (*RPA2*), SET Domain And Mariner Transposase Fusion Gene (*SETMAR*), tumor Protein P53 Binding Protein 1 (*TP53BP1*), INO80 Complex ATPase Subunit (*INO80*), SWI/SNF-Related, Matrix-Associated Actin-Dependent Regulator Of Chromatin, Subfamily A, Containing DEAD/H Box 1 (*SMARCAD1*), Minichromosome Maintenance 9 Homologous Recombination Repair Factor (*MCM9*) and Nucleosome Assembly Protein 1 Like 1 (*NAP1L1)* are directly involved in different points of the double-strand break repair cascade (Figure 44B).

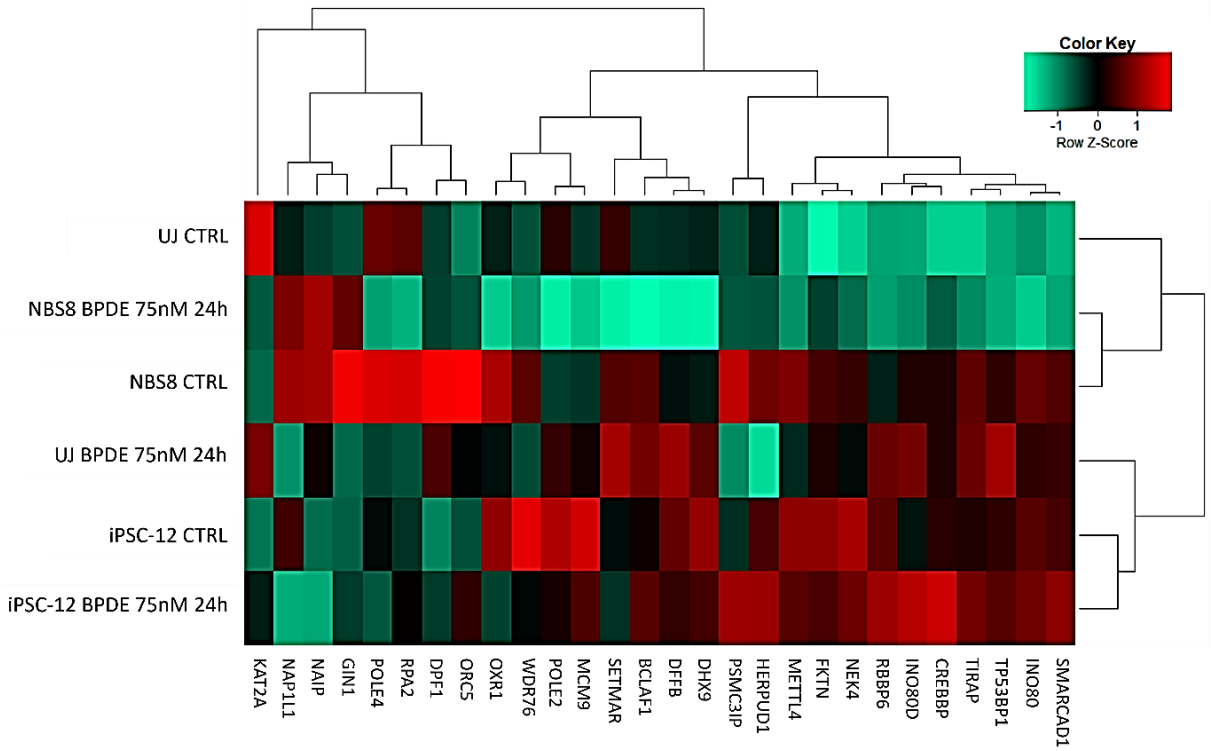

Figure 43: **Pearson's heatmap of 28 DNA damage response and repair genes downregulated in NBS8 hiPSCs after BPDE exposure.** hiPSCs were treated with 75nM of BPDE for 24h, then had their RNA extracted and used for microarray analysis.

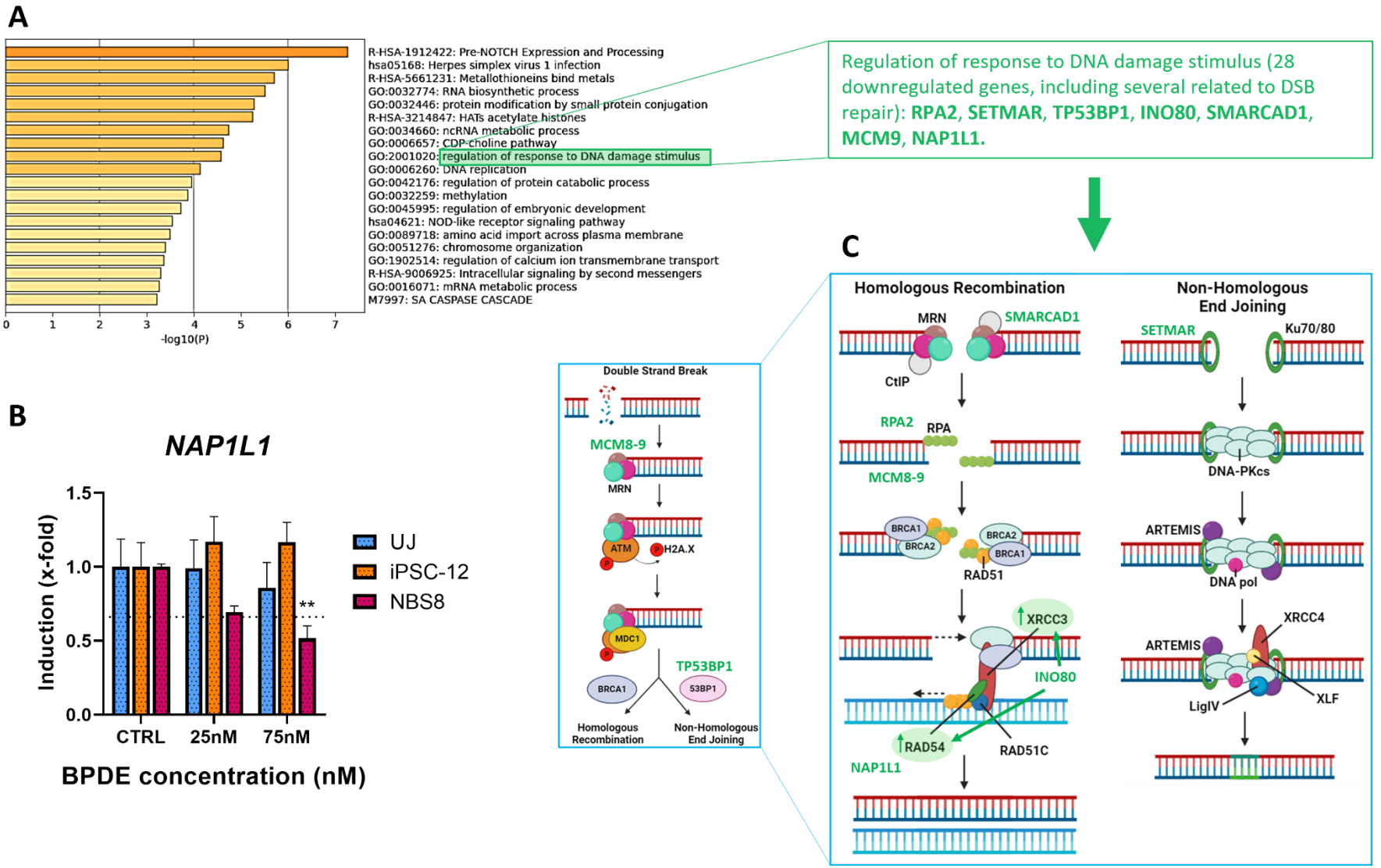

Figure 44: **Exposure to BPDE downregulates genes related to DNA damage repair in NBS8 hiPSCs.** WT and NBS8 hiPSCs were treated with 25nm and 75nM of BPDE for 24h, then had their RNA extracted and used for microarray analysis and qRT-PCR. **(A)** Metascape analysis of 273 genes downregulated in NBS8 after BPDE exposure. **(B)** qRT-PCR for *NAP1L1*. N=3, **p<0.01. Dashed lines mark 0.6 -fold. **(C)** Diagram of the double-strand break repair pathway. In green, the downregulated DSBR related genes and the repair step in which they are involved.

3.6. Effects of BPDE exposure on healthy and NBS-patient derived neural progenitor cells (NPCs)

UJ, iPSC-12 and NBS8 hiPSCs were differentiated into NPCs in order to assert whether there are differences in the DNA damage response to BPDE between pluripotent and progenitor cells. NPCs were exposed to BPDE at the concentrations of 25nM and 75nM for 24h, then investigated for key markers identified in BPDE exposed hiPSCs.

3.6.1. Characterization of NPCs derived from NBS-patient and WT hiPSCs

The WT hiPSCs UJ and iPSC-12, as well as the NBS patient-derived NBS8 hiPSCs, were differentiated into neural progenitor cells (NPCs) as described on 2.1.3. RNA was isolated from the NPCs and used to evaluate the expression of the pluripotency marker *OCT4*, the dual pluripotency and NPC-associated marker *SOX2*, and the NPC markers SRY-Box Transcription Factor 1 (*SOX1*) and *PAX6*. The NPC gene expression was compared to RNA from their parental, undifferentiated hiPSCs. NPC cultures were also immunostained with antibodies against the NPC markers SOX2, Ki67, SOX1, Nestin, and the neuron marker TUJ1.

OCT4 analysis shows that it was downregulated (< 0.05-fold) in all three lines after NPC differentiation, while the levels of *SOX2* remained constant. *SOX1* gene expression was upregulated between 50-fold to 150-fold in all lines, while the levels of *PAX6* reached around 6000-fold higher than in the hiPSC control (Figure 45).

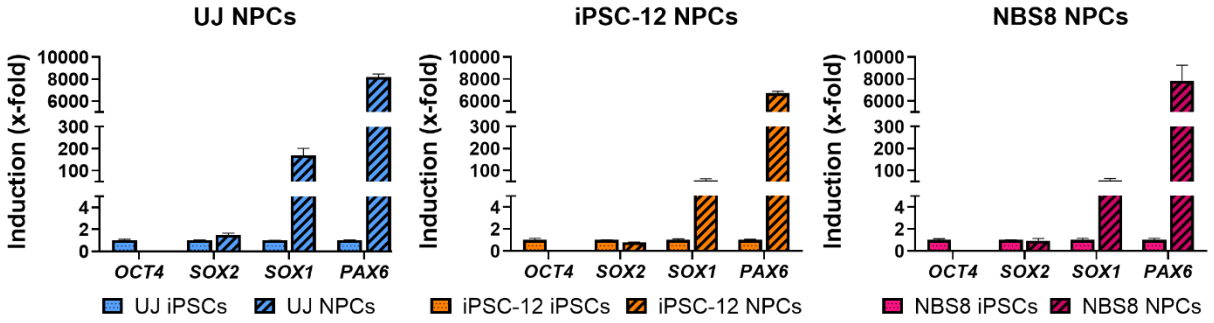

Figure 45: Transcriptional characterization of hiPSC-derived NPCs. NPC's RNA was harvested for qRT-PCR analysis. Gene expression of key markers was compared to their undifferentiated parental hiPSCs. NPCs no longer express *OCT4*, while maintaining comparable expression of *SOX2*. NPCs also express SOX1 and PAX6, two key NPC transcription factors. N=3. Error bar depicts 95% confidence interval.

To confirm that the transcription of NPC markers translated into protein expression, NPCs were stained for the transcription factors SOX2 and SOX1, the proliferation marker Ki67, and the structural proteins Nestin and TUJ1 (Figure 46). Over 90% of cells were stained for SOX2 (Supplementary Figure 7A) and Nestin (Supplementary Figure 7B), while around 85% were stained for SOX1 (Supplementary Figure 7C) and between 55% and 60% were positive for Ki67 (Supplementary Figure 7D). Lastly, TUJ1+ neurons were only sporadically seen in the culture, averaging about one per well of a 24-well plate. Both gene expression and immunocytochemistry indicated the successful differentiation of NPCs.

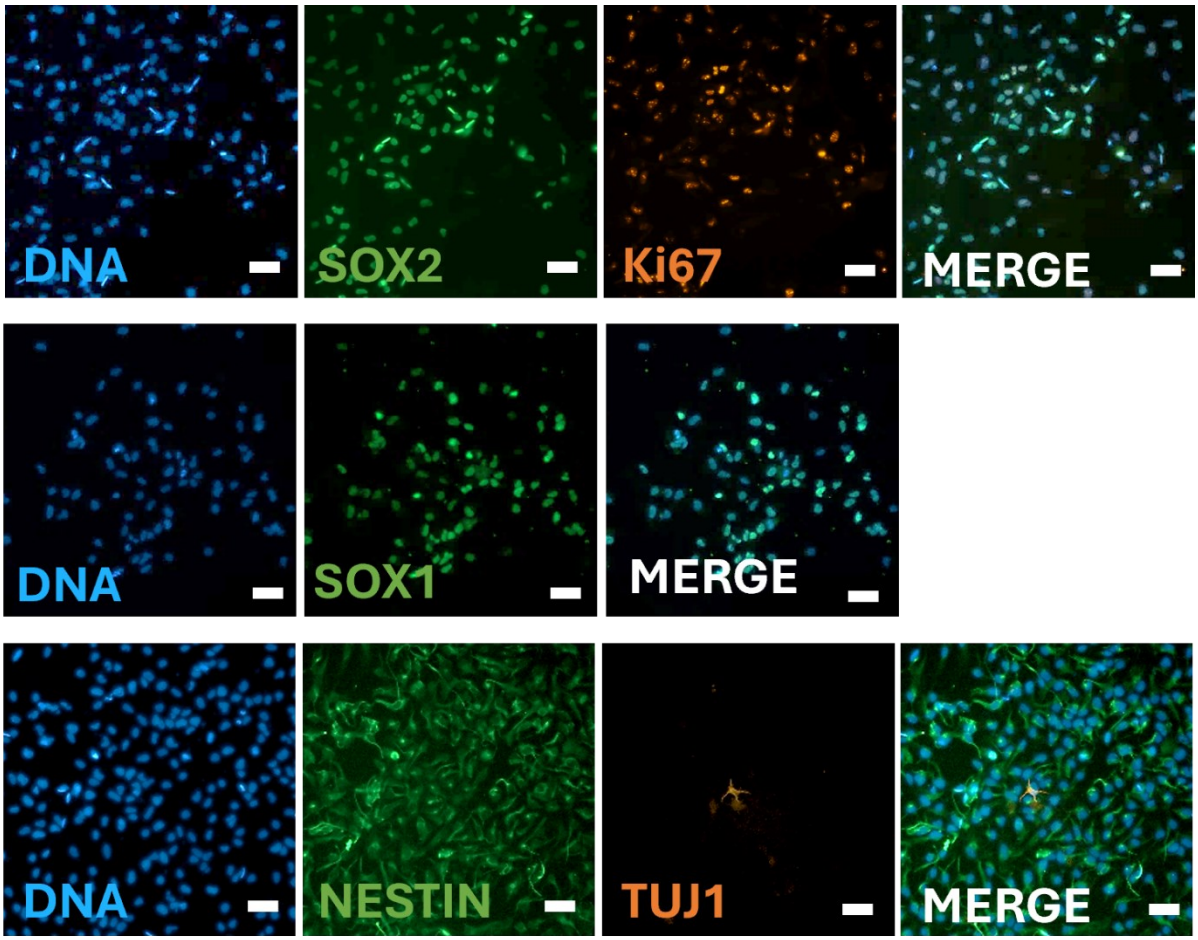

Figure 46: Immunocytochemistry characterization of hiPSC-derived NPCs. Representative immunocytochemistry of hiPSC NPCs for key NPC markers SOX2, Ki67, SOX1, Nestin, and the neuron markerTUJ1. Scale bar 50µm.

3.6.2. BPDE exposure does not influence the expression of key NPC markers

NPCs were treated with 25nM and 75nM of BPDE for 24h. and qRT-PCR was used to investigate whether the treatment affected the gene expression of key NPC markers. The gene expression levels of *SOX2*, *SOX1* and *PAX6* remained stable after genotoxic

exposure (Figure 47Figure 1). To confirm these findings, the NPCs were immunostained for SOX2, SOX1 and nestin, and the number of cells positive for all three markers were also unchanged after BPDE treatment (Figure 48; Supplementary Figure 8, Supplementary Figure 9, Supplementary Figure 10).

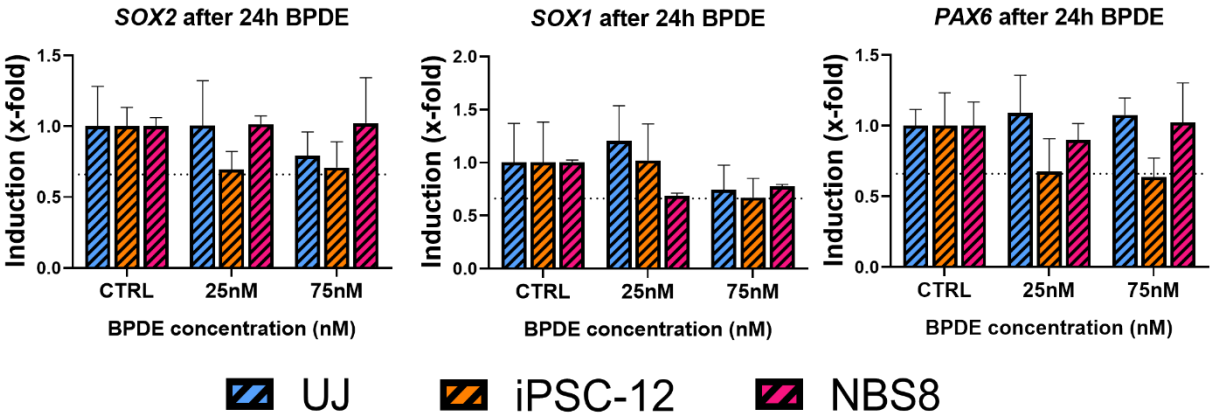

Figure 47: Expression of key markers *SOX2*, *SOX1* and *PAX6* remain unchanged in NPCs after BPDE exposure. NPCs were exposed to 25nM and 75nM of BPDE for 24h, then RNA was extracted for qRT-PCR for *SOX2*, *SOX1* and *PAX6*. N=3. Error bar depicts 95% confidence interval. Dashed lines mark 0.6 -fold.

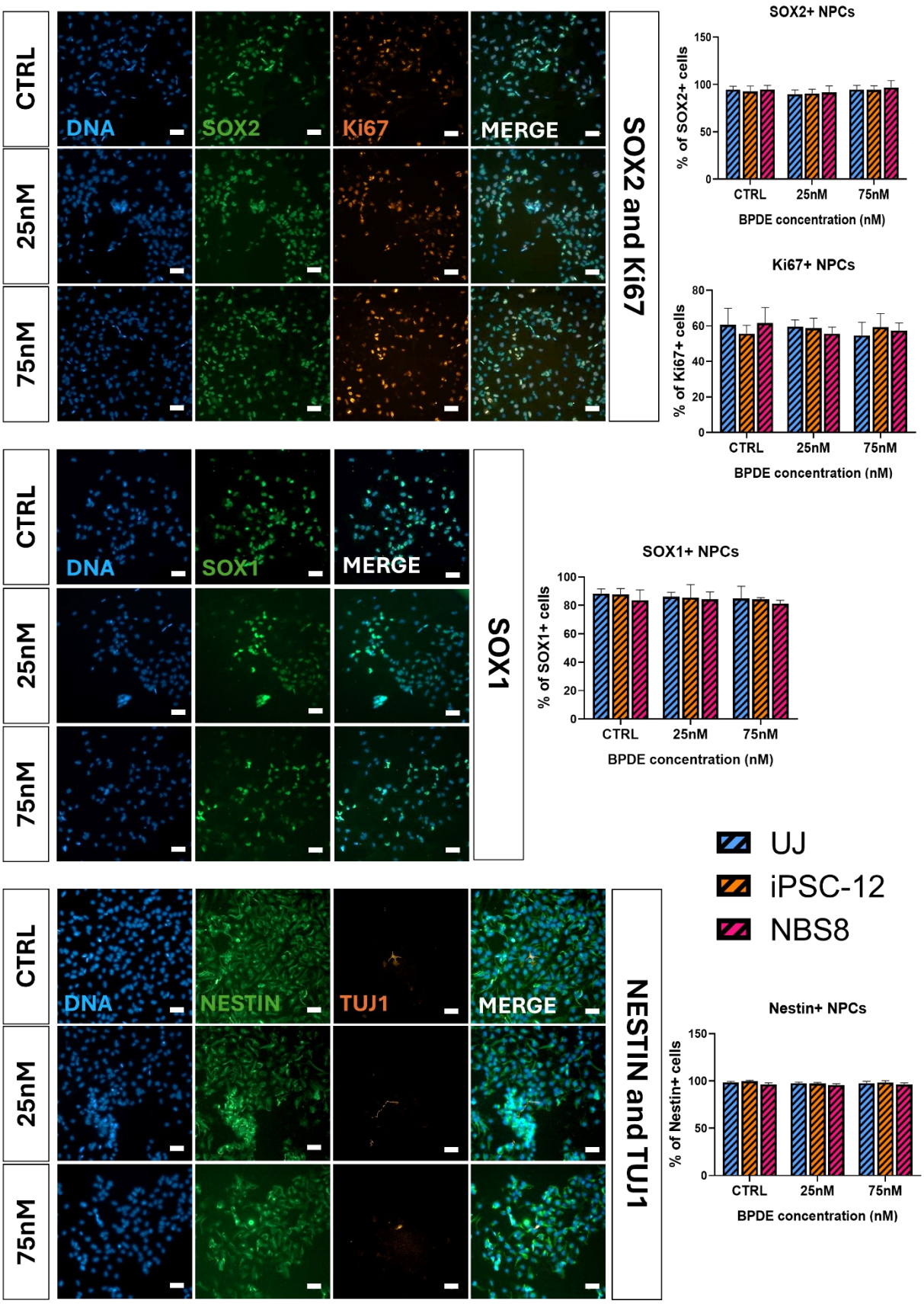

Figure 48: BPDE exposure on NPCs does not affect immunocytochemistry of key NPC markers. NPCs were exposed to BPDE at 25nM and 75nM concentrations for 24h, the fixed for key NPC markers SOX2, Ki67, SOX1, Nestin and the neuron marker TUJ1. Percentage of positive cells shown. Total cell number was calculated using DAPI stained nuclei. N=3, mean +/- standard deviation shown. Scale bar 50μm.

3.6.3. NPCs are more resistant to the cytotoxic effects of BPDE than hiPSCs

NPCs were exposed to BPDE for 24h at the concentrations of 25nM and 75nM, then were analysed for key apoptotic markers and the results were compared with the ones obtained from their parental hiPSCs. While *TNFRSF10A* and *CASP3* were upregulated in hiPSCs after BPDE treatment, no regulation occurred in NPCs. The intrinsic apoptotic markers *BBC3* and *BAX* remained unchanged in both cell types (Figure 49).

Upon investigating the protein expression of caspase 3, as well as that of its active form cleaved caspase 3, it was revealed that BPDE exposure had a lessened effect on cleaved caspase 3 levels in NPCs when compared to hiPSCs. A slight upregulation of cleaved caspase 3 could be seen on iPSC-12 NPCs after BPDE exposure, but levels remained stable on both other NPC lines (Figure 50). These results suggest that hiPSCs showed a lower resistance to BPDE cytotoxicity after 24h of exposure than their differentiated NPCs.

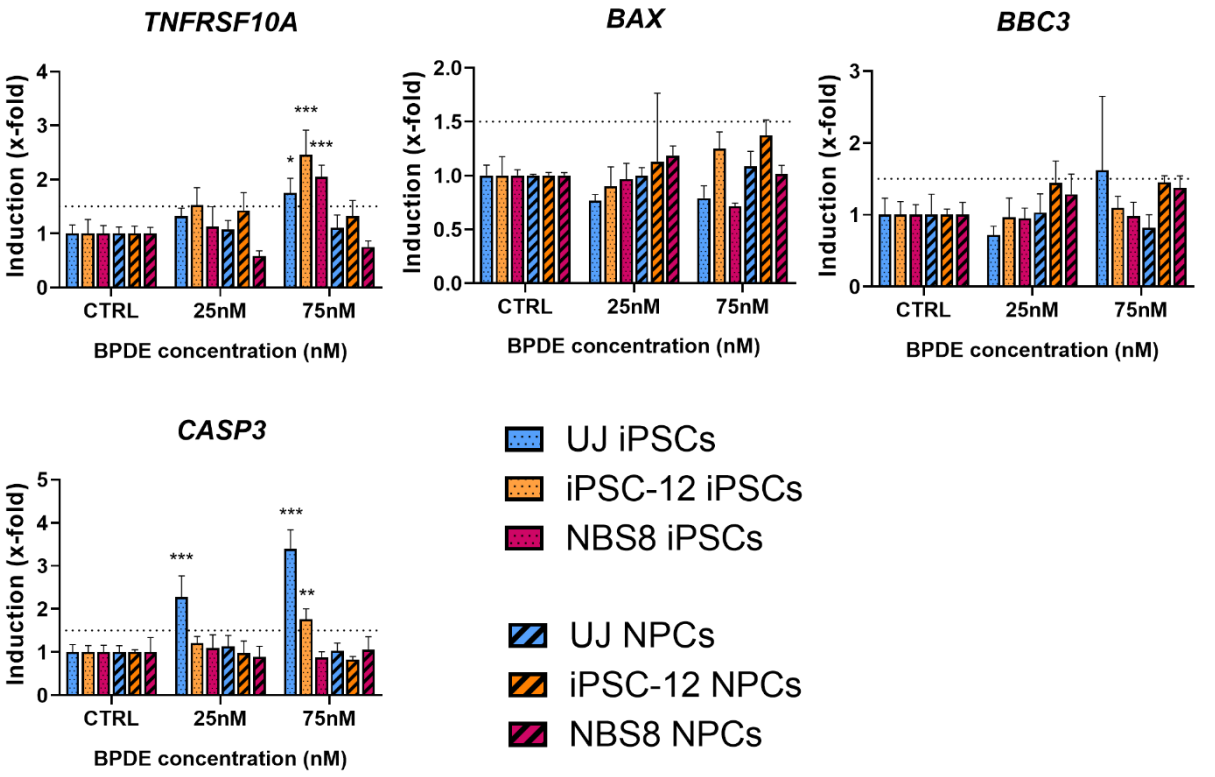

Figure 49: BPDE exposure does not influence the gene expression of key apoptotic markers on NPCs. hiPSCs and NPCs were treated with 25nM and 75nM of BPDE for 24h, then RNA was extracted for qRT-PCR for *TNFRSF10A*, *CASP3*, *BAX* and *BBC3*. N=3, *p<0.05, **p<0.01, ***p<0.001. Error bar depicts 95% confidence interval. Dashed lines mark 1.5-fold.

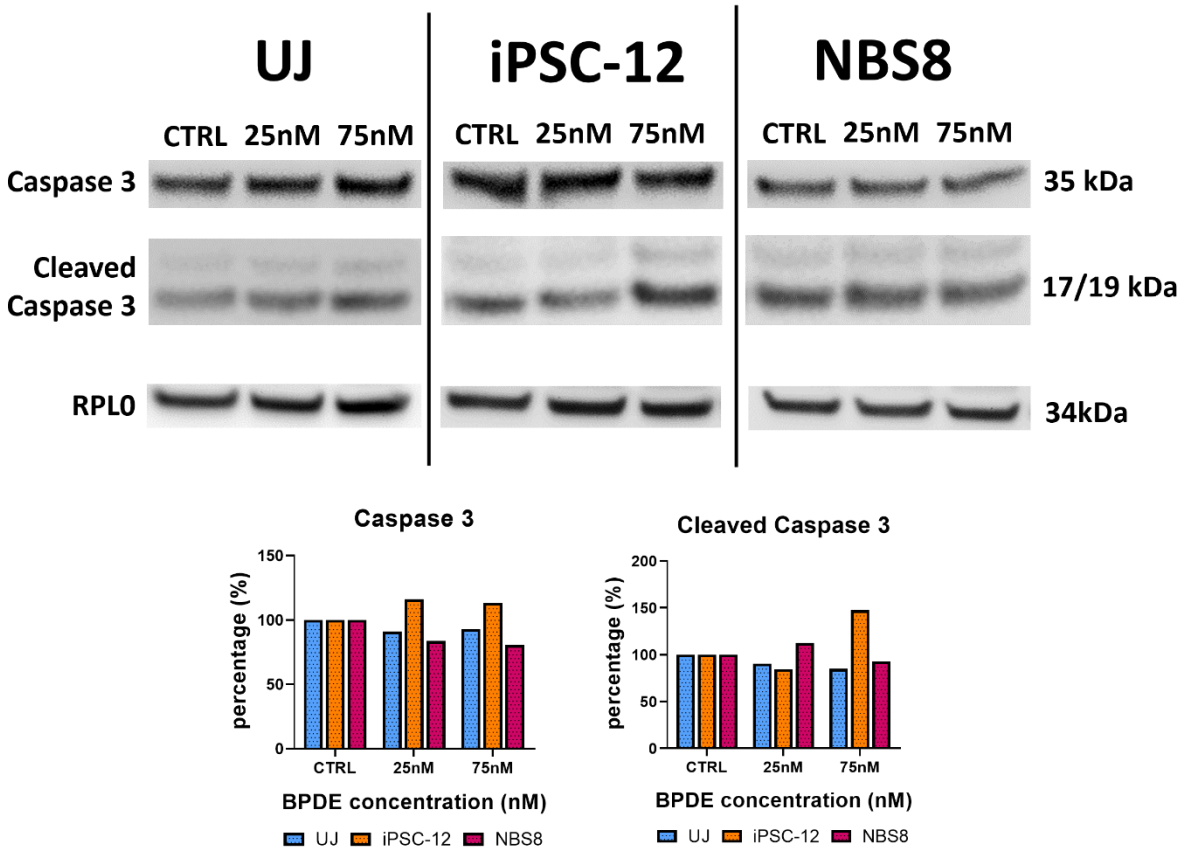

Figure 50: BPDE exposure is less cytotoxic on NPCs compared to their parental hiPSCs. NPCs were treated with 25nM and 75nM of BPDE for 24h, then protein was extracted for western blot for caspase 3 and slightly cleaved caspase 3. N=1, RPL0 was used for loading control.

3.6.4. NPCs have a differentiated DNA damage response to BPDE exposure when compared to hiPSCs

A set of key DNA damage response targets were chosen to be investigated from the results of the microarray analysis of hiPSC exposed to BPDE, as well as targets known to be regulated by BPDE in the literature. NPCs derived from hiPSCs had a different DNA damage response when compared to their undifferentiated hiPSCs under the same treatment conditions. While *ATM*, *CHEK1* and *CHEK2* maintained a stable gene expression in both hiPSCs and NPCs after BPDE treatment, the upregulation of *ATR* which was noted in NBS8 hiPSCs after exposure to both 25nM and 75nM BPDE (1.6-fold and 7.1-fold respectively) was not observed in their differentiated NPC progeny (Figure 51).

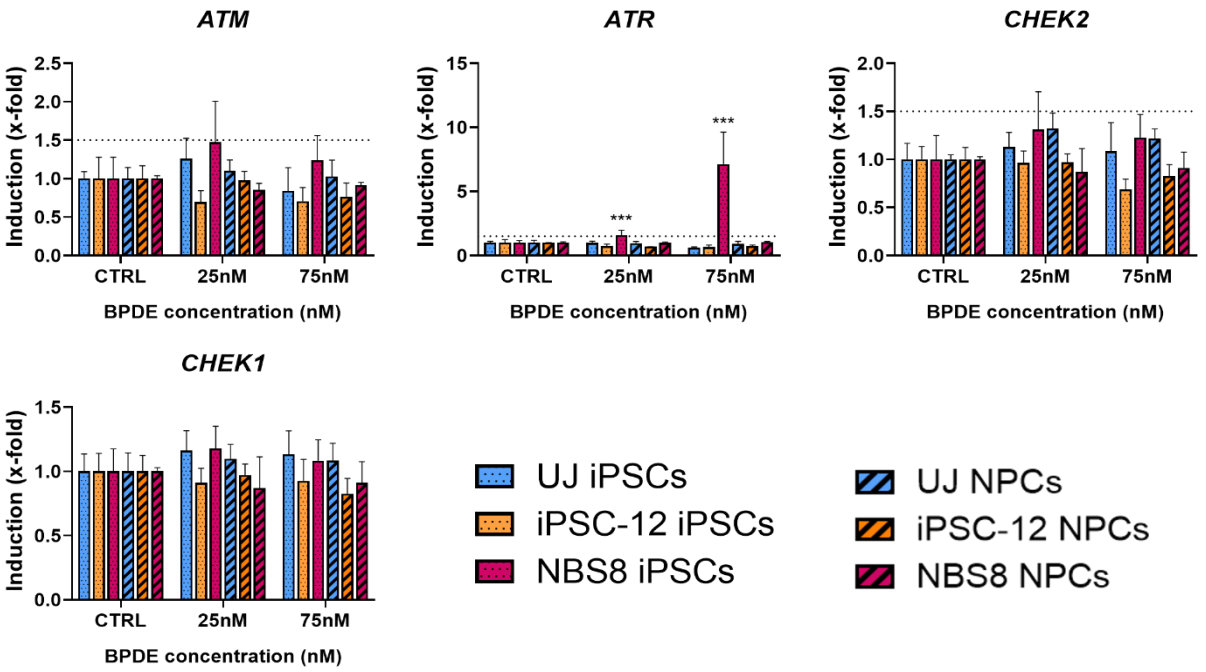

Figure 51: NPCs exposed to BPDE had no changes in the gene expression of DNA damage response targets. hiPSCs and NPCs were treated with 25nM and 75nM of BPDE for 24h and RNA was harvested for qRT-PCR for *ATM*, *ATR*, *CHEK1* and *CHEK2*. N=3, ***p<0.001. Error bar depicts 95% confidence interval. Dashed lines mark 1.5-fold.

With the intent to analyze the p53-mediated DNA damage response, the gene expression of p53 was measured, as well as that of the p53 regulators *MDM2* and *cJUN* and the p53-inducible cell cycle regulators *CDKN1A* and *GADD45A*. While *TP53* (Figure 52A) was downregulated after BPDE exposure in WT hiPSC and *MDM2* (Figure 52B) was downregulated in NBS8 hiPSCs, the same was not seen in WT NPCs and NBS8 NPCs. *cJUN*, *CDKN1A* and *GADD45A* which were all upregulated in hiPSC after treatment were unchanged in NPCs, with the exception of *GADD45A* which was slightly upregulated (1.8-fold) in iPSC-12 NPCs (Figure 52C to E).

Investigation of the protein expression of MDM2 in NPCs after BPDE exposure revealed a similar pattern to that observed in hiPSCs, with the expression being enhanced in WT NPCs after treatment, but unchanged in NBS8 NPCs. Interestingly, p53 protein expression was only enhanced in iPSC-12 NPCs after genotoxic exposure, while the expression of cJUN was unchanged in all three NPC cell lines (Figure 53).

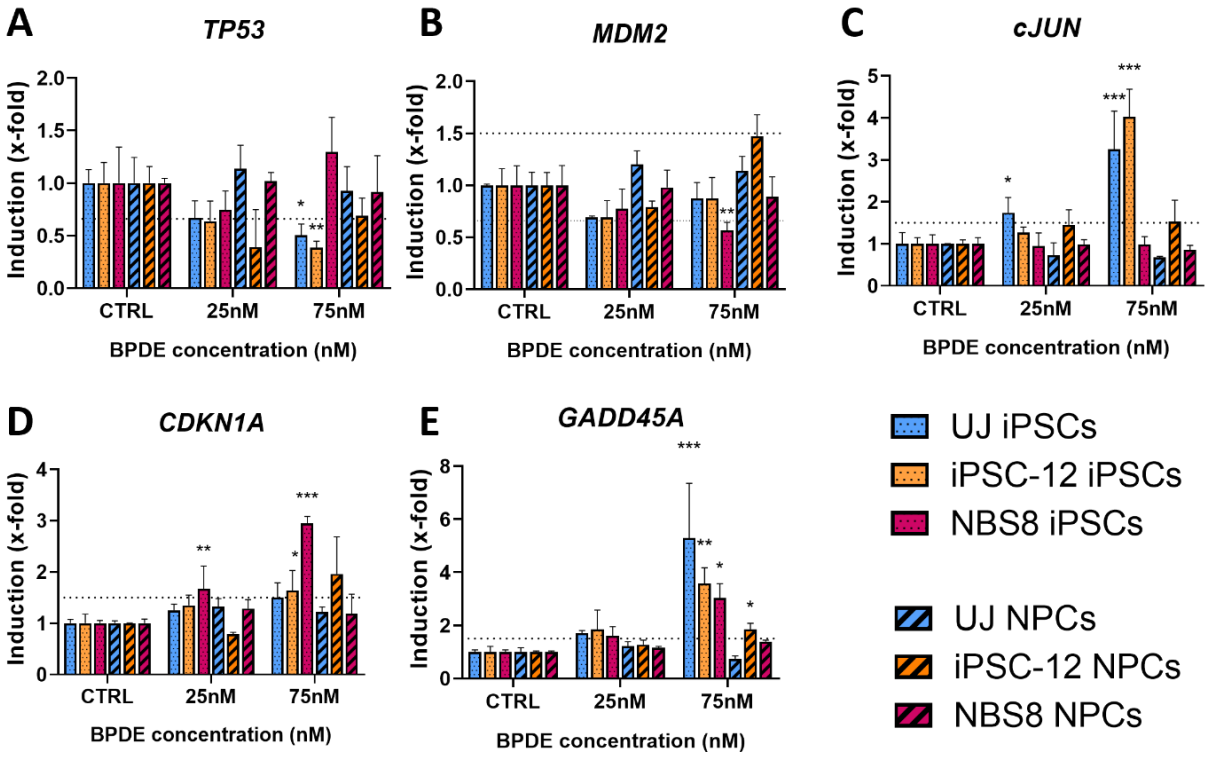

Figure 52: BPDE exposure on NPCs differentially regulated *TP53*, and gene targets related to cell cycle control and p53 modulation when compared to hiPSCs. hiPSCs and were treated with 25nM and 75nM of BPDE for 24h and RNA was harvested for qRT-PCR for **(A)** *TP53*, **(B)** *MDM2*, **(C)** *cJUN* and **(D)** *CDKN1A* and **(E)** *GADD45A*. N=3, *p<0.05, **p<0.01 ***p<0.001. Error bar depicts 95% confidence interval. Dashed lines mark 1.5- and 0.6-fold.

Next, the gene expression of three p53-inducible genes related to bulky DNA-adduct repair, *POLH*, *XPC* and *DDB2*, was investigated. In hiPSCs, the expression of *POLH* was upregulated in all three cell lines after BPDE treatment, which was not seen in NPCs (Figure 54A). *XPC* and *DDB2* were upregulated in NBS8 hiPSCs in both tested concentrations, but in NPCs *XPC* expression was unchanged after BPDE exposure (Figure 54B) and *DDB2* was only upregulated at 75nM (1.5-fold) and less than in their hiPSC counterparts (3-fold) (Figure 54C).

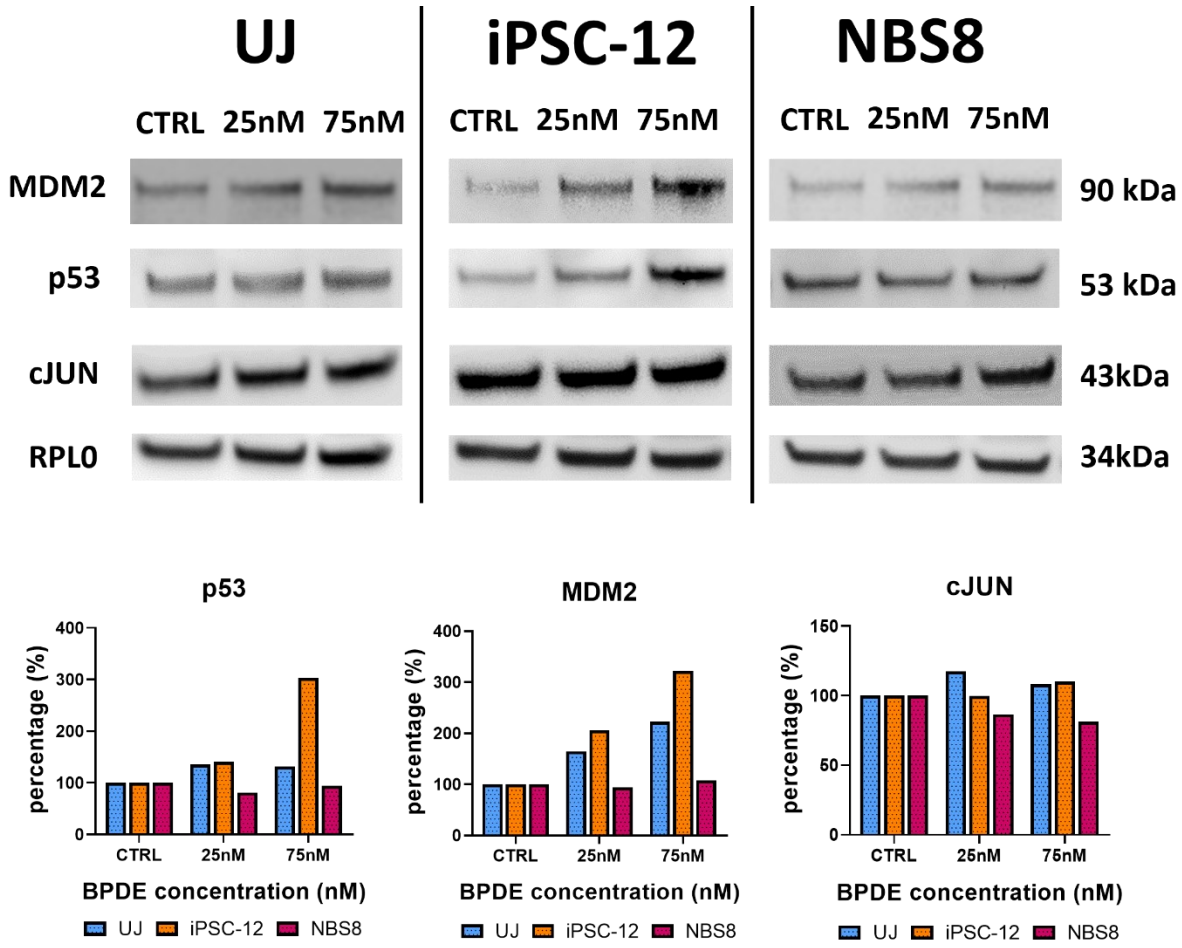

Figure 53: BPDE exposure enhanced the protein expression of MDM2 on WT NPCs, but not on NBS8 NPCs. NPCs were treated with 25nM and 75nM of BPDE for 24h and protein was harvested for western blot for p53, MDM2 and cJUN. N=1. RPL0 was used as loading control.

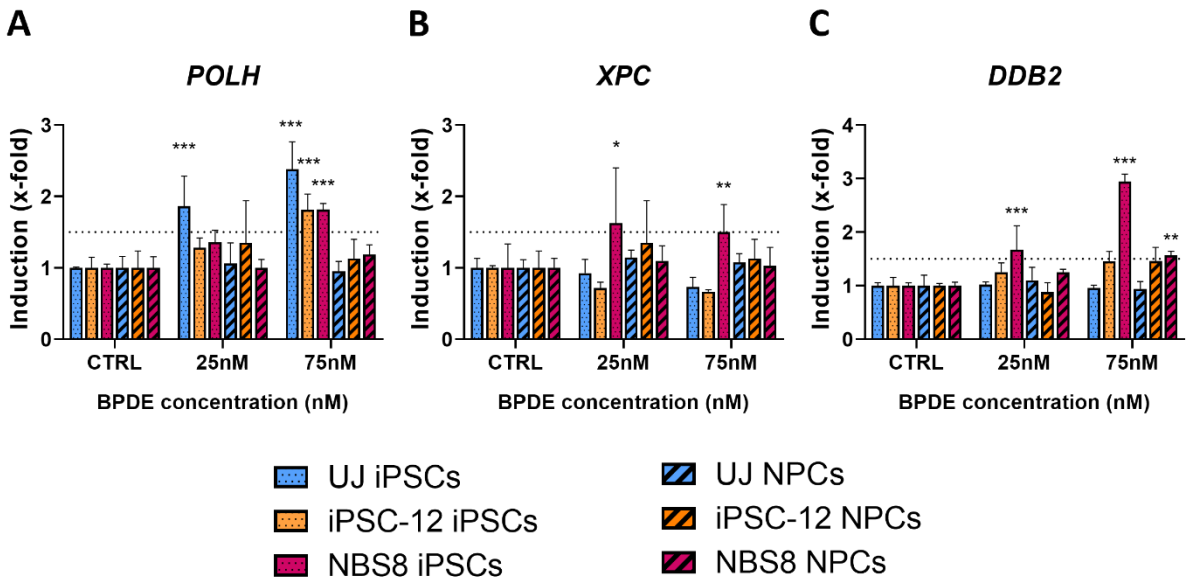

Figure 54: DDB2 expression is enhanced in NBS8 hiPSCs and NPCs after BPDE exposure. hiPSCs and NPCs were treated with 25nM and 75nM of BPDE for 24h and RNA was harvested for qRT-PCR for **(A)** *POLH*, **(B)** *XPC* and **(C)** DDB2. N=3, *p<0,05, **p<0,01 ***p<0,001. Error bar depicts 95% confidence interval. Dashed lines mark 1.5-fold.

Lastly, the effects of BPDE on the expression levels of γ-H2AX were evaluated. Remarkably, while there was no difference in the levels of γ-H2AX after BPDE exposure, the levels of endogenous γ-H2AX in NBS8 NPCs were six-fold higher than in their WT counterparts (Figure 55). This phenomenon was not observed in hiPSCs and could indicate a higher basal level of DNA-double strand breaks in NBS-derived NPCs than in WT NPCs.

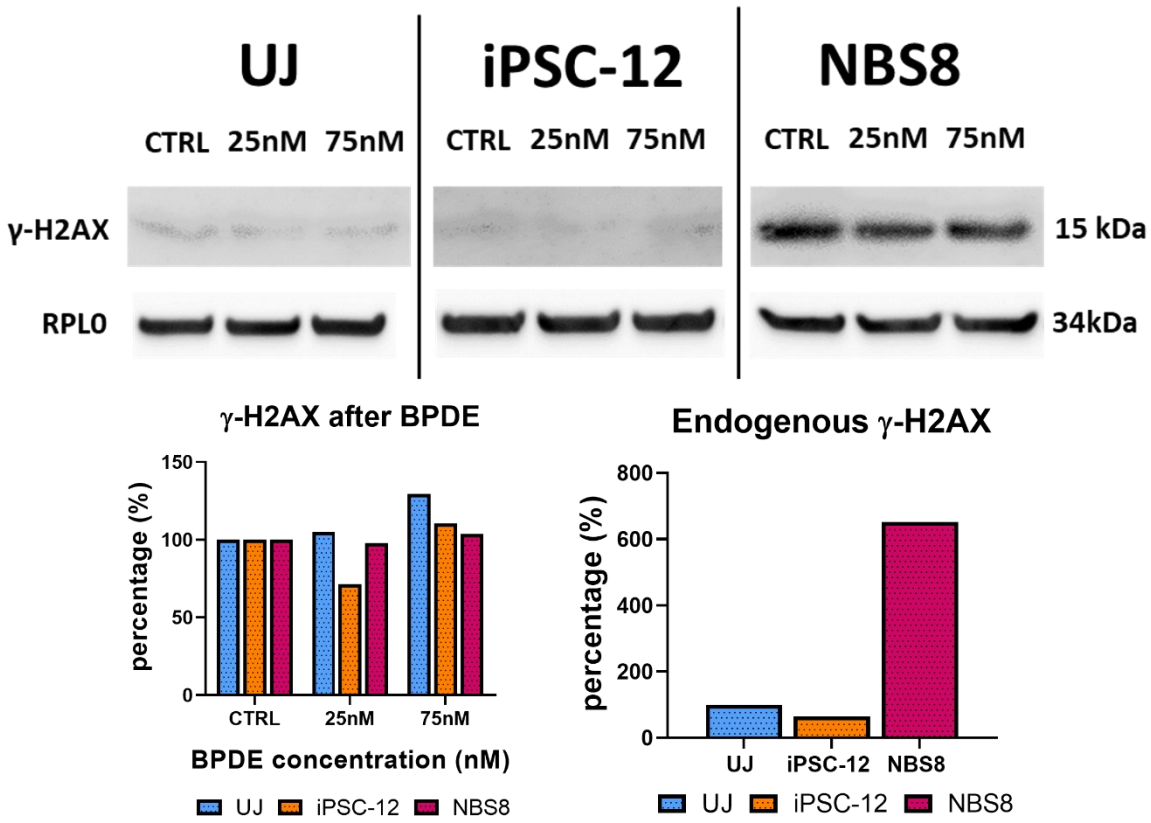

Figure 55: NBS8 NPCs have an enhanced endogenous expression of γ-H2AX when compared to WT NPCs. NPCs were treated with 25nM and 75nM of BPDE for 24h and protein was harvested for western blot for γ-H2AX. N=1. RPL0 was used as loading control.

3.7. Effects of BPDE exposure on hepatic endoderm derived from WT hiPSCs

In order to investigate the DNA damage response to BPDE in progenitor cells of the endoderm lineage, UJ and iPSC-12 hiPSCs were differentiated into HE cells and exposed to BPDE at the concentrations of 25nM and 75nM for 24h, then evaluated for key markers identified in BPDE exposed hiPSCs. The results were compared to those obtained from their parental hiPSCs.

3.7.1. Characterization of HE derived from wild-type hiPSCs

UJ and iPSC-12 hiPSC were differentiated into hepatic endoderm (HE) following the protocol described on 2.1.5. RNA was isolated at the last day of differentiation and used to evaluate the expression of the HE-associated markers *HNF4α*, *AFP*, Keratin 18 (*KRT18*) and keratin 19 (*KRT19*), as well as the pluripotency associated marker *OCT4* and the hepatocyte-associated marker albumin (*ALB*). The HE gene expression was compared to RNA extracted from primary human hepatocytes (PHH) and from fetal liver, while their parental, undifferentiated hiPSCs were used as control. Furthermore, HE cultures were immunostained with antibodies against AFP and HNF4α, to confirm their protein expression.

OCT4 analysis shows that it was downregulated in both cell lines after HE differentiation (< 0.001-fold), in levels comparable to PHH and fetal liver (Figure 56A). Conversely, *HNF4α* was upregulated between 250 and 500-fold, once again comparable to the two liver lines (Figure 56B). *AFP* was upregulated in comparable amounts in HE and fetal liver cells, but not in PHH (Figure 56C), while *ALB* was sharply upregulated in PHH and fetal liver (between $4x10^6$ and $9x10^6$-fold), while comparatively very little upregulated in HE cells (around 200-fold)(Figure 56B).

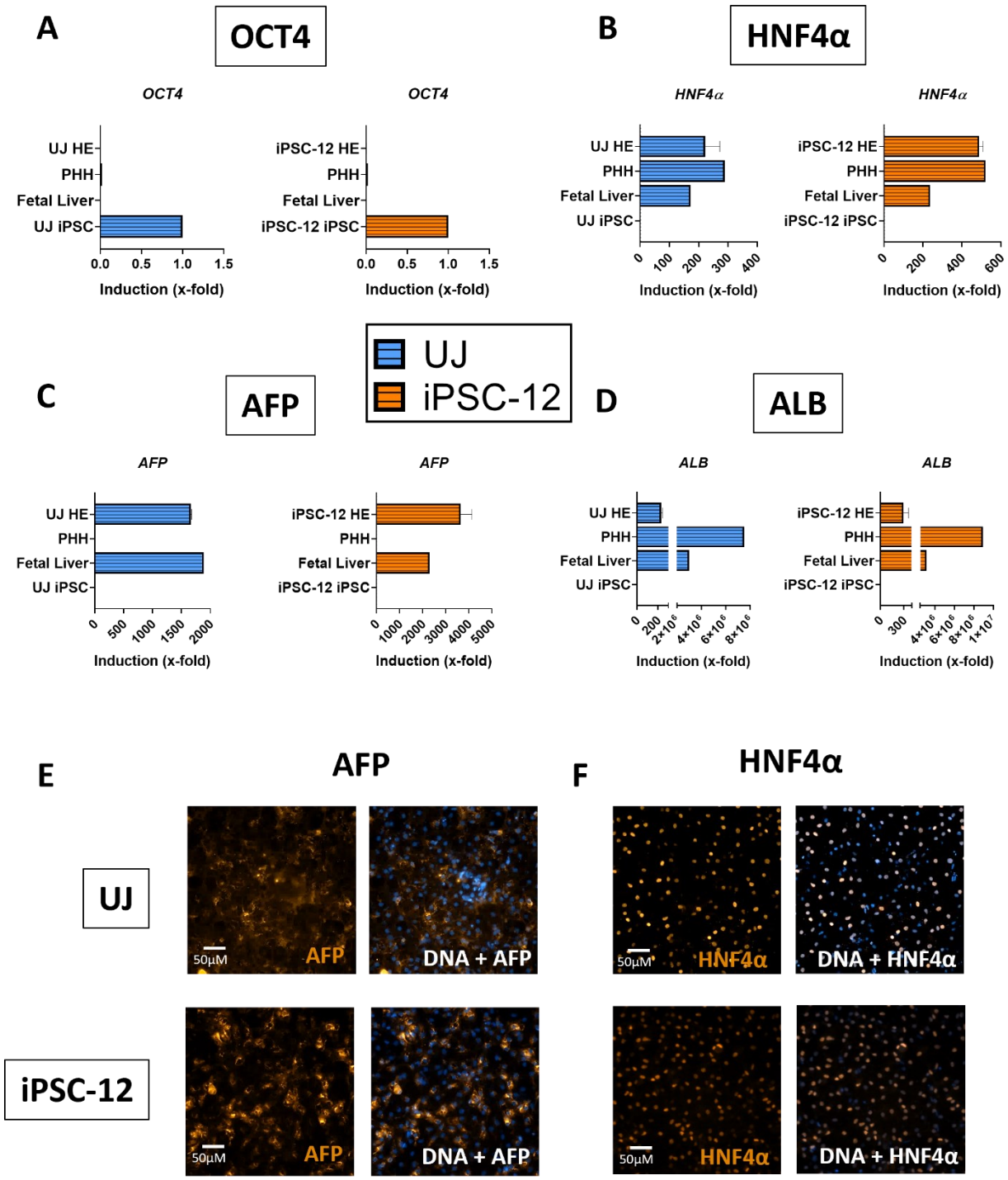

Figure 56: Characterization of hiPSC-derived HE cells. HE cells transcription was compared to fetal liver cells and primary human hepatocytes (PHH) through qRT-PCR. Their undifferentiated parental hiPSCs were used as control. HE cells no longer express **(A)** *OCT4*, while expressing **(B)** *HNF4α*, **(C)** *AFP* and modest levels of **(D)** *ALB*. Immunocytochemistry for **(E)** AFP and **(F**) HNF4α confirms the expression of both markers. N=3 for HE cells and N=1 for hiPSCs, fetal liver cells and PHH. Error bar depicts 95% confidence interval.

Immunocytochemistry for AFP (Figure 56E) and HNF4α (Figure 56F) revealed wide spread expression of both markers in the HE cultures. Additionally, the HE cells expressed both *KRT18* (mean >5-fold)(Figure 57A) and *KRT19* (mean >16-fold)(Figure 57B), markers associated with liver differentiation and cholangiocyte

differentiation, respectively, while neither PHH nor fetal liver had any *KRT19* expression. The results indicate the successful differentiation of both hiPSCs lines into HE cell.

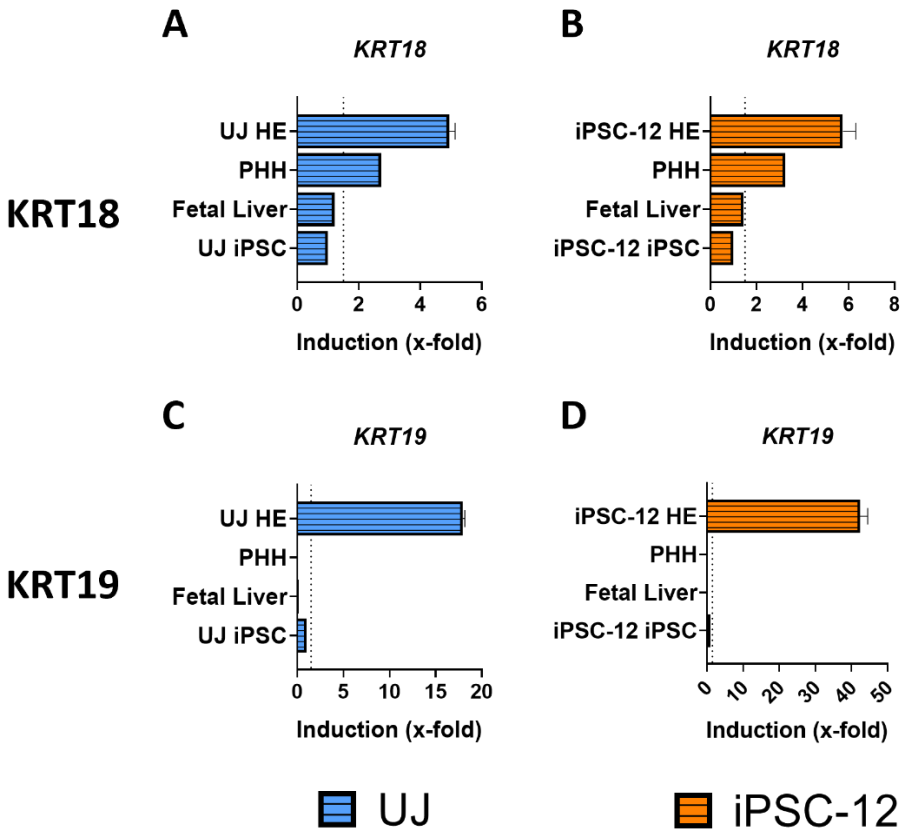

Figure 57 HE cells express keratinocyte markers related to cholangiocytes and hepatocytes. HE cells express both **(A)** *KRT18*, a hepatocyte associated marker and **(B)** *KRT19*, a cholangiocyte associated marker. N=3 for UJ HE and N=1 for the rest. Error bar depicts 95% confidence interval.

3.7.2. BPDE downregulates the gene expression of key HE markers

Next, to assess whether BPDE exposure had an influence on the progenitor state of HE cells, UJ and iPSC-12 HEs were subjected to 25nM and 75nM of BPDE for 24h, then analysed for key HE markers. Immunocytochemistry for AFP did not reveal any perceivable difference in expression after BPDE exposure (Figure 58A and B), consistent with the results observed in *AFP*'s gene expression (Figure 58C). Interestingly, 25nM, but not 75nM, of BPDE downregulated (mean < 0.6 -fold) the gene expression of *HNF4α* in both cell lines (Figure 58D), although no difference could be visually observed in the immunocytochemistry (Figure 58E and F).

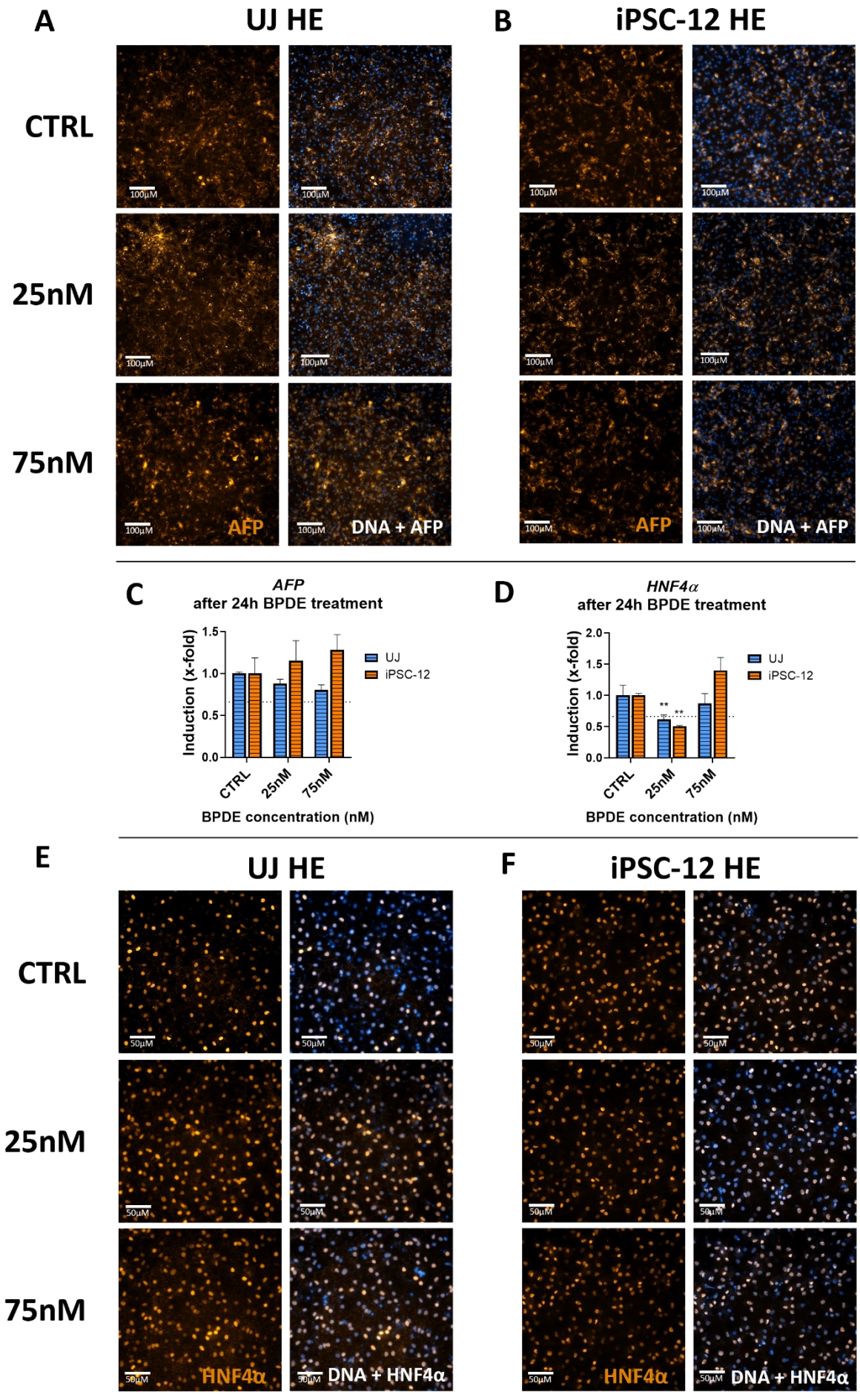
A
UJ HE
B
iPSC-12 HE
CTRL
25nM
75nM
100µM
AFP
DNA + AFP
C
AFP
after 24h BPDE treatment
Induction (x-fold)
1.5
1.0
0.5
0.0
UJ
iPSC-12
CTRL
25nM
75nM
BPDE concentration (nM)
D
HNF4α
after 24h BPDE treatment
Induction (x-fold)
2.0
1.5
1.0
0.5
0.0
**
**
UJ
iPSC-12
CTRL
25nM
75nM
BPDE concentration (nM)
E
UJ HE
F
iPSC-12 HE
CTRL
25nM
75nM
50µM
HNF4α
DNA + HNF4α

Figure 58 BPDE treatment altered the gene expression of *HNF4α* but had no visible difference on HNF4α immunostaining. HE cells were treated with 25nM and 75nM of BPDE for 24h. **(A)** AFP immunocytochemistry. qRT-PCR for **(B)** *AFP* and **(C)** *HNF4α*. N=3, **p<0.01. Error bar depicts 95% confidence interval. Dashed lines mark 0.6-fold. **(D)** HNF4α immunocytochemistry. Scale bar 50μM.

BPDE did not interfere with the expression of *ALB* (Figure 59A), but 75nM treatment downregulated (mean 0.63-fold) the expression of *KRT18* (Figure 59B) in iPSC-12 HE, as well as *KRT19* (mean < 0.6- fold) in both cell lines (Figure 59C). It is possible that BPDE exposure interferes with the HE cells capacity for differentiation into hepatocytes and cholangiocytes.

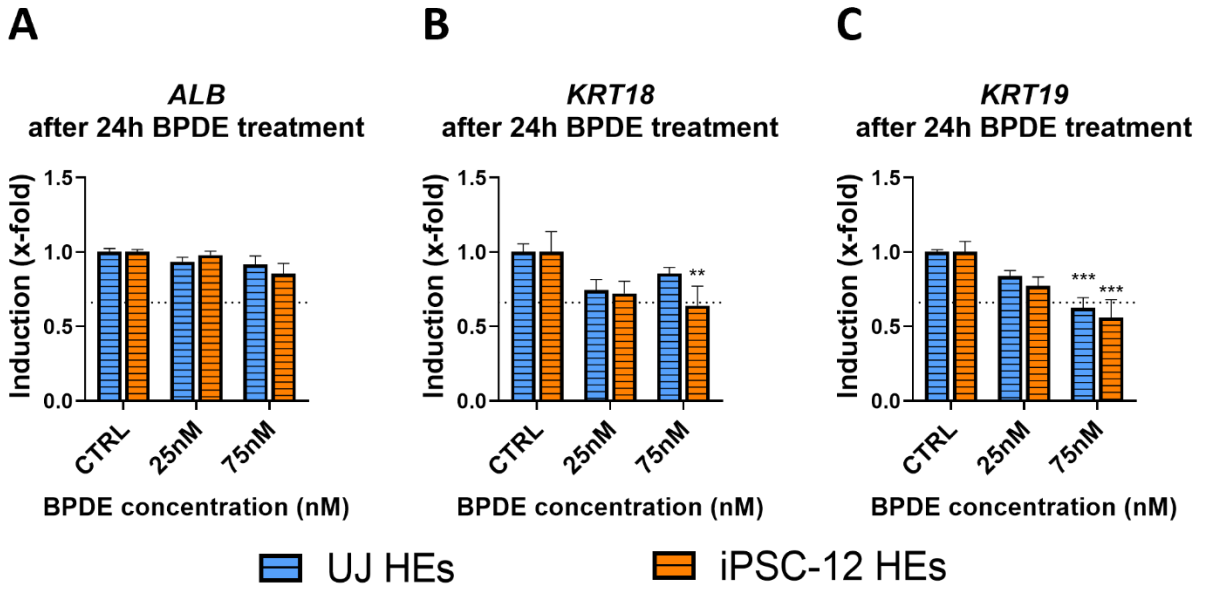

Figure 59: BPDE exposure downregulates *KRT18* and *KRT19* gene expression. HE cells were treated with 25nM and 75nM of BPDE for 24h, then RNA was extracted for qRT-PCR for **(A)** *ALB*, **(B)** *KRT18* and **(C)** *KRT19*. N=3, **p<0.01, ***p<0.001. Error bar depicts 95% confidence interval. Dashed lines mark 0.6-fold.

3.7.3. HE cells have a less pronounced apoptotic response to BPDE when compared to their parental hiPSC lines

Key apoptotic response markers which were evaluated in hiPSCs after BPDE exposure were also investigated in their differentiated HE progeny. In hiPSCs, genotoxic exposure upregulated the gene expression of the extrinsic apoptotic marker *TNFRSF10A* and of the executioner caspase *CASP3*, but no difference was seen after treatment in HE cells (Figure 60A and B). The expression of the intrinsic apoptotic markers *BAX* and *BBC3* were unchanged in both hiPSCs and HE cells (Figure 60C and D). The protein expression of caspase 3 in HE cells was also measured and no change was observed after BPDE treatment (Figure 60E).

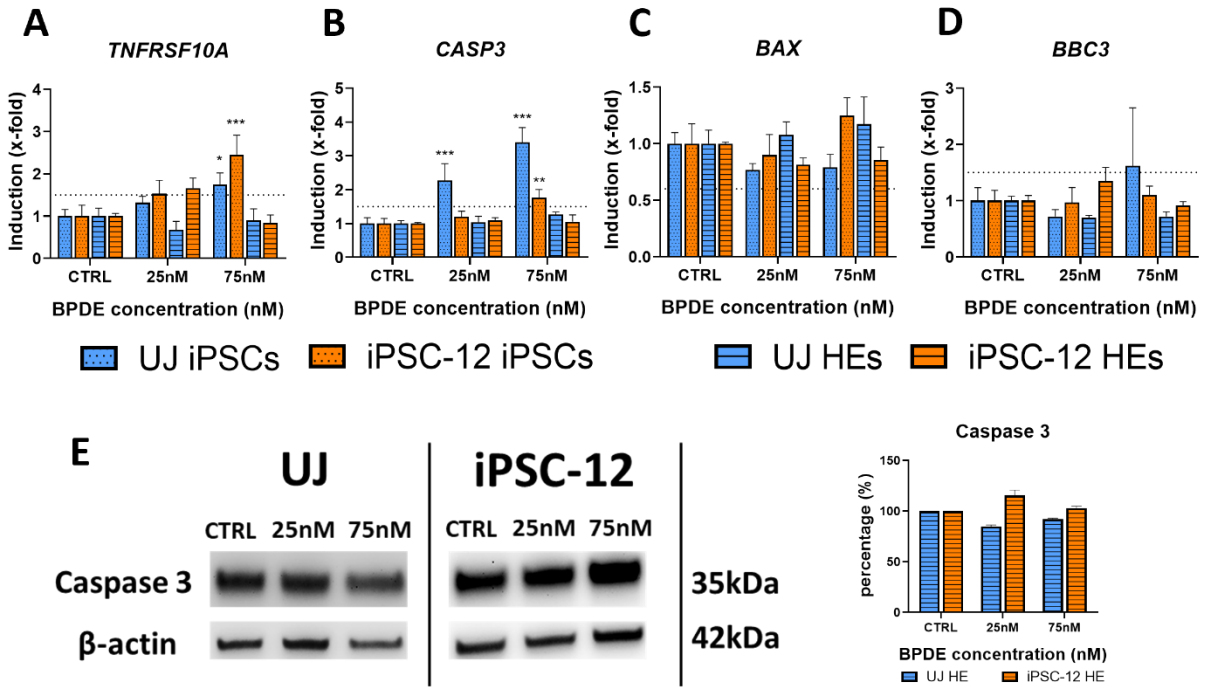

Figure 60: BPDE upregulated genes related to apoptosis in hiPSCs, but not in differentiated HE cells treated with the same concentrations. UJ and iPSC-12 hiPSCs and HE cells were treated with 25nM and 75nM of BPDE for 24h, the RNA was extracted for qRT-PCR and protein for western blot. qRT-PCR for **(A)** *TNFRSF10A*, **(B)** *CASP3*, **(C)** *BAX* and **(D)** *BBC3*. N=3, *p<0.05, **p<0.01, ***p<0.001. Error bar depicts 95% confidence interval. Dashed lines mark 1.5- and 0.6-fold. Western blot for **(E)** caspase 3. N=2, mean +/- standard deviation shown. β-actin was used for loading control.

3.9.4. BPDE exposure upregulates *CHEK2* gene expression in HE cells

Using the results obtained through the microarray analysis of hiPSC exposed to BPDE, as well as information obtained from the literature, selected targets were investigated through qRT-PCR and western blot to evaluate the DNA damage response of HE in comparison to their parental hiPSC lines. Interestingly, the same concentration of genotoxin treatment elicited a different response in hiPSCs than that observed in HE cells. *ATM* was upregulated (mean 1.9- fold) at 25nM in iPSC-12 HE cells (Figure 61A) and, most notably, both tested concentrations of BPDE upregulated by 2 to 4-fold the gene expression of *CHEK2*, exclusively in HE cells (Figure 61B). The expression of *ATR* and *CHEK1* remained unaffected in all lines and concentrations (Figure 61C and D).

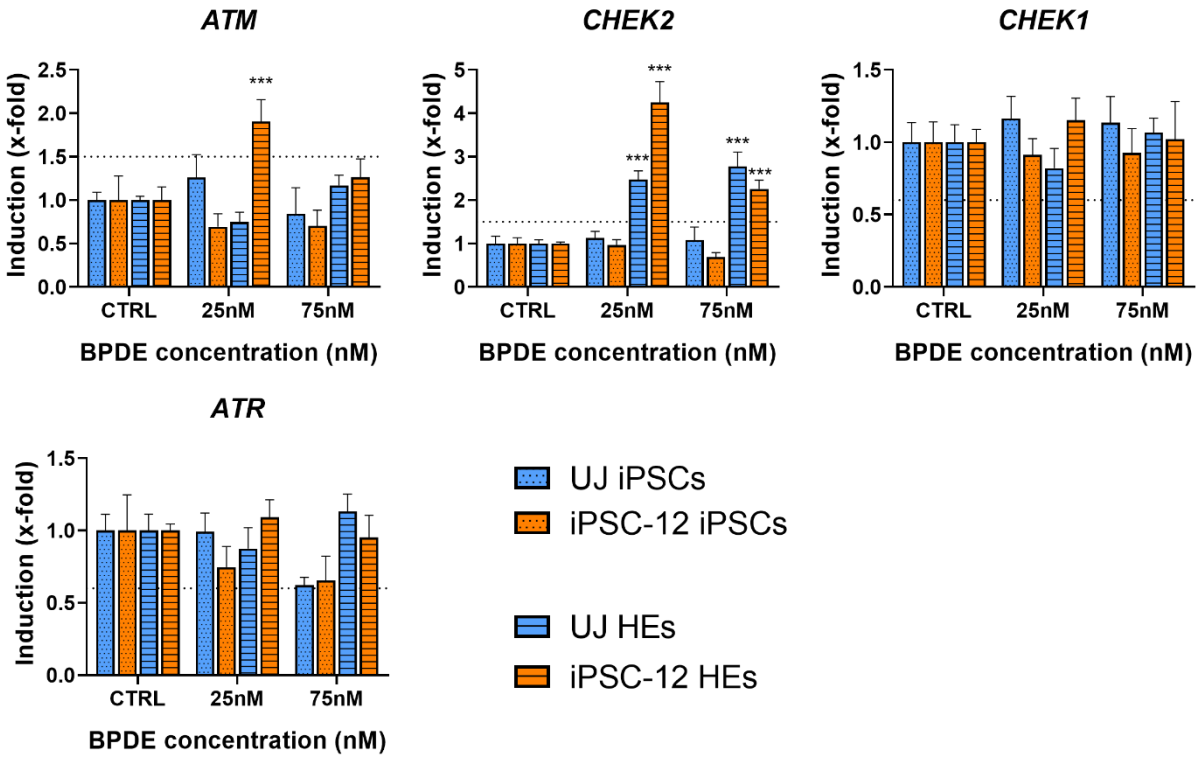

Figure 61: BPDE upregulated *ATM* and *CHEK2* expression in HE cells. UJ and iPSC-12 hiPSCs and HE cells were treated with 25nM and 75nM of BPDE for 24h then RNA was harvested for qRT-PCR for **(A)** *ATM,* **(B)** *CHEK2,* **(C)** *CHEK1,* and **(D)** *ATR.* N=3, ***p<0.001. Error bar depicts 95% confidence interval. Dashed lines mark 1.5- and 0.6-fold.

Next, the gene expression of a known downstream target of *ATM* and *CHEK2*, p53, was measured. *TP53* expression was downregulated in hiPSCs after BPDE exposure but not in HE cells, and the p53 regulators *MDM2* and *cJUN* also had no difference in expression in the HE cells. Additionally, the gene expression of p53-inducible cell cycle regulators *CDKN1A* and *GADD45A* was also unchanged (Figure 62). Western blot for MDM2, p53 and cJUN revealed that the protein levels of these targets also remained constant after BPDE exposure (Figure 63).

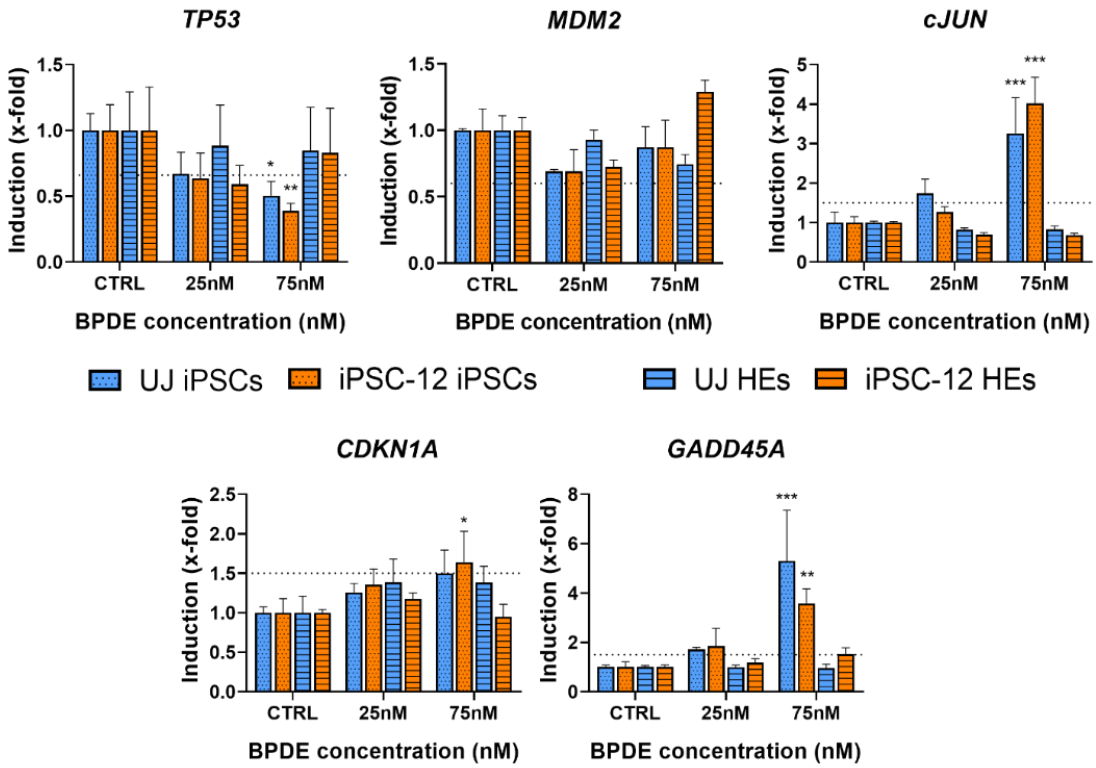

Figure 62: BPDE exposure did not affect the gene expression of genes related to p53-mediated cell cycle regulation in HE cells. UJ and iPSC-12 hiPSCs and HE cells were treated with 25nM and 75nM of BPDE for 24h, then RNA was extracted and used for qRT-PCR of *TP53*, *MDM2*, *cJUN*, *CDKN1A* and *GADD45A*. N=3, *p<0.05, **p<0.01, ***p<0.001. Error bar depicts 95% confidence interval. Dashed lines mark 1.5- and 0.6-fold.

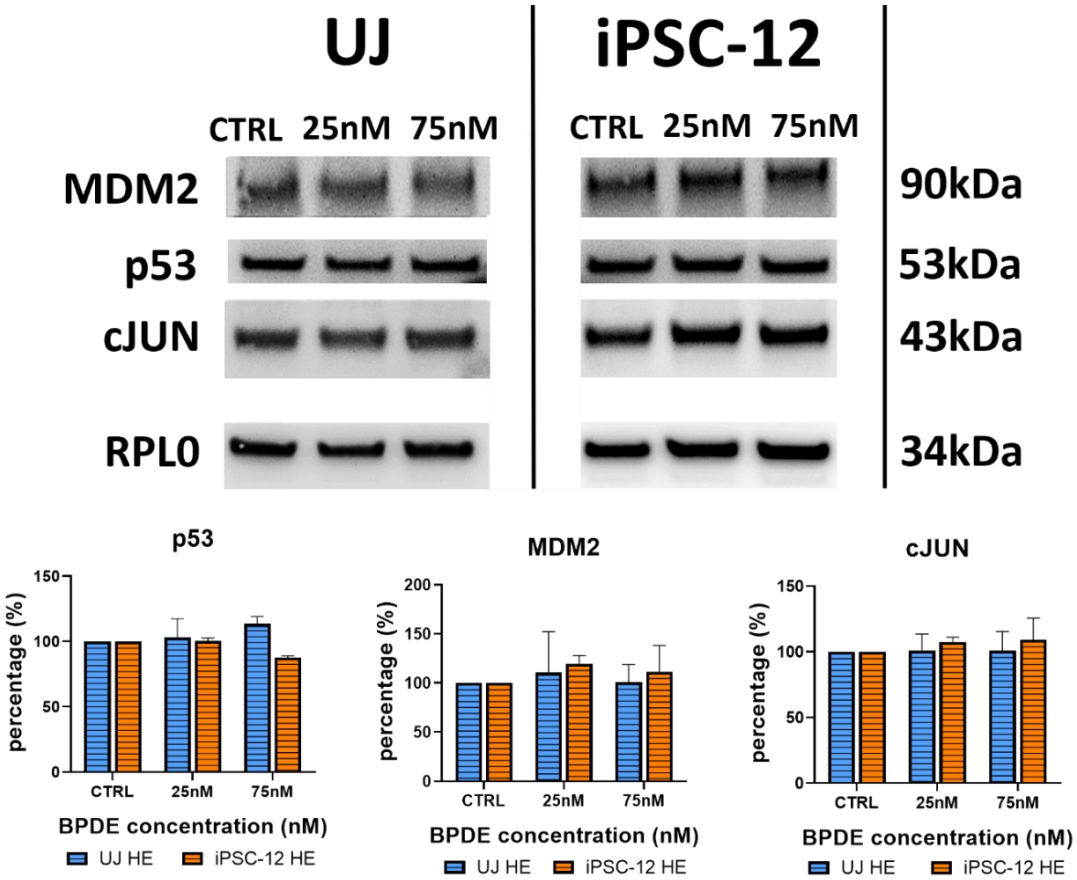

Figure 63: Protein levels of MDM2, p53 and cJUN in HE cells were not affect by BPDE exposure. HE cells were treated with 25nM and 75nM of BPDE for 24h, then protein was extracted and used for western blot for p53, MDM2 and cJUN. N=2, mean +/- standard deviation shown. RPL0 was used for loading control.

Lastly, the expression of *XPC*, *DDB2* and *POLH*, all p53 inducible genes related to bulky adduct repair, was also assessed. *XPC* and *DDB2* had no difference in expression either in hiPSCs or HE cells, but *POLH* was upregulated in both hiPSC lines, but only in iPSC-12 HE cells (1.5- fold). Overall, the same concentration of genotoxin treatment elicited a less pronounced response in HE cells than that observed in hiPSCs, with less regulation of DNA damage response components, although the upregulation of *CHEK2* was only observed in HE cells.

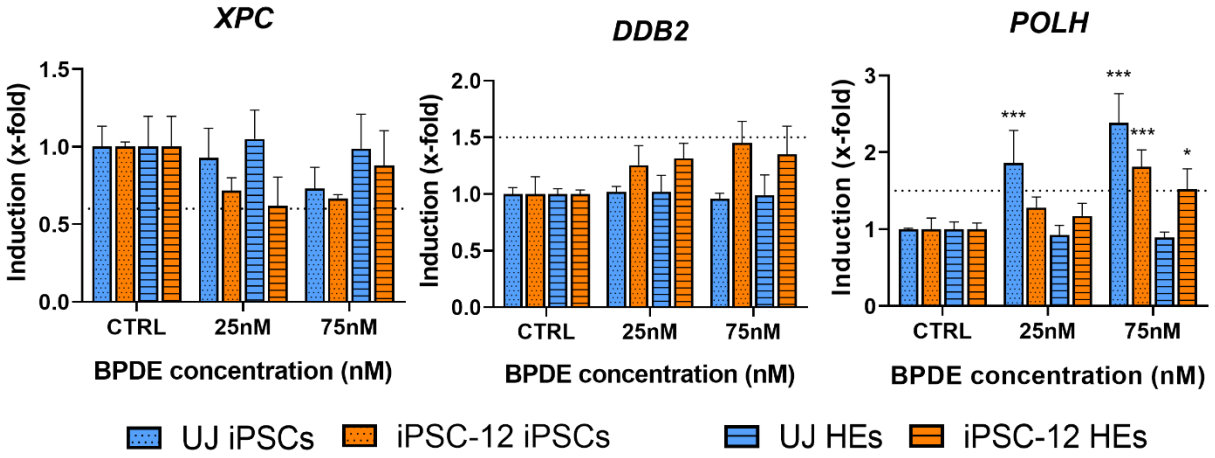

Figure 64: BPDE did not alter the gene expression of p53-inducible DNA repair genes *XPC*, *POLH* and *DDB2* in HE cells. UJ and iPSC-12 hiPSCs and HE cells were treated with 25nM and 75nM of BPDE for 24h, then RNA was extracted and used for qRT-PCR for *XPC*, *DDB2* and *POLH*. N=3, *p<0.05, ***p<0.001. Error bar depicts 95% confidence interval. Dashed lines mark 1.5- and 0.6-fold.

3.8. Effects of BPDE exposure on neuronal cultures derived from UJ hiPSCs

After observing the different responses of hiPSC, NPCs and HE cells to BPDE, UJ hiPSCs were differentiated into pos-mitotic neurons to investigate the effects of BPDE in non-progenitor cells. Since pos-mitotic cells have a less robust DNA damage response than proliferating cells, and with the intent to investigate a longer-term effect of BPDE exposure, UJ neurons were exposed to BPDE for 72h before analysis.

3.8.1. Characterization of neuronal cultures derived from UJ hiPSCs

UJ hiPSC were differentiated into NPCs and subsequently in neuronal cultures following the protocol described on 2.1.4. RNA was isolated at the last day of differentiation and qRT-PCR was done to evaluate the expression of neuron-associated markers, the structural proteins class III beta-tubulin (*TUBB3*, codes for the protein TUJ1) and *MAP2*, as well as the transcription factor RNA binding fox-1 homolog 3 (*RBFOX3*). The gene expression of the pluripotency marker *OCT4* and the NPC marker *PAX6* were also analysed, along with *SOX2*. The neuronal culture gene expression was compared to RNA extracted from UJ NPCs and their parental, undifferentiated hiPSCs were used as control. Neuronal cultures were also immunostained for TUJ1 and MAP2, and two astrocyte markers GFAP and s100b.

OCT4 was downregulated in NPCs and neuronal cultures compared to hiPSC (0.01-fold), while *SOX2* expression remained constant in all cultures. *PAX6* was upregulated by 8000-fold in NPCs and eight times less (1000-fold) in neuronal cultures. In neuronal cultures, *TUBB3* was upregulated 27-fold, *MAP2* 100-fold and *RBFOX3* 40-fold, while the upregulation in NPCs was far more modest at 2-fold, 3-fold, and 1.8-fold respectively (Figure 65).

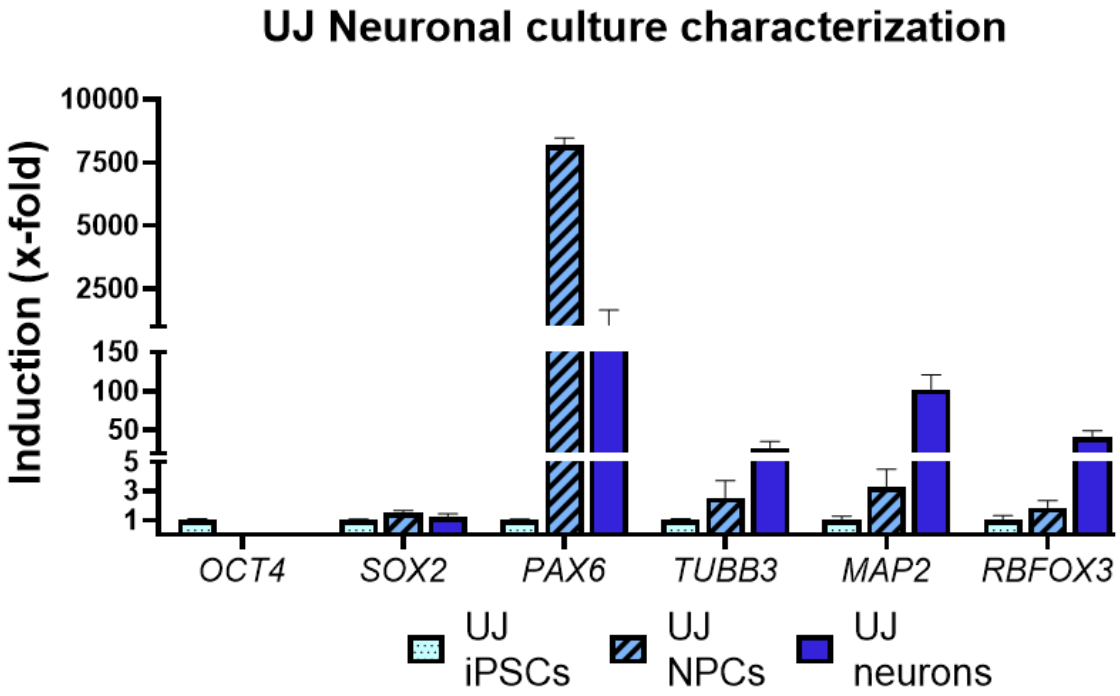

Figure 65: Characterization of hiPSC-derived neuronal cultures. Neuronal culture gene expression was measured and compared to NPCs. Their undifferentiated parental hiPSCs were used as control. qRT PCR for *OCT4*, *TUBB3*, *MAP2, RBFOX3*, *PAX6* and *SOX2*. N=3, Error bar depicts 95% confidence interval. N=3. Error bar depicts 95% confidence interval.

Next, neuronal cultures were immunostained for TUJ1, a marker for immature neurons, and GFAP, a marker for astrocytes. TUJ1 staining revealed neuron clusters with a dense TUJ1+ neuronal network, while no GFAP+ cells could be identified. Staining for MAP2, a marker for mature neurons, and s100b, another astrocyte marker, similarly showed intense MAP2+ arborization and a lack of s100b+ cells (Figure 66).

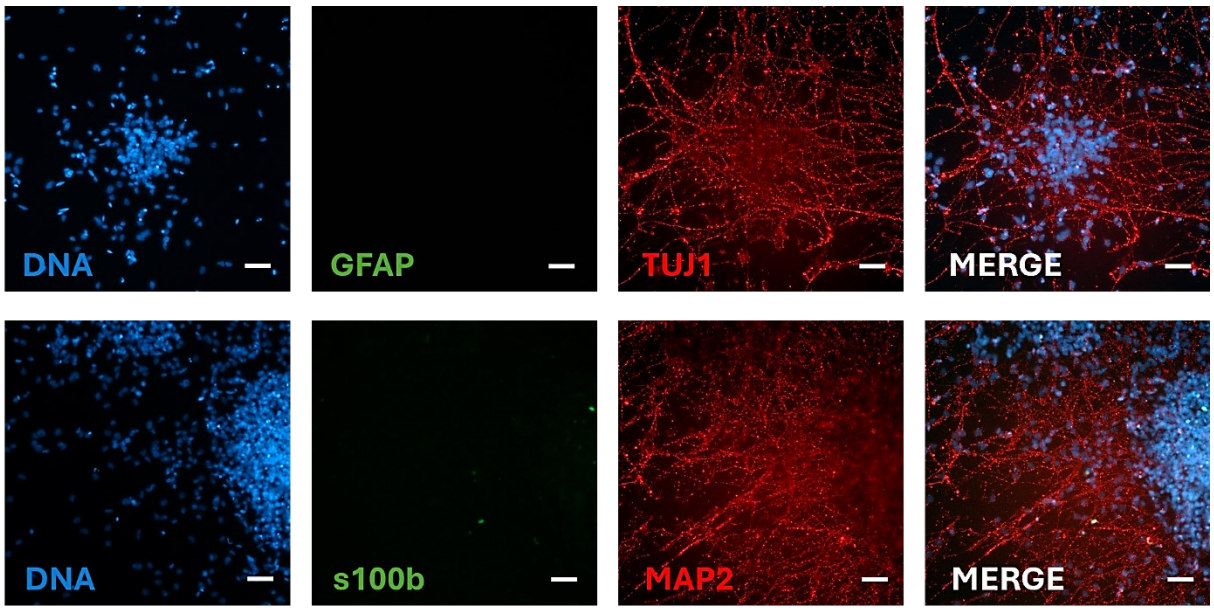

Figure 66: Immunocytochemistry characterization of hiPSC-derived neuronal cultures. Day 14 UJ neuronal cultures were stained for TUJ1, GFAP, MAP2 and s100b. Cultures showed a network of TUJ1+ and MAP2+ cells and no presence of GFAP+ or S100B+ cells. Scale bar 50µm.

3.8.2. BPDE upregulated targets related to the intrinsic apoptotic pathway in neuronal cultures

Apoptotic targets involved in the extrinsic and intrinsic apoptotic pathways, as well as the executioner caspase caspase 3 had their gene expression measured through qRT-PCR after 72h of BPDE exposure. The expression levels of the extrinsic apoptotic marker *TNFRSF10A* remained unchanged after treatment, and the same was observed with *CASP3*. Conversely, the intrinsic apoptosis markers *BAX* and *BBC3* were upregulated after treatment by 1.8-fold and 1.7-fold respectively (Figure 67).

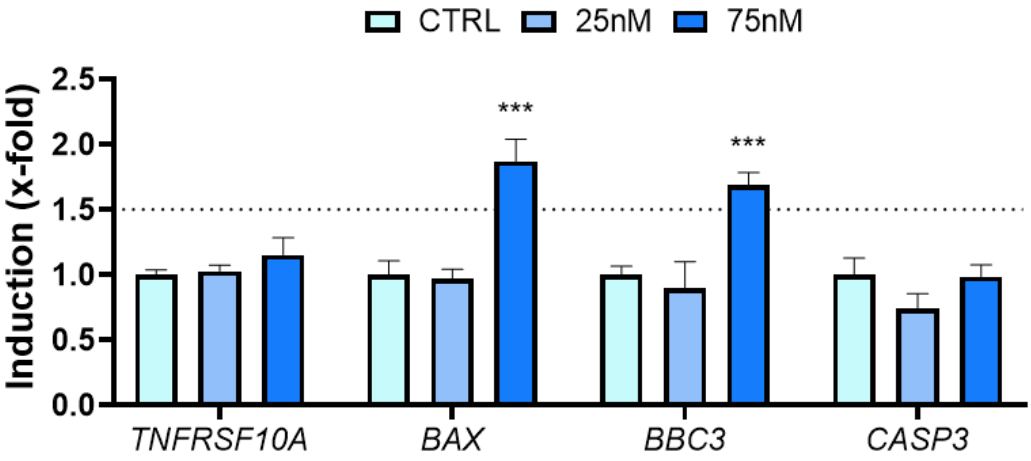

Figure 67: BPDE upregulated the gene expression of intrinsic apoptosis genes in neuronal cultures. Day 14 UJ neuronal cultures were treated with BPDE for 72h and had their RNA extracted for qRT-PCR analysis for *BAX*, *BBC3*, *TNFRSF10A* and *CASP3*. N=3, ***p<0.001. Error bar depicts 95% confidence interval. Dashed lines mark 1.5-fold.

Next, the protein expression of caspase 3 and its active form cleaved caspase 3 were also assessed. BPDE exposure did not influence the expression of caspase 3, but upregulated cleaved caspase 3 (Figure 68).

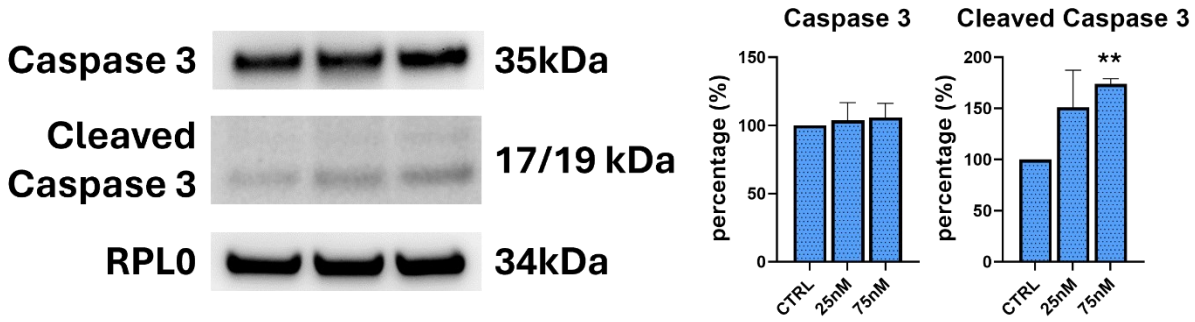

Figure 68: Cleaved caspase 3 was upregulated in neuronal cultures after BPDE exposure. Day 14 UJ neuronal cultures were treated with BPDE for 72h and had their protein extracted for western blot analysis of caspase 3 and cleaved caspase 3. RPL0 was used as loading control. N=2, **p<0.01. +/- standard deviation shown.

3.8.3. BPDE exposure upregulates targets related to the p53-mediated DNA damage response in neuronal cultures

With the intention of evaluating the p53-mediated response to BPDE, the gene expression of *TP53*, as well as that of two p53 regulators, *MDM2* and *cJUN*, were measured. Both TP53 and cJUN gene expression was stable after treatment, while MDM2 was upregulated (mean 1.5- fold) (Figure 69A). The protein levels of these targets were measured and corroborated with the results seen in the qRT-PCR, with the expression of p53 and cJUN remaining stable, while MDM2 expression was increased (Figure 69B).

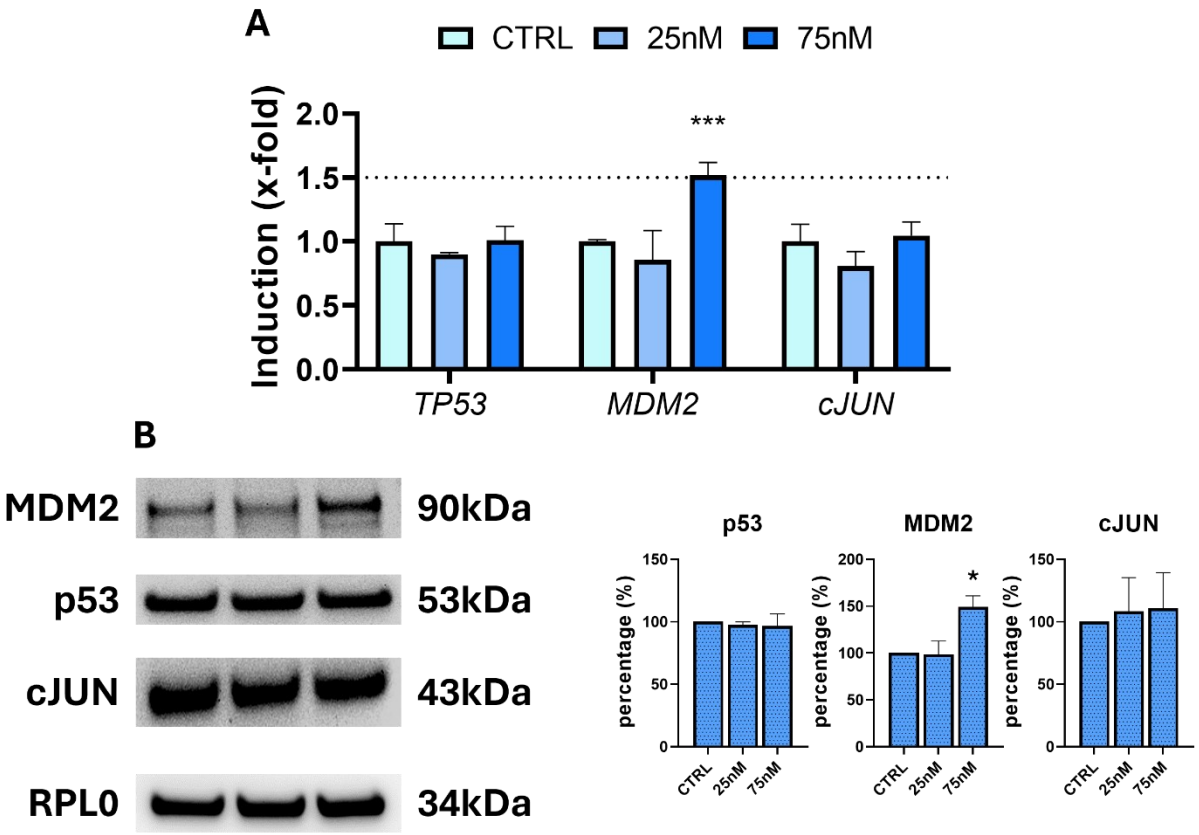

Figure 69: BPDE upregulated the gene and protein expression of MDM2 in neuronal cultures but had no effect on p53 or cJUN expression. Day 14 UJ neuronal cultures were treated with BPDE for 72h and had their RNA and protein extracted for qRT-PCR and western blot analysis. **(A)** qRT-PCR for *MDM2*, *TP53* and *cJUN*. N=3, *p<0.001. Error bar depicts 95% confidence interval. Dashed lines mark 1.5-fold. **(B)** Western blot for MDM2, p53 and cJUN. RPL0 was used as loading control. N=2, *p<0.05. +/- standard deviation shown.

Next, the gene expression of four known upstream targets in the p53-mediated DNA damage cascade were investigated, *ATR*, *ATM*, *CHEK1* and *CHEK2*. The first three genes did not change their expression after BPDE treatment, but the kinase CHEK2 was upregulated (1.5-fold) in both tested concentrations (Figure 70).

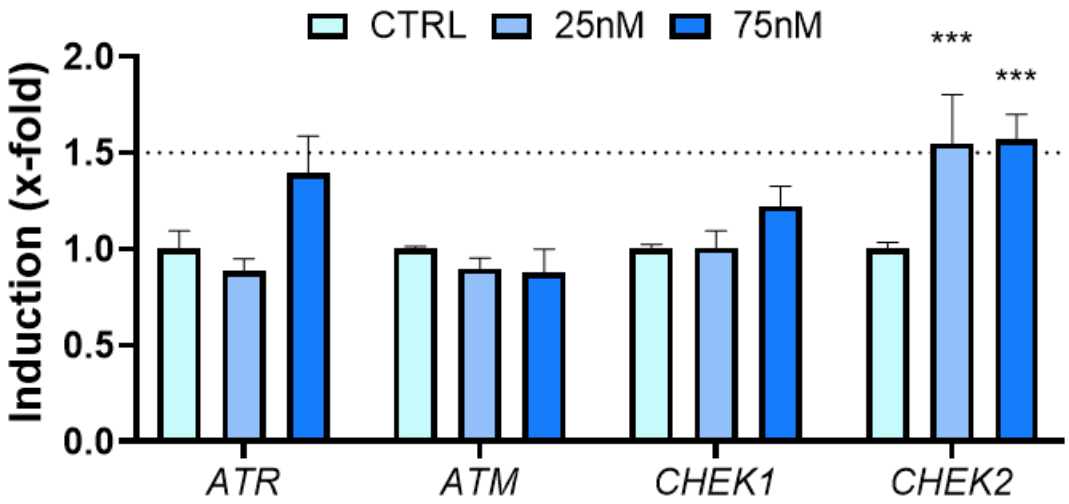

Figure 70: BPDE upregulated the gene expression of *CHEK2* in neuronal cultures. Day 14 UJ neuronal cultures were treated with BPDE for 72h and had their RNA extracted for qRT-PCR analysis for *ATR*, *ATM, CHEK1* and *CHEK2*. N=3, ***p<0.001. Error bar depicts 95% confidence interval. Dashed lines marks 1.5-fold.

CHEK2 is an important player in cell cycle regulation after DNA damage response and it has also been linked to senescence. Therefore, we assessed the gene expression of *CDKN1A* and *GADD45A*, which are p53 targets that have been associated with both cell cycle regulation and senescence after cellular DNA damage (220,221). qRT-PCR revealed the upregulation of *CDKN1A* expression (2.5-fold) after 75nM of BPDE exposure, but no difference in *GADD45A* levels (Figure 71).

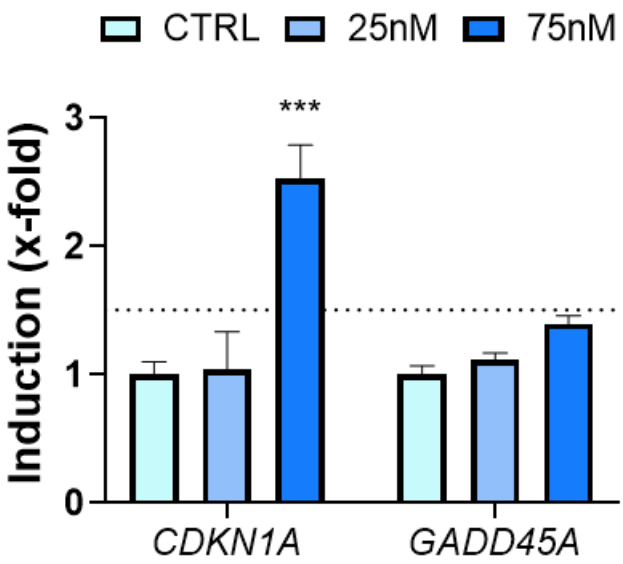

Figure 71: Exposure to BPDE upregulated the gene expression of *CDKN1A* in neuronal cultures. Day 14 UJ neuronal cultures were treated with BPDE for 72h and had their RNA extracted for qRT-PCR analysis for *CDKN1A* and *GADD45A*. N=3, ***p<0.001. Error bar depicts 95% confidence interval. Dashed line mark 1.5-fold.

Lastly, to investigate the p53-mediated bulky DNA repair response of neuronal cultures after BPDE exposure., the gene expression of *POLH*, *XPC* and *DDB2* was measured. The TLS DNA polymerase *POLH* did not differ in expression after BPDE treatment, while the NER components *XPC* and *DDB2* were upregulated in a dose-dependent manner, with the highest BPDE concentration inducing a 3-fold upregulation of XPC and a 2.2-fold upregulation of DDB2 (Figure 72).

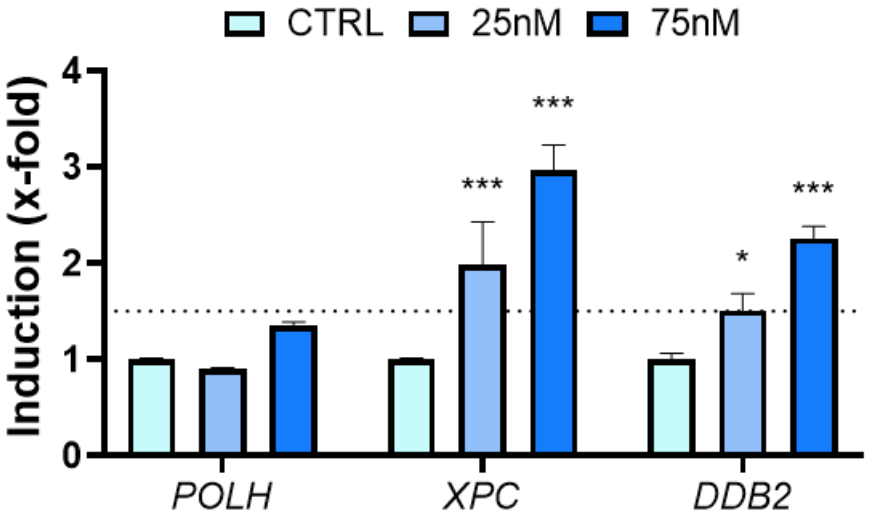

Figure 72: BPDE upregulated the gene expression of *XPC* and *DDB2* in a concetration-dependent manner in neuronal cultures. Day 14 UJ neuronal cultures were treated with BPDE for 72h and had their RNA extracted for qRT-PCR analysis. The levels of *POLH* remained stable after treatment, while *XPC* and *DDB2* were upregulated in both tested concentrations. N=3, ***p<0.001. Error bar depicts 95% confidence interval. Dashed line marks 1.5-fold.

3.9. Summary of results from BPDE exposure experiments in hiPSCs and their differentiated progeny

Different cell types react differently to genotoxic exposure; therefore, this study evaluated the effects of the genotoxin BPDE in hiPSCs and their differentiated progeny of NPCs, HE cells and neurons. Additionally, the effects of BPDE on hiPSC and NPCs with an NBN-impairment and how it differed from the effects on WT cells were also assessed. Microarray analysis was conducted in NBS patient-derived and WT hiPSCs exposed to BPDE. Those results, together with the available literature of the effects of BPDE in other cell types, gave us a set of targets to investigate at the mRNA and protein level. The results are summarized in Figure 73 and Figure 74.

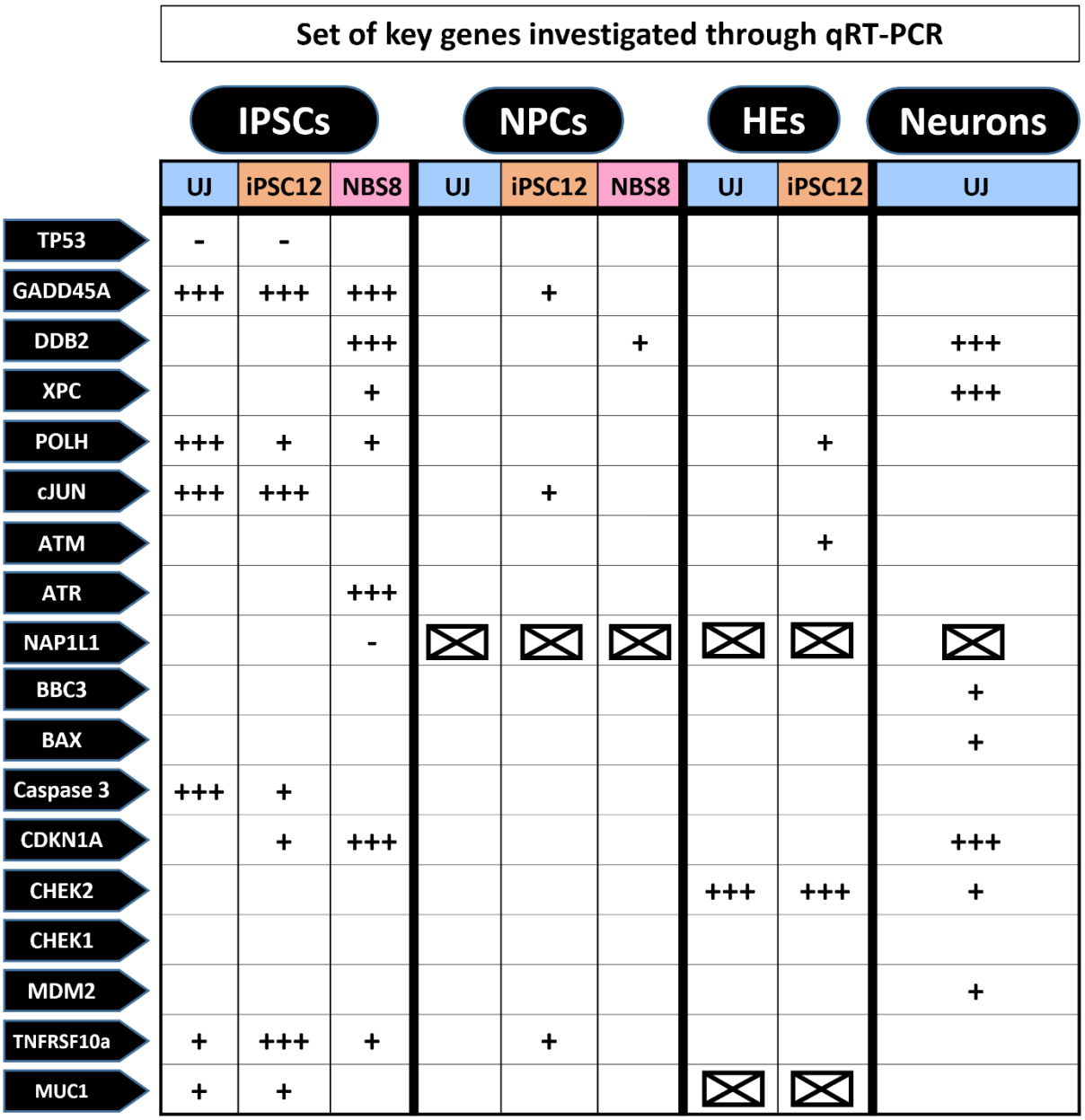

Symbols key	
+++	>2.0x -fold
+	>1.5x -fold
-	< 0.6x -fold

Figure 73: Summary table of results from the set of genes investigated after BPDE exposure. Cells were exposed to BPDE in the concentrations of 25nM and 75nM for 24h or, in the case of neuronal cultures, 72h. Then, their RNA was extracted and used for qRT-PCR. The table summarizes the results obtained from the investigation of known BPDE targets as seen on the literature and those that were identified as BPDE targets through microarray analysis of BPDE exposed hiPSCs. Empty cells indicate no change in expression. One and two crosses indicate over 1.5x -fold or over 2x -fold increase in expression compared to control, respectively. The minus sign indicates a downregulation of at least less than 0.6x -fold. Blocked cells indicates that the target was not investigated in that cell line.

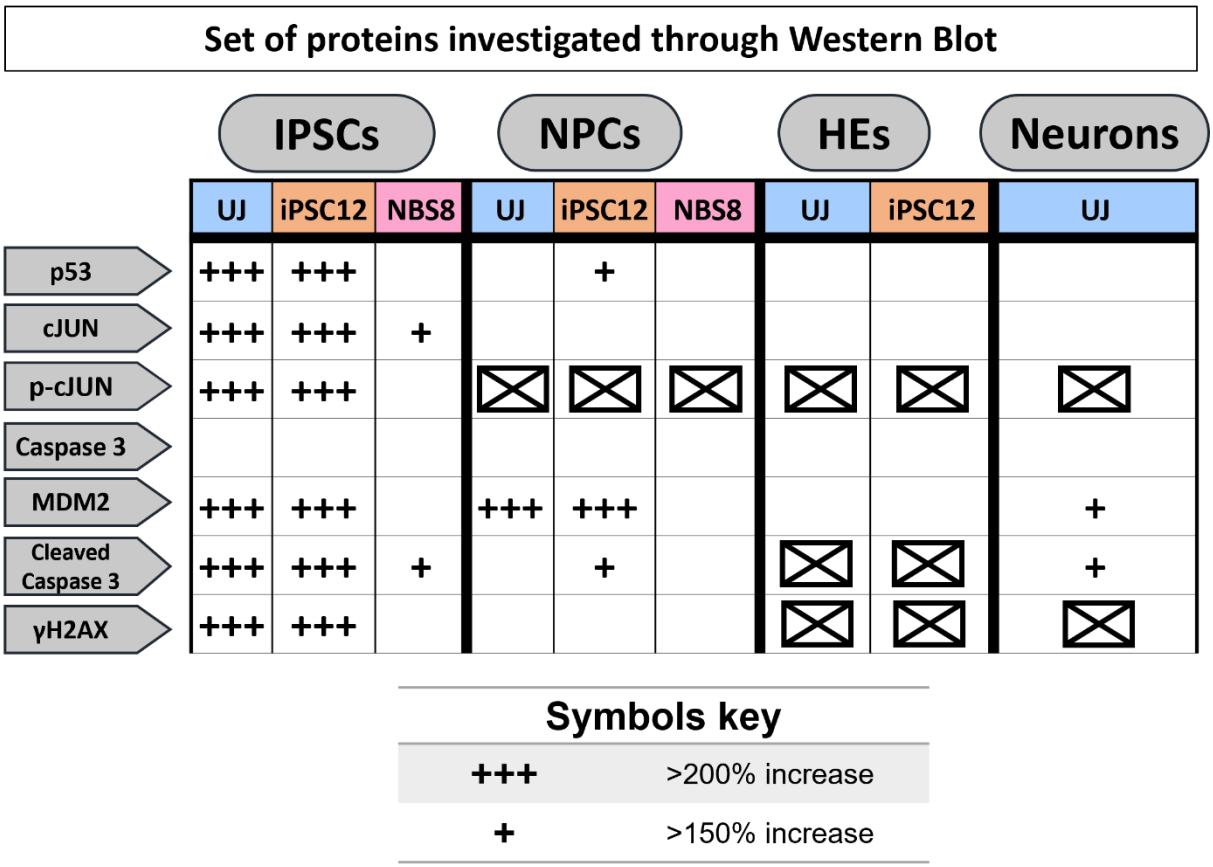

Figure 74: Summary table of results from the set of proteins investigated after BPDE exposure. Cells were exposed to BPDE in the concentrations of 25nM and 75nM for 24h or, in the case of neuronal cultures, 72h. Then, their protein was extracted and used for western blot. The table summarizes the results obtained from the investigation of proteins related to the DNA damage response. Empty cells indicate no change in expression. One and two crosses indicate over 150% or over 200% increase in protein expression compared to control, respectively. Blocked cells indicates that the target was not investigated in that cell line.

An observation from the summary is that NBS8 cells, particularly NBS8 hiPSCs, present a different DNA damage response upon BPDE exposure than their WT counterparts. For example, NBS8 hiPSCs upregulate the mRNA expression of *XPC* and I, genes involved in NER, while showing a lesser upregulation of targets involved in the apoptotic response such as cleaved caspase 3. Secondly, the different cell types have a differentiated response to BPDE exposure. hiPSCs have generally a more robust DNA damage response, with the regulation of several targets related to cell cycle checkpoint, apoptosis, and DNA damage repair. NPCs had a very moderate response, as did HE cells. Neuronal cultures which were exposed to BPDE for 72h had a focused response of NER, cell cycle regulators and intrinsic apoptosis markers which more closely resembles that of a classic BPDE response observed in the literature in other somatic cells.

4. Discussion

4.1. Discussion of results from NBS2 line stabilization and characterization

The reprogramming of fibroblasts of NBS patients into iPSCs suffers from many hurdles due to the genomic instability of the fibroblasts and their tendency to enter premature senescence in culture. Roughly only 1 in 10 attempts of reprogramming are successful (167). The NBS2 line reprogramming was paused early in development due to the difficulty in keeping the reprogrammed cells alive and in their iPSC state.

Cell culture passaging techniques can have a huge impact on culture quality, particularly for pluripotent stem cells. An optimized passaging protocol can reduce DNA damage and apoptosis, increasing cell survival and stability (222). We tried different reagents for cell passaging, both enzyme-based (accutase and TrypLE) and non-enzyme based (PBS and ReLeSR) (Figure 11). The enzyme-based methods were associated with the use of Y-27632, an inhibitor of Rho kinase (ROCK) activity which has been reported to enhance cell survival and colony formation of ESCs and iPSCs (206,223). The best results were obtained with the use of ReLeSR, a reagent that allows for cell passaging without the need for centrifugation or cell scraping, therefore reducing the need for cell manipulation. Furthermore, it also selectively dissociates iPSCs, helping to separate them from differentiated cells.

The subsequent immunocytochemistry characterization of NBS2 iPSCs confirmed the presence of key pluripotency markers in most cells (Figure 12). However, the karyotype of these cells revealed the presence of a partial trisomy on the long arm of chromosome 1 (1q trisomy) (Figure 13). Patients with a partial 1q trisomy are rare and often present dysmorphic features, severe psychomotor retardation, heart defects and intellectual disability. It is suspected that this phenotype is partially caused by dysregulated WTN signaling (224). While the karyotype of the parental fibroblast that gave rise to the NBS2 line could not be obtained, the Institute for Medical Genetics - Charité Berlin, did not report that the donor of the fibroblasts had the severe phenotype associated with the mutation. This makes it likely that the mutation was acquired during the reprograming process.

Due to the severity of the phenotype associated with the mutation and our inability to stabilize another, non-mutated clone, the NBS2 line was not characterized further, and its development was discontinued.

4.2. Discussion of results from difficulties in the neurodifferentiation of NBS-impaired iPSC lines

Among the clinical manifestations of NBS, progressive microcephaly is one of the most striking (166) and studying its etiology has helped scientists to identify the roles of the Nibrin protein in nervous system homeostasis and development.

Highly proliferative neuroprogenitors generate elevated levels of DNA damage and thus, require a functional DNA damage repair machinery. Accumulation of DNA damage due to defective repair can lead to ceased proliferation and apoptosis (225). Our attempts to generate NPCs from an NBS patient-derived iPSC line reinforces that notion. NBS8 NPCs suffered from excessive death and low proliferation rates (Figure 14A), consistent with findings that show that NBN has a prominent role in the proliferation and homeostasis of neuroprogenitors (226,227). The expansion of NPCs as 3D floating spheres has been reported to have increased efficiency (228) and in the case of NBS8 NPCs, it was capable of partially overcoming the low expansion efficiency of the 2D culture method (Figure 14B).

The further differentiation of NBS8 NPCs into 2D neuronal cultures was severely impaired. iPSC-derived NPCs can be differentiated into cortical lineage neurons through culturing with different neurotrophic factors, forming neuronal networks and expressing characteristic markers like TUJ1 and MAP2 (66,229). During the differentiation into neuronal cultures, WT cells showed progressive neuronal formation and arborization, visible both in brightfield microscopy (Figure 15 A and B) and through immunocytochemistry for TUJ1 and MAP2 (Figure 16 A and C). NBS8 cultures, on the other hand, developed almost no visible arborization or network formation (Figure 15 C and D) and had very few TUJ1+ cells (Figure 16 B). The NBS8 culture had extensive MAP2 staining, but the MAP2+ cells showed abnormal morphology and virtually no neurite formation (Figure 16D). Several studies regarding NBN function in neurodevelopment help explain this phenotype. Research done on iPSC models derived from NBS patients reveals transcriptional dysregulation in NBS-NPCs when compared to WT-NPCs, with the downregulation of dozens of genes related to neural system development and neurogenesis (51). In that same vein, hiPSC-derived NBS

cerebral organoids are smaller than their WT counterparts, suffering with disrupted cyto-architecture and premature differentiation (170). Moreover, NBN is important during neurodevelopment in both migrating and post-mitotic neurons in ways which are independent to DNA damage repair. Nbn deletion compromises neurite arborization in post-mitotic neurons and neuronal migration through the cortical layers during mice development, due to a dysregulation of the Notch signaling pathway (230). The evidence suggests that NBS8 NPCs in culture have difficulty generating viable and morphologically typical neurons due to a combination of transcriptional dysregulation of neurogenesis and aberrant Notch activity.

4.3. Discussion of results from effects of BPDE on the viability of cerebral organoids derived from WT- and NBS8 iPSCs

hiPCS have enormous potential when it comes to disease modelling. While some hurdles still haven't been surpassed, such as differentiation bias due to poor epigenetic reprogramming and the difficulties in modelling mature, adult-like cells (16,20), the advantages are undeniable, particularly the generation of cells with the genetic background of specific diseases (14).

Our lab has previously generated cerebral organoids from iPSCs derived from NBS patients, which recapitulated certain aspects of the disease (170). We attempted to investigate the effects of BPDE in the same model. At day 20, our cerebral organoids showed neural rosettes composed of neuroprogenitors and the formation of a cortical plate of neurons. We identified that the NBS8 organoids were smaller than their WT counterparts by about 25%, a phenomenon observed before in NBS-derived iPSC cerebral organoids (Martins et al., 2022).

Since there are no experiments in the literature using BPDE on 3D *in vitro* cultures, the doses used on the cell viability assay were based on data from 2D cultures of somatic cells (213). NBS8 organoids showed 25% loss of viability after 72h of exposure to the highest dose of 100μM of BPDE and on brightfield microscope the outer cell layer of the NBS8 organoids was surrounded by debris. WT organoids, on the other hand, suffered no detectable loss of viability in any of the concentrations. Since the NBS8 organoids were 25% smaller than the WT ones, there was a concern that any differential effects that could be observed from BPDE treatment were due mostly to their difference in size and the possibility that BPDE could diffuse better through the

smaller organoids. It is a known problem that cerebral organoids often suffer from poor diffusion, which can lead to necrotic cores due to oxygen and nutrients not being able to reach the inner organoid (231). In a living organism, B[a]p and its metabolites can travel through the circulatory system to reach cells in the whole body (127–129), but our organoids lack vascularization. These factors led our cerebral organoid model to be deemed not suitable for investigating the effects of BPDE exposure.

4.4. Discussion of results from basal expression of genes related to the genotoxic exposure response in healthy and NBS-patient derived hiPSC, and human fibroblasts

Cells which suffer from NBN-impairment, such as those derived from NBS patients, have a disturbed response to genotoxic exposure, with a delayed CHEK2- and p53-mediated DNA damage response (169,232). Moreover, in control conditions, these cells have been reported to have downregulated transcription pathways related to cell cycle, mitosis and apoptosis inducing genes, while having upregulation of pathways related to mitosis- and apoptosis-inhibiting genes (51,167).

Using a focused qRT-PCR array, we investigated the gene expression levels in NBS8 hiPSCs of 76 genes involved in different aspects of the response to genotoxic agents and compared them to WT hiPSCs. In general, the expression of these markers remained similar between the mutated and WT lines, with only 8 genes identified as differentially regulated genes (Figure 19). 2 of the 4 downregulated genes in NBS8 hiPSCs, *CALCR*, and *DDIT3,* are known positive regulators of apoptosis (209,210), agreeing with previous results that suggest NBS hiPSCs have deficient pro-apoptotic signalling (51), but *FAS*, a death receptor which plays an important role in extrinsic apoptosis (233), was upregulated, although it is worth noting that non-apoptotic functions of this protein have recently been described in stem cells (234,235) (Solodeev et al., 2018; Rippo et al., 2013). *GADD45A*, which was also downregulated, is a protein with diverse functions. It has been implicated as enhancing the reprograming efficiency of somatic cells into iPSCs (236). Upon genotoxic stress, it assumes multiple roles related to cell cycle arrest, DNA repair and apoptosis (237,238). The last downregulated gene, *ABCG2*, is a xenobiotic transporter and key player in the resistance to genotoxic compounds in many cancer cell types (239), which could play a role in exacerbating NBS8 cells deficient genotoxic exposure response. However,

HSP1B and *XRCC4*, both involved in DSBR, were upregulated, which may hint at a compensatory mechanism against NBS hiPSCs deficient DSBR (51).

The DNA damage response (DDR) machinery is of extreme importance in stem cells as it allows for highly proliferative progenitors to maintain their genomic integrity during endogenous and exogenous DNA damaging episodes (240). Pluripotent stem cells in particular have shown to have higher base levels of gene expression of DDR genes, particularly those involved in DSBR, than terminally differentiated and even progenitor cells such as bone marrow stromal cells, osteoclasts and fibroblasts (241–243).

To further our understanding of the differences in the DDR between hiPSCs and differentiated cells, the focused array was also performed with normal human dermal fibroblasts (NHDF), and the results were compared to the two hiPSC lines (Figure 20). 28 genes were found to be differentially regulated. *CDKN1A* is a cell cycle regulator that negatively regulates the transition to the G1 and S phases. The highly proliferative state of pluripotent stem cells is maintained partially through *CDKN1A* repression (244), and accordingly, the two hiPSC lines had much lower expression of this gene. Conversely, they also had a much higher expression of *CDC25A*, a key positive regulator of cyclin-dependent kinases and promoter of all active phases of the cell cycle (245) (Shen and Huang, 2012). This suggests that the proliferation difficulties of NBS-hiPSCs are not directly related to *CDKN1A* or *CDC25A* transcriptional dysregulation. Interestingly, the levels of *TP73*, but not its homolog, *TP53* (Supplementary Figure 2), were also upregulated in hiPSCs. P53 overexpression is well-known for inducing differentiation of pluripotent stem cells (246), but the role of p73 in these cells is poorly understood, although previous research has shown that overexpression of p73 can enhance hiPSC generation and that cells generated in this way are resistant to differentiation (247).

The 25 other genes which were found to be upregulated in hiPSCs are all implicated in DNA damage repair, more specifically in DSBR, BER, MMR, NER and TLS. 11 of them are involved in DSBR, a pathway known to be particularly effective in stem cells (248). 5 components of the BER pathway were also upregulated, as well as two components of the MMR pathway and 4 genes related to the response to bulky DNA adducts. These results corroborate with hESC and hiPSC data found in the literature (241–243) and indicate that our hiPSCs, regardless of the presence or absence of an

NBS mutation, possess a more robust DNA damage response in several pathways than NHDF.

4.5. Discussion of results from effects of BPDE exposure on healthy and NBS-patient derived hiPSCs

B[a]p is an important environmental contaminant. Its most carcinogenic metabolite, BPDE, has been reported as forming DNA-adducts in human eggs and sperm, and those adducts can be paternally transmitted to the embryo (116–118). Moreover, B[a]p can be carried through the maternal circulatory system to reach the developing embryo, which are themselves metabolically capable (110,111). Despite that, the potential harmful effects of BPDE exposure on stem cells, and particularly ESCs, are poorly understood. In this study we sought to clarify the effects of BPDE exposure on ESCs by utilizing a hiPSC model. Furthermore, we also investigated BPDE effects on hiPSCs derived from NBS patients, which are deficient in DNA damage repair.

To assess the kinetics of BPDE-DNA adducts formation and repair, a southern blot using an anti-BPDE-DNA adduct antibody was performed (Figure 21) according to a previously described protocol (213). It was unsuccessful, however, showing staining at control conditions and no difference in band intensity after BPDE treatment. Extensive testing of the antibody in different staining conditions was carried out but the issue persisted (Figure 22). Since BPDE treatment elicited a response at the mRNA and protein level consistent with DNA damage response and repair of bulky adducts in different cell types (as shown in the subsequent results), it was concluded that the antibody is binding non-specifically to DNA.

BPDE stimulates the transcription of DDR genes and evokes the DNA damage repair machinery in exposed somatic cells, particularly of processes related to cell cycle regulation, inflammation, NER , cancer onset and apoptosis. To elucidate the effects of BPDE on hiPSCs at the transcriptional level, we performed for the first time a whole-genome transcriptomic analysis of hiPSCs, both WT (UJ and iPSC-12) and NBS patient-derived (NBS8), exposed to BPDE. The bioinformatics analysis of the resulting dataset revealed GOs and KEGG pathways which were regulated after BPDE treatment in hiPSCs, but also differentially regulated between WT and mutant cells.

The GO analysis of genes which were upregulated after BPDE exposure on hiPSCs revealed several upregulated clusters regarding both positive and negative regulation

of apoptosis (Figure 25). Curiously, while reports of BPDE exposure on somatic cells reported the upregulation of the intrinsic apoptotic pathway, and genes such as *BAX* and *BBC3* (249–251), hiPSCs showed a distinct upregulation of the extrinsic apoptotic pathway, confirmed through qRT-PCR (Figure 26 A, B and C). Closer examination of the cell death response, however, revealed some interesting differences between the WT and mutant lines. Upon BPDE exposure, the ic50 of NBS8 hiPSCs was double that of the WT lines (Figure 24). It was also observed that, although the gene expression of *TNFRSF10A* was upregulated in all three cell lines, the expression of the executioner caspase *CASP3* was only upregulated in WT cells, and the same was observed in the protein expression of cleaved caspase 3, the active form of the caspase 3 protein (Figure 26). NBN-impaired cells have been reported as having deficient cell cycle and apoptosis regulation (51,167) (Halevy et al., 2016; Mlody et al., 2017), which translates into a delayed genotoxic exposure response, with suboptimal cell cycle arrest that leads to deficient apoptotic response and continued proliferation after DNA damage (51,169,232) and the results seen here seem in agreement with a disturbed apoptotic response in the NBS8 hiPSCs.

Although the occurrence of unresolved DNA damage is detrimental to all cells, it is particularly catastrophic in stem cells, since it can result in the stabilization and fast propagation of mutants and lead to malignancies (240). As was already mentioned, pluripotent stem cells have highly efficient DNA repair systems, but in case of failure to repair DNA lesions they will either rapidly undergo apoptosis (252) or suffer a p53-mediated loss of pluripotency by repressing the transcription factors OCT4 and NANOG, as well activating genes associated with differentiation (253,254).

Interestingly, our results show that 24h of BPDE exposure on hiPSCs did not influence the gene expression of *OCT4* and *NANOG*, or that of targets associated with triggering differentiation such as *BMP4* or *GREM1* (Figure 27 A and B). The nuclear expression of OCT4 also remained stable (Figure 27C). This suggests that our cells retained their pluripotency for at least 24h after BPDE exposure. Momcilovic et al. observed similar results in hiPSCs exposed to γ-irradiation, indicating that this is not an occurrence restricted only to BPDE as a genotoxic agent (242).

BPDE treatment has been documented to induce cell cycle arrest, although the exact nature of the arrest seems dependent on the treatment dose, the cell type, and the phase in the cell cycle that the cells were in at the start of treatment (213,255,256).

The GOs of hiPSC exposed to BPDE revealed an upregulated cluster related to DNA damage-induced cell cycle arrest, where *CDKN1A*, *MUC1*, *PRAP1* and *PLK2* were present (Figure 28). Further analysis was conducted and showed that *CDKN1A* and *MUC1*, a p53-associated cell cycle regulator (257), were differentially regulated in the WT and mutant lines after BPDE exposure (Figure 29), lending support to the reports of perturbed cell cycle arrested signalling after genotoxic exposure in NBN-impaired cells (51,169,232). *GADD45A*, on the other hand, was upregulated in all cell lines after treatment. GADD45A is known to stimulate cell cycle arrest upon genotoxic exposure (258,259) and it is also a documented component of the NER pathway and important for the repair of bulky DNA adducts (260–262). But, despite BPDE exposure inducing the upregulation of cell cycle arrest-related genes, Ki67 stainings (Figure 30), EdU incorporation assays (Figure 31) and cell cycle analysis via flow cytometry for PI (Figure 32) all indicated that hiPSCs had no change in the number of cells in S-phase and no change in their cell cycle distribution. This could be related to the timepoint of the analysis, since it has been shown that hiPSCs exposed to γ-irradiation show cell cycle arrest at the G2/M phase in the first 9h after exposure, but after 24h their cell cycle distribution returns to the same pattern as non-irradiated controls (242).

Different cell types exposed to BPDE present a p53-mediated DNA damage response, with the upregulation of p53 and several of its upstream and downstream effectors. Among them are included the NER components DDB2 and XPC (213,249,251,263,264); the TLS polymerase POLH (213,264); mouse double minute 2 (MDM2), a p53 regulator (249,250,265); and transcription factor JUN (cJUN), a member of the activator protein 1 (AP-1) family of transcription factors (249,250,265).

Bioinformatic analysis of hiPSC exposed to BPDE revealed upregulated clusters related to the p53 signalling pathway (Figure 33) and investigation of the gene and protein expression of p53, MDM2 and cJUN, as well as ser 73 phospho-cJUN, revealed a general pattern of upregulation of these targets in WT hiPSC and little or no regulation in NBS8 cells (Figure 34, Figure 35, Figure 36, Figure 37).

TP53 gene expression was downregulated and p53 expression was increased in WT hiPSCs after BPDE exposure, while NBS8 hiPSCs showed no p53 regulation (Figure 30). To better understand the lower levels of p53 protein in NBS8 cells we measured the mRNA and protein levels of MDM2, a p53-inducible protein that acts as a downregulator of p53, targeting it for degradation, and acting as an inhibitor of p53

transcriptional activities (181,266). MDM2 was significantly increased in WT hiPSCs but not in NBS8 hiPSC, however, so it is unlikely that the low levels of p53 in NBS8 hiPSC are caused by MDM2-mediated degradation.

cJUN has a variety of roles during the DNA damage response. It can exert a protective effect, functionally interacting with p53 to enhance DNA repair (267), repressing p53 and p21 mRNA expression to allow for cell cycle progression and proliferation (268) and it plays a role in genotoxic resistance and activation of DNA damage repair (269–271). It is interesting to note that the phosphorylation of cJUN at ser-63/73 by c-Jun N-terminal kinases (JNKs) seems to be essential for its protective role against DNA-damaging agents (270,271). However, cJUN has also been linked to cellular stress-induced apoptosis, which seems to occur through the sustained upregulation of cJUN levels and, at least in some cell types, enhanced extrinsic apoptotic signalling (272,273). The upregulation of cJUN and ser-73 p-cJUN in BPDE treated WT hiPSCs could help explain the downregulation of *TP53* and the low or no upregulation of *CDKN1A* mRNA levels seen in these cells and hint at a protective effect being elicited, however, a possible apoptotic effect through the extrinsic apoptotic pathway cannot be discarded. Lastly, cJUN activation may play a role in the maintenance of the pluripotent state after genotoxic exposure, since it has been linked to inhibiting the exit of the pluripotent state in ESCs (274).

In hESCs, DNA damage induces the activation of the ATR/CHEK1 and ATM/CHEK2 response pathways, which leads to phosphorylation of CDC25A by CHEK1 and CHEK2, promoting cell cycle arrest. Remarkably, this arrest seems to be largely p21-independent, since although there is a p53-mediated upregulation of *CDKN1A* transcription after damage, there is no p21 accumulation in the hESCs (275). We see that *ATM*, *ATR*, *CHEK1* and *CHEK2* transcription remained largely unchanged after BPDE exposure in hiPSCs, except for a sharp upregulation of *ATR* in NBS8 hiPSCs (Figure 38). It has been shown that cells which are deficient in p53 elicit an ATR-dependent checkpoint signalling that enhances cell survival (276). Considering the known difficulties with the p53-mediated damage response faced by NBN-impaired cells (169,170,232), the increase in ATR could be due to a compensatory DDR mechanism. ATR is known to phosphorylate H2AX following replicative stress (277), therefore we also investigated the protein levels of γ-H2AX, often used as a marker for DNA double-strand breaks (Figure 39). However, the levels of γ-H2AX were higher after BPDE treatment in WT hiPSC than in NBS8 hiPSCs, and furthermore, correlated

closely with the expression levels of cleaved caspase 3, making it more likely that γ-H2AX increase observed here is linked to its role in the apoptotic process (278).

We also investigated the gene expression of targets downstream of the p53 pathway which are involved in the repair and bypass of bulky DNA adducts, XPC, DDB2 and POLH. The increase of XPC, DDB2 and POLH after BPDE exposure has been identified *in vitro* in a variety of cell types (213,249,251,263,264), and it is also present in the mouth buccal cells of humans 24h after cigarette consumption (213), indicating it to be an important part of the response to BPDE in somatic cells. Interestingly, both *XPC* and *DDB2*, DNA damage sensors and key components of the NER pathway (279), were only significantly upregulated after BPDE treatment in NBS8 hiPSCs, but not in WT hiPSCs. *POLH* expression, however, was upregulated in all three hiPSC lines. POLH is a TLS DNA polymerase, and it is involved in the error-prone bypass of BPDE-adducts by inserting an adenine molecule opposite to the dG-N^2-BPDE adduct (280,281). Induction of POLH by BPDE has been implicated in enhanced cell survival, but at the expense of a higher number of genomic mutations (213,249), and it could be a worrying adaptative response in hiPSCs. Besides indirectly enhancing the mutation frequency in exposed cells, BPDE has also been described as an activator of cancer-related transcription networks (250). In control conditions, NBS8 hiPSCs have enhanced cancer-related transcription when compared to WT hiPSCs (Figure 41), something which has been previously noted (167). Interestingly, BPDE exposure further exacerbated this cancerous profile in NBS8 hiPSC while the effects on WT hiPSC weren't nearly as drastic (Figure 42). No GO or KEGG pathway associated with cancer occur in BPDE treated WT hiPSCs, but it enhances several in NBS8 hiPSCs that are associated with metastasis, angiogenesis and poor cancer prognosis, such as ERK1/2 and MAPK signalling (282), the CXCL12-activated CXCR4 signalling pathway (216), vascular endothelial growth factor production (218) and RAP1 signalling (283).

Another effect of BPDE exposure which was exclusive to NBS8 hiPSCs was the downregulation of 28 genes which are involved with DNA damage repair, among them 7 genes directly involved with DSBR (Figure 43, Figure 44). Repression of DNA repair components by BPDE has been described before in somatic cells (264,284) and it has been linked to the p21/DREAM/ E2F Transcription Factor 1 (E2F1) pathway, in which p21 overexpression leads to activation of the DREAM complex and E2F1 abrogation, resulting in transcriptional repression of several DNA repair pathways (264). While the mechanisms of DNA repair repression in NBS8 hiPSCs were not investigated, it is

worth noting that *CDKN1A* (p21) gene expression was upregulated almost twice as much in NBS8 hiPSCs than in iPSC-12 hiPSCs, and not at all in UJ hiPSCs (Figure 29), which may provide a link to the differences in DNA repair genes expression between WT and NBS8-hiPSCs. Regardless, this DNA repair repression may be particularly detrimental to NBS-hiPSCs since they are already deficient in DNA damage repair, and this could contribute to an even greater mutational load and formation of malignancies.

Overall, hiPSCs show a p53-mediated response to BPDE exposure. However, NBS8 hiPSCs have a lessened response compared to WT hiPSCs, with less apoptosis and no p53, cJUN or MDM2 increase. Furthermore, NBS8 hiPSCs suffer from repression of DNA damage response transcription and enhanced transcription of cancer-related pathways after BPDE treatment.

4.6. Discussion of results from effects of BPDE exposure on NPCs derived from healthy and NBS-patient derived hiPSCs

Since PSCs and their differentiated progeny react differently to genotoxic insults (241,243), we differentiated WT and NBS patient-derived hiPSC into NPCs and exposed them to 25nM and 75nM of BPDE for 24h, the same conditions used on the hiPSCs. From the findings obtained in the investigation of the effects of BPDE exposure in hiPSCs, we acquired a set of DNA damage response targets which were also investigated on the hiPSC-derived NPCs.

Our hiPSC-derived NPC cultures had predominant mRNA and/or protein expression of key NPC markers, such as SOX2, SOX1, PAX6, and Nestin, as well as the proliferation marker Ki67, while only sporadically developing TUJ1+ neurons (Figure 45, Figure 46). This indicated that the differentiation was successful and that the cultures were stably maintaining proliferating NPCs. Reportedly, stem cells have varied mechanisms to prevent and repair DNA damage and when that fails, resulting in the accumulation of genomic mutations, to induce cell senescence, terminal differentiation and/or apoptosis (285–288). Neural stem cells are no exception and have been shown to lose stem cell markers and suffer cell cycle arrest and terminal differentiation following ionizing radiation-induced DNA damage (289,290) and excessive DNA damage to NPCs has been linked to premature neuronal differentiation during embryonic development (291). We investigated the effects of BPDE exposure on the expression of key NPC markers and concluded that there were no significant

differences between control and treated conditions, including in the number of proliferating NPCs as measured by Ki67 staining (Figure 47; Figure 48). It is possible that the timepoint of 24h, associated with the low doses of BPDE, were not enough to induce the loss of progenitor markers. In the literature, NPCs subjected to ionizing radiation suffered marked cell death and loss of Ki67 staining in the first 24h, while the loss of stem markers was only prominent starting at 48h post exposure (289,290).

Investigation into the gene expression of apoptotic markers, both of the extrinsic and intrinsic apoptosis pathways, and of Caspase 3 and cleaved caspase 3 protein expression, revealed that NPCs had a weaker apoptotic response to BPDE exposure than their hiPSC progenitors (Figure 49; Figure 50). The analysis of several DDR markers that were modulated after BPDE exposure in hiPSCs followed a similar trend. The mRNA expression of *ATM*, *ATR*, *CHEK2*, *CHEK1*, *TP53*, *MDM2*, *cJUN*, *POLH*, *XPC* and *CDKN1A* was unchanged in NPCs after BPDE treatment, while *GADD45A* was slightly upregulated in iPSC-12 NPCs and *DDB2* was slightly upregulated in NBS8 NPCs. The protein expression of cJUN was stable in all NPC lines after BPDE exposure, while p53 was increased in iPSC-12 NPCs only and MDM2 was only increased in the WT NPCs. This is in line with previous observations in the literature which describes that PSCs have less resistance to several types of genotoxic-induced apoptosis than differentiated cells, while also having a stronger DDR in reaction to the same amount of genotoxic exposure (241,243,292), but it is the first time that the same effect has been demonstrated in relation to BPDE exposure. Lastly, measurements of γ-H2AX through western blot showed that it was not upregulated in reaction to BPDE exposure in NPCs (Figure 55), unlike their hiPSC counterparts (Figure 39). However, the levels of endogenous γ-H2AX in NBS8 NPCs in control conditions were more than six times higher than in the WT NPCs, something which was not observed between WT hiPSCs and NBS8 hiPSC. It has been previously reported that WT and NBS patient-derived hiPSCs have the same number of γ-H2AX foci in control conditions as detected through immunocytochemistry (51) but in cerebral organoids derived from NBS-hiPSCs, there is an increased number of γ-H2AX foci in the NPCs when compared to WT organoids (170). Double-strand breaks are abundant in developing NPCs and seem to play a role in neural function and neuronal formation (293) and it is possible that the deficient repair in NBS NPCs may result in the accumulation of endogenous double-strand breaks.

In summary, NPCs maintained their stem cell characteristics after BPDE exposure and had a weaker DNA damage response than their parental hiPSCs. The notable exception was MDM2 protein expression, which was increased in WT cells in both hiPSCs and NPCs after treatment, but not on NBS8 hiPSCs and NPCs.

4.7. Discussion of results from effects of BPDE exposure on HE cells derived from healthy hiPSCs

Once we had investigated the effects of BPDE in NPCs, which are progenitor cells of ectodermic origin, we then wished to compare the effects of this genotoxin in progenitor cells of endodermic origin. Therefore, we differentiated hiPSCs derived from healthy donors (UJ and iPSC-12) into hepatic endoderm (HE) cells, liver progenitors which can differentiate into different liver cell types such as cholangiocytes and hepatocytes (294), then exposed them to 25nM an 75nM of BPDE for 24h.

Our hiPSC-derived HE cells no longer expressed the pluripotency gene *OCT4* (Figure 56A), while expressing *AFP* (Figure 56C), which is produced mostly produced in the fetal liver during development (295), at levels comparable to the fetal liver. hiPSC-HE cells also expressed *HNF4α* (Figure 56B), a transcriptional regulator essential for liver development and function (296), while only expressing modest levels of *ALB* (Figure 56B), whose production is almost exclusive to hepatocytes (297). Immunocytochemistry confirmed the protein expression of AFP and HNF4α (Figure 56). Lastly, hiPSC-HEs expressed both *KRT18* and *KRT19* (Figure 57), which are associated with hepatocytes and cholangiocytes, respectively (298). These results indicate the successful differentiation of hiPSCs into HE cells, with characteristics similar to that of progenitors in the developing liver.

Interestingly, BPDE exposure downregulated *HNF4α* mRNA expression, but only on the lowest concentration (Figure 58D), and no difference was observed on HNF4α nuclear staining after treatment (Figure 58 E and F). Loss of HNF4α in hepatocytes has been previously linked to induce dedifferentiation and formation of hepatocellular carcinoma (299,300). B[a]p exposure in HepaRG and HepG2 cells, both human hepatic in vitro lines, has been shown to downregulate *HNF4α* mRNA expression (301,302), but no information related to exposure in liver progenitors is available, and neither is any information related to direct BPDE exposure.

Accumulation of DNA damage in hepatic progenitors has been associated with the activation of cellular senescence and to negatively interfere with their proliferation and differentiation (303,304). BPDE exposed HE cells, showed a downregulation of the mRNA levels of *KRT19*, a hepatic progenitor and cholangiocyte marker, after BPDE treatment. Low KRT19 levels have been suggested to interfere with the cholangiocyte differentiation process of liver progenitor cells (305). Of note, *CHEK2* gene expression was upregulated in both cell lines and in both tested concentrations. Upon the induction of genotoxic stress, CHEK2 acts by inducing cell cycle arrest, stimulating the initiation of DNA repair, and inducing senescence and apoptosis (306,307). Interestingly, while exposure to other DNA damaging agents such as 1,2-Dimethylhydrazine and ionizing radiation in somatic cells has been described as increasing *CHEK2* expression (308,309), such effect has never described after BPDE exposure. Overall, BPDE exposure elicited a less robust DNA repair response in HE cells than what was seen in hiPSCs, with the notable exception of *CHEK2* gene upregulation, while also inducing *KRT19* and *HNF4α* downregulation. While that could point to BPDE interfering with the HE cells status as progenitors and their differentiation capacity (303,304), more investigation is needed to elucidate these findings.

4.8. Discussion of results from effects of BPDE exposure on neuronal cultures derived from healthy hiPSCs

Once we had investigated the effects of BPDE exposure on pluripotent stem cells, as well as their derived progenitors NPCs and HE cells, we wished to evaluate these effects on non-progenitor cells. For that end, we differentiated UJ hiPSCs into neuronal cultures composed of MAP2+ and TUJ1+ networks of neurons (Figure 66), then exposed them to 25nM and 75nM BPDE for 72h.

Since B[a]p is highly lipophilic, it can easily cross the blood-brain barrier and the placenta, and several studies point to the nervous system being the target of deleterious B[a]p-induced effects, both during neurodevelopment and after (119,121,125,127,128). BPDE-DNA adducts can be found in the brain of rabbits, rat and mice after B[a]p exposure (127,129,310) and it is likely that B[a]p metabolites can reach the brain through the circulatory system, as well as the brain itself being capable of metabolizing B[a]p (128). Despite that, the possible effects of BPDE exposure on CNS cells have been poorly investigated. Here we have, for the first time, studied this genotoxin in the context of human neuronal exposure.

BPDE elicited an apoptotic response in these cultures, more specifically upregulating genes related to the intrinsic apoptotic pathway such as *BAX* and *BBC3*, but not *TNFRSF10A* or *CASP3* (Figure 67). Moreover, cleaved caspase 3 expression was also upregulated (Figure 68). Induction of apoptosis through the BBC3/BAX/caspase cascade pathway is a well-documented characteristic of BPDE exposure in somatic cells (249–251). Interestingly, human neuroblastoma cell lines exposed to BPDE only show apoptotic signaling in doses 6 times higher than the highest dose used in our work (134), suggesting that actual human neurons may be more sensitive to BPDE exposure than previously thought.

Next, we wished to assess the p53-mediated response to BPDE exposure. We saw that p53 itself was not upregulated either at the mRNA or protein levels, but that the p53 regulator MDM2 was (Figure 69). It's interesting to note that increased expression of MDM2 in the brain has been correlated to enhanced neuronal survival following a variety of insults, including DNA damaging events, and the mechanism is linked to MDM2-targeted p53 degradation (311–314). Further investigation of upstream components of the p53-mediated DNA damage response cascade revealed the upregulation of *CHEK2* mRNA, while downstream in the cascade *CDNK1A* was also upregulated (Figure 70 and Figure 71). Interestingly, DNA damage in post-mitotic neurons has been reported to induce p21-dependent senescence, a cell stress response characterized by apoptosis resistance and the secretion of pro-inflammatory markers, and that is associated with neurodegenerative diseases like Alzheimer's and ALS (315,316). Additionally, the overexpression of CHEK2 in somatic cells triggers a seemingly p53 independent but p21 dependent senescence phenotype (220). BPDE has been reported as inducing senescence in different proliferating somatic cells (264,317,318) and these results warrant a further look into the possible induction of senescence in post-mitotic neuronal cells by BPDE.

Lastly, we also investigated the mRNA expression of *XPC* and *DDB2*, components of NER, and *POLH*, part of the TLS pathway (Figure 72). As mentioned previously, these three targets have been shown to be activated by BPDE exposure in different somatic cell types *in vitro* and *in vivo*, and seem to be an integral part of the BPDE exposure response in these cells (213,249,251,264). *XPC* and *DDB2* were upregulated after BPDE treatment in a dose-dependent manner, which agrees with what is observed in the literature in somatic cells, who show a sustained upregulation of XPC and DDB2 for up to 96h after BPDE exposure (213). *POLH* was not upregulated.in our neuronal

cells after BPDE treatment, however, it's important to note that TLS is a form of replication-dependent repair, which naturally precludes it from being used by the post-mitotic neurons, where forms of replication-independent repair like NER, BER and DNA single-strand break repair are predominant (319). Since POLH-mediated TLS has been implicated in enhancing the survival of somatic cells after BPDE exposure (213), the lack of this pathway in neurons could have detrimental effects on their survival.

In summary, BPDE exposure in neurons elicited an intrinsic apoptotic response, as well as the upregulation of NER and cell cycle arrest/senescence markers, but not of TLS.

4.9. Concluding remarks

To the best of our knowledge, this is the first time the effects of BPDE exposure on hPSCs have been investigated, and it's also the first time these effects have been compared in human cell types of increasing maturation and originating from different different embryonic layers: PSCs (hiPSCs), ectodermic progenitors (NPCs), endodermic progenitors (HE cells) and post-mitotic, somatic cells (neurons). Additionally, we also assessed the effects of BPDE on hiPSC and NPCs with an NBS mutation, and how it differed from the effects on WT cells.

We saw that hiPSC and NPCs harbouring an NBS mutation reacted differently to BPDE treatment than WT cells, showing less apoptotic response, no p53 or MDM2 increase and particularly in the case of NBS-hiPSCs, increased transcription of cancer-related targets and the repression of DNA-repair pathways transcription.

We also saw that different cell types react differently to BPDE exposure. hiPSCs had a robust response compared to NPCs and HE cells, enhancing the mRNA and/or protein expression of several targets related to DNA damage response, apoptosis and cell cycle checkpoints. The neuronal cultures were exposed to BPDE for a longer period of time than the stem cells so a direct comparison between them must be done carefully, but their DNA damage response was more similar to that observed in other somatic cells in the literature, with enhanced expression of NER, intrinsic apoptosis and cell cycle regulator markers.

This work is only the beginning and further research is needed to confirm some of our observations and elucidate the mechanisms behind them. One key point is that, while

we observed in our cells a DNA damage repair response consistent with that elicited by BPDE-DNA adduct formation, we were unable to confirm the presence of BPDE-DNA adducts through Southern blot, which will need to be addressed in the future with other identification methods. Other highlights worth of more investigation are the hints pointing to potential senescence in neuronal cultures exposed to BPDE and the mechanisms behind the drastic differences between the response of WT and NBS-mutated cells to BPDE exposure.

Overall, the data here presented emphasises the differences in the DNA damage response between pluripotent stem cells, progenitor cells and somatic cells and highlights the necessity for further investigation of the effects of BPDE on the embryonic development stage, while also exploring the differential DNA damage response to BPDE mounted by healthy cells and those with an NBS mutation.

References:

1. Hubrecht, Carter. The 3Rs and Humane Experimental Technique: Implementing Change. Animals. 2019 Sep 30;9(10):754.

2. Van Norman GA. Limitations of Animal Studies for Predicting Toxicity in Clinical Trials. JACC Basic Transl Sci. 2019 Nov;4(7):845–54.

3. Van Norman GA. Limitations of Animal Studies for Predicting Toxicity in Clinical Trials. JACC Basic Transl Sci. 2020 Apr;5(4):387–97.

4. Romito A, Cobellis G. Pluripotent Stem Cells: Current Understanding and Future Directions. Stem Cells Int. 2016;2016:1–20.

5. Thomson JA, Itskovitz-Eldor J, Shapiro SS, Waknitz MA, Swiergiel JJ, Marshall VS, et al. Embryonic Stem Cell Lines Derived from Human Blastocysts. Science. 1998 Nov 6;282(5391):1145–7.

6. Lo B, Parham L. Ethical Issues in Stem Cell Research. Endocr Rev. 2009 May 1;30(3):204–13.

7. Takahashi K, Yamanaka S. Induction of Pluripotent Stem Cells from Mouse Embryonic and Adult Fibroblast Cultures by Defined Factors. Cell. 2006 Aug;126(4):663–76.

8. Nowrouzi A, Glimm H, Von Kalle C, Schmidt M. Retroviral Vectors: Post Entry Events and Genomic Alterations. Viruses. 2011 Apr 29;3(5):429–55.

9. Stadtfeld M, Nagaya M, Utikal J, Weir G, Hochedlinger K. Induced Pluripotent Stem Cells Generated Without Viral Integration. Science. 2008 Nov 7;322(5903):945–9.

10. Okita K, Nakagawa M, Hyenjong H, Ichisaka T, Yamanaka S. Generation of Mouse Induced Pluripotent Stem Cells Without Viral Vectors. Science. 2008 Nov 7;322(5903):949–53.

11. Kim D, Kim CH, Moon JI, Chung YG, Chang MY, Han BS, et al. Generation of Human Induced Pluripotent Stem Cells by Direct Delivery of Reprogramming Proteins. Cell Stem Cell. 2009 Jun;4(6):472–6.

12. Yakubov E, Rechavi G, Rozenblatt S, Givol D. Reprogramming of human fibroblasts to pluripotent stem cells using mRNA of four transcription factors. Biochem Biophys Res Commun. 2010 Mar;394(1):189–93.

13. Kwok CK, Sébastien I, Hariharan K, Meiser I, Wihan J, Altmaier S, et al. Scalable expansion of iPSC and their derivatives across multiple lineages. Reprod Toxicol. 2022 Sep;112:23–35.

14. Paik DT, Chandy M, Wu JC. Patient and Disease–Specific Induced Pluripotent Stem Cells for Discovery of Personalized Cardiovascular Drugs and Therapeutics. Ohlstein EH, editor. Pharmacol Rev. 2020 Jan;72(1):320–42.

15. Csöbönyeiová M, Klein M, Kuniaková M, Varga I, Danišovič Ľ. Induced Pluripotent Stem Cell-Derived Organoids: Their Implication in COVID-19 Modeling. Int J Mol Sci. 2023 Feb 9;24(4):3459.

16. Scesa G, Adami R, Bottai D. iPSC Preparation and Epigenetic Memory: Does the Tissue Origin Matter? Cells. 2021 Jun 11;10(6):1470.

17. Guo Y, Pu WT. Cardiomyocyte Maturation: New Phase in Development. Circ Res. 2020 Apr 10;126(8):1086–106.

18. Xie Y, Yao J, Jin W, Ren L, Li X. Induction and Maturation of Hepatocyte-Like Cells In Vitro: Focus on Technological Advances and Challenges. Front Cell Dev Biol. 2021 Nov 26;9:765980.

19. Kim J, Koo BK, Knoblich JA. Human organoids: model systems for human biology and medicine. Nat Rev Mol Cell Biol. 2020 Oct;21(10):571–84.

20. Bas-Cristóbal Menéndez A, Du Z, Van Den Bosch TPP, Othman A, Gaio N, Silvestri C, et al. Creating a kidney organoid-vasculature interaction model using a novel organ-on-chip system. Sci Rep. 2022 Nov 30;12(1):20699.

21. Easley CA. Induced Pluripotent Stem Cells (iPSCs) in Developmental Toxicology. In: Hansen JM, Winn LM, editors. Developmental Toxicology [Internet]. New York, NY: Springer New York; 2019 [cited 2022 Dec 9]. p. 19–34. (Methods in Molecular Biology; vol. 1965). Available from: http://link.springer.com/10.1007/978-1-4939-9182-2_3

22. Kim TW, Che JH, Yun JW. Use of stem cells as alternative methods to animal experimentation in predictive toxicology. Regul Toxicol Pharmacol. 2019 Jul;105:15–29.

23. Oksanen M, Petersen AJ, Naumenko N, Puttonen K, Lehtonen Š, Gubert Olivé M, et al. PSEN1 Mutant iPSC-Derived Model Reveals Severe Astrocyte Pathology in Alzheimer's Disease. Stem Cell Rep. 2017 Dec;9(6):1885–97.

24. Graffmann N, Martins S, Ljubikj T, Matte JC, Bohndorf M, Wruck W, et al. Generation of a Crigler-Najjar Syndrome Type I patient-derived induced pluripotent stem cell line CNS705 (HHUUKDi005-A). Stem Cell Res. 2021 Mar;51:102167.

25. Graffmann N, Ncube A, Martins S, Fiszl AR, Reuther P, Bohndorf M, et al. A stem cell based in vitro model of NAFLD enables the analysis of patient specific individual metabolic adaptations in response to a high fat diet and AdipoRon interference. Biol Open. 2020 Jan 1;bio.054189.

26. Paolini Sguazzi G, Muto V, Tartaglia M, Bertini E, Compagnucci C. Induced Pluripotent Stem Cells (iPSCs) and Gene Therapy: A New Era for the Treatment of Neurological Diseases. Int J Mol Sci. 2021 Dec 20;22(24):13674.

27. Younes M, Georgiadis N. Toxicological Risk Assessment. In: Reichl FX, Schwenk M, editors. Regulatory Toxicology [Internet]. Berlin, Heidelberg: Springer Berlin Heidelberg; 2020 [cited 2024 Feb 1]. p. 1–12. Available from: http://link.springer.com/10.1007/978-3-642-36206-4_29-3

28. Luconi M, Sogorb MA, Markert UR, Benfenati E, May T, Wolbank S, et al. Human-Based New Approach Methodologies in Developmental Toxicity Testing: A Step Ahead from the State of the Art with a Feto–Placental Organ-on-Chip Platform. Int J Environ Res Public Health. 2022 Nov 28;19(23):15828.

29. Warkany J. Why I doubted that thalidomide was the cause of the epidemic of limb defects of 1959 to 1961. Teratology. 1988 Sep;38(3):217–9.

30. Kim JH, Scialli AR. Thalidomide: The Tragedy of Birth Defects and the Effective Treatment of Disease. Toxicol Sci. 2011 Jul;122(1):1–6.

31. MacRae SL, Croken MM, Calder RB, Aliper A, Milholland B, White RR, et al. DNA repair in species with extreme lifespan differences. Aging. 2015 Dec 30;7(12):1171–82.

32. Galloway SM. International regulatory requirements for genotoxicity testing for pharmaceuticals used in human medicine, and their impurities and metabolites. Environ Mol Mutagen. 2017 Jun;58(5):296–324.

33. Kirkland D, Aardema M, Henderson L, Müller L. Evaluation of the ability of a battery of three in vitro genotoxicity tests to discriminate rodent carcinogens and non-carcinogens. Mutat Res Toxicol Environ Mutagen. 2005 Jul;584(1–2):1–256.

34. Kirkland D, Aardema M, Müller L, Hayashi M. Evaluation of the ability of a battery of three in vitro genotoxicity tests to discriminate rodent carcinogens and non-carcinogens. Mutat Res Toxicol Environ Mutagen. 2006 Sep;608(1):29–42.

35. Avila AM, Bebenek I, Bonzo JA, Bourcier T, Davis Bruno KL, Carlson DB, et al. An FDA/CDER perspective on nonclinical testing strategies: Classical toxicology approaches and new approach methodologies (NAMs). Regul Toxicol Pharmacol. 2020 Jul;114:104662.

36. Liu Q, Huang R, Hsieh J, Zhu H, Tiwari M, Liu G, et al. Landscape Analysis of the Application of Artificial Intelligence and Machine Learning in Regulatory Submissions for Drug Development From 2016 to 2021. Clin Pharmacol Ther. 2023 Apr;113(4):771–4.

37. Zushin PJH, Mukherjee S, Wu JC. FDA Modernization Act 2.0: transitioning beyond animal models with human cells, organoids, and AI/ML-based approaches. J Clin Invest. 2023 Nov 1;133(21):e175824.

38. Cherianidou A, Seidel F, Kappenberg F, Dreser N, Blum J, Waldmann T, et al. Classification of Developmental Toxicants in a Human iPSC Transcriptomics-Based Test. Chem Res Toxicol. 2022 May 16;35(5):760–73.

39. Seidel F, Cherianidou A, Kappenberg F, Marta M, Dreser N, Blum J, et al. High Accuracy Classification of Developmental Toxicants by In Vitro Tests of Human Neuroepithelial and Cardiomyoblast Differentiation. Cells. 2022 Oct 27;11(21):3404.

40. Cherianidou A, Kappenberg F, Seidel F, Acharya A, Papazoglou P, Srinivasan SP, et al. Transcriptome-based prediction of drugs, inhibiting cardiomyogenesis in human induced pluripotent stem cells. Cell Death Discov. 2023 Aug 29;9(1):321.

41. Lauschke K, Rosenmai AK, Meiser I, Neubauer JC, Schmidt K, Rasmussen MA, et al. A novel human pluripotent stem cell-based assay to predict developmental toxicity. Arch Toxicol. 2020 Nov;94(11):3831–46.

42. Yin F, Zhu Y, Wang Y, Qin J. Engineering Brain Organoids to Probe Impaired Neurogenesis Induced by Cadmium. ACS Biomater Sci Eng. 2018 Mar 29;acsbiomaterials.8b00160.

43. Basu A, Ghosh P, Bhattacharjee A, Patra AR, Bhattacharya S. Prevention of myelosuppression and genotoxicity induced by cisplatin in murine bone marrow cells: effect of an organovanadium compound vanadium(III)-l-cysteine. Mutagenesis. 2015 Jul 1;30(4):509–17.

44. Hajra S, Patra AR, Basu A, Bhattacharya S. Prevention of doxorubicin (DOX)-induced genotoxicity and cardiotoxicity: Effect of plant derived small molecule indole-3-carbinol (I3C) on oxidative stress and inflammation. Biomed Pharmacother. 2018 May;101:228–43.

45. Reyes ME, Ma J, Grove ML, Ater JL, Morrison AC, Hildebrandt MAT. RNA sequence analysis of inducible pluripotent stem cell-derived cardiomyocytes reveals altered expression of DNA damage and cell cycle genes in response to doxorubicin. Toxicol Appl Pharmacol. 2018 Oct;356:44–53.

46. Morizane R, Lam AQ, Freedman BS, Kishi S, Valerius MT, Bonventre JV. Nephron organoids derived from human pluripotent stem cells model kidney development and injury. Nat Biotechnol. 2015 Nov;33(11):1193–200.

47. Das D, Li J, Cheng L, Franco S, Mahairaki V. Human Forebrain Organoids from Induced Pluripotent Stem Cells: A Novel Approach to Model Repair of Ionizing Radiation-Induced DNA Damage in Human Neurons. Radiat Res. 2020 Jun 4;194(2):191.

48. Kaplowitz N. Biochemical and Cellular Mechanisms of Toxic Liver Injury. Semin Liver Dis. 2002 May 16;22(02):137–44.

49. Kumar NN, Chan YL, Chen H, Oliver BG. Editorial: Effects of environmental toxins on brain health and development. Front Mol Neurosci. 2023 Feb 8;16:1149776.

50. Zhang N, An MC, Montoro D, Ellerby LM. Characterization of Human Huntington's Disease Cell Model from Induced Pluripotent Stem Cells. PLoS Curr. 2010 Oct 28;2:RRN1193.

51. Halevy T, Akov S, Bohndorf M, Mlody B, Adjaye J, Benvenisty N, et al. Chromosomal Instability and Molecular Defects in Induced Pluripotent Stem Cells from Nijmegen Breakage Syndrome Patients. Cell Rep. 2016 Aug;16(9):2499–511.

52. Yagi T, Ito D, Okada Y, Akamatsu W, Nihei Y, Yoshizaki T, et al. Modeling familial Alzheimer's disease with induced pluripotent stem cells. Hum Mol Genet. 2011 Dec 1;20(23):4530–9.

53. Chailangkarn T, Trujillo CA, Freitas BC, Hrvoj-Mihic B, Herai RH, Yu DX, et al. A human neurodevelopmental model for Williams syndrome. Nature. 2016 Aug;536(7616):338–43.

54. Tukker A. Is the time right for in vitro neurotoxicity testing using human iPSC-derived neurons? ALTEX [Internet]. 2016 [cited 2024 Feb 22]; Available from: http://www.altex.org/index.php/altex/article/view/156

55. Schinke C, Fernandez Vallone V, Ivanov A, Peng Y, Körtvelyessy P, Nolte L, et al. Modeling chemotherapy induced neurotoxicity with human induced pluripotent stem cell (iPSC) -derived sensory neurons. Neurobiol Dis. 2021 Jul;155:105391.

56. Tukker AM, Wijnolts FMJ, de Groot A, Westerink RHS. Human iPSC-derived neuronal models for in vitro neurotoxicity assessment. NeuroToxicology. 2018 Jul;67:215–25.

57. Sirenko O, Parham F, Dea S, Sodhi N, Biesmans S, Mora-Castilla S, et al. Functional and Mechanistic Neurotoxicity Profiling Using Human iPSC-Derived Neural 3D Cultures. Toxicol Sci. 2019 Jan 1;167(1):58–76.

58. Chambers SM, Fasano CA, Papapetrou EP, Tomishima M, Sadelain M, Studer L. Highly efficient neural conversion of human ES and iPS cells by dual inhibition of SMAD signaling. Nat Biotechnol. 2009 Mar;27(3):275–80.

59. Noisa P, Raivio T, Cui W. Neural Progenitor Cells Derived from Human Embryonic Stem Cells as an Origin of Dopaminergic Neurons. Stem Cells Int. 2015;2015:1–10.

60. Walsh P, Truong V, Nayak S, Saldías Montivero M, Low WC, Parr AM, et al. Accelerated differentiation of human pluripotent stem cells into neural lineages via an early intermediate ectoderm population. Stem Cells. 2020 Nov 1;38(11):1400–8.

61. Kirkeby A, Grealish S, Wolf DA, Nelander J, Wood J, Lundblad M, et al. Generation of Regionally Specified Neural Progenitors and Functional Neurons from Human Embryonic Stem Cells under Defined Conditions. Cell Rep. 2012 Jun;1(6):703–14.

62. Hu BY, Weick JP, Yu J, Ma LX, Zhang XQ, Thomson JA, et al. Neural differentiation of human induced pluripotent stem cells follows developmental principles but with variable potency. Proc Natl Acad Sci. 2010 Mar 2;107(9):4335–40.

63. Brás J, Henriques D, Moreira R, Santana MM, Silva-Pedrosa R, Adão D, et al. Establishment and characterization of human pluripotent stem cells-derived brain organoids to model cerebellar diseases. Sci Rep. 2022 Jul 22;12(1):12513.

64. Birey F, Andersen J, Makinson CD, Islam S, Wei W, Huber N, et al. Assembly of functionally integrated human forebrain spheroids. Nature. 2017 May 4;545(7652):54–9.

65. Jo J, Xiao Y, Sun AX, Cukuroglu E, Tran HD, Göke J, et al. Midbrain-like Organoids from Human Pluripotent Stem Cells Contain Functional Dopaminergic and Neuromelanin-Producing Neurons. Cell Stem Cell. 2016 Aug;19(2):248–57.

66. Gunhanlar N, Shpak G, Van Der Kroeg M, Gouty-Colomer LA, Munshi ST, Lendemeijer B, et al. A simplified protocol for differentiation of electrophysiologically mature neuronal networks from human induced pluripotent stem cells. Mol Psychiatry. 2018 May;23(5):1336–44.

67. Velasco S, Kedaigle AJ, Simmons SK, Nash A, Rocha M, Quadrato G, et al. Individual brain organoids reproducibly form cell diversity of the human cerebral cortex. Nature. 2019 Jun;570(7762):523–7.

68. Eigenhuis KN, Somsen HB, Van Der Kroeg M, Smeenk H, Korporaal AL, Kushner SA, et al. A simplified protocol for the generation of cortical brain organoids. Front Cell Neurosci. 2023 Apr 4;17:1114420.

69. Almazroo OA, Miah MK, Venkataramanan R. Drug Metabolism in the Liver. Clin Liver Dis. 2017 Feb;21(1):1–20.

70. Fisher ES, Curry SC. Evaluation and treatment of acetaminophen toxicity. In: Advances in Pharmacology [Internet]. Elsevier; 2019 [cited 2024 Apr 20]. p. 263–72. Available from: https://linkinghub.elsevier.com/retrieve/pii/S1054358918300504

71. Godoy P, Hewitt NJ, Albrecht U, Andersen ME, Ansari N, Bhattacharya S, et al. Recent advances in 2D and 3D in vitro systems using primary hepatocytes, alternative hepatocyte sources and non-parenchymal liver cells and their use in investigating mechanisms of hepatotoxicity, cell signaling and ADME. Arch Toxicol. 2013 Aug;87(8):1315–530.

72. Hannoun Z, Steichen C, Dianat N, Weber A, Dubart-Kupperschmitt A. The potential of induced pluripotent stem cell derived hepatocytes. J Hepatol. 2016 Jul;65(1):182–99.

73. Maurel P, editor. Hepatocytes: Methods and Protocols [Internet]. Totowa, NJ: Humana Press; 2010 [cited 2024 Feb 10]. (Methods in Molecular Biology; vol. 640). Available from: https://link.springer.com/10.1007/978-1-60761-688-7

74. Atkins JT, George GC, Hess K, Marcelo-Lewis KL, Yuan Y, Borthakur G, et al. Pre-clinical animal models are poor predictors of human toxicities in phase 1 oncology clinical trials. Br J Cancer. 2020 Nov 10;123(10):1496–501.

75. Matz P, Wruck W, Fauler B, Herebian D, Mielke T, Adjaye J. Footprint-free human fetal foreskin derived iPSCs: A tool for modeling hepatogenesis associated gene regulatory networks. Sci Rep. 2017 Jul 24;7(1):6294.

76. Jozefczuk J, Prigione A, Chavez L, Adjaye J. Comparative Analysis of Human Embryonic Stem Cell and Induced Pluripotent Stem Cell-Derived Hepatocyte-Like Cells Reveals Current Drawbacks and Possible Strategies for Improved Differentiation. Stem Cells Dev. 2011 Jul;20(7):1259–75.

77. Pashos EE, Park Y, Wang X, Raghavan A, Yang W, Abbey D, et al. Large, Diverse Population Cohorts of hiPSCs and Derived Hepatocyte-like Cells Reveal Functional Genetic Variation at Blood Lipid-Associated Loci. Cell Stem Cell. 2017 Apr;20(4):558-570.e10.

78. Teo AKK, Valdez IA, Dirice E, Kulkarni RN. Comparable Generation of Activin-Induced Definitive Endoderm via Additive Wnt or BMP Signaling in Absence of Serum. Stem Cell Rep. 2014 Jul;3(1):5–14.

79. Qiu S, Li Y, Imakura Y, Mima S, Hashita T, Iwao T, et al. An Efficient Method for the Differentiation of Human iPSC-Derived Endoderm toward Enterocytes and Hepatocytes. Cells. 2021 Apr 6;10(4):812.

80. Graffmann N, Scherer B, Adjaye J. In vitro differentiation of pluripotent stem cells into hepatocyte like cells – Basic principles and current progress. Stem Cell Res. 2022 May;61:102763.

81. Hakem R. DNA-damage repair; the good, the bad, and the ugly. EMBO J. 2008 Feb 20;27(4):589–605.

82. Lane DP. p53, guardian of the genome. Nature. 1992 Jul;358(6381):15–6.

83. Hwa Yun B, Guo J, Bellamri M, Turesky RJ. DNA adducts: Formation, biological effects, and new biospecimens for mass spectrometric measurements in humans. Mass Spectrom Rev. 2020 Mar;39(1–2):55–82.

84. Huang Y, Li L. DNA crosslinking damage and cancer - a tale of friend and foe. Transl Cancer Res. 2013;2(3).

85. Niedernhofer LJ, Daniels JS, Rouzer CA, Greene RE, Marnett LJ. Malondialdehyde, a Product of Lipid Peroxidation, Is Mutagenic in Human Cells. J Biol Chem. 2003 Aug;278(33):31426–33.

86. Jamieson ER, Lippard SJ. Structure, Recognition, and Processing of Cisplatin−DNA Adducts. Chem Rev. 1999 Sep 8;99(9):2467–98.

87. Scharer OD. Nucleotide Excision Repair in Eukaryotes. Cold Spring Harb Perspect Biol. 2013 Oct 1;5(10):a012609–a012609.

88. Petruseva IO, Evdokimov AN, Lavrik OI. Molecular Mechanism of Global Genome Nucleotide Excision Repair. Acta Naturae. 2014 Mar 15;6(1):23–34.

89. Duan M, Speer RM, Ulibarri J, Liu KJ, Mao P. Transcription-coupled nucleotide excision repair: New insights revealed by genomic approaches. DNA Repair. 2021 Jul;103:103126.

90. Okuda M, Nakazawa Y, Guo C, Ogi T, Nishimura Y. Common TFIIH recruitment mechanism in global genome and transcription-coupled repair subpathways. Nucleic Acids Res. 2017 Dec 15;45(22):13043–55.

91. Rimel JK, Taatjes DJ. The essential and multifunctional TFIIH complex. Protein Sci. 2018 Jun;27(6):1018–37.

92. Sale JE, Lehmann AR, Woodgate R. Y-family DNA polymerases and their role in tolerance of cellular DNA damage. Nat Rev Mol Cell Biol. 2012 Mar;13(3):141–52.

93. Quinet A, Lerner LK, Martins DJ, Menck CFM. Filling gaps in translesion DNA synthesis in human cells. Mutat Res Toxicol Environ Mutagen. 2018 Dec;836:127–42.

94. Kannouche PL, Wing J, Lehmann AR. Interaction of Human DNA Polymerase with Monoubiquitinated PCNA: A Possible Mechanism for the Polymerase Switch in Response to DNA Damage. Mol Cell.

95. Park JM, Yang SW, Yu KR, Ka SH, Lee SW, Seol JH, et al. Modification of PCNA by ISG15 Plays a Crucial Role in Termination of Error-Prone Translesion DNA Synthesis. Mol Cell. 2014 May;54(4):626–38.

96. Chakravarti D, Venugopal D, Mailander PC, Meza JL, Higginbotham S, Cavalieri EL, et al. The role of polycyclic aromatic hydrocarbon–DNA adducts in inducing mutations in mouse skin. Mutat Res Toxicol Environ Mutagen. 2008 Jan;649(1–2):161–78.

97. Sushkova S, Deryabkina I, Antonenko E, Kizilkaya R, Rajput V, Vasilyeva G. Benzo[a]pyrene degradation and bioaccumulation in soil-plant system under artificial contamination. Sci Total Environ. 2018 Aug;633:1386–91.

98. Das DN, Bhutia SK. Inevitable dietary exposure of Benzo[a]pyrene: carcinogenic risk assessment an emerging issues and concerns. Curr Opin Food Sci. 2018 Dec;24:16–25.

99. Boysen G, Hecht SS. Analysis of DNA and protein adducts of benzo[a]pyrene in human tissues using structure-specific methods. Mutat Res Mutat Res. 2003 Jan;543(1):17–30.

100. Shiizaki K, Kawanishi M, Yagi T. Modulation of benzo[a]pyrene–DNA adduct formation by CYP1 inducer and inhibitor. Genes Environ. 2017 Dec;39(1):14.

101. Eisenstadt Eri, Warren AJ, Porter J, Atkins D, MILLERt JH. Carcinogenic epoxides of benzo[alpyrene and cyclopenta[cd]pyrene induce base substitutions via specific transversions. Proc Natl Acad Sci USA. 1982;

102. Melendez-Colon VJ, Luch A, Seidel A, Baird WM. Cancer initiation by polycyclic aromatic hydrocarbons results from formation of stable DNA adducts rather than apurinic sites. Carcinogenesis. 1999 Oct;20(10):1885–91.

103. Pfeifer GP, Denissenko MF, Olivier M, Tretyakova N, Hecht SS, Hainaut P. Tobacco smoke carcinogens, DNA damage and p53 mutations in smoking-associated cancers. Oncogene. 2002 Oct 21;21(48):7435–51.

104. Liu Z, Muehlbauer KR, Schmeiser HH, Hergenhahn M, Belharazem D, Hollstein MC. p53 Mutations in Benzo(a)Pyrene-Exposed Human p53 Knock-in Murine Fibroblasts Correlate with p53 Mutations in Human Lung Tumors. Cancer Res. 2005 Apr 1;65(7):2583–7.

105. Lee YCA, Cohet C, Yang YC, Stayner L, Hashibe M, Straif K. Meta-analysis of epidemiologic studies on cigarette smoking and liver cancer. Int J Epidemiol. 2009 Dec;38(6):1497–511.

106. Petrick JL, Campbell PT, Koshiol J, Thistle JE, Andreotti G, Beane-Freeman LE, et al. Tobacco, alcohol use and risk of hepatocellular carcinoma and intrahepatic cholangiocarcinoma: The Liver Cancer Pooling Project. Br J Cancer. 2018 Apr;118(7):1005–12.

107. Briedé JJ, Godschalk RWL, Emans MTG, De Kok TMCM, Van Agen E, Van Maanen JMS, et al. *In Vitro* and *In Vivo* Studies on Oxygen Free Radical and DNA Adduct Formation in Rat Lung and Liver during Benzo[a]pyrene Metabolism. Free Radic Res. 2004 Jan;38(9):995–1002.

108. Arlt VM, Stiborova M, Henderson CJ, Thiemann M, Frei E, Aimova D, et al. Metabolic activation of benzo[a]pyrene in vitro by hepatic cytochrome P450 contrasts with detoxification in vivo: experiments with hepatic cytochrome P450 reductase null mice. Carcinogenesis. 2007 Oct 4;29(3):656–65.

109. Chen S, Wang L, Lunn RM, Tsai W, Lee P, Lee C, et al. Polycyclic aromatic hydrocarbon-DNA adducts in liver tissues of hepatocellular carcinoma patients and controls. Int J Cancer. 2002 May;99(1):14–21.

110. Filler R, LEWt KJ. Developmental onset of mixed-function oxidase activity in preimplantation mouse embryos. Dev Biol. 1981;

111. Rouet P, Dansette PM, Weston A, Frayssinet C. Metabolism of benzo[a]pyrene by mouse brain microsomes during perinatal development. Chem Biol Interact. 1984 Jan;48(1):115–9.

112. Arnould J, Verhoest P, Bach V, Libert J, Belegaud J. Detection of benzo[a]pyrene-DNA adducts in human placenta and umbilical cord blood. Hum Exp Toxicol. 1997 Dec;16(12):716–21.

113. Ye Y, Jiang S, Zhang C, Cheng Y, Zhong H, Du T, et al. Environmental Pollutant Benzo[a]pyrene Induces Recurrent Pregnancy Loss through Promoting Apoptosis and Suppressing Migration of Extravillous Trophoblast. Gomez E, editor. BioMed Res Int. 2020 Oct 16;2020:1–10.

114. Barbieri O, Ognio E, Rossi O, Astigiano S, Rossi L. Embryotoxicity of Benzo(a)pyrene and Some of Its Synthetic Derivatives in Swiss Mice. 1986;46.

115. Yamaguchi A, Uchida M, Ishibashi H, Hirano M, Ichikawa N, Arizono K, et al. Potential mechanisms underlying embryonic developmental toxicity caused by benzo[a]pyrene in Japanese medaka (Oryzias latipes). Chemosphere. 2020 Mar;242:125243.

116. Zenzes MT. Detection of benzo(a)pyrene diol epoxide– DNA adducts in sperm of men exposed to cigarette smoke. 1999;72(2).

117. Zenzes M. Immunodetection of benzo[a]pyrene adducts in ovarian cells of women exposed to cigarette smoke. Mol Hum Reprod. 1998 Feb 1;4(2):159–65.

118. Zenzes MT. Detection of benzo[a]pyrene diol epoxide-DNA adducts in embryos from smoking couples: evidence for transmission by spermatozoa. Mol Hum Reprod. 1999 Feb 1;5(2):125–31.

119. Das M, Seth TPK, Mukhtar H. Distribution of benzo(a)pyrene in discrete regions of rat brain. Bull Env Contam Toxicol. 1985;

120. Ramesh A, Inyang F, Hood DB, Archibong AE, Knuckles ME, Nyanda AM. Metabolism, bioavailability, and toxicokinetics of Benzo(α)pyrenein F-344 rats following oral administration. Exp Toxicol Pathol. 2001 Jan;53(4):275–90.

121. Saunders CR, Shockley DC, Knuckles ME. Behavioral Effects Induced by Acute Exposure to Benzo(a)pyrene in F-344 Rats. 2001;

122. Saunders CR, Das SK, Ramesh A, Shockley DC, Mukherjee S. Benzo(a)pyrene-induced acute neurotoxicity in the F-344 rat: role of oxidative stress. J Appl Toxicol. 2006 Sep;26(5):427–38.

123. Nathalie Grova. Sub-acute administration of benzo[a]pyrene (B[a]P) reduces anxiety-related behaviour in adult mice and modulates regional expression of N-methyl-D-aspartate (NMDA) receptors genes in relevant brain regions. 2008;

124. Zhang W, Tian F, Zheng J, Li S, Qiang M. Chronic Administration of Benzo(a)pyrene Induces Memory Impairment and Anxiety-Like Behavior and Increases of NR2B DNA Methylation. He W, editor. PLOS ONE. 2016 Feb 22;11(2):e0149574.

125. Das SK, Aparna S, Patri M. Chronic waterborne exposure to benzo[a]pyrene induces locomotor dysfunction and development of neurodegenerative phenotypes in zebrafish. Neurosci Lett. 2020 Jan;716:134646.

126. Cherif LS, Cao-Lei L, Farinelle S, Muller CP, Turner JD, Schroeder H, et al. Assessment of 9-OH- and 7,8-diol-benzo[a]pyrene in Blood as Potent Markers of Cognitive Impairment Related to benzo[a]pyrene Exposure: An Animal Model Study. Toxics. 2021 Mar 8;9(3):50.

127. Nie J, Duan L, Yan Z, Niu Q. Tau Hyperphosphorylation is Associated with Spatial Learning and Memory After Exposure to Benzo[a]pyrene in SD Rats. Neurotox Res. 2013 Nov;24(4):461–71.

128. Chepelev NL, Moffat ID, Bowers WJ, Yauk CL. Neurotoxicity may be an overlooked consequence of benzo[a]pyrene exposure that is relevant to human health risk assessment. Mutat Res Mutat Res. 2015 Apr;764:64–89.

129. Chepelev NL, Long AS, Bowers WJ, Gagné R, Williams A, Kuo B, et al. Transcriptional profiling of the mouse hippocampus supports an NMDAR-mediated neurotoxic mode of action for benzo[*a*]pyrene. Environ Mol Mutagen. 2016 Jun;57(5):350–63.

130. McCallister MM, Maguire M, Ramesh A, Aimin Q, Liu S, Khoshbouei H, et al. Prenatal exposure to benzo(a)pyrene impairs later-life cortical neuronal function. NeuroToxicology. 2008 Sep;29(5):846–54.

131. Wan T, Au DWT, Mo J, Chen L, Cheung KM, Kong RYC, et al. Assessment of parental benzo[a]pyrene exposure-induced cross-generational neurotoxicity and changes in offspring sperm DNA methylome in medaka fish. Environ Epigenetics. 2022 Jun 25;8(1):dvac013.

132. Knecht AL, Truong L, Marvel SW, Reif DM, Garcia A, Lu C, et al. Transgenerational inheritance of neurobehavioral and physiological deficits from developmental exposure to benzo[a]pyrene in zebrafish. Toxicol Appl Pharmacol. 2017 Aug;329:148–57.

133. Lin YC, Wu CY, Hu CH, Pai TW, Chen YR, Wang WD. Integrated Hypoxia Signaling and Oxidative Stress in Developmental Neurotoxicity of Benzo[a]Pyrene in Zebrafish Embryos. Antioxidants. 2020 Aug 11;9(8):731.

134. Lyu Y, Ren XK, Guo CC, Li ZF, Zheng JP. Benzo(a)pyrene-7,8-dihydrodiol-9,10-epoxide induces ferroptosis in neuroblastoma cells through redox imbalance. J Toxicol Sci. 2022;47(12):519–29.

135. Weng M. Benzo6a9pyrene diol epoxide up-regulates COX-2 expression through NF-$kappa;B in rat astrocytes. Toxicol Lett. 2004 Jul;151(2):345–55.

136. Shanbhag NM, Evans MD, Mao W, Nana AL, Seeley WW, Adame A, et al. Early neuronal accumulation of DNA double strand breaks in Alzheimer's disease. Acta Neuropathol Commun. 2019 Dec;7(1):77.

137. Thadathil N, Hori R, Xiao J, Khan MM. DNA double-strand breaks: a potential therapeutic target for neurodegenerative diseases. Chromosome Res. 2019 Dec;27(4):345–64.

138. Pessina F, Gioia U, Brandi O, Farina S, Ceccon M, Francia S, et al. DNA Damage Triggers a New Phase in Neurodegeneration. Trends Genet. 2021 Apr;37(4):337–54.

139. Konopka A, Atkin JD. DNA Damage, Defective DNA Repair, and Neurodegeneration in Amyotrophic Lateral Sclerosis. Front Aging Neurosci. 2022 Apr 27;14:786420.

140. Kisby GE, Fry RC, Lasarev MR, Bammler TK, Beyer RP, Churchwell M, et al. The Cycad Genotoxin MAM Modulates Brain Cellular Pathways Involved in Neurodegenerative Disease and Cancer in a DNA Damage-Linked Manner. Feany MB, editor. PLoS ONE. 2011 Jun 23;6(6):e20911.

141. Spencer PS, Palmer VS, Kisby GE. Western Pacific ALS-PDC: Evidence implicating cycad genotoxins. J Neurol Sci. 2020 Dec;419:117185.

142. Kisby GE, Spencer PS. Genotoxic Damage During Brain Development Presages Prototypical Neurodegenerative Disease. Front Neurosci. 2021 Dec 2;15:752153.

143. Cannan WJ, Pederson DS. Mechanisms and Consequences of Double-Strand DNA Break Formation in Chromatin. J Cell Physiol. 2016 Jan;231(1):3–14.

144. Blackford AN, Jackson SP. ATM, ATR, and DNA-PK: The Trinity at the Heart of the DNA Damage Response. Mol Cell. 2017 Jun;66(6):801–17.

145. Mao Z, Bozzella M, Seluanov A, Gorbunova V. Comparison of nonhomologous end joining and homologous recombination in human cells. DNA Repair. 2008 Oct 1;7(10):1765–71.

146. Wang Q, Goldstein M, Alexander P, Wakeman TP, Sun T, Feng J, et al. Rad17 recruits the MRE11-RAD50-NBS1 complex to regulate the cellular response to DNA double-strand breaks. EMBO J. 2014 Apr 16;33(8):862–77.

147. Furuta T, Takemura H, Liao ZY, Aune GJ, Redon C, Sedelnikova OA, et al. Phosphorylation of Histone H2AX and Activation of Mre11, Rad50, and Nbs1 in Response to Replication-dependent DNA Double-strand Breaks Induced by Mammalian DNA Topoisomerase I Cleavage Complexes. J Biol Chem. 2003 May;278(22):20303–12.

148. Kozlov SV, Graham ME, Jakob B, Tobias F, Kijas AW, Tanuji M, et al. Autophosphorylation and ATM Activation. J Biol Chem. 2011 Mar;286(11):9107–19.

149. Lavin M, Kozlov S, Gatei M, Kijas A. ATM-Dependent Phosphorylation of All Three Members of the MRN Complex: From Sensor to Adaptor. Biomolecules. 2015 Oct 23;5(4):2877–902.

150. Zhao F, Kim W, Kloeber JA, Lou Z. DNA end resection and its role in DNA replication and DSB repair choice in mammalian cells. Exp Mol Med. 2020 Oct;52(10):1705–14.

151. Rao Q, Liu M, Tian Y, Wu Z, Hao Y, Song L, et al. Cryo-EM structure of human ATR-ATRIP complex. Cell Res. 2018 Feb;28(2):143–56.

152. Ceccaldi R, Sarangi P, D'Andrea AD. The Fanconi anaemia pathway: new players and new functions. Nat Rev Mol Cell Biol. 2016 Jun;17(6):337–49.

153. Walsh CS. Two decades beyond BRCA1/2: Homologous recombination, hereditary cancer risk and a target for ovarian cancer therapy. Gynecol Oncol. 2015 May;137(2):343–50.

154. Bhat KP, Cortez D. RPA and RAD51: fork reversal, fork protection, and genome stability. Nat Struct Mol Biol. 2018 Jun;25(6):446–53.

155. Mazin AV, Mazina OM, Bugreev DV, Rossi MJ. Rad54, the motor of homologous recombination. DNA Repair. 2010 Mar;9(3):286–302.

156. Szakal B, Branzei D. Hot on RAD51C: structure and functions of RAD51C-XRCC3. Mol Oncol. 2023 Oct;17(10):1950–2.

157. Li X, Heyer WD. Homologous recombination in DNA repair and DNA damage tolerance. Cell Res. 2008 Jan;18(1):99–113.

158. Zahid S, Seif El Dahan M, Iehl F, Fernandez-Varela P, Le Du MH, Ropars V, et al. The Multifaceted Roles of Ku70/80. Int J Mol Sci. 2021 Apr 16;22(8):4134.

159. Chaplin AK, Hardwick SW, Stavridi AK, Buehl CJ, Goff NJ, Ropars V, et al. Cryo-EM of NHEJ supercomplexes provides insights into DNA repair. Mol Cell. 2021 Aug;81(16):3400-3409.e3.

160. Chen S, Lee L, Naila T, Fishbain S, Wang A, Tomkinson AE, et al. Structural basis of long-range to short-range synaptic transition in NHEJ. Nature. 2021 May 13;593(7858):294–8.

161. Daley JM, Sung P. 53BP1, BRCA1, and the Choice between Recombination and End Joining at DNA Double-Strand Breaks. Mol Cell Biol. 2014 Apr 1;34(8):1380–8.

162. McKinnon PJ, Caldecott KW. DNA Strand Break Repair and Human Genetic Disease. Annu Rev Genomics Hum Genet. 2007 Sep 1;8(1):37–55.

163. K.H. Chrzanowska. Eleven polish patients with microcephaly, immunodeficiency, and chromosomal instability: The Nijmegen breakage syndrome. 1995;

164. Maser RS, Zinkel R, Petrini JHJ. An alternative mode of translation permits production of a variant NBS1 protein from the common Nijmegen breakage syndrome allele. Nat Genet. 2001;27.

165. Włodarczyk M, Lejman M. Chromosomal instability associated with adverse outcome: a case report of patient with Nijmegen breakage syndrome and rapidly developed T-NHL with complex karyotype. Mol Cytogenet. 2020 Dec;13(1):35.

166. Chrzanowska KH, Gregorek H, Digweed M. Nijmegen breakage syndrome (NBS). 2012;

167. Mlody B, Wruck W, Martins S, Sperling K, Adjaye J. Nijmegen Breakage Syndrome fibroblasts and iPSCs: cellular models for uncovering disease-associated signaling pathways and establishing a screening platform for anti-oxidants. Sci Rep. 2017 Aug 8;7(1):7516.

168. Stracker TH, Petrini JHJ. The MRE11 complex: starting from the ends. Nat Rev Mol Cell Biol. 2011 Feb;12(2):90–103.

169. Jongmans W, Vuillaume M, Chrzanowska K, Smeets D, Sperling K, Hall J. Nijmegen Breakage Syndrome Cells Fail To Induce the p53-Mediated DNA Damage Response following Exposure to Ionizing Radiation. Mol Cell Biol. 1997 Sep 1;17(9):5016–22.

170. Martins S, Erichsen L, Datsi A, Wruck W, Goering W, Chatzantonaki E, et al. Impaired p53-Mediated DNA Damage Response Contributes to Microcephaly in Nijmegen Breakage Syndrome Patient-Derived Cerebral Organoids. Cells. 2022 Feb 25;11(5):802.

171. Hernández Borrero LJ, El-Deiry WS. Tumor suppressor p53: Biology, signaling pathways, and therapeutic targeting. Biochim Biophys Acta BBA - Rev Cancer. 2021 Aug;1876(1):188556.

172. Xiong Y, Zhang Y, Xiong S, Williams-Villalobo AE. A Glance of p53 Functions in Brain Development, Neural Stem Cells, and Brain Cancer. Biology. 2020 Sep 11;9(9):285.

173. Williams AB, Schumacher B. p53 in the DNA-Damage-Repair Process. Cold Spring Harb Perspect Med. 2016 May;6(5):a026070.

174. Olivier M, Hollstein M, Hainaut P. TP53 Mutations in Human Cancers: Origins, Consequences, and Clinical Use. Cold Spring Harb Perspect Biol. 2010 Jan 1;2(1):a001008–a001008.

175. Hwang BJ, Ford JM, Hanawalt PC, Chu G. Expression of the *p48* xeroderma pigmentosum gene is p53-dependent and is involved in global genomic repair. Proc Natl Acad Sci. 1999 Jan 19;96(2):424–8.

176. Adimoolam S, Ford JM. p53 and DNA damage-inducible expression of the xeroderma pigmentosum group C gene. Proc Natl Acad Sci. 2002 Oct;99(20):12985–90.

177. Wang YH, Ho TLF, Hariharan A, Goh HC, Wong YL, Verkaik NS, et al. Rapid recruitment of p53 to DNA damage sites directs DNA repair choice and integrity. Proc Natl Acad Sci. 2022 Mar 8;119(10):e2113233119.

178. Stracker TH, Usui T, Petrini JHJ. Taking the time to make important decisions: The checkpoint effector kinases Chk1 and Chk2 and the DNA damage response. DNA Repair. 2009 Sep 2;8(9):1047–54.

179. Hine CM, Li H, Xie L, Mao Z, Seluanov A, Gorbunova V. Regulation of Rad51 promoter. Cell Cycle. 2014 Jul;13(13):2038–45.

180. Lane DP, Cheok CF, Brown C, Madhumalar A, Ghadessy FJ, Verma C. Mdm2 and p53 are highly conserved from placozoans to man. Cell Cycle. 2010 Feb;9(3):540–7.

181. Barak Y, Juven T, Haffner R, Oren M. mdm2 expression is induced by wild type p53 activity. EMBO J. 1993 Feb;12(2):461–8.

182. Williams BR, Mirzoeva OK, Morgan WF, Lin J, Dunnick W, Petrini JHJ. A Murine Model of Nijmegen Breakage Syndrome. Curr Biol. 2002 Apr;12(8):648–53.

183. Zhu J, Petersen S, Tessarollo L, Nussenzweig A. Targeted disruption of the Nijmegen breakage syndrome gene NBS1 leads to early embryonic lethality in mice. Curr Biol. 2001 Jan;11(2):105–9.

184. Hustinx TWJ, Scheres JMJC, Weemaes CMR, ter Haar BGA, Janssen AH. Karyotype instability with multiple 7/14 and 7/7 rearrangements. Hum Genet. 1979 Jan;49(2):199–208.

185. Omi N, Tokuda Y, Ikeda Y, Ueno M, Mori K, Sotozono C, et al. Efficient and reliable establishment of lymphoblastoid cell lines by Epstein-Barr virus transformation from a limited amount of peripheral blood. Sci Rep. 2017 Mar 8;7(1):43833.

186. Tupler R, Marseglia GL, Stefanini M, Prosperi E, Chessa L, Nardo T, et al. A variant of the Nijmegen breakage syndrome with unusual cytogenetic features and intermediate cellular radiosensitivity. J Med Genet. 1997 Mar 1;34(3):196–202.

187. Seemanova E. Nijmegen breakage syndrome (NBS) with neurological abnormalities and without chromosomal instability. J Med Genet. 2005 Aug 23;43(3):218–24.

188. Waltes R, Kalb R, Gatei M, Kijas AW, Stumm M, Sobeck A, et al. Human RAD50 Deficiency in a Nijmegen Breakage Syndrome-like Disorder. Am J Hum Genet. 2009 May;84(5):605–16.

189. Berardinelli F, Sgura A, Di Masi A, Leone S, Cirrone GAP, Romano F, et al. Radiation-induced telomere length variations in normal and in Nijmegen Breakage Syndrome cells. Int J Radiat Biol. 2014 Jan;90(1):45–52.

190. Mlody B, Adjaye J. Generation of iPSC lines from a Nijmegen Breakage Syndrome patient. Stem Cell Res. 2015;4.

191. Prigione A, Fauler B, Lurz R, Lehrach H, Adjaye J. The Senescence-Related Mitochondrial/Oxidative Stress Pathway is Repressed in Human Induced Pluripotent Stem Cells. Stem Cells. 2010 Apr 1;28(4):721–33.

192. Bohndorf M, Ncube A, Spitzhorn LS, Enczmann J, Wruck W, Adjaye J. Derivation and characterization of integration-free iPSC line ISRM-UM51 derived from SIX2-positive renal cells isolated from urine of an African male expressing the CYP2D6 *4/*17 variant which confers intermediate drug metabolizing activity. Stem Cell Res. 2017 Dec;25:18–21.

193. Livak KJ, Schmittgen TD. Analysis of Relative Gene Expression Data Using Real-Time Quantitative PCR and the 2−ΔΔCT Method. Methods. 2001 Dec;25(4):402–8.

194. Gentleman RC, Carey VJ, Bates DM, Bolstad B, Dettling M, Dudoit S, et al. Bioconductor: open software development for computational biology and bioinformatics. Genome Biol. 2004;5(10):R80.

195. Carvalho BS, Irizarry RA. A framework for oligonucleotide microarray preprocessing. Bioinformatics. 2010 Oct 1;26(19):2363–7.

196. Warnes GR, Bolker B, Bonebakker L, Gentleman R, Liaw WHA, Lumley T, et al. gplots: Various R Programming Tools for Plotting Data [Internet]. 2015. Available from: http://CRAN.R-project.org/package=gplots

197. Graffmann N, Ring S, Kawala MA, Wruck W, Ncube A, Trompeter HI, et al. Modeling Nonalcoholic Fatty Liver Disease with Human Pluripotent Stem Cell-Derived Immature Hepatocyte-Like Cells Reveals Activation of PLIN2 and Confirms Regulatory Functions of Peroxisome Proliferator-Activated Receptor Alpha. Stem Cells Dev. 2016 Aug 1;25(15):1119–33.

198. Chen H, Boutros PC. VennDiagram: a package for the generation of highly-customizable Venn and Euler diagrams in R. BMC Bioinformatics. 2011;12(1):35.

199. Smyth GK. Linear Models and Empirical Bayes Methods for Assessing Differential Expression in Microarray Experiments. Stat Appl Genet Mol Biol [Internet]. 2004 [cited 2011 Oct 28];3(1). Available from: http://www.bepress.com/sagmb/vol3/iss1/art3

200. Falcon S, Gentleman R. Using GOstats to test gene lists for GO term association. Bioinforma Oxf Engl. 2007 Jan 15;23(2):257–8.

201. Wickham H. Ggplot2: elegant graphics for data analysis. New York: Springer; 2009. 212 p. (Use R!).

202. Kanehisa M, Furumichi M, Tanabe M, Sato Y, Morishima K. KEGG: new perspectives on genomes, pathways, diseases and drugs. Nucleic Acids Res. 2017 Jan 4;45(D1):D353–61.

203. Zhou Y, Zhou B, Pache L, Chang M, Khodabakhshi AH, Tanaseichuk O, et al. Metascape provides a biologist-oriented resource for the analysis of systems-level datasets. Nat Commun. 2019 Apr 3;10(1):1523.

204. Ihaka R, Gentleman R. R: A Language for Data Analysis and Graphics. 2024;

205. An H, Landis J T, Bailey A G, Marron J S, Dittmer D P. dr4pl: A Stable Convergence Algorithm for the 4 Parameter Logistic Model. R J. 2019;11(2):171.

206. Watanabe K, Ueno M, Kamiya D, Nishiyama A, Matsumura M, Wataya T, et al. A ROCK inhibitor permits survival of dissociated human embryonic stem cells. Nat Biotechnol. 2007 Jun;25(6):681–6.

207. Junop MS. Crystal structure of the Xrcc4 DNA repair protein and implications for end joining. EMBO J. 2000 Nov 15;19(22):5962–70.

208. Sottile ML, Nadin SB. Heat shock proteins and DNA repair mechanisms: an updated overview. Cell Stress Chaperones. 2018 May;23(3):303–15.

209. Li T, Su L, Lei Y, Liu X, Zhang Y, Liu X. DDIT3 and KAT2A Proteins Regulate TNFRSF10A and TNFRSF10B Expression in Endoplasmic Reticulum Stress-mediated Apoptosis in Human Lung Cancer Cells. J Biol Chem. 2015 Apr;290(17):11108–18.

210. Wookey P, Gupta P, Bittencourt L, Cheung S, Hare D, Furness S. Methods to measure calcitonin receptor activity, up-regulated in cell stress, apoptosis and autophagy. F1000Research. 2021 Oct 7;10:1019.

211. Mo W, Zhang JT. Human ABCG2: structure, function, and its role in multidrug resistance.

212. Sjakste N, Riekstiņa U. DNA damage and repair in the differentiation of stem cells and cells of connective cell lineages: A trigger or a complication? Eur J Histochem.

213. Christmann M, Boisseau C, Kitzinger R, Berac C, Allmann S, Sommer T, et al. Adaptive upregulation of DNA repair genes following benzo(a)pyrene diol epoxide protects against cell death at the expense of mutations. Nucleic Acids Res. 2016 Dec 15;44(22):10727–43.

214. Bruno S, Darzynkiewicz Z. Cell cycle dependent expression and stability of the nuclear protein detected by Ki-67 antibody in HL-60 cells. Cell Prolif. 1992 Jan;25(1):31–40.

215. Salic A, Mitchison TJ. A chemical method for fast and sensitive detection of DNA synthesis *in vivo*. Proc Natl Acad Sci. 2008 Feb 19;105(7):2415–20.

216. Guo F, Wang Y, Liu J, Mok SC, Xue F, Zhang W. CXCL12/CXCR4: a symbiotic bridge linking cancer cells and their stromal neighbors in oncogenic communication networks. Oncogene. 2016 Feb 18;35(7):816–26.

217. Fu L, Chen S, He G, Chen Y, Liu B. Targeting Extracellular Signal-Regulated Protein Kinase 1/2 (ERK1/2) in Cancer: An Update on Pharmacological Small-Molecule Inhibitors. J Med Chem. 2022 Oct 27;65(20):13561–73.

218. Yang Y, Cao Y. The impact of VEGF on cancer metastasis and systemic disease. Semin Cancer Biol. 2022 Nov;86:251–61.

219. Braicu, Buse, Busuioc, Drula, Gulei, Raduly, et al. A Comprehensive Review on MAPK: A Promising Therapeutic Target in Cancer. Cancers. 2019 Oct 22;11(10):1618.

220. Aliouat-Denis CM, Dendouga N, Van Den Wyngaert I, Goehlmann H, Steller U, Van De Weyer I, et al. p53-Independent Regulation of p21Waf1/Cip1 Expression and Senescence by Chk2. Mol Cancer Res. 2005 Nov 29;3(11):627–34.

221. Zaidi MR, Liebermann DA, editors. Gadd45 Stress Sensor Genes [Internet]. Cham: Springer International Publishing; 2022 [cited 2024 May 9]. (Advances in Experimental Medicine and Biology; vol. 1360). Available from: https://link.springer.com/10.1007/978-3-030-94804-7

222. Takahashi K, Okubo C, Nakamura M, Iwasaki M, Kawahara Y, Tabata T, et al. A stress-reduced passaging technique improves the viability of human pluripotent cells. Cell Rep Methods. 2022 Feb;2(2):100155.

223. Claassen DA, Desler MM, Rizzino A. ROCK inhibition enhances the recovery and growth of cryopreserved human embryonic stem cells and human induced pluripotent stem cells. Mol Reprod Dev. 2009 Aug;76(8):722–32.

224. Morris MLM, Baroneza JE, Teixeira P, Medina CTN, Cordoba MS, Versiani BR, et al. Partial 1q Duplications and Associated Phenotype. Mol Syndromol. 2015;6(6):297–303.

225. McKinnon PJ. DNA repair deficiency and neurological disease. Nat Rev Neurosci. 2009 Feb;10(2):100–12.

226. Frappart PO, Tong WM, Demuth I, Radovanovic I, Herceg Z, Aguzzi A, et al. An essential function for NBS1 in the prevention of ataxia and cerebellar defects. Nat Med. 2005 May;11(5):538–44.

227. Zhou Z, Bruhn C, Wang ZQ. Differential function of NBS1 and ATR in neurogenesis. DNA Repair. 2012 Feb;11(2):210–21.

228. Zhou S, Szczesna K, Ochalek A, Kobolák J, Varga E, Nemes C, et al. Neurosphere Based Differentiation of Human iPSC Improves Astrocyte Differentiation. Stem Cells Int. 2016;2016:1–15.

229. Bell S, Hettige N, Silveira H, Peng H, Wu H, Jefri M, et al. Differentiation of Human Induced Pluripotent Stem Cells (iPSCs) into an Effective Model of Forebrain Neural Progenitor Cells and Mature Neurons. BIO-Protoc [Internet]. 2019 [cited 2024 Apr 12];9(5). Available from: https://bio-protocol.org/e3188

230. Zhou ZW, Kirtay M, Schneble N, Yakoub G, Ding M, Rüdiger T, et al. NBS1 interacts with Notch signaling in neuronal homeostasis. Nucleic Acids Res. 2020 Nov 4;48(19):10924–39.

231. Qian X, Song H, Ming G li. Brain organoids: advances, applications and challenges. Development. 2019 Apr 15;146(8):dev166074.

232. Buscemi G, Savio C, Zannini L, Miccichè F, Masnada D, Nakanishi M, et al. Chk2 Activation Dependence on Nbs1 after DNA Damage. Mol Cell Biol. 2001 Aug 1;21(15):5214–22.

233. Curtin JF, Cotter TG. Live and let die: regulatory mechanisms in Fas-mediated apoptosis. Cell Signal. 2003 Nov;15(11):983–92.

234. Solodeev I, Meilik B, Volovitz I, Sela M, Manheim S, Yarkoni S, et al. Fas-L promotes the stem cell potency of adipose-derived mesenchymal cells. Cell Death Dis. 2018 Jun 11;9(6):695.

235. Rippo MR, Babini L, Prattichizzo F, Graciotti L, Fulgenzi G, Tomassoni Ardori F, et al. Low FasL levels promote proliferation of human bone marrow-derived mesenchymal stem cells, higher levels inhibit their differentiation into adipocytes. Cell Death Dis. 2013 Apr 18;4(4):e594–e594.

236. Chen K, Long Q, Wang T, Zhao D, Zhou Y, Qi J, et al. Gadd45a is a heterochromatin relaxer that enhances iPS cell generation. EMBO Rep. 2016 Nov;17(11):1641–56.

237. Chandramouly G. Gadd45 in DNA Demethylation and DNA Repair. In: Zaidi MR, Liebermann DA, editors. Gadd45 Stress Sensor Genes [Internet]. Cham: Springer International Publishing; 2022. p. 55–67. Available from: https://doi.org/10.1007/978-3-030-94804-7_4

238. Moskalev AA, Smit-McBride Z, Shaposhnikov MV, Plyusnina EN, Zhavoronkov A, Budovsky A, et al. Gadd45 proteins: Relevance to aging, longevity and age-related pathologies. Ageing Res Rev. 2012 Jan;11(1):51–66.

239. Mo W, Zhang JT. Human ABCG2: structure, function, and its role in multidrug resistance. Int J Biochem Mol Biol. 2012;3(1):1–27.

240. Vitale I, Manic G, De Maria R, Kroemer G, Galluzzi L. DNA Damage in Stem Cells. Mol Cell. 2017 May;66(3):306–19.

241. Maynard S, Swistowska AM, Lee JW, Liu Y, Liu ST, Da Cruz AB, et al. Human Embryonic Stem Cells Have Enhanced Repair of Multiple Forms of DNA Damage. Stem Cells. 2008 Sep 1;26(9):2266–74.

242. Momcilovic O, Knobloch L, Fornsaglio J, Varum S, Easley C, Schatten G. DNA Damage Responses in Human Induced Pluripotent Stem Cells and Embryonic Stem Cells. Capogrossi MC, editor. PLoS ONE. 2010 Oct 15;5(10):e13410.

243. Liedtke S, Biebernick S, Radke TF, Stapelkamp D, Coenen C, Zaehres H, et al. DNA Damage Response in Neonatal and Adult Stromal Cells Compared With Induced Pluripotent Stem Cells: DNA Damage Defense in iPSCs Versus Stromal Cells. STEM CELLS Transl Med. 2015 Jun;4(6):576–89.

244. Chang HM, Martinez NJ, Thornton JE, Hagan JP, Nguyen KD, Gregory RI. Trim71 cooperates with microRNAs to repress Cdkn1a expression and promote embryonic stem cell proliferation. Nat Commun. 2012 Jun 26;3(1):923.

245. Shen T, Huang S. The Role of Cdc25A in the Regulation of Cell Proliferation and Apoptosis. Anticancer Agents Med Chem. 2012 May 1;12(6):631–9.

246. Lin T, Lin Y. p53 switches off pluripotency on differentiation. Stem Cell Res Ther. 2017 Dec;8(1):44.

247. Lin Y, Cheng Z, Yang Z, Zheng J, Lin T. DNp73 improves generation efficiency of human induced pluripotent stem cells. BMC Cell Biol. 2012 Dec;13(1):9.

248. Mani C, Reddy PH, Palle K. DNA repair fidelity in stem cell maintenance, health, and disease. Biochim Biophys Acta BBA - Mol Basis Dis. 2020 Apr;1866(4):165444.

249. Piberger AL, Krüger CT, Strauch BM, Schneider B, Hartwig A. BPDE-induced genotoxicity: relationship between DNA adducts, mutagenicity in the in vitro PIG-A assay, and the transcriptional response to DNA damage in TK6 cells. Arch Toxicol. 2018 Jan;92(1):541–51.

250. Souza T, Jennen D, van Delft J, van Herwijnen M, Kyrtoupolos S, Kleinjans J. New insights into BaP-induced toxicity: role of major metabolites in transcriptomics and contribution to hepatocarcinogenesis. Arch Toxicol. 2016 Jun;90(6):1449–58.

251. Hockley SL, Arlt VM, Brewer D, te Poele R, Workman P, Giddings I, et al. AHR- and DNA-Damage-Mediated Gene Expression Responses Induced by Benzo(*a*)pyrene in Human Cell Lines. Chem Res Toxicol. 2007 Dec 1;20(12):1797–810.

252. Dumitru R, Gama V, Fagan BM, Bower JJ, Swahari V, Pevny LH, et al. Human Embryonic Stem Cells Have Constitutively Active Bax at the Golgi and Are Primed to Undergo Rapid Apoptosis. Mol Cell. 2012 Jun;46(5):573–83.

253. Lin T, Chao C, Saito S, Mazur SJ, Murphy ME, Appella E, et al. p53 induces differentiation of mouse embryonic stem cells by suppressing Nanog expression. Nat Cell Biol. 2005 Feb;7(2):165–71.

254. Li M, He Y, Dubois W, Wu X, Shi J, Huang J. Distinct Regulatory Mechanisms and Functions for p53-Activated and p53-Repressed DNA Damage Response Genes in Embryonic Stem Cells. Mol Cell. 2012 Apr;46(1):30–42.

255. Jeffy BD, Chen EJ, Gudas JM, Romagnolo DF. Disruption of Cell Cycle Kinetics by Benzo[a]pyrene: Inverse Expression Patterns of BRCA-1 and p53 in MCF-7 Cells Arrested in S and G2. Neoplasia. 2000 Sep;2(5):460–70.

256. Hamouchene H, Arlt VM, Giddings I, Phillips DH. Influence of cell cycle on responses of MCF-7 cells to benzo[a]pyrene. BMC Genomics. 2011 Dec;12(1):333.

257. Wei X, Xu H, Kufe D. Human MUC1 oncoprotein regulates p53-responsive gene transcription in the genotoxic stress response. Cancer Cell. 2005 Feb;7(2):167–78.

258. Wang XW, Zhan Q, Coursen JD, Khan MA, Kontny HU, Yu L, et al. GADD45 induction of a G_2 /M cell cycle checkpoint. Proc Natl Acad Sci. 1999 Mar 30;96(7):3706–11.

259. Jin S, Tong T, Fan W, Fan F, Antinore MJ, Zhu X, et al. GADD45-induced cell cycle G2-M arrest associates with altered subcellular distribution of cyclin B1 and is independent of p38 kinase activity. Oncogene. 2002 Dec 12;21(57):8696–704.

260. Smith ML, Kontny HU, Zhan Q, Sreenath A, O'Connor PM, Fornace AJ. Antisense GADD45 expression results in decreased DNA repair and sensitizes cells to u.v.-irradiation or cisplatin. Oncogene. 1996 Nov 21;13(10):2255–63.

261. Smith ML, Ford JM, Hollander MC, Bortnick RA, Amundson SA, Seo YR, et al. p53-Mediated DNA Repair Responses to UV Radiation: Studies of Mouse Cells Lacking *p53* , *p21* , and/or *gadd45* Genes. Mol Cell Biol. 2000 May 1;20(10):3705–14.

262. Hollander MC, Kovalsky O, Salvador JM, Kim KE, Patterson AD, Haines DC, et al. Dimethylbenzanthracene carcinogenesis in Gadd45a-null mice is associated with decreased DNA repair and increased mutation frequency. Cancer Res. 2001 Mar 15;61(6):2487–91.

263. Hockley SL, Arlt VM, Jahnke G, Hartwig A, Giddings I, Phillips DH. Identification through microarray gene expression analysis of cellular responses to benzo(a)pyrene and its diol-epoxide that are dependent or independent of p53. Carcinogenesis. 2008 Jan;29(1):202–10.

264. Allmann S, Mayer L, Olma J, Kaina B, Hofmann TG, Tomicic MT, et al. Benzo[a]pyrene represses DNA repair through altered E2F1/E2F4 function marking an early event in DNA damage-induced cellular senescence. Nucleic Acids Res. 2020 Dec 2;48(21):12085–101.

265. Dreij K, Rhrissorrakrai K, Gunsalus KC, Geacintov NE, Scicchitano DA. Benzo[a]pyrene diol epoxide stimulates an inflammatory response in normal human lung fibroblasts through a p53 and JNK mediated pathway. Carcinogenesis. 2010 Jun;31(6):1149–57.

266. Kussie PH, Gorina S, Marechal V, Elenbaas B, Moreau J, Levine AJ, et al. Structure of the MDM2 Oncoprotein Bound to the p53 Tumor Suppressor Transactivation Domain. Science. 1996 Nov 8;274(5289):948–53.

267. Scherer SJ, Maier SM, Seifert M, Hanselmann RG, Zang KD, Müller-Hermelink HK, et al. p53 and c-Jun Functionally Synergize in the Regulation of the DNA Repair Gene hMSH2 in Response to UV. J Biol Chem. 2000 Dec;275(48):37469–73.

268. Schreiber M, Kolbus A, Piu F, Szabowski A, Mohle-Steinlein U, Tian J, et al. Control of cell cycle progression by c-Jun is p53 dependent. Genes Dev. 1999 Mar 1;13(5):607–19.

269. Xia Y, Yang W, Bu W, Ji H, Zhao X, Zheng Y, et al. Differential Regulation of c-Jun Protein Plays an Instrumental Role in Chemoresistance of Cancer Cells. J Biol Chem. 2013 Jul;288(27):19321–9.

270. Wisdom R. c-Jun regulates cell cycle progression and apoptosis by distinct mechanisms. EMBO J. 1999 Jan 4;18(1):188–97.

271. Potapova O, Basu S, Mercola D, Holbrook NJ. Protective Role for c-Jun in the Cellular Response to DNA Damage. J Biol Chem. 2001 Jul;276(30):28546–53.

272. Kasibhatla S, Brunner T, Genestier L, Echeverri F, Mahboubi A, Green DR. DNA Damaging Agents Induce Expression of Fas Ligand and Subsequent Apoptosis in T Lymphocytes via the Activation of NF-□B and AP-. Mol Cell.

273. Roos WP, Kaina B. DNA damage-induced cell death: From specific DNA lesions to the DNA damage response and apoptosis. Cancer Lett. 2013 May;332(2):237–48.

274. Li QV, Dixon G, Verma N, Rosen BP, Gordillo M, Luo R, et al. Genome-scale screens identify JNK–JUN signaling as a barrier for pluripotency exit and endoderm differentiation. Nat Genet. 2019 Jun;51(6):999–1010.

275. Suvorova II, Kozhukharova IV, Nikolsky NN, Pospelov VA. Activation of ATM/ATR signaling in human embryonic stem cells after DNA damage. Cell Tissue Biol. 2014 Mar;8(2):122–32.

276. Reinhardt HC, Aslanian AS, Lees JA, Yaffe MB. p53-Deficient Cells Rely on ATM- and ATR-Mediated Checkpoint Signaling through the p38MAPK/MK2 Pathway for Survival after DNA Damage. Cancer Cell. 2007 Feb;11(2):175–89.

277. Ward IM, Chen J. Histone H2AX Is Phosphorylated in an ATR-dependent Manner in Response to Replicational Stress. J Biol Chem. 2001 Dec;276(51):47759–62.

278. Lu J, Wei Q, Bondy ML, Li D, Brewster A, Shete S, et al. Polymorphisms and haplotypes of the NBS1 gene are associated with risk of sporadic breast cancer in non-Hispanic white women <=55 years. Carcinogenesis. 2006 May 16;27(11):2209–16.

279. Ribeiro-Silva C, Sabatella M, Helfricht A, Marteijn JA, Theil AF, Vermeulen W, et al. Ubiquitin and TFIIH-stimulated DDB2 dissociation drives DNA damage handover in nucleotide excision repair. Nat Commun. 2020 Sep 28;11(1):4868.

280. Zhang Y, Wu X, Guo D, Rechkoblit O, Geacintov NE, Wang Z. Two-step error-prone bypass of the (+)- and (−)-trans-anti-BPDE-N2-dG adducts by human DNA polymerases □ and □. Mutat Res. 2002;

281. Chiapperino D, Kroth H, Kramarczuk IH, Sayer JM, Masutani C, Hanaoka F, et al. Preferential Misincorporation of Purine Nucleotides by Human DNA Polymerase η Opposite Benzo[a]pyrene 7,8-Diol 9,10-Epoxide Deoxyguanosine Adducts. J Biol Chem. 2002 Apr;277(14):11765–71.

282. Guo Y, Pan W, Liu S, Shen Z, Xu Y, Hu L. ERK/MAPK signalling pathway and tumorigenesis (Review). Exp Ther Med [Internet]. 2020 Jan 15 [cited 2024 May 10]; Available from: http://www.spandidos-publications.com/10.3892/etm.2020.8454

283. Looi CK, Hii LW, Ngai SC, Leong CO, Mai CW. The Role of Ras-Associated Protein 1 (Rap1) in Cancer: Bad Actor or Good Player? Biomedicines. 2020 Sep 7;8(9):334.

284. Lu X, Shao J, Li H, Yu Y. Early whole-genome transcriptional response induced by benzo[a]pyrene diol epoxide in a normal human cell line. Genomics. 2009 Apr;93(4):332–42.

285. Wang J, Lu X, Sakk V, Klein CA, Rudolph KL. Senescence and apoptosis block hematopoietic activation of quiescent hematopoietic stem cells with short telomeres. Blood. 2014 Nov 20;124(22):3237–40.

286. Yamashita M, Nitta E, Suda T. Aspp1 Preserves Hematopoietic Stem Cell Pool Integrity and Prevents Malignant Transformation. Cell Stem Cell. 2015 Jul;17(1):23–34.

287. Cai X, Gao L, Teng L, Ge J, Oo ZM, Kumar AR, et al. Runx1 Deficiency Decreases Ribosome Biogenesis and Confers Stress Resistance to Hematopoietic Stem and Progenitor Cells. Cell Stem Cell. 2015 Aug;17(2):165–77.

288. Inomata K, Aoto T, Binh NT, Okamoto N, Tanimura S, Wakayama T, et al. Genotoxic Stress Abrogates Renewal of Melanocyte Stem Cells by Triggering Their Differentiation. Cell. 2009 Jun;137(6):1088–99.

289. Schneider L, Pellegatta S, Favaro R, Pisati F, Roncaglia P, Testa G, et al. DNA Damage in Mammalian Neural Stem Cells Leads to Astrocytic Differentiation Mediated by BMP2 Signaling through JAK-STAT. Stem Cell Rep. 2013 Aug;1(2):123–38.

290. Barazzuol L, Ju L, Jeggo PA. A coordinated DNA damage response promotes adult quiescent neural stem cell activation. Hamada H, editor. PLOS Biol. 2017 May 10;15(5):e2001264.

291. Homma H, Tanaka H, Jin M, Jin X, Huang Y, Yoshioka Y, et al. DNA damage in embryonic neural stem cell determines FTLDs' fate via early-stage neuronal necrosis. Life Sci Alliance. 2021 Jul;4(7):e202101022.

292. Luo LZ, Gopalakrishna-Pillai S, Nay SL, Park SW, Bates SE, Zeng X, et al. DNA Repair in Human Pluripotent Stem Cells Is Distinct from That in Non-Pluripotent Human Cells. Emanueli C, editor. PLoS ONE. 2012 Mar 6;7(3):e30541.

293. Alt FW, Schwer B. DNA double-strand breaks as drivers of neural genomic change, function, and disease. DNA Repair. 2018 Nov;71:158–63.

294. Wu F, Wu D, Ren Y, Huang Y, Feng B, Zhao N, et al. Generation of hepatobiliary organoids from human induced pluripotent stem cells. J Hepatol. 2019 Jun;70(6):1145–58.

295. Gitlin D, Perricelli A. Synthesis of a-Fetoprotein by Liver, Yolk Sac, and Gastrointestinal Tract of the Human Conceptus.

296. Thakur A, Park K, Cullum R, Fuglerud BM, Khoshnoodi M, Drissler S, et al. HNF4A guides the MLL4 complex to establish and maintain H3K4me1 at gene regulatory elements. Commun Biol. 2024 Jan 31;7(1):144.

297. Roll GR, Willenbring H. Transplanted nonviable human hepatocytes produce appreciable serum albumin levels in mice. Stem Cell Res. 2010 Nov;5(3):267–70.

298. Hamesch K, Guldiken N, Aly M, Hüser N, Hartmann D, Rufat P, et al. Serum keratin 19 (CYFRA21-1) links ductular reaction with portal hypertension and outcome of various advanced liver diseases. BMC Med. 2020 Dec;18(1):336.

299. Bonzo JA, Ferry CH, Matsubara T, Kim JH, Gonzalez FJ. Suppression of Hepatocyte Proliferation by Hepatocyte Nuclear Factor 4α in Adult Mice. J Biol Chem. 2012 Mar;287(10):7345–56.

300. Ning BF, Ding J, Yin C, Zhong W, Wu K, Zeng X, et al. Hepatocyte Nuclear Factor 4α Suppresses the Development of Hepatocellular Carcinoma. Cancer Res. 2010 Oct 1;70(19):7640–51.

301. Kreuzer K, Böhmert L, Alhalabi D, Buhrke T, Lampen A, Braeuning A. Identification of a transcriptomic signature of food-relevant genotoxins in human HepaRG hepatocarcinoma cells. Food Chem Toxicol. 2020 Jun;140:111297.

302. Jennen DGJ, Magkoufopoulou C, Ketelslegers HB, Van Herwijnen MHM, Kleinjans JCS, Van Delft JHM. Comparison of HepG2 and HepaRG by Whole-Genome Gene Expression Analysis for the Purpose of Chemical Hazard Identification. Toxicol Sci. 2010 May;115(1):66–79.

303. Kaji K, Factor VM, Andersen JB, Durkin ME, Tomokuni A, Marquardt JU, et al. DNMT1 is a required genomic regulator for murine liver histogenesis and regeneration. Hepatology. 2016 Aug;64(2):582–98.

304. Kossatz U, Breuhahn K, Wolf B, Hardtke-Wolenski M, Wilkens L, Steinemann D, et al. The cyclin E regulator cullin 3 prevents mouse hepatic progenitor cells from becoming tumor-initiating cells. J Clin Invest. 2010 Nov 1;120(11):3820–33.

305. Liu Y, Higashitsuji H, Itoh K, Yamaguchi K, Umemura A, Itoh Y, et al. *Onecut1* partially contributes to the liver progenitor cell transition and acquisition of metastatic potential in hepatocellular carcinoma [Internet]. 2022 [cited 2024 May 16]. Available from: http://biorxiv.org/lookup/doi/10.1101/2022.09.20.508738

306. Zannini L, Delia D, Buscemi G. CHK2 kinase in the DNA damage response and beyond. J Mol Cell Biol. 2014 Dec 1;6(6):442–57.

307. Mustofa MdK, Tanoue Y, Tateishi C, Vaziri C, Tateishi S. Roles of CHK2 / CHEK2 in guarding against environmentally induced DNA damage and replication-stress. Environ Mol Mutagen. 2020 Aug;61(7):730–5.

308. Lin YW, Wang JL, Chen HM, Zhang YJ, Rong-Lu, Ren LL, et al. Folic Acid supplementary reduce the incidence of adenocarcinoma in a mouse model of colorectal cancer: microarray gene expression profile. J Exp Clin Cancer Res. 2011 Dec;30(1):116.

309. Cahill T, Da Silveira WA, Renaud L, Wang H, Williamson T, Chung D, et al. Investigating the effects of chronic low-dose radiation exposure in the liver of a hypothermic zebrafish model. Sci Rep. 2023 Jan 17;13(1):918.

310. Stowers SJ, Anderson MW. Formation and persistence of benzo(a)pyrene metabolite-DNA adducts. Environ Health Perspect. 1985 Oct;62:31–9.

311. Van Alstyne M, Simon CM, Sardi SP, Shihabuddin LS, Mentis GZ, Pellizzoni L. Dysregulation of Mdm2 and Mdm4 alternative splicing underlies motor neuron death in spinal muscular atrophy. Genes Dev. 2018 Aug 1;32(15–16):1045–59.

312. Engel T, Sanz-Rodgriguez A, Jimenez-Mateos EM, Concannon CG, Jimenez-Pacheco A, Moran C, et al. CHOP regulates the p53–MDM2 axis and is required for neuronal survival after seizures. Brain. 2013 Feb;136(2):577–92.

313. Barrio E, Vecino R, Sánchez-Morán I, Rodríguez C, Suárez-Pindado A, Bolaños JP, et al. Preconditioning-Activated AKT Controls Neuronal Tolerance to Ischemia through the MDM2–p53 Pathway. Int J Mol Sci. 2021 Jul 6;22(14):7275.

314. Thotala D, Hallahan D, Yazlovitskaya E. Glycogen synthase kinase 3b inhibitors protect hippocampal neurons from radiation-induced apoptosis by regulating MDM2-p53 pathway. Cell Death Differ.

315. Jurk D, Wang C, Miwa S, Maddick M, Korolchuk V, Tsolou A, et al. Postmitotic neurons develop a p21-dependent senescence-like phenotype driven by a DNA damage response. Aging Cell. 2012 Dec;11(6):996–1004.

316. Sah E, Krishnamurthy S, Ahmidouch MY, Gillispie GJ, Milligan C, Orr ME. The Cellular Senescence Stress Response in Post-Mitotic Brain Cells: Cell Survival at the Expense of Tissue Degeneration. Life. 2021 Mar 11;11(3):229.

317. Kress JM, Dio LD, Heck L, Pulliero A, Izzotti A, Laarmann K, et al. Human primary endothelial cells are impaired in nucleotide excision repair and sensitive to benzo[a]pyrene compared with smooth muscle cells and pericytes. Sci Rep. 2019 Sep 24;9(1):13800.

318. Ling X, Yang W, Zou P, Zhang G, Wang Z, Zhang X, et al. TERT regulates telomere-related senescence and apoptosis through DNA damage response in male germ cells exposed to BPDE in vitro and to B[a]P in vivo. Environ Pollut. 2018 Apr;235:836–49.

319. Li X, Cao G, Liu X, Tang TS, Guo C, Liu H. Polymerases and DNA Repair in Neurons: Implications in Neuronal Survival and Neurodegenerative Diseases. Front Cell Neurosci. 2022 Jun 30;16:852002.

Supplementary figures

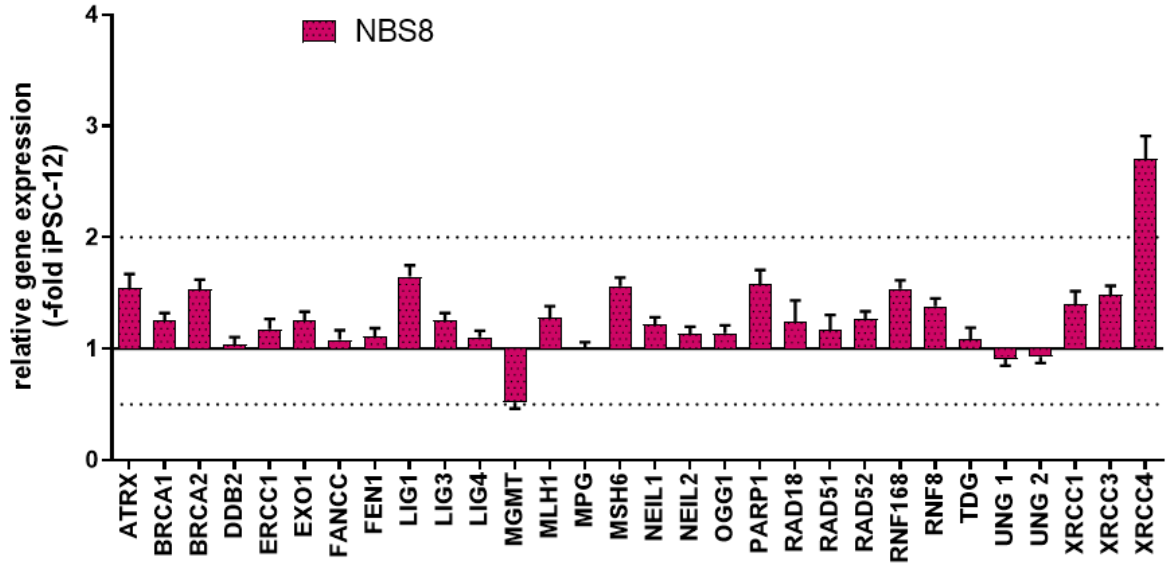

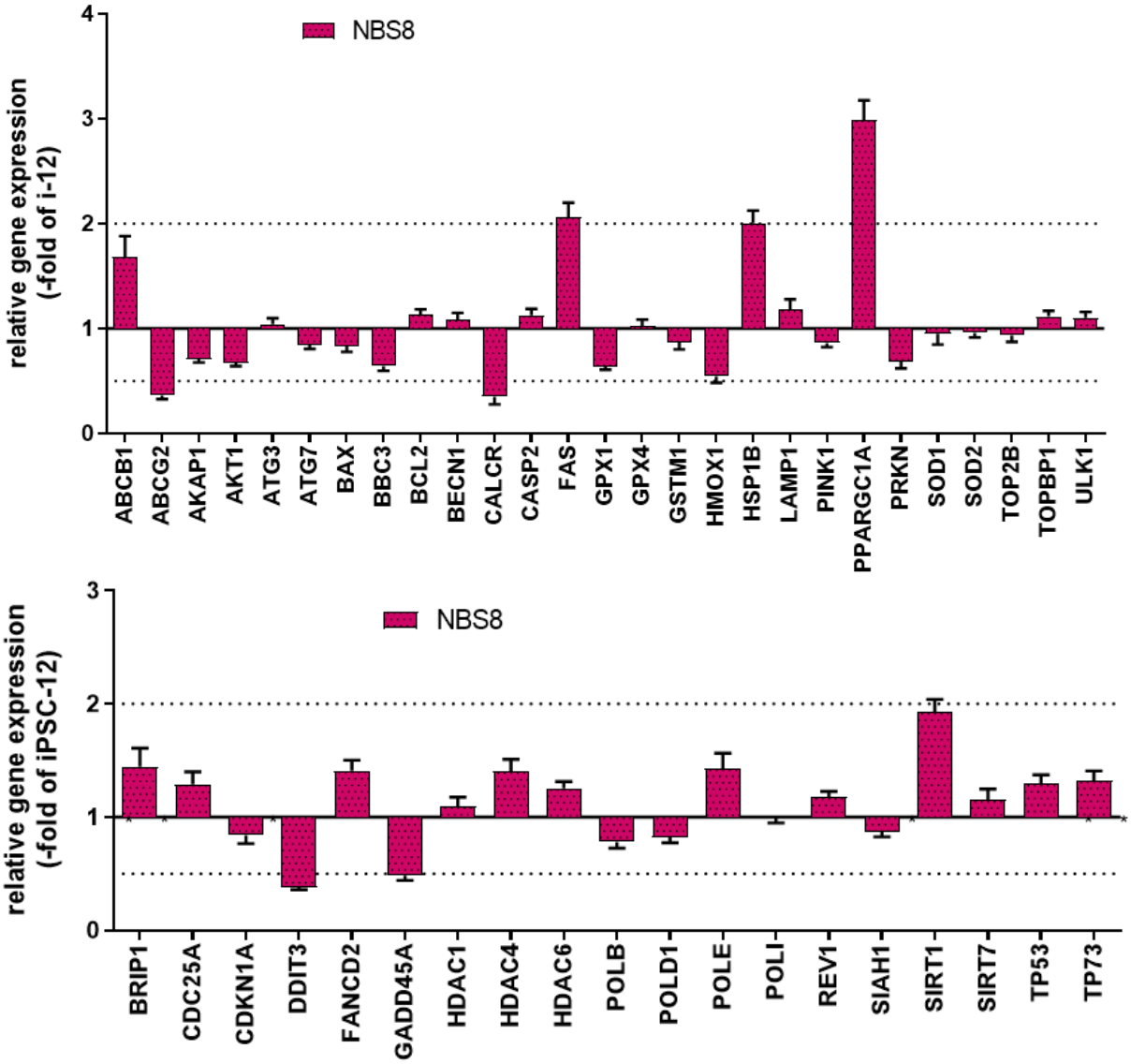

Supplementary Figure 1: Comparative gene expression of 76 genes involved in genotoxic exposure response in NBS8 and iPSC-12 hiPSCs. Fold change of NBS8 is shown, iPSC-12 hiPSCs were used as control. Mean of 3 technical triplicates, +/- standard deviation of the mean.

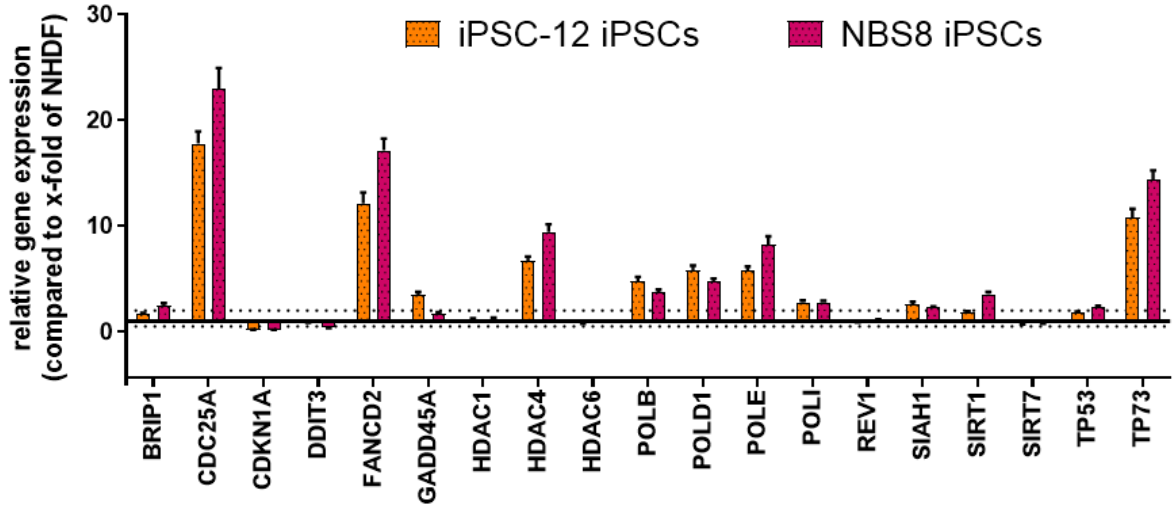

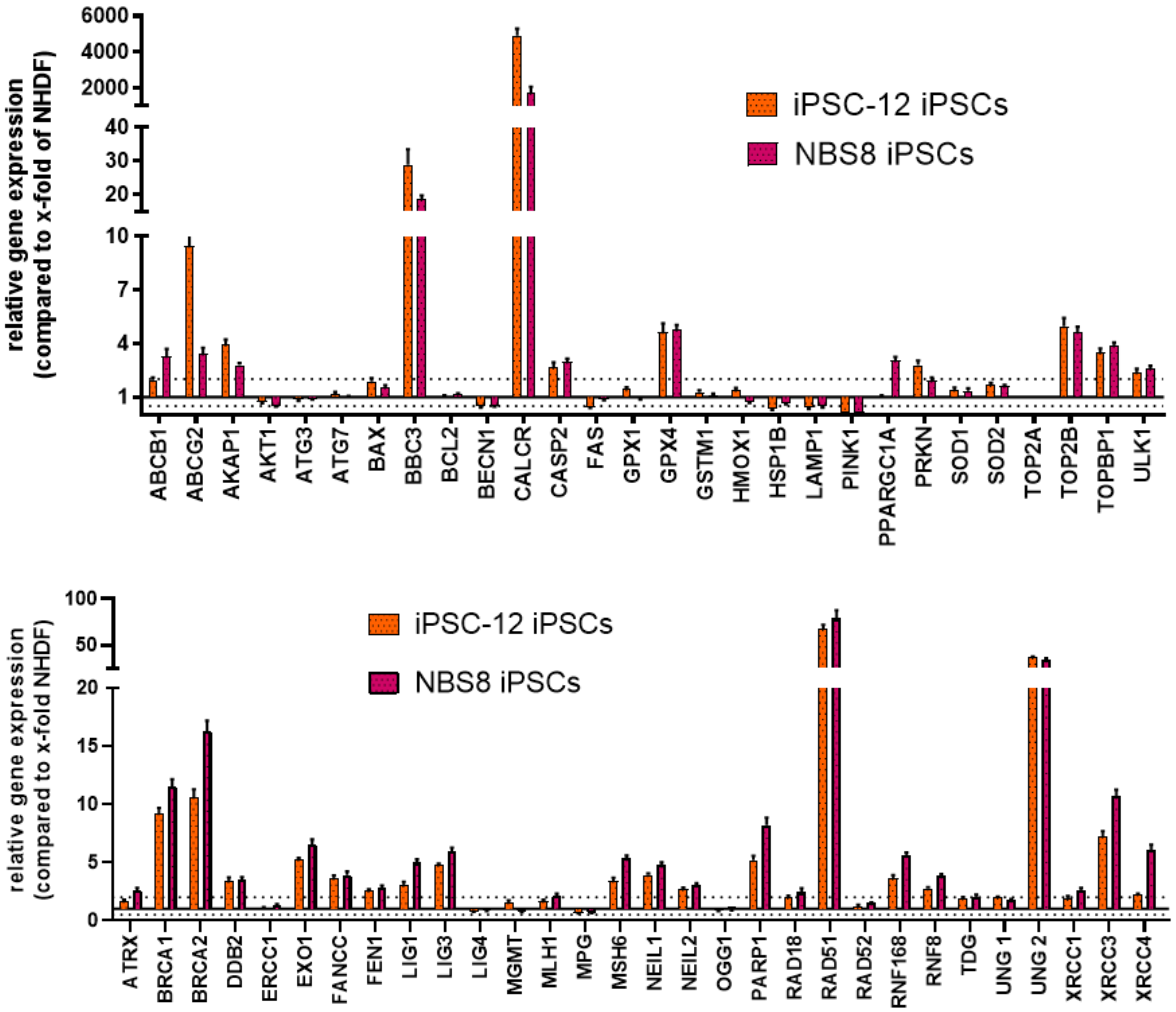

Supplementary Figure 2: Comparative gene expression of 76 genes involved in genotoxic exposure response in hiPSCs and NHDF Fold change of NBS8 and iPSC-12 hiPSCs is shown, NHDF were used as control. Mean of 3 technical triplicates, +/- standard deviation of the mean.

Universitätsklinikum
Düsseldorf

Heinrich Heine
Universität
Düsseldorf

Institut für Humangenetik

Institut für Humangenetik Postfach 101007, D-40001 Düsseldorf

An Herrn Prof. Dr. Adjaye
Institut für Stammzellforschung
Geb.14.80
Moorenstr. 5
40225 Düsseldorf

Direktorin
Prof. Dr. med. Dagmar Wieczorek
Telefon 0211 81-06795
Fax 0211 81-06083
humangenetik@uni-duesseldorf.de
Genetische Beratungsstelle
Mo, Di, Do und Fr, nach telefonischer Vereinbarung, ☎ (0211) 81-06088

Webseite des Instituts
www.uniklinik-duesseldorf.de/humangenetik

Ansprechpartner:	Durchwahl:	E-Mail:	Datum: 21.06.2022
Prof. Dr. med. Dagmar Wieczorek	0211 81-06795	humangenetik@uni-duesseldorf.de	

Zytogenetische Begutachtung Ihrer Zelllinie iPSC 263 (Nimegen Breakage Syndrom).
N. Frau Bohndorf // Geb. 14.80 // Institut für Stammzellforschung // hier

Bearbeitungsnummer: 54109

Sehr geehrter Herr Prof. Adjaye,

Probeneingang: Zellkultur 07.06.2022 Abnahmedatum: ?

Verdachtsdiagnose: Zelllinie
Initialer Befund: keiner

Kulturansätze: Langzeitkultur

Labor
0211 81-05131
Frau Dr. B. Hildebrandt
0211 81-06788

Bänderungstechnik: GTG
unauffällig (150-400 Bd.)
auffällig (Bd.)

25 Mitosen ausgewertet
0 Unauffällig männlich ☐ weiblich ☐
25 Klonal verändert
0 Einzelzellaberration/en

Karyotyp: 46,XX,dup(1)(q12q42)[25]

Beurteilung: Wir fanden in der Zelllinie **iPSC 263** in 25 Mitosen einen strukturell veränderten weiblichen Karyotyp. Wir fanden in allen Mitosen eine Duplikation des langen Arms von Chromosom 1. Der lange Arm lag somit partiell trisom vor.

Die Zelllinie ist zytogenetisch auffällig.

Mit freundlichen Grüßen,

(Dr. rer. nat. B. Hildebrandt) (Prof. Dr. med. Dagmar Wieczorek)

Dieser Befund wurde im Rahmen von diagnostischen Untersuchungen erstellt und darf nur mit Zustimmung der Institutsleitung für wissenschaftliche Zwecke verwendet werden.

Das Institut ist nach DIN EN ISO 15189 im Bereich Medizinische Laboratoriumsdiagnostik für die in der Urkunde (s. Homepage) aufgeführten Prüfverfahren akkreditiert.

DAkkS Deutsche Akkreditierungsstelle D-ML-13362-03-00

Supplementary Figure 3: Karyotype report from NBS2 iPSC line.

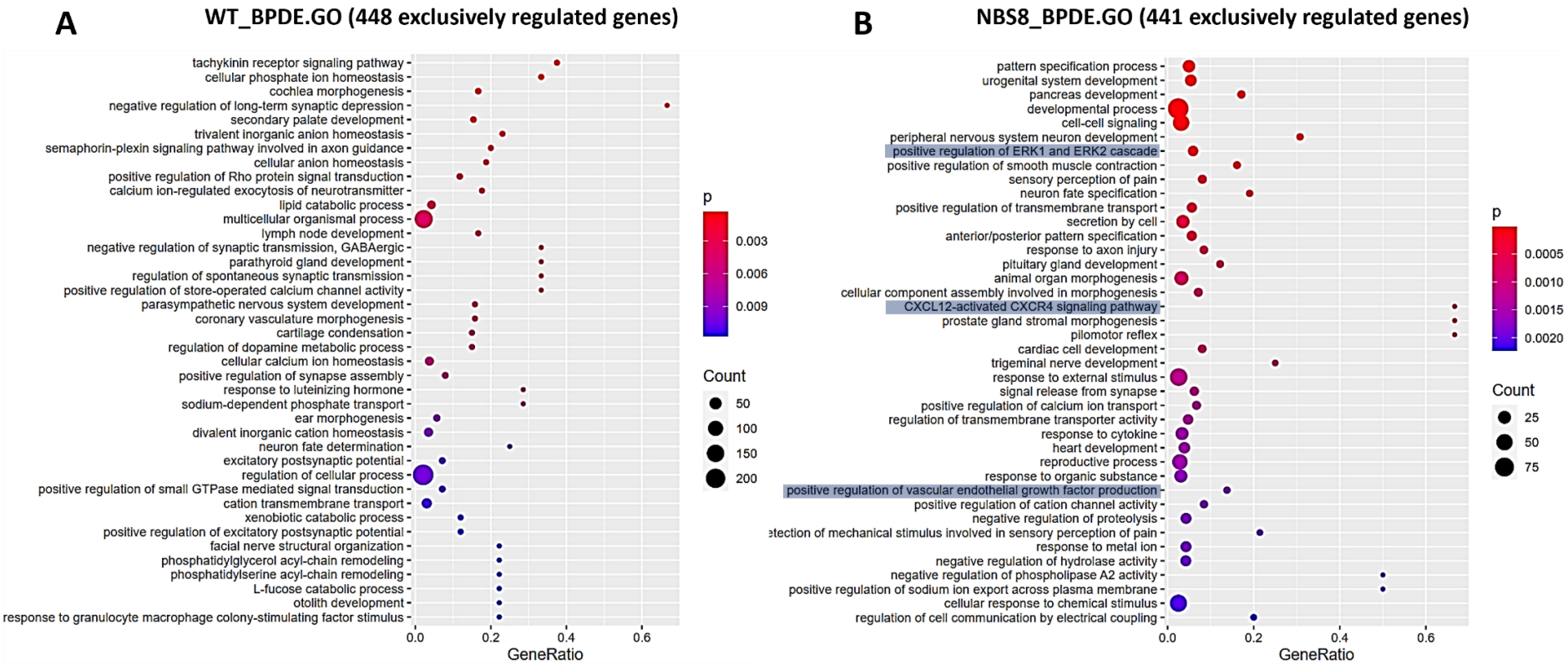

Supplementary Figure 4: BPDE treatment enhances cancer-related GO clusters in NBS8 ihPSCs. Cancer-related clusters are highlighted in purple. **(A)** GO from 448 genes exclusively regulated in WT hiPSCs after BPDE treatment. **(B)** GO from 441 genes exclusively regulated in NBS8 hiPSCs after BPDE treatment.

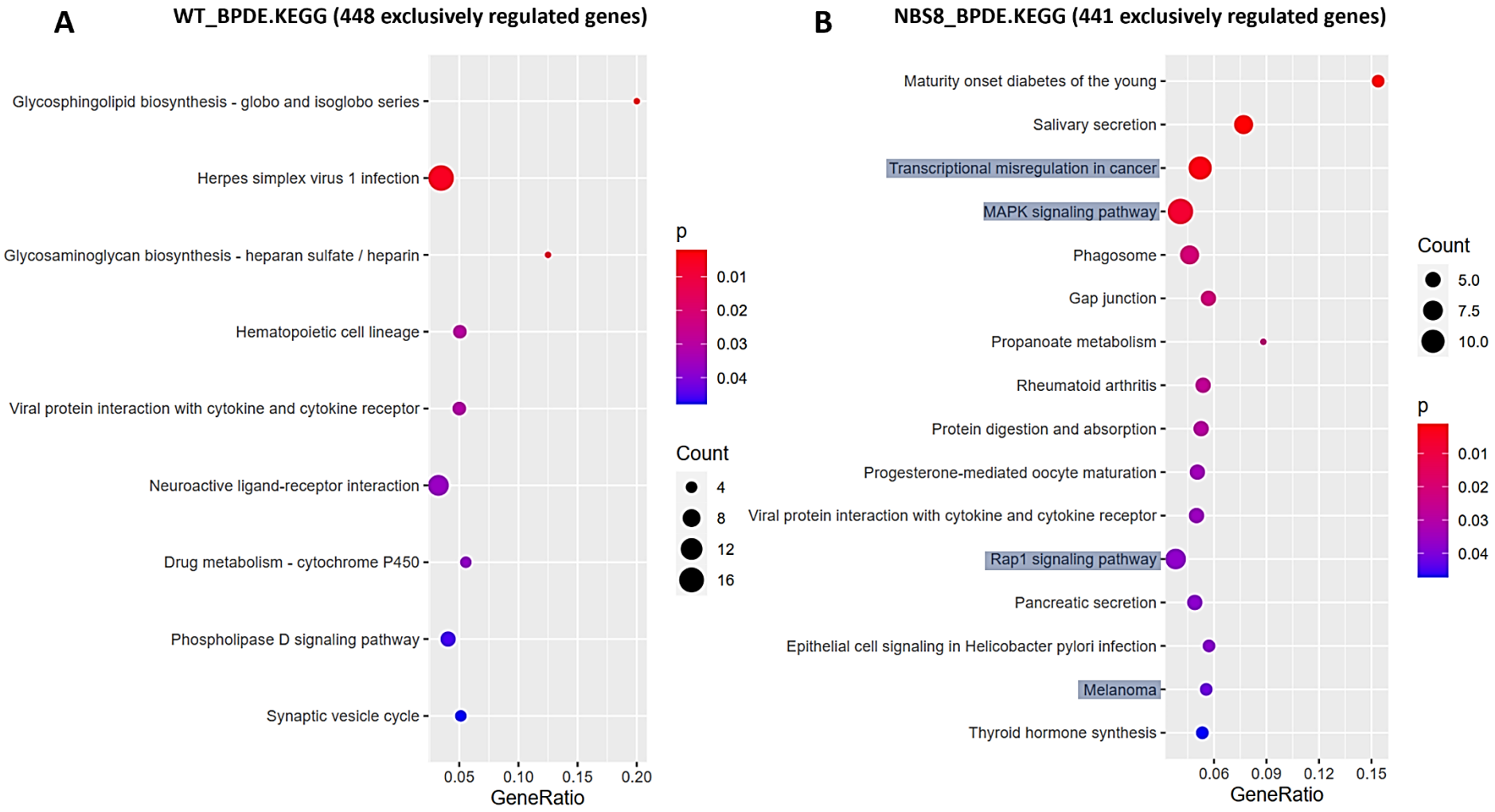

Supplementary Figure 5: BPDE treatment enhances cancer-related KEGG pathways in NBS8 ihPSCs. Cancer-related clusters are highlighted in purple. **(A)** KEGG pathways from 448 genes exclusively regulated in WT hiPSCs after BPDE treatment. **(B)** KEGG pathways from 441 genes exclusively regulated in NBS8 hiPSCs after BPDE treatment.

A

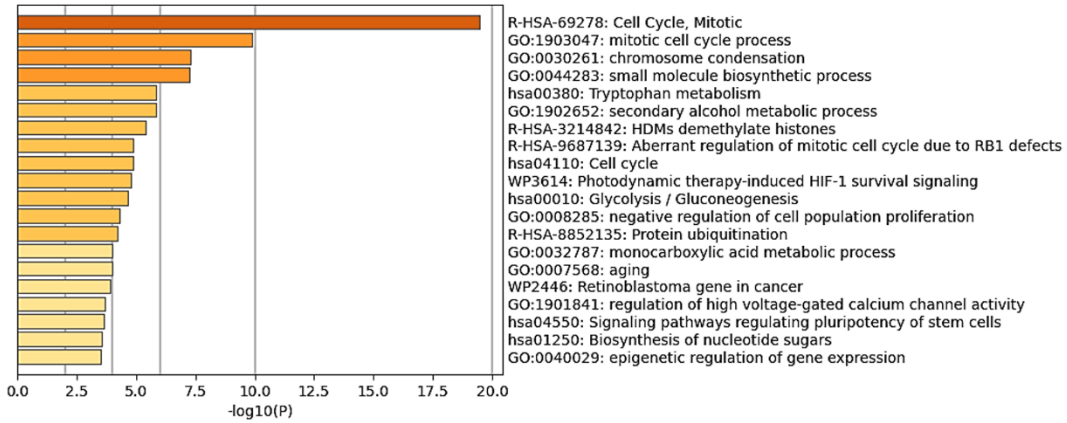

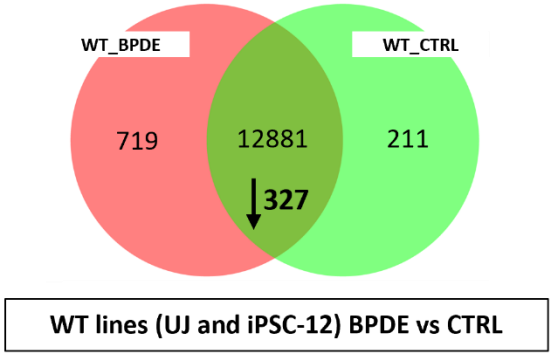

B

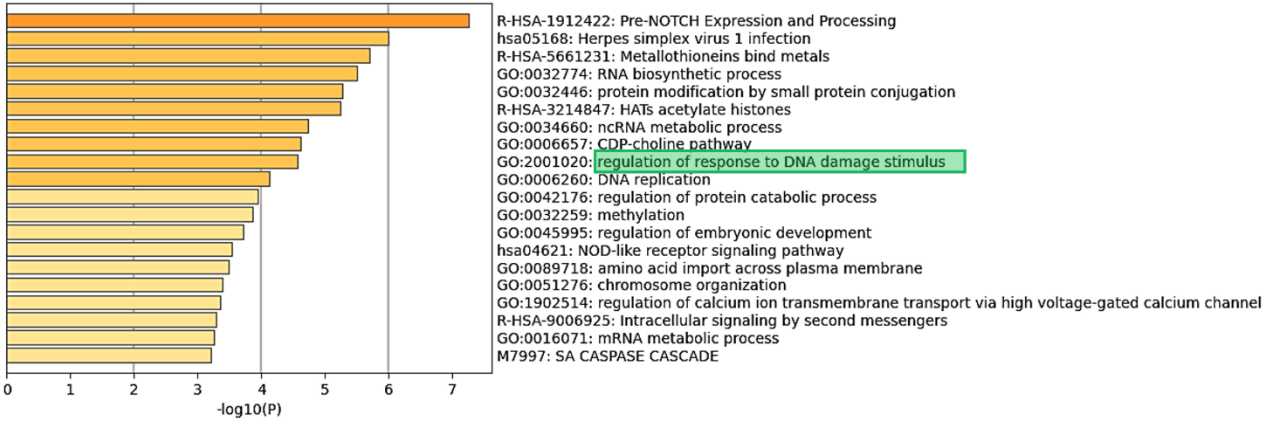

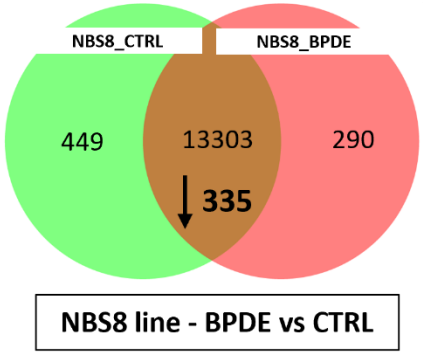

Supplementary Figure 6: Exposure to BPDE downregulates DNA damage response genes in NBS8. (A) Metascape analysis from 327 genes downregulated in WT hiPSCs after BPDE treatment. **(B)** Metascape analysis from 335 genes downregulated in NBS8 hiPSCs after BPDE treatment. Cluster “regulation of response to DNA damage stimulus” is highlighted in green.

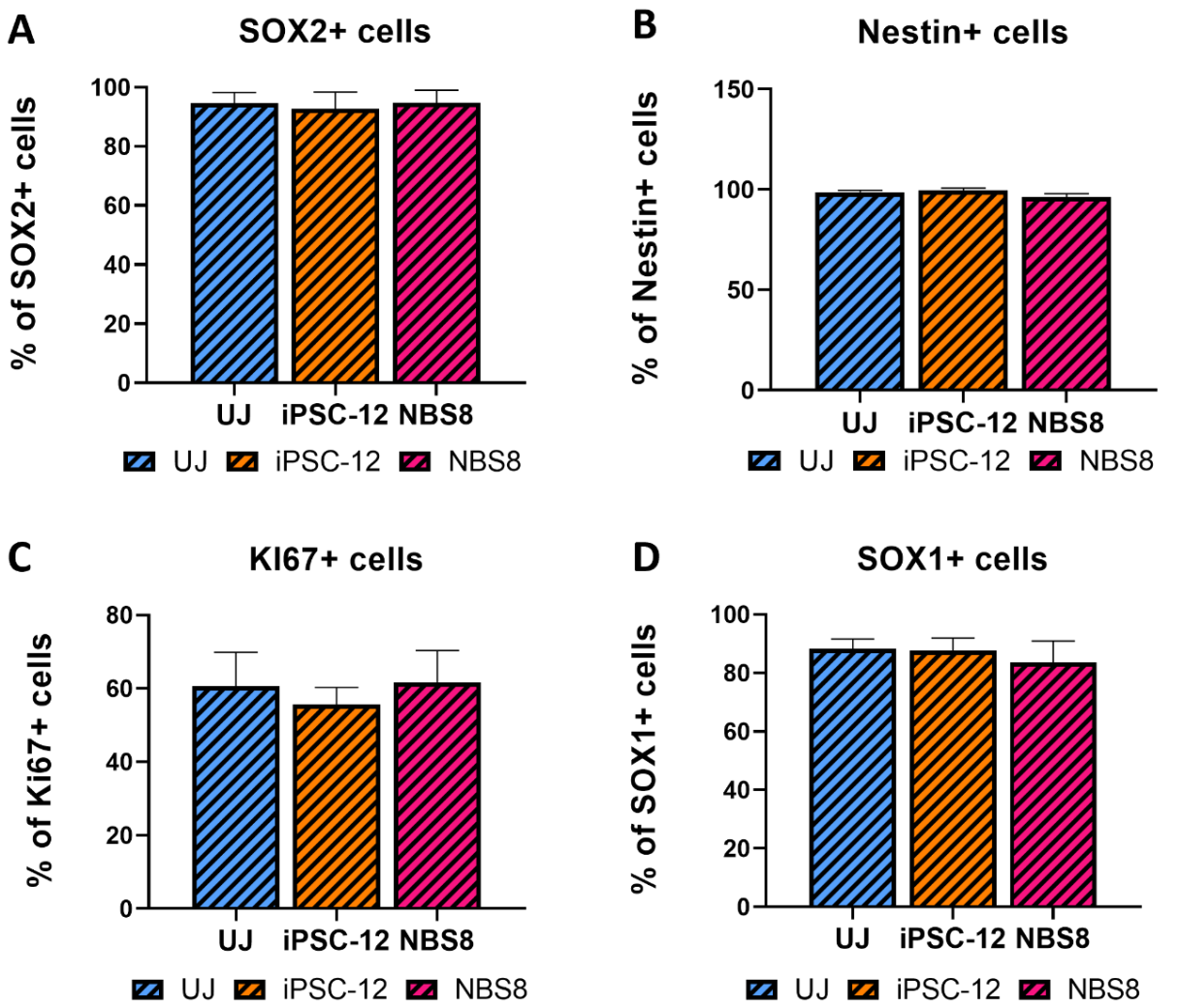

Supplementary Figure 7: Percentage of positive cells stained with key NPC markers in immunocytochemistry. DAPI stained nuclei was used as control. N=7, +/- standard deviation is shown. **(A)** SOX2, **(B)** Nestin, **(C)** Ki67 and **(D)** SOX1.

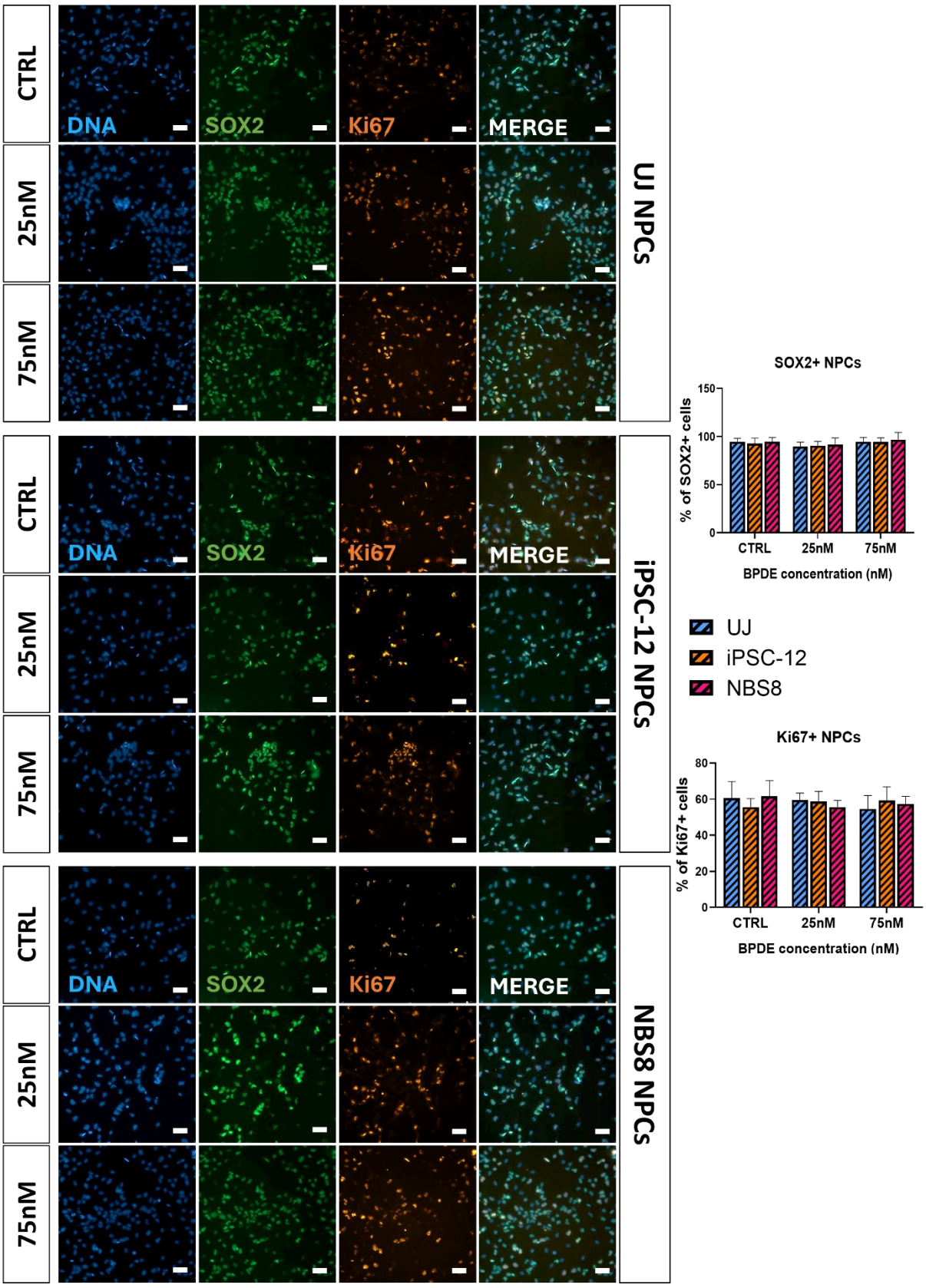

Supplementary Figure 8: Immunocytochemistry of NPCs after BPDE treatment stained for SOX2 and Ki67. Percentage of positive cells is shown. Total cell numbers were calculated by DAPI stained nuclei. N=3, +/- standard deviation. Scale bar 50µm.

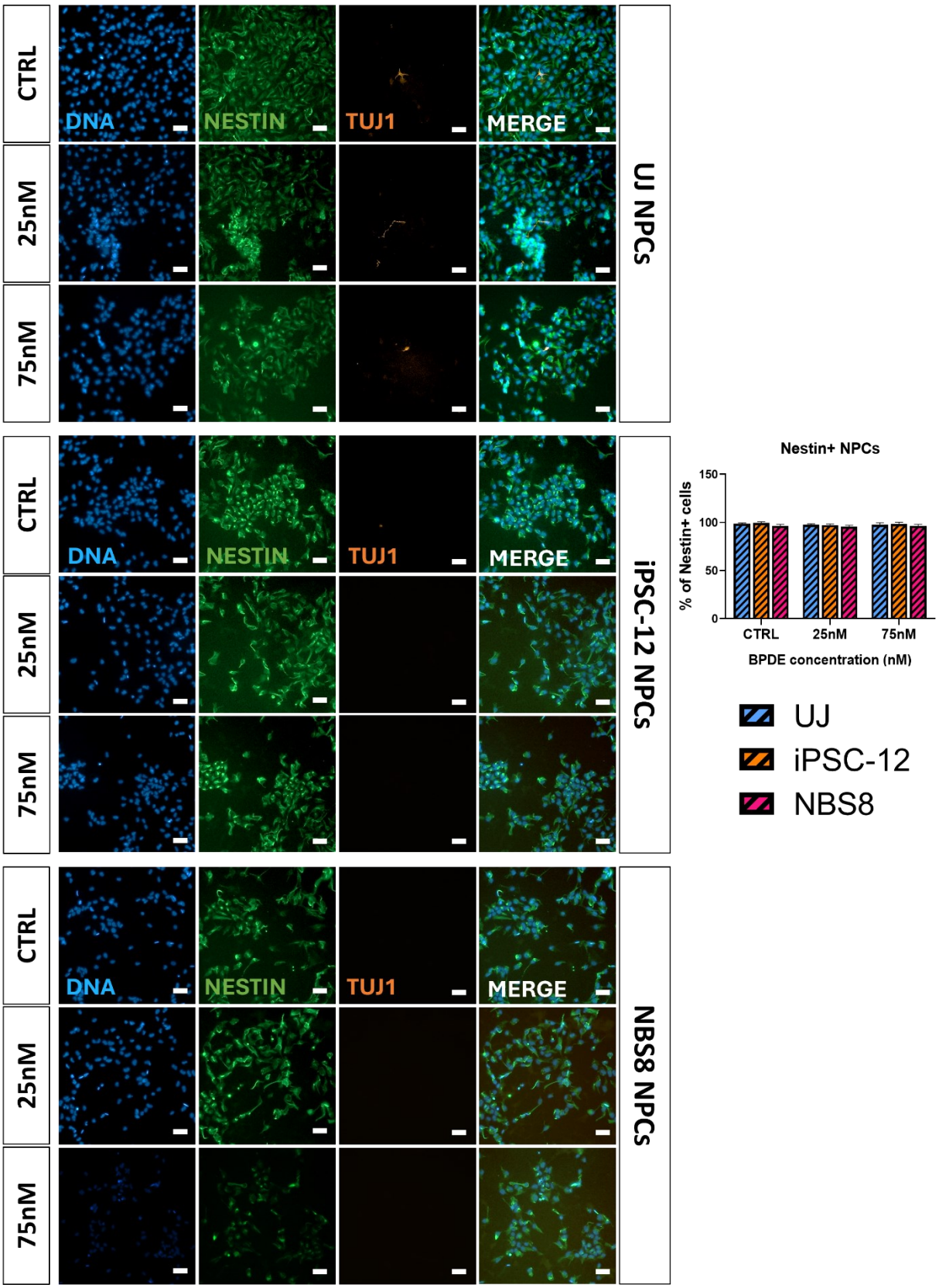

Supplementary Figure 9: Immunocytochemistry of NPCs after BPDE treatment stained for nestin and tuj1. Percentage of positive cells is shown. Total cell numbers were calculated by DAPI stained nuclei. N=3, +/- standard deviation. Scale bar 50µm.

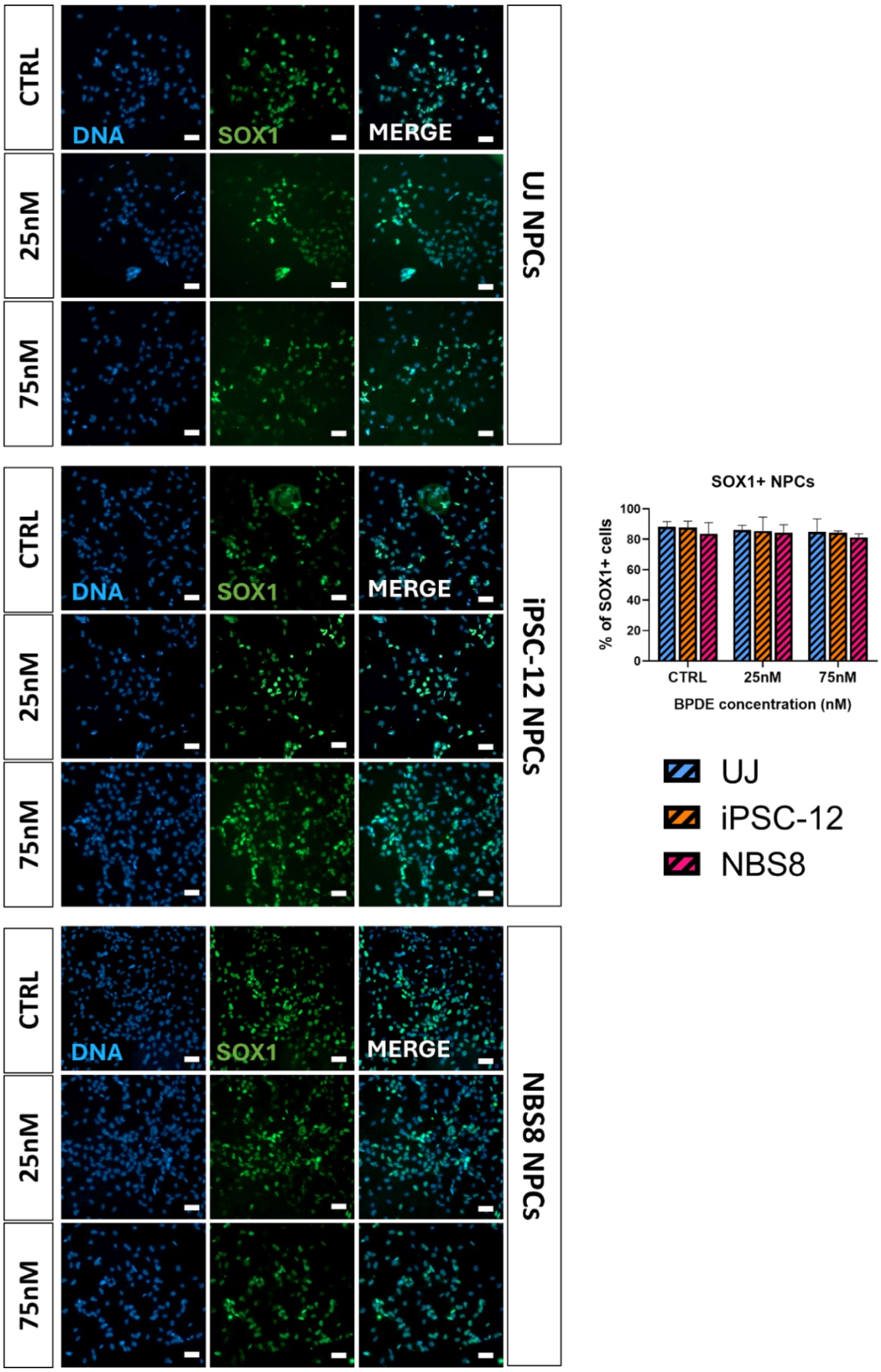

Supplementary Figure 10: Immunocytochemistry of NPCs after BPDE treatment stained for SOX1. Percentage of positive cells is shown. Total cell numbers were calculated by DAPI stained nuclei. N=3, +/- standard deviation. Scale bar 50µm.

Acknowledgements

Thank you

to my family;

to my girlfriend;

to my friends;

to my lab mates and members of the ISRM;

to my supervisor Prof. Dr. James Adjaye;

to my mentor Dr. Nina Graffmann;

to my colleagues and professors from the GRK2578;

to everyone who supported, listened, advised, helped, hugged me when I needed a hug and told me to get a grip when I needed to get a grip.

It’s hard to stand alone and I was lucky to have much help along the way.

Thank you.